

# **Spatiotemporal Evolution of Headwall Erosion Rates in Glacial Landscapes in the Swiss Alps**

## **Kumulative Dissertation**

zur Erlangung des akademischen Grades

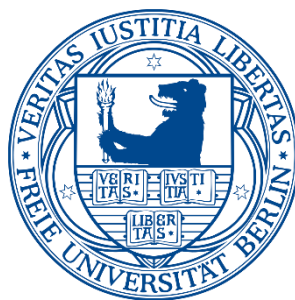
Doktor der Naturwissenschaften

(Dr. rer. nat.)

eingereicht im Fachbereich Geowissenschaften

der Freien Universität Berlin

angefertigt am Deutschen GeoForschungsZentrum Potsdam



**Katharina Wetterauer**

Berlin, Herbst 2023



Erstgutachter: Prof. Dr. Dirk Scherler  
*Freie Universität Berlin, Deutsches GeoForschungsZentrum*

Zweitgutachter: Prof. Dr. Bodo Bookhagen  
*Universität Potsdam*

Tag der Disputation: 16. Februar 2024



# Eidesstattliche Erklärung

Hiermit erkläre ich, die vorliegende Dissertation selbstständig und ohne unzulässige Hilfe angefertigt zu haben. Bei der Verfassung dieser Dissertation wurden keine anderen als die im Text und Literaturverzeichnis aufgeführten Hilfsmittel und Quellen verwendet. Beiträge von Koautoren zu publizierten oder zur Publikation vorbereiteten Manuskripten sind im Vorwort ("Preface") dieser Arbeit dargelegt. Ich versichere, dass die vorgelegte elektronische Version mit der schriftlichen Version der Dissertation übereinstimmt. Ein Promotionsverfahren zu einem früheren Zeitpunkt an einer anderen Hochschule oder einem anderen Fachbereich wurde nicht beantragt.

*Potsdam, 14. November 2023*

---

Katharina Wetterauer



*„Nicht der Berg ist es, den man bezwingt,  
sondern das eigene Ich.“*

(Edmund Hillary)



# Summary

High-alpine landscapes are exposed to pronounced temperature rise due to climate change. In particular, glacial and periglacial dynamics such as glacier retreat and permafrost thaw are accelerating, affecting the stability of rockwalls and posing hazards to the alpine environment. With recent deglaciation, rockfall activity and the production of debris are observed to increase. As the erosion of so-called headwalls above glaciers and associated debris deposition onto the ice surface increase, a thick supraglacial debris cover can form, modifying glacial mass balance and potentially delaying glacier retreat. Yet, debris supply rates and their changes vary spatially. To predict the evolution of glacial landscapes with climate change therefore requires to temporally and spatially examine rockwall erosion and potential temperature-related patterns. However, *in situ* measurements of rockwall erosion rates, specifically at headwalls, are rare as they are potentially dangerous in the difficult-to-access terrain, and the few existing records are often based on short-term monitoring from the last few decades.

This thesis examines spatiotemporal records of headwall erosion in the Swiss Alps on longer terms to study glacial landscape dynamics with climate change. Headwall erosion rates were quantified by concentrations of the *in situ*-produced cosmogenic nuclide  $^{10}\text{Be}$  in medial moraine debris, obtained by interval-sampling along longitudinal moraine profiles. In a first small-scale case study, the archive function of medial moraines and temporal evolution of headwall erosion are studied in detail. Two medial moraine records were combined with a simple glacier transport model to account for the additional accumulation of  $^{10}\text{Be}$  during post-depositional downglacier debris transport and to assess the time of headwall erosion. Systematically varying  $^{10}\text{Be}$  concentrations over approximately the last 200 years indicate an increase in headwall erosion from the end of the Little Ice Age towards the following deglaciation period. This trend is reflected by different debris grain size fractions, implying that the records are unaffected by episodic large-scale erosion. In a follow-up study on a small mountain massif, temporal and spatial patterns of rockwall erosion are examined for five nearby glaciers and in relation to spatially distinct rockwall morphology. As an extension of the first study, ice cover changes across each debris source area were quantified to assess the potential contribution of recently deglaciated bedrock of possibly low  $^{10}\text{Be}$  concentrations, which seems to be low at most sites. Compared to the data from the first study, temporally constant  $^{10}\text{Be}$  concentrations over the last 100 years imply more stable rockwall erosion throughout the deglaciation period. At the same time, rockwall erosion rates are higher at steeper north faces in the massif. In a final, still ongoing study on a large-scale glacier catchment, two high-resolution medial moraine records are combined for the first time with paired *in situ*  $^{14}\text{C}/^{10}\text{Be}$  analysis to resolve erosional landscape transience in more detail. Preliminary analyses suggest that conditions that caused an apparent pulse in erosion in one of two major debris source areas may be minor in the other due to differing headwall deglaciation histories. Yet, such rapid changes in transient landscapes, debris supply from long-time exposed or recently deglaciated surfaces, and post-depositional  $^{10}\text{Be}$  accumulation pose methodological challenges to derive rockwall erosion rates directly from measured medial moraine  $^{10}\text{Be}$  concentrations and require debris particle tracing in glacial landscapes and future research. Eventually, the studies of this thesis demonstrate that  $^{10}\text{Be}$  concentrations along medial moraines provide systematic results in landscapes that typically erode stochastically. Headwall erosion seems to be controlled by slope and temperature, and to accelerate at the transition of the Little Ice Age to deglaciation before stabilizing again - both observations that ultimately highlight the climate sensitivity of glacial landscapes.

# Zusammenfassung

Hochalpine Landschaften sind aufgrund des Klimawandels einem starken Temperaturanstieg ausgesetzt, wobei sich insbesondere glaziale und periglaziale Dynamiken beschleunigen, wie der Rückzug der Gletscher und das Auftauen des Permafrosts. Diese Veränderungen beeinträchtigen unter anderem auch die Stabilität von Felswänden und stellen eine Gefahr für die alpine Umwelt dar. Beobachtungen deuten darauf hin, dass Steinschläge und Felsstürze sowie die Produktion von Schutt mit dem rezenten Eisrückgang im Hochgebirge zunehmen. Nimmt die Erosion sogenannter Stirnwände am Kopf von Gletschern zu und steigt die damit verbundene Schuttablagerung auf der Eisoberfläche an, kann sich eine dicke supraglaziale Schuttdecke bilden, die die Massenbilanz der Gletscher verändert und den Gletscherrückzug möglicherweise verzögert. Allerdings unterscheiden sich die Raten des Schutteintrags und deren Veränderungen räumlich. Prognosen über die Entwicklung glazialer Landschaften im Zuge des Klimawandels erfordern daher sowohl zeitliche als auch räumliche Untersuchungen der Erosion alpiner Felswände sowie potenzieller temperaturbedingter Muster. Bisher gibt es jedoch nur wenige *in situ* Messungen von Erosionsraten an Felswänden und insbesondere an Gletscher-Stirnwänden, da diese in dem schwer zugänglichen Gelände potenziell gefährlich sind. Außerdem beruhen die wenigen vorhandenen Datensätze häufig nur auf Kurzzeitbeobachtungen der letzten Jahrzehnte.

In der vorliegenden Doktorarbeit werden raumzeitliche Daten zur Erosion von Gletscher-Stirnwänden in den Schweizer Alpen über längere Zeiträume analysiert, um die Dynamiken glazialer Landschaften in Zeiten des Klimawandels näher zu untersuchen. Erosionsraten der Stirnwände wurden dabei anhand von Konzentrationen des *in situ*-produzierten kosmogenen Nuklids  $^{10}\text{Be}$  in Mittelmoränenschutt quantifiziert, wofür Intervall-Proben entlang von Längsprofilen der Moränen genommen wurden. In einer ersten kleinräumigen Fallstudie werden zunächst die Archivfunktion von Mittelmoränen sowie die zeitliche Entwicklung der Stirnwanderosion im Detail untersucht. Hierfür wurden zwei Mittelmoränen-Datensätze mit einem einfachen Gletschertransportmodell kombiniert, um die zusätzliche  $^{10}\text{Be}$ -Akkumulation in Schutt nach seiner Ablagerung und während seines Transports gletscherabwärts sowie den Zeitraum der Stirnwanderosion abzuschätzen. Systematisch variierende  $^{10}\text{Be}$ -Konzentrationen über die letzten 200 Jahre deuten hierbei auf eine Zunahme der Stirnwanderosion vom Ende der Kleinen Eiszeit in die sich anschließende Phase des Gletscherschwundes hin. Dieser Trend spiegelt sich in verschiedenen Korngrößenfraktionen des Schutts wider, was darauf hindeutet, dass die Datensätze nicht durch episodische, erosive Großereignisse verzerrt werden. In einer Folgestudie an einem kleinen Gebirgsmassiv werden anschließend sowohl zeitliche als auch räumliche Muster der Felswanderosion an fünf nahe gelegenen Gletschern untersucht und mit räumlich unterschiedlichen Fels-Morphologien in Beziehung gesetzt. Als Erweiterung der ersten Studie wurden zudem Veränderungen in der Eisbedeckung jedes Schuttquellengebiets quantifiziert, um den eventuellen Eintrag von Festgestein abzuschätzen, das erst kürzlich eisfrei wurde und niedrigere  $^{10}\text{Be}$ -Konzentrationen aufweisen könnte. An den meisten Standorten wurde dieser Eintrag als gering eingestuft. Im Vergleich zu den Datensätzen der ersten Studie verweisen zeitlich stabilere  $^{10}\text{Be}$ -Konzentrationen über die letzten 100 Jahre auf konstantere Felswanderosion während Zeiten des Gletscherschwundes hin. Gleichzeitig erscheinen die Erosionsraten für steilere Nordwände des Massivs höher. Abschließend werden in einer noch laufenden Studie an einem großflächigeren Gletscher Einzugsgebiet zwei hochauflösende Mittelmoränen-Datensätze erstmals mit *in situ*  $^{14}\text{C}/^{10}\text{Be}$  Analysen kombiniert, um die Erosion

in Landschaften, die sich in einem Übergangszustand befinden, noch detaillierter zu erfassen. Vorläufige Analysen deuten darauf hin, dass Bedingungen, die einen offensichtlichen Erosionsschub in einem der beiden großen Schuttquellengebiete verursachten, in dem anderen Gebiet kaum oder nur in geringem Maße vorhanden sind. Dies könnte auf einen unterschiedlich stark ausgeprägten Eisrückgang an den jeweiligen Stirnwänden zurückzuführen sein. Solche rapiden Veränderungen in transienten Landschaften, der Schutteintrag von längerfristig exponierten oder erst kürzlich eisfrei gewordenen Oberflächen und die zusätzliche  $^{10}\text{Be}$ -Akkumulation in Schutt nach seiner Ablagerung stellen jedoch die direkte Ableitung von Felswand-Erosionsraten aus  $^{10}\text{Be}$ -Konzentrationen in Mittelmoränenschutt vor methodische Herausforderungen, die die Verfolgung von Schuttpartikeln in glazialen Landschaften erfordern und weiterer Erforschung bedürfen. Schließlich zeigen die Untersuchungen dieser Doktorarbeit, dass  $^{10}\text{Be}$ -Konzentrationen entlang von Mittelmoränen systematische Ergebnisse für Landschaften liefern, die für gewöhnlich stochastisch erodieren. Die Stirnwanderosion scheint von der Hangneigung und Temperatur abzuhängen und sich zunächst während der Übergangsphase von der Kleinen Eiszeit in die anschließende Gletscherschwund-Phase zu beschleunigen, bevor sie sich wieder stabilisiert - beides Beobachtungen, die letztlich die Klimasensitivität von Gletscherlandschaften verdeutlichen.

# Preface

In this thesis, I present my scientific studies on the "*Spatiotemporal Evolution of Headwall Erosion Rates in Glacial Landscapes in the Swiss Alps*" as part of the ERC-funded project "COLD - Climate Sensitivity of Glacial Landscape Dynamics". The thesis is written in cumulative form and includes a general introduction, three individual studies, and a summary conclusion. The individual studies are prepared in manuscript style of scientific journals, with the first and second published, and the third in progress for submission. As the individual manuscripts are written in a way that they can be read and understood on their own, there will be repetition of introductory and methodological content throughout the thesis. Chapter structure, contents, and contributions from co-authors are as follows:

**Chapter 1** is the general introduction of this thesis, in which I outline the need to study and quantify rockwall erosion in climate-sensitive glacial landscapes, highlight the current state of science as well as research gaps, and present the methodological strategy for pursuing the research questions underlying this work.

**Chapter 2** presents the first scientific study entitled "*Temporal evolution of headwall erosion rates derived from cosmogenic nuclide concentrations in the medial moraines of Glacier d'Otemma, Switzerland*". It examines headwall erosion rates through time and the function of medial moraines as archives of headwall erosion above glaciers for a small-scale case study. The chapter is published in *Earth Surface Processes and Landforms* (**Wetterauer et al., 2022a**), the corresponding dataset is available as accompanying data publication at *GFZ Data Services* (**Wetterauer et al., 2022b**). Authors of the study are Katharina Wetterauer, Dirk Scherler, Leif S. Anderson, and Hella Wittmann. KW carried out sample collection, sample preparation, data evaluation, and modelling. DS conceived and supervised the project, derived the remotely-sensed glacier surface velocities, and was the main advisor during sample collection, data evaluation, and modelling. LSA supported sample collection and was available for discussion during data evaluation and modelling. HW was the main advisor during sample preparation and responsible for the *in situ*  $^{10}\text{Be}$  laboratory training. KW prepared the initial draft, figures and tables, and adjusted the manuscript based on the comments and edits of DS, LSA, and HW.

**Chapter 3** presents the second scientific study entitled "*Spatial and temporal variations in rockwall erosion rates derived from cosmogenic  $^{10}\text{Be}$  in medial moraines at five valley glaciers around Pigne d'Arolla, Switzerland*". It expands on the first study and examines rockwall erosion rates at five morphologically distinct sites to study spatiotemporal erosional patterns across a small mountain massif. The chapter is published in *Earth Surface Dynamics* (**Wetterauer & Scherler, 2023a**), the corresponding dataset is available as accompanying data publication at *GFZ Data Services* (**Wetterauer & Scherler, 2023b**). Authors of the study are Katharina Wetterauer and Dirk Scherler. KW carried out sample collection and preparation, conducted the data analyses, and prepared the manuscript based on the comments and edits of DS. DS conceived and supervised the project and was the main advisor during data analyses and manuscript drafting.

**Chapter 4** presents the third scientific study entitled “*Two different histories of headwall erosion at Grosser Aletschgletscher, Switzerland: first insights from medial moraine cosmogenic nuclides*”. It examines spatiotemporal changes in headwall erosion and erosional transience at high resolution at the largest glacier in the European Alps. The study is still in progress to be submitted to a scientific journal at a later stage. The presented results and explanations are thus preliminary. The scientific focus was designed by Katharina Wetterauer and Dirk Scherler. So far, KW carried out sample collection, sample preparation, data evaluation, and prepared the manuscript. DS conceived the project and was the main advisor during all steps so far. In the further course, the study will be supported by Guillaume Jouvét.

**Chapter 5** is the final synthesis of this thesis, in which I return to the initial research questions and consider the three scientific studies together as well as in context with previous studies on high-alpine glacial landscapes.

# List of Figures

<b>Figure 1.1:</b> Sediment production, deposition, and transport in glacial landscapes.....	2
<b>Figure 1.2:</b> Examples of stochastic rockwall erosion within glacial settings in the European Alps .....	3
<b>Figure 1.3:</b> Enhanced rockfall activity and supraglacial debris cover expansion in the European Alps after the Little Ice Age ..	5
<b>Figure 1.4:</b> Schematic of processes and conditions affecting concentrations of <i>in situ</i> -produced cosmogenic <sup>10</sup> Be in medial moraine debris.....	12
<b>Figure 1.5:</b> Overview of the glacier sites in Switzerland investigated as part of this thesis.....	15
<b>Figure 2.1:</b> Glacier d’Otemma, Switzerland .....	21
<b>Figure 2.2:</b> Debris source area Petit Mont Collon .....	22
<b>Figure 2.3:</b> Glacier d’Otemma and debris source area Petit Mont Collon in 2010, 1973, and 1850....	26
<b>Figure 2.4:</b> Schematic of the headwall-glacier-system and setup of the debris trajectory model .....	27
<b>Figure 2.5:</b> [ <sup>10</sup> Be] <sub>measured</sub> in medial moraine samples along Glacier d’Otemma.....	28
<b>Figure 2.6:</b> Medial moraine data of Glacier d’Otemma through time .....	30
<b>Figure 2.7:</b> Chronological overview on available historical datasets from Petit Mont Collon .....	35
<b>Figure 3.1:</b> Pigne d’Arolla massif, Switzerland .....	44
<b>Figure 3.2:</b> Morphology of ice-free rock faces and slopes of the Pigne d’Arolla massif .....	45
<b>Figure 3.3:</b> Glacier surface velocities, reconstructed from 10 boulder-tracking periods .....	52
<b>Figure 3.4:</b> Glacier change at the four new study sites since 1880 .....	53
<b>Figure 3.5:</b> Comparison of uncorrected [ <sup>10</sup> Be] <sub>measured</sub> and transport-corrected [ <sup>10</sup> Be] <sub>rockwall</sub> .....	56
<b>Figure 3.6:</b> Ice cover changes across deglaciating source rockwalls in the Pigne d’Arolla massif.....	59
<b>Figure 3.7:</b> Comparison of apparent mean rockwall erosion rates .....	63
<b>Figure 4.1:</b> Grosser Aletschgletscher, Switzerland .....	70
<b>Figure 4.2:</b> <sup>10</sup> Be and <sup>14</sup> C records along the Kranzberg and Trugberg medial moraine .....	75
<b>Figure 4.3:</b> Headwall morphology at Kranzberg and Trugberg in 1850, 1973, and 2016.....	76
<b>Figure 4.4:</b> <sup>10</sup> Be production rates across ice-free source headwalls in 1850, 1973, and 2016 .....	77
<b>Figure 4.5:</b> Historical images of the ice confluences at Kranzberg and Trugberg .....	79
<b>Figure 5.1:</b> Systematic temporal variability in all currently existing medial moraine records.....	86
<b>Figure A1:</b> Grain size spectra of the medial moraine samples from Glacier d’Otemma.....	108
<b>Figure A2:</b> Data used to simulate medial moraine debris transport on Glacier d’Otemma.....	110
<b>Figure A3:</b> Vertical ice surface change of Glacier d’Otemma .....	112
<b>Figure A4:</b> ELA estimates for Glacier d’Otemma.....	115
<b>Figure A5:</b> Glacier mass balance records from the European Alps.....	115
<b>Figure A6:</b> Downglacier debris particle distances at Glacier d’Otemma .....	117
<b>Figure A7:</b> Debris particle trajectories at Glacier d’Otemma .....	118
<b>Figure B1:</b> Hillshade images of ice-free rockwalls at Pigne d’Arolla in 2017, 1973, and 1850 .....	123
<b>Figure B2:</b> Weighted debris supply/deposition along the medial moraine of Glacier du Brenay .....	124
<b>Figure B3:</b> Modelled debris particle trajectories at Glacier du Brenay .....	125
<b>Figure B4:</b> Modelled debris particle trajectories at Glacier de Cheilon, Pièce, and Tsijiore Nouve..	126
<b>Figure B5:</b> Orthoimage from 1983 indicating englacial debris transport .....	127
<b>Figure B6:</b> Permafrost distribution map .....	128

# List of Tables

<b>Table 1.1:</b> Published rockwall erosion rates from different quantification approaches .....	6
<b>Table 2.1:</b> Data for medial moraine debris samples collected on Glacier d’Otemma .....	23
<b>Table 2.2:</b> Measured AMS $^{10}\text{Be}/^9\text{Be}$ ratios and $^{10}\text{Be}$ concentrations .....	24
<b>Table 2.3:</b> Modelled sample ages, burial depth, and $^{10}\text{Be}_{\text{transport}}$ , as well as derived $^{10}\text{Be}_{\text{headwall}}$ and apparent headwall erosion rates .....	29
<b>Table 2.4:</b> Computed headwall $^{10}\text{Be}$ production rates and absorption mean free paths .....	34
<b>Table 3.1:</b> Medial moraine debris samples from the Pigne d’Arolla massif, as well as AMS data ....	50
<b>Table 3.2:</b> Model results with samples ages, burial depth, and $^{10}\text{Be}_{\text{transport}}$ , as well as $^{10}\text{Be}_{\text{rockwall}}$ and derived minimum and maximum apparent rockwall erosion rates .....	55
<b>Table 3.3:</b> Geomorphic parameters of source rockwalls in the years 1850, 1973, and 2017 .....	57
<b>Table 4.1:</b> Medial moraine samples from Grosser Aletschgletscher and AMS $^{10}\text{Be}$ data .....	72
<b>Table 4.2:</b> AMS $^{14}\text{C}$ data and derived $^{14}\text{C}/^{10}\text{Be}$ ratios .....	73
<b>Table A1:</b> List of parameters used within the 1D debris particle trajectory model.....	111
<b>Table A2:</b> Recent and past glacier surface velocities at Glacier d’Otemma from Glen’s flow law ..	113
<b>Table B1:</b> Comparison of model results using different glacier surface velocity projections.....	129
<b>Table B2:</b> 40-year record of glacier surface velocities at Glacier du Brenay .....	131
<b>Table B3:</b> 40-year record of glacier surface velocities at Glacier de Cheilon .....	132
<b>Table B4:</b> 40-year record of glacier surface velocities at Glacier de Pièce .....	134
<b>Table B5:</b> 40-year record of glacier surface velocities at Glacier de Tsijiore Nouve .....	135

# List of Publications

- Chapter 2**  
(published article)
- Wetterauer, K., Scherler, D., Anderson, L.S. & Wittmann, H. (2022a) Temporal evolution of headwall erosion rates derived from cosmogenic nuclide concentrations in the medial moraines of Glacier d'Otemma, Switzerland.  
*Earth Surface Processes and Landforms*, 47, 2437-2454.  
<https://doi.org/10.1002/esp.5386>  
\*This work is distributed under the Creative Commons Attribution 4.0 License
- Appendix A**  
(published data)
- Wetterauer, K., Scherler, D., Anderson, L.S. & Wittmann, H. (2022b) Sample and modelling data for cosmogenic  $^{10}\text{Be}$  in medial moraine debris of Glacier d'Otemma, Switzerland.  
*GFZ Data Services*.  
<https://doi.org/10.5880/GFZ.3.3.2021.007>
- Chapter 3**  
(published article)
- Wetterauer, K. & Scherler, D. (2023a) Spatial and temporal variations in rockwall erosion rates derived from cosmogenic  $^{10}\text{Be}$  in medial moraines at five valley glaciers around Pigne d'Arolla, Switzerland.  
*Earth Surface Dynamics*, 11, 1013-1033.  
<https://doi.org/10.5194/esurf-11-1013-2023>  
\*This work is distributed under the Creative Commons Attribution 4.0 License
- Appendix B**  
(published data)
- Wetterauer, K. & Scherler, D. (2023b) Medial moraine cosmogenic  $^{10}\text{Be}$  data and glacier surface velocities from four Swiss valley glaciers around Pigne d'Arolla.  
*GFZ Data Services*.  
<https://doi.org/10.5880/GFZ.3.3.2023.002>
- Chapter 4**  
(manuscript in preparation)
- Wetterauer, K. & Scherler, D. (in prep.) Two different histories of headwall erosion at Grosser Aletschgletscher, Switzerland: first insights from medial moraine cosmogenic nuclides.

# Table of contents

Summary .....	i
Zusammenfassung .....	ii
Preface .....	iv
List of Figures .....	vi
List of Tables .....	vii
List of Publications .....	viii

<b>1 Introduction.....</b>	<b>1</b>
1.1 Climate sensitivity of glacial landscape dynamics .....	1
1.2 Quantifying rates of high-alpine rockwall erosion .....	6
1.3 <i>In situ</i> -produced cosmogenic nuclides as tracer of Earth surface processes .....	8
1.3.1 Cosmogenic nuclide geochemistry.....	8
1.3.2 Cosmogenic nuclides in high-alpine glacial landscapes .....	9
1.3.3 Headwall <sup>10</sup> Be in medial moraine debris.....	11
1.4 Research aims and questions .....	14
<b>2 Temporal evolution of headwall erosion rates derived from cosmogenic nuclide concentrations in the medial moraines of Glacier d’Otemma, Switzerland .....</b>	<b>17</b>
2.1 Introduction.....	18
2.2 Glacial headwalls and medial moraines.....	19
2.3 Study area .....	20
2.3.1 Glacier d’Otemma and its catchment .....	20
2.3.2 Medial moraines and their source areas .....	21
2.4 Material and methods.....	23
2.4.1 Medial moraine samples .....	23
2.4.2 Cosmogenic nuclides in medial moraine debris .....	25
2.4.3 Computation of downglacier debris transport .....	26
2.5 Results.....	28
2.5.1 Measured <sup>10</sup> Be concentrations .....	28
2.5.2 Transport and headwall <sup>10</sup> Be concentrations, and sample ages.....	30
2.5.3 Apparent headwall erosion rates.....	31
2.6 Discussion.....	31
2.6.1 Grain size-dependent <sup>10</sup> Be concentrations.....	31
2.6.2 Temporal variations in apparent headwall erosion rates .....	33
2.6.3 Medial moraines in comparison .....	36
2.6.4 Methodological conclusions and future opportunities.....	37
2.7 Conclusions.....	38
2.8 Data availability .....	39
2.9 Acknowledgements .....	39

### **3 Spatial and temporal variations in rockwall erosion rates derived from cosmogenic $^{10}\text{Be}$ in medial moraines at five valley glaciers around Pigne d’Arolla, Switzerland.. 41**

3.1	Introduction .....	42
3.2	Study area .....	43
3.2.1	Pigne d’Arolla massif.....	43
3.2.2	Glacier du Brenay .....	46
3.2.3	Glacier de Cheilon .....	46
3.2.4	Glacier d’Otemma.....	46
3.2.5	Glacier de Pièce .....	47
3.2.6	Glacier de Tsijiore Nouve.....	47
3.3	Material and methods .....	48
3.3.1	$^{10}\text{Be}$ -derived rockwall erosion rates from medial moraine debris .....	48
3.3.1.1	Debris sampling, $^{10}\text{Be}$ measurements, and $^{10}\text{Be}$ production in rockwalls..	49
3.3.1.2	Debris transport time and additional $^{10}\text{Be}$ production .....	51
3.3.2	Source rockwall analysis.....	54
3.4	Results .....	54
3.4.1	Glacier surface velocities, estimated $^{10}\text{Be}$ transport concentrations, and sample ages.....	54
3.4.2	Measured $^{10}\text{Be}$ and estimated $^{10}\text{Be}$ rockwall concentrations .....	56
3.4.3	Apparent rockwall erosion rates .....	56
3.4.4	Source rockwall morphology .....	57
3.5	Discussion .....	58
3.5.1	How “apparent” are the rockwall erosion rate estimates? .....	58
3.5.2	Spatial trends in apparent rockwall erosion .....	62
3.6	Conclusions .....	65
3.7	Data availability .....	66
3.8	Acknowledgements .....	66

### **4 Two different histories of headwall erosion at Grosser Aletschgletscher, Switzerland: first insights from medial moraine cosmogenic nuclides..... 67**

4.1	Introduction .....	68
4.2	Study area .....	69
4.2.1	Grosser Aletschgletscher.....	69
4.2.2	Kranzberg and Trugberg medial moraine .....	71
4.3	Material and methods .....	71
4.3.1	Sample collection and processing .....	71
4.3.2	Principles of paired $^{14}\text{C}/^{10}\text{Be}$ analysis.....	73
4.3.3	Topographic analysis .....	74
4.4	Results .....	74
4.4.1	Measured $^{10}\text{Be}$ and $^{14}\text{C}$ concentrations .....	74
4.4.2	Debris source area characteristics .....	75

4.5	Discussion and implications.....	77
4.5.1	Preliminary assessment of minimum headwall erosion rates.....	77
4.5.2	Contrasting histories of headwall erosion at two nearby source areas.....	78
4.5.3	Outlook.....	81
4.5.4	Preliminary conclusions.....	82
4.6	Data availability.....	83
4.7	Acknowledgements.....	83
<b>5</b>	<b>Synthesis and conclusions.....</b>	<b>85</b>
	<b>References.....</b>	<b>91</b>
	<b>Appendix A: supplement of Chapter 2.....</b>	<b>107</b>
	<b>Appendix B: supplement of Chapter 3.....</b>	<b>121</b>
	<b>Appendix C: sample IGSN.....</b>	<b>137</b>
	<b>Danksagung.....</b>	<b>139</b>



# Introduction

## 1.1 Climate sensitivity of glacial landscape dynamics

Cold mountain landscapes are particularly sensitive to climatic changes (Haeberli & Beniston, 1998). During the late 20th century, global warming has been anomalously high compared to the last millennium (Mann *et al.*, 1999). The surface temperatures of the last decade were 1.1 °C higher on average than during the period from 1850 to 1900 (IPCC, 2022), and recent warming trends of 0.3 °C per decade in the mountains outpace the global average of 0.2 °C per decade (e.g., Hock *et al.*, 2019). As warming is considered an elevation-dependent process, especially high-alpine regions are confronted by amplified and more rapid temperature changes (Pepin *et al.*, 2015). With temperature rise, in particular glacial and periglacial areas face changes in precipitation and ice accumulation that will affect the mass balance and dynamics within the high-alpine cryosphere. In response, the rates at which mountain glaciers retreat or permafrost degrades are changing, too. Globally, glacier retreat has accelerated towards the end of the 20th century (e.g., Haeberli *et al.*, 1999; Dyurgerov & Meier, 2000), and glaciers are projected to lose about 26 to 41% of their current mass by 2100, causing 49 to 83% of glaciers to disappear (Rounce *et al.*, 2023). However, the magnitude at which the high-alpine cryosphere changes spatially varies (e.g., Farinotti *et al.*, 2020). For the European Alps, projections even indicate near-complete deglaciation by 2100 (Rounce *et al.*, 2023) and the disappearance of mountain permafrost in narrow summits of the Mont Blanc massif below 3850 m (Magnin *et al.*, 2017). Apart from the drastic consequences on the mountain water budget, changes in melt water runoff, mass-wasting processes, and sediment fluxes will alter the hazard patterns and vulnerability of the alpine environment, community, and economy. Therefore, and in particular as the mountain population is expected to grow (e.g., Hock *et al.*, 2019), understanding and quantifying the rates at which cold mountain landscapes change is critical for predicting and mitigating hazards (e.g., Evans & Clague, 1994; Haeberli & Beniston 1998; Hock *et al.*, 2019).

Bedrock erosion and associated sediment production are key surface processes, driving the evolution of cold mountain landscapes (**Figure 1.1**). In glacial settings, erosion is a combination of subglacial erosion acting at the glacier bed and periglacial rockwall erosion dominated by frost damage (e.g., Slaymaker, 2011). Although glaciers are commonly considered most effective in erosion (Hallet *et al.*, 1996), periglacial rockwall erosion and retreat are also central in shaping glaciated terrains, yet less well understood (e.g., Heimsath & McGlynn, 2008).

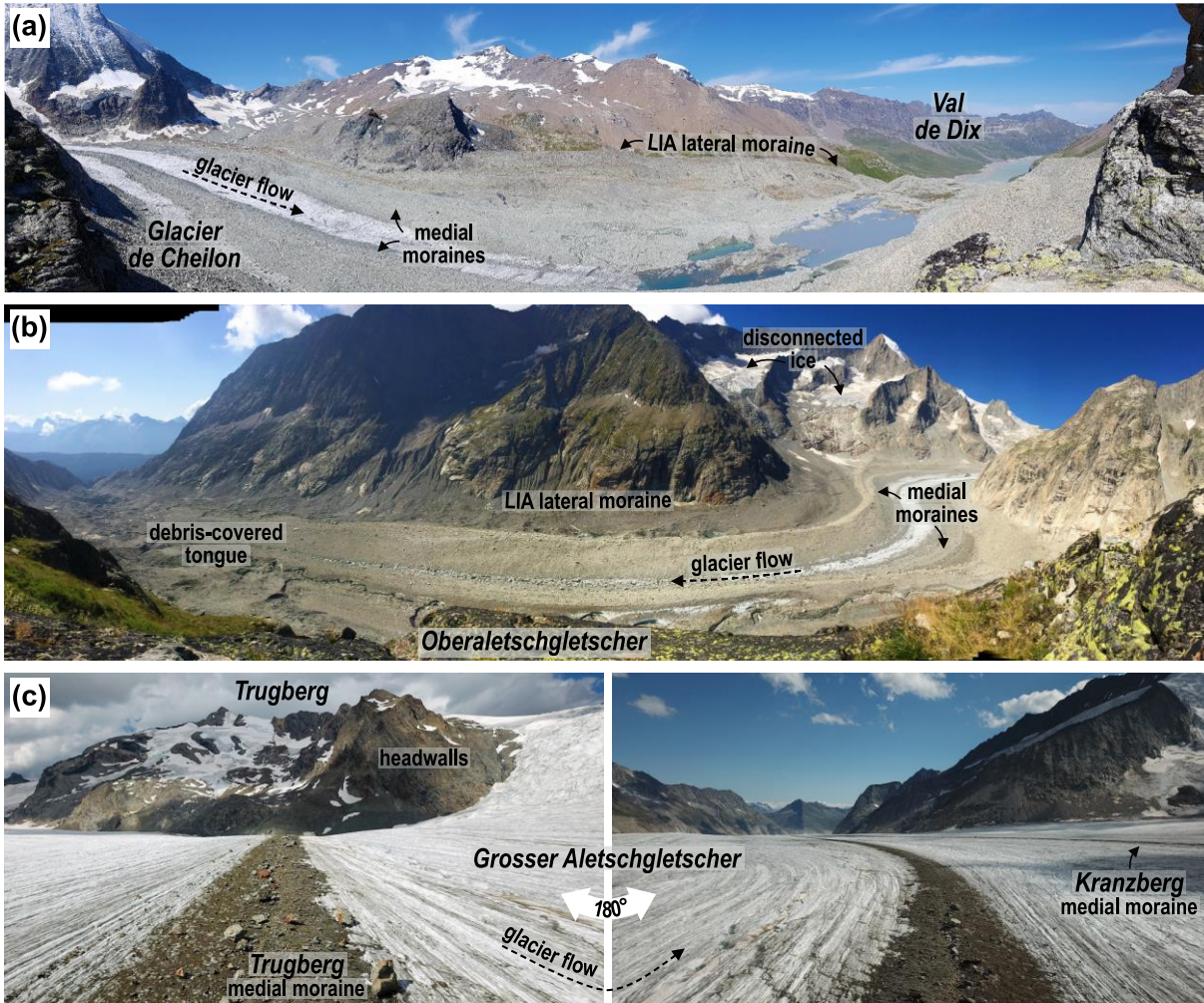


**Figure 1.1:** Sediment production, deposition, and transport in glacial landscapes. (a) View into Val de Dix in the Swiss Alps along Glacier de Cheilon. Note the pronounced recent medial moraines and lateral deposits from the previous greater glacial extent during the Little Ice Age (LIA). (b) View into the valley of Oberaletschgletscher in the Swiss Alps. Note the steepness of source rockwalls that deliver debris to the glacier, and the transition of the medial moraines into a fully debris-covered glacier tongue (field panoramas taken in 2021 and 2019, respectively). (c) Views along the Trugberg medial moraine of Grosser Aletschgletscher in the Swiss Alps, with an upglacier view (left) onto the debris source area Trugberg and a downglacier view (right) towards Konkordiaplatz. Note the parallel running Kranzberg medial moraine in the background (drone images from fieldwork 2019 courtesy of Deniz Gök).

The erosion of steep ice-free rockwalls typically is described as stochastic, proceeding through the mobilization of fractured bedrock by frequent small-scale rockfalls and infrequent large-scale rock avalanches (Figure 1.2; e.g., Boulton & Deynoux, 1981; Small *et al.*, 1997; Anderson, 2000; Arsenaault & Meigs, 2005). The underlying destabilizing processes are assumed to be temperature-sensitive and currently attributed to mainly three interacting physical concepts: (i) Mountain permafrost (i.e., frozen ground at or below 0 °C for at least two consecutive years) is an abundant and important stabilizer in many high-alpine rockwalls, reaching rock depths up to several decametres. Recently, permafrost degradation is considered as the thermal response of bedrock to atmospheric warming. Rockwalls destabilize as the bulk rock mass strength weakens, increasing the likelihood of rockwall failure (e.g., Haeberli *et al.*, 1997; Harris *et al.*, 2009; Huggel *et al.*, 2012; Krautblatter *et al.*, 2013; Smith *et al.*, 2022).

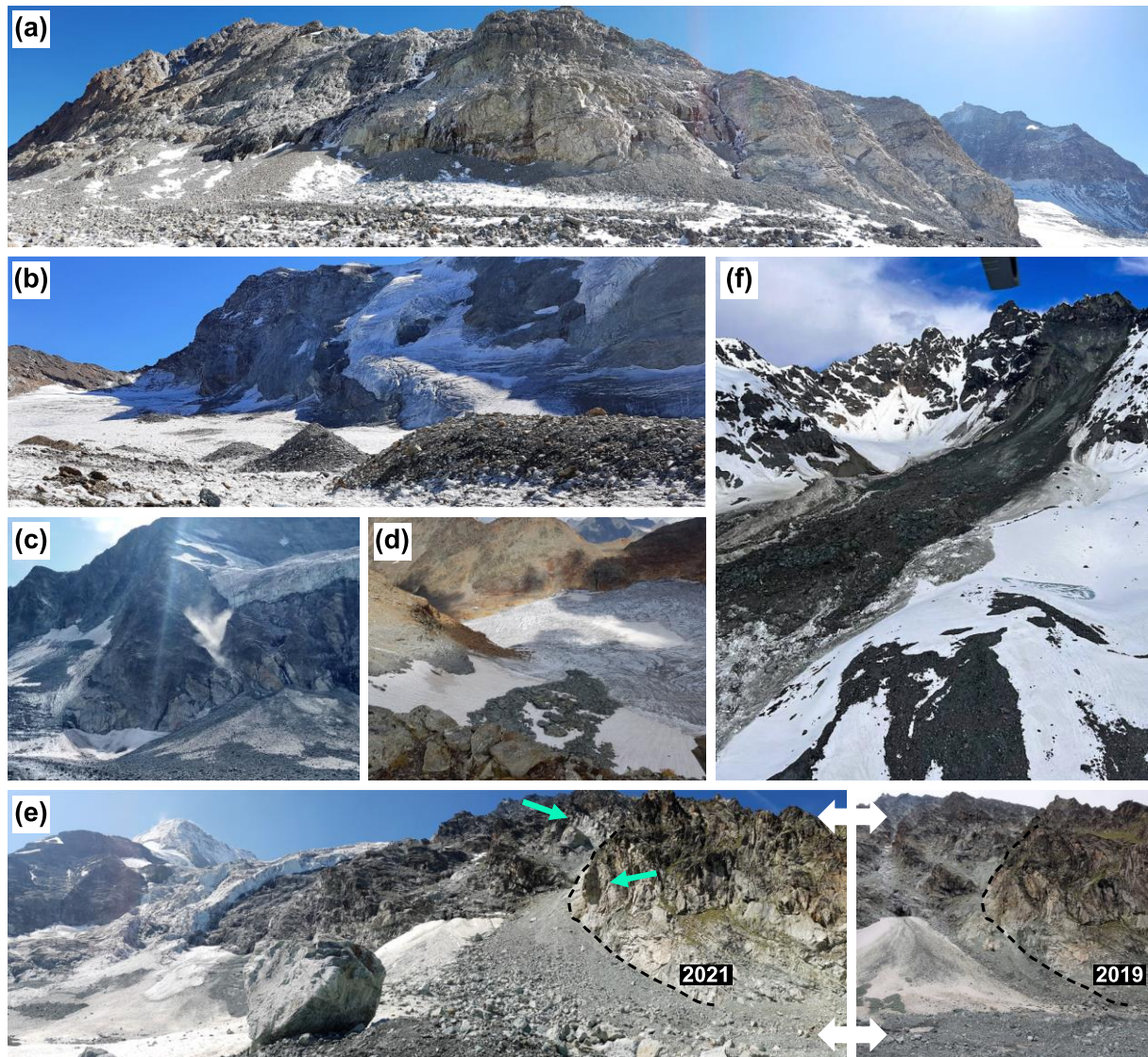


**Figure 1.2:** Examples of stochastic rockwall erosion within glacial settings in the European Alps. Deposits of frequent small-scale rockfalls onto the ice surface at the head of (a) Glacier d’Otemma, (b) Glacier d’Arolla, and (c) Glacier de Pièce in Switzerland, as well as of infrequent medium-scale rockfalls and rock avalanches onto (d) Wütenkarferner in Austria and (e) Glacier de Tsjiore Nouve in Switzerland (field photographs taken between 2018–2021). Note the rockfall captured in (c) and the rockfall scars indicated in (e) from an event which must have occurred between August 2019 and 2021. (f) Deposit of the large-scale rock avalanche from the summit of the Fluchthorn in Austria in June 2023 (© Zeitungsfoto.At/ Riccardo Mizio, 2023).

(ii) Frost cracking (i.e., the breakdown of rock by freezing) favours the growth of bedrock fractures, where water supply is sufficient and where rockwalls extend into an elevation-dependent temperature window between  $-3$  and  $-8$  °C (Anderson, 1998). The process is thought to proceed predominantly through ice segregation as water migrates to freezing fronts in rockwall fractures, and to a lesser extent by volumetric expansion of water upon freezing (e.g., Walder & Hallet, 1985; Hallet *et al.*, 1991; Murton *et al.*, 2006; Hales & Roering, 2007; Matsuoka & Murton, 2008). As temperatures warm and permafrost thaws, frost-cracking efficacy locally may increase according to the altitudinal shift of the favourable subfreezing temperature conditions, and could particularly intensify the basal undercutting of steep rockwalls above glaciers (Scherler, 2014). Frost damage in rockwalls close to glacier surfaces is also suggested to intensify, as permafrost that has penetrated into freshly exposed bedrock after ice subsidence begins to thaw (Wegmann *et al.*, 1998). (iii) Glacial debuttressing through

deglaciation (i.e., removal of supporting ice by glacier retreat) is commonly assumed to destabilize bedrock slopes adjacent to glaciers. Changes in the mechanical stress field due to the unloading by ice and the following bedrock relaxation initiate enhanced rockfall activity or slope failure (e.g., Evans & Clague, 1994; Ballantyne, 2002a; McColl, 2012). Yet, the individual operating mechanisms of these concepts and their interplay are still subject of ongoing debates, and the data base so far is still rather theoretical and experimental in nature.

Where headwalls (i.e., steep rockwalls at the head of valley glaciers) deposit loose fractured rock onto glaciers and where the subsequent downglacier transport of this debris occurs at the ice surface, a supraglacial debris cover can form (**Figure 1.1**; e.g., Boulton & Eyles, 1979; Kirkbride, 1995). Supraglacial debris alters ice ablation as a function of thickness. Sub-debris melt rates increasingly reduce as the debris cover thickens above ~2 cm, and the insulating effect of a 10 cm thick cover already has the potential to reduce melt rates by ~50% (e.g., Østrem, 1959; Mattson *et al.*, 1993; Kayastha *et al.*, 2000). Therefore, a continuous supraglacial debris cover can significantly increase glacier length as a function of high debris supply rates (e.g., Anderson & Anderson, 2016) and allows debris-covered glaciers to exist at lower elevations compared to clean-ice glaciers (**Figure 1.1b**, **Figure 1.3c**; e.g., Deline, 2005; Scherler *et al.*, 2011a). This headwall-glacier-coupling suggests that the climate sensitivity of both systems may be closely related (Scherler & Egholm, 2020) and ultimately leads to the question if temperature-driven headwall destabilization, erosion, and the resultant increasing debris supply rates may retard glacier retreat (e.g., Scherler *et al.*, 2011b).

Observations on rockwall instabilities during the recent post-Little Ice Age (LIA) deglaciation period indeed support enhanced rockfall activity (**Figure 1.3a,b**) related to current temperature rise and glacial thinning (e.g., Holm *et al.*, 2004; Fischer *et al.*, 2006, 2013; Gruber & Haerberli, 2007; Ravanel *et al.*, 2010; Ravanel & Deline, 2011; Hartmeyer *et al.*, 2020a) or extreme warming events (Gruber *et al.*, 2004; Ravanel *et al.*, 2017). Large slope failures appear more frequently, causing extensive runout deposits on glacier surfaces as a likely response to atmospheric warming (Huggel, 2009; Huggel *et al.*, 2010) and glacial debuttressing (Evans & Clague, 1999). Along with the increasing debris supply, supraglacial debris cover appears to be expanding in several mountain ranges post-LIA (**Figure 1.3c**; e.g., Kirkbride, 1993; Deline, 2005; Bolch *et al.*, 2008; Glasser *et al.*, 2016). This observation is becoming increasingly important in the debate on the transformation of clean-ice glaciers to debris-covered glaciers and eventually rock glaciers, the climatically more resilient end-member (e.g., Whalley, 1974; Monnier & Kinnard, 2015; Anderson *et al.*, 2018).

Similar to these present-day changes, slope failures have been observed to follow Late Pleistocene deglaciation (Cossart *et al.*, 2008; Prager *et al.*, 2008; Ballantyne *et al.*, 2014a, 2014b; Curry, 2021). Over multiple glacial cycles, initially high sediment flux rates during early deglaciation after glacier retreat are thought to rapidly adjust to lower non-glacial background rates as glacially-conditioned sources become exhausted (e.g., Church & Ryder, 1972; Ballantyne, 2002a; Antoniazza & Lane, 2021). In other cases, it has been postulated that large rock avalanches that fell on glaciers triggered glacial advances and stagnation independent of climatic forcing (Tovar *et al.*, 2008; Vacco *et al.*, 2010; Menounos *et al.*, 2013).

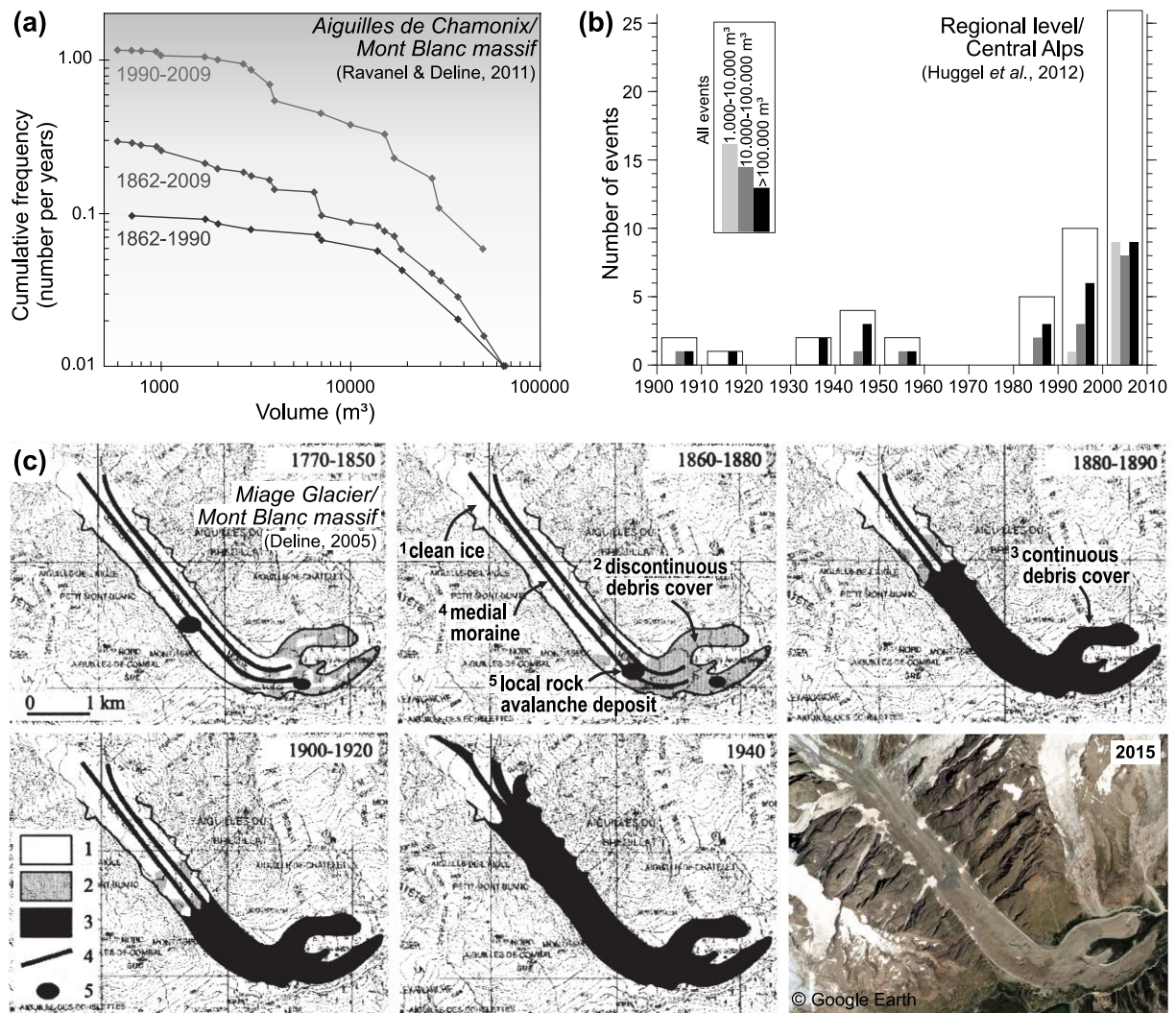


**Figure 1.3:** Enhanced rockfall activity and supraglacial debris cover expansion in the European Alps after the Little Ice Age. **(a)** Rockfall occurrence on the north side of the Aiguilles de Chamonix in France between 1862 and 2009, with an increase in frequency in the recent observation period 1990-2009 compared to 1862-1990 (redrawn from Ravanel & Deline, 2011). **(b)** Number of rock slope failures in the Central Alps between 1900 and 2010, with a large increase in frequency for the most recent decades (redrawn from Huggel *et al.*, 2012). **(c)** Evolution of Miage Glacier in Italy since the end of the Little Ice Age, transforming from a “clean ice state” around 1850 towards a continuously debris-covered state in 1940 (modified from Deline, 2005). For recent comparison, the same section is also shown as Google Earth view from 2015 (<https://earth.google.com>, accessed: 11 August 2023).

Aside from the above described theoretical and observational framework, our understanding of the impact of climate forcing and change on high-alpine rockwall instabilities in general, and on the headwall-glacier-coupling in particular, is still limited. The complexity of mechanisms interacting and the lack of *in situ* measurements make it difficult to assess on which time scales individual mechanisms operate, to predict which geomorphic feedback processes may dominate, and if fluctuations stabilize on the short or long term. In particular, long-term records of rockwall erosion rates are poorly constrained. This challenges integrating bedrock erosion and sediment production into process-based models to realistically project high-alpine changes under ongoing atmospheric warming. Deriving records of headwall erosion rates through time and assessing spatiotemporal patterns in debris supply thus is essential to anticipate the climate sensitivity of glacial landscape dynamics.

## 1.2 Quantifying rates of high-alpine rockwall erosion

Quantifying high-alpine rockwall erosion and specifically headwall erosion in the steep and stochastic glacial landscapes is not trivial (e.g., Heimsath & McGlynn, 2008). To assess rockwall erosion rates, researchers have applied different techniques across a variety of mountainous settings, ranging from direct short-term to indirect long-term observations. Estimates by example studies mentioned below largely span three orders of magnitudes from  $\sim 0.01$  to  $10 \text{ mm yr}^{-1}$  (**Table 1.1**), integrate across different timescales, and may be subject to different biases (e.g., Ganti *et al.*, 2016).

**Table 1.1:** Published rockwall erosion rates from different quantification approaches by selected studies.

Time scale	Method	Study	Location	Erosion rate ( $\text{mm yr}^{-1}$ )	
Multi-year	terrestrial laser scanning	Rabatel <i>et al.</i> (2008)	Tour Ronde / Europ. Alps	8.4	
	terrestrial laser scanning	Kenner <i>et al.</i> (2011)	Gemsstock / Europ. Alps	6.5	
	terrestrial laser scanning	Strunden <i>et al.</i> (2015)	Lauterbrunnen Valley / Europ. Alps	0.04-0.08	
	terrestrial laser scanning	Hartmeyer <i>et al.</i> (2020b)	Kitzsteinhorn / Europ. Alps	0.35-10.32	
	snow fields, rockfall collectors	Rapp (1960)	Kärkevagge / Lappland	0.04-0.15	
	snow fields, painted rockwalls	Matsuoka & Sakai (1999)	Hosozawa Cirque / Japanese Alps	0.01	
	rockfall collectors	Sass (2005)	Europ. Alps	0.03-0.7	
	rockfall collectors	Krautblatter <i>et al.</i> (2012)	Reintal / Europ. Alps	0.29	
Decadal	digital terrain model	Fischer <i>et al.</i> (2013)	Monte Rosa / Europ. Alps	50	
Centennial	lichenometry	André (1986)	Kongsfjorden / Svalbard	0.0-0.7	
	lichenometry	Sass (2010)	Finsteral Valley / Europ. Alps	0.4-1.5	
	supraglacial debris flux	Heimsath & McGlynn (2008)	Annapurna Range / Himalaya	1.3	
	supraglacial debris flux	Fischer <i>et al.</i> (2013)	Monte Rosa / Europ. Alps	0.9-1.8	
	supraglacial debris flux	Banerjee & Wani (2018)	Himalaya	0.04-1.0	
	supraglacial debris flux	McCarthy <i>et al.</i> (2022)	High-Mountain Asia	0.03-0.14	
Millennial	talus volume	Olyphant (1983)	Blanca Massif / Colorado	0.05-0.82	
	talus volume	Hoffmann & Schrott (2002)	Reintal / Europ. Alps	0.1-1.0	
	talus volume	Sass (2007)	Europ. Alps	0.2-0.85	
	talus volume	Moore <i>et al.</i> (2009)	Sierra Nevada / California	0.02-1.22	
	talus volume	Siewert <i>et al.</i> (2012)	Longyeardalen /Svalbard	0.33-1.96	
Centennial /millennial	rockglacier volume	Humlum (2000)	Disko Island / Greenland	2-15	
	rockglacier volume	Monnier & Kinnard (2015)	Juncal Massif / Andes	0.05-2.45	
	rockglacier volume	Lehmann <i>et al.</i> (2022)	Combeynot Massif / Europ. Alps	1.0-2.5	
	cosmogenic nuclides	Heimsath & McGlynn (2008)	Annapurna Range / Himalaya	0.14-1.31	
	cosmogenic nuclides	Seong <i>et al.</i> (2009)	Baltoro Glacier / Karakoram	0.65-2.48	
	cosmogenic nuclides	Ward & Anderson (2011)	Kichatna Mountains / Alaska Range	0.47-1.33	
	cosmogenic nuclides	Guillon <i>et al.</i> (2015)	Mont Blanc massif / Europ. Alps	0.29	
	cosmogenic nuclides	Mair <i>et al.</i> (2019, 2020)	Eiger / Europ. Alps	0.5-3.5	
	cosmogenic nuclides	Sarr <i>et al.</i> (2019)	Mont Blanc massif / Europ. Alps	0.11-1.08	
	cosmogenic nuclides	Scherler & Egholm (2020)	Chhota Shigri Glacier / Himalaya	0.57-1.30	
					Exhumation rate ( $\text{mm yr}^{-1}$ )
	Millions	thermochronology	Shuster <i>et al.</i> (2005)	Klinaklini Valley/ British Columbia	$\geq 5$
		thermochronology	Glottzbach <i>et al.</i> (2011)	Mont Blanc massif / Europ. Alps	0.15-2.0
thermochronology		Valla <i>et al.</i> (2012)	Rhône Valley / Europ. Alps	0.4-4	
thermochronology		Herman <i>et al.</i> (2013)	worldwide	$\leq 0.01-7$	
thermochronology		Lease (2018)	Revelation Mountains / Alaska Range	$\leq 0.3-1.6$	

Over short timescales (years to decades; **Table 1.1**), rockwall erosion rates have been frequently derived from surface volume changes quantified through repeat terrestrial laser scanning (e.g., Rabatel *et al.*, 2008; Kenner *et al.*, 2011; Strunden *et al.*, 2015; Hartmeyer *et al.*, 2020b), time series of digital terrain models (Fischer *et al.*, 2013), and natural traps or rockfall collectors at the rockwall base (e.g., Rapp, 1960; Matsuoka & Sakai, 1999; Sass, 2005; Krautblatter *et al.*, 2012). Although these techniques provide high-resolution datasets, estimates are limited to short recent time periods and small areas due to the necessity of repeated

monitoring. Short-term records therefore may be biased by stochastic and interannual variability and recent climate change (Scherler & Egholm, 2020). Over long timescales (millions of years; **Table 1.1**), low-temperature thermochronology enables to assess the exhumation history of glaciated mountain ranges (e.g., Shuster *et al.*, 2005; Glotzbach *et al.*, 2011; Valla *et al.*, 2012; Lease, 2018). Commonly, thermochronometric age-derived erosion rates integrate up to hundreds of million years, insufficient to resolve temporal variability throughout individual glacial cycles (Herman *et al.*, 2013).

In contrast to these rather consistent short- and long-term approaches, attempts to quantify rockwall erosion over intermediate timescales (centuries to millennia; **Table 1.1**) are more varied. Amongst others, Holocene estimates stem from volume quantifications of talus debris, but commonly involve major assumptions on the total accumulation timespan and the temporal variability throughout deglaciation (e.g., Olyphant, 1983; Hoffmann & Schrott, 2002; Sass, 2007; Moore *et al.*, 2009; Siewert *et al.*, 2012). Researchers have also derived rockwall retreat rates by constraining the volume flux of headwall debris to glaciers based on supraglacial debris cover thicknesses (e.g., Heimsath & McGlynn, 2008; Fischer *et al.*, 2013; Banerjee & Wani, 2018; McCarthy *et al.*, 2022) or the debris volume in rock glaciers (e.g., Humlum, 2000; Monnier & Kinnard, 2015; Lehmann *et al.*, 2022). Yet, major uncertainties still arise from reconstructing glacier flow through time and from resolving englacial debris concentrations at debris-covered glaciers or the internal structure of rock glaciers. Rather controversial is the approximation of rockwall erosion rates by lichenometry on talus debris, particularly due to the limited understanding on lichen biology (e.g., André, 1986; Sass, 2010).

Novel instead is the use of *in situ*-produced cosmogenic nuclides as a measure of rockwall erosion in glacial settings to bridge the gap between short- and long-term estimates (**Table 1.1**). Few studies recently have started to quantify rockwall erosion rates using nuclide concentrations from either within bare rockwall surfaces (Mair *et al.*, 2019, 2020), valley ridge crests and sidewalls (Heimsath & McGlynn, 2008), or within supraglacial debris (e.g., Seong *et al.*, 2009; Guillon *et al.*, 2015; Sarr *et al.*, 2019). In particular, the approach of downglacier-interval-sampling of medial moraines introduced by Ward and Anderson (2011) and adopted by Scherler and Egholm (2020) seems promising to derive erosion rates of well-defined source rockwalls from  $^{10}\text{Be}$  concentrations within supraglacial debris and at the same time assess their erosion rate history through time. Yet, these strategies and associated opportunities but also challenges in glacial landscapes are largely unexplored.

This thesis builds on the innovative downglacier-interval-sampling approach of the two pioneering studies by Ward and Anderson (2011) and Scherler and Egholm (2020) to study high-alpine rockwall erosion. Therefore, and due to the hitherto overall limited applications and experiences with cosmogenic nuclide-derived rockwall erosion rates, I will introduce the cosmogenic nuclide methodology (see Section **1.3.1**), its current state of application and limits in glacial landscapes (see Section **1.3.2**), as well as the strategic concept underlying this thesis (see Section **1.3.3**) in more detail in a following additional introductory subchapter.

## 1.3 *In situ*-produced cosmogenic nuclides as tracer of Earth surface processes

### 1.3.1 Cosmogenic nuclide geochemistry

Across a variety of geomorphic settings, cosmogenic nuclides have become an increasingly applied tool to trace Earth surface processes throughout the Quaternary. These rare isotopes are the product of cosmic rays interacting with atoms in the atmosphere (*meteoric*) and the uppermost few metre of the Earth's surface (*in situ*). In rocks or soils, in particular concentrations of the *in situ*-produced radionuclides  $^{10}\text{Be}$ ,  $^{26}\text{Al}$ ,  $^{36}\text{Cl}$ , and  $^{14}\text{C}$  are measured to date landforms and to quantify the rates at which surface processes such as erosion or deposition operate. As these radionuclides are retained inside the rock or soil until they decay, they are usually absent prior to exposure. Therefore, their respective half-lives allow for distinct temporal application ranges on the order of  $10^2$  to  $10^6$  years, being longest for  $^{10}\text{Be}$  (half-life 1.4 Myr) and shortest for  $^{14}\text{C}$  (half-life 5.7 kyr). Since this thesis examines the erosion of headwalls above glaciers, I continue to refer to the term “rock” and only focus on the principles of *in situ*-produced cosmogenic nuclide analysis relevant to the quantification of rates within this setting. Unless otherwise stated, this introductory subchapter is based on the reviews by Gosse and Phillips (2001), Cockburn and Summerfield (2004), Dunai (2010), and von Blanckenburg and Willenbring (2014), and their references, and draws on the underlying physical theory as laid out in Lal (1991).

*In situ*-produced cosmogenic nuclides form when cascades of high-energy secondary cosmic ray particles (mostly neutrons and muons) hit minerals within bedrock surfaces and break apart target atoms to form residual nuclides. At the rock surface, nuclide production occurs primarily through neutron spallation reactions. It depends on the intensity of the cosmic radiation according to the geographic location, time, and local shielding. The cosmic ray flux and nuclide production are higher at higher latitudes where rays more easily penetrate the geomagnetic field, at times when the geomagnetic field is weak, and at higher altitude where the air pressure is lower. Moreover, the nuclide production in bedrock also varies due to topographic shielding. Steep terrain diminishes the exposure to cosmic radiation, as does shielding by snow and/or ice cover. Therefore, determining local nuclide production rates requires normalizations based on well-established spatial, temporal, and atmospheric scaling models, as well as corrections for the irradiation geometry and local shielding conditions. Overall, with only a few atoms per mineral gram per year, nuclide production rates are very low and both nuclide- and mineral-specific. For example, in quartz, the surface production rate at sea level high latitude (SLHL) of  $^{10}\text{Be}$  is  $4.01 \text{ atoms g}^{-1} \text{ yr}^{-1}$  and only a third of the  $^{14}\text{C}$  production of  $12.24 \text{ atoms g}^{-1} \text{ yr}^{-1}$  (Borchers *et al.*, 2016). With depth into the rock, the cosmic ray flux is attenuated according to the rock density and inclination of the rock surface. This attenuation restricts nuclide production by neutron spallation largely to the upper 2 to 3 m of the bedrock surface, within which concentrations decrease approximately exponentially with depth. As the surface erodes, bedrock that used to lie deeper passes through this zone of production. Therefore, measured concentrations integrate the residence time of rock while being exhumed from depth to the surface due to erosion. At even greater depth, nuclide production is dominated by muonic reactions, as the less reactive muons penetrate deeper. Depending on the nuclide, the muonic

contribution differs, being with <2% of the total surface  $^{10}\text{Be}$  production in quartz (Balco, 2017) relatively low, compared to ~20% for  $^{14}\text{C}$  (Lupker *et al.*, 2015).

Where bedrock erodes in cosmogenic steady state (i.e., nuclide production equals nuclide removal by decay and erosion), the *in situ*-produced cosmogenic nuclide concentration in bedrock is inversely proportional to the rate of rock surface removal. Nuclide concentrations are thus higher where slow bedrock erosion allows for longer exposure times. Assuming no initial nuclide concentration prior to bedrock exposure, the underlying steady-state relation is expressed according to Lal (1991) and Granger and Riebe (2014):

$$N(z) = \sum_i \frac{P_i(0)}{\lambda + \frac{E\rho}{\Lambda_i}} e^{-\frac{z\rho}{\Lambda_i}} \quad (1.1)$$

where  $N(z)$  is the nuclide concentration (atoms  $\text{g}^{-1}$ ) as a function of bedrock depth  $z$  (cm),  $i$  distinguishes the production mechanism by neutron spallation or muons,  $P_i(0)$  is the respective surface production rate (atoms  $\text{g}^{-1} \text{yr}^{-1}$ ),  $\lambda$  is the nuclide decay constant ( $\text{yr}^{-1}$ ),  $E$  is the bedrock erosion rate ( $\text{cm yr}^{-1}$ ),  $\rho$  is the bedrock density ( $\text{g cm}^{-3}$ ), and  $\Lambda_i$  is the respective attenuation length ( $\text{g cm}^{-2}$ ) that defines the distance over which the cosmic ray flux decreases by 63%. At the bedrock surface ( $z = 0$ ) and for nuclides such as  $^{10}\text{Be}$ , where the muonic surface contribution is small, Equation 1.1 can be simplified and  $E$  is commonly solved by:

$$E = \left( \frac{P(0)}{N} - \lambda \right) \frac{\Lambda}{\rho} \quad (1.2)$$

Rates of denudation and erosion are largely derived from  $^{10}\text{Be}$  concentrations in quartz minerals, as production rates in this combination are best constrained. Moreover, the long-lived radionuclide along with the resilience and ubiquity of quartz enables analyses across various Quaternary landscapes. Particularly common is the quantification and analysis of catchment-average erosion rates from  $^{10}\text{Be}$  concentrations in fluvial sediment samples. Following the “let nature do the averaging” concept (von Blanckenburg, 2005), this approach of amalgamating  $^{10}\text{Be}$  concentrations has proven to be very efficient and has been applied across small to large river catchments around the world (e.g., Brown *et al.*, 1995; Granger *et al.*, 1996; Schaller *et al.*, 2001; von Blanckenburg, 2005; Wittmann *et al.*, 2007; DiBiase *et al.*, 2010; Godard *et al.*, 2012; Delunel *et al.*, 2020). Nevertheless, it has been noted that the conventional conversion of  $^{10}\text{Be}$  concentrations to spatially-averaged erosion rates is complicated, because rates of glacial processes in the upstream catchment and the isotopic signature of glacially-derived sediments are difficult to constrain (Godard *et al.*, 2012). In glacial landscapes, this now routine application from fluvial settings is therefore less straightforward and requires additional considerations (e.g., Scherler & Egholm, 2020).

### 1.3.2 Cosmogenic nuclides in high-alpine glacial landscapes

Surface exposure dating of glacial landforms so far is the most common cosmogenic nuclide application in high-alpine glacial settings (e.g., Ivy-Ochs & Kober, 2008; Balco, 2011). In mountain regions around the world, particularly  $^{10}\text{Be}$  concentrations within glacially polished bedrock surfaces and glacial deposits such as abandoned terminal moraines have served to infer

sequences of glacier fluctuations and paleo-climatic conditions throughout the late Pleistocene and Holocene (e.g., Gosse *et al.*, 1995; Ivy-Ochs *et al.*, 1999, 2006; Barrows *et al.*, 2002; Briner *et al.*, 2005; Owen *et al.*, 2005; Schaefer *et al.*, 2006) or estimate the depth of subglacial erosion (e.g., Fabel *et al.* 2004; Wirsig *et al.*, 2017). Nonetheless, these chronological studies have encountered challenges when interpreting nuclide concentrations in glacial rocks. Fundamental to surface exposure dating are a nuclide inventory that has accumulated exclusively during the recent exposure event and a simple uninterrupted exposure history. However, inherited nuclide inventories from previous episodes of rock exposure and their insufficient reset by subglacial erosion can result in apparent rock exposure ages being too old, whereas post-exposure shielding or erosion of surfaces lead to ages being too young (e.g., Balco, 2011; Hippe, 2017). Affected moraine boulder ages are thought to represent outliers within the bulk of dates from a moraine, with inheritance holding true in only ~2% of the cases (Putkonen & Swanson, 2003), but post-depositional shielding being more important (Heyman *et al.*, 2011). To account for this, studies increasingly try to assess recent complex exposure histories by  $^{14}\text{C}$ - $^{10}\text{Be}$  exposure-burial dating (e.g., Goehring *et al.*, 2011, 2013; Hippe *et al.*, 2014; Wirsig *et al.*, 2016; Schimmelpfennig *et al.*, 2022). The pairing of the long-lived  $^{10}\text{Be}$  and short-lived  $^{14}\text{C}$  allows to resolve disequilibrium and intermittent burial due to differential decay, improving the temporal resolution of glacier chronologies (e.g., Hippe, 2017). Where exposure histories are well-constrained,  $^{14}\text{C}/^{10}\text{Be}$  ratios further have been used to derive rates of subglacial erosion (Goehring *et al.*, 2011; Schimmelpfennig *et al.*, 2022) as the ratio is modified by erosion due to the higher muonic  $^{14}\text{C}$  production at depth relative to  $^{10}\text{Be}$  (Hippe, 2017).

Cosmogenic nuclide-derived rockwall erosion rates, however, are rare. Previous records (**Table 1.1**) were derived either directly from the erosive surface or indirectly from their deposits. Comparatively direct, Mair *et al.* (2019, 2020) quantified rockwall erosion rates at the Eiger in the Swiss Alps using  $^{36}\text{Cl}$  and  $^{10}\text{Be}$  concentrations along six rock face depth profiles and attributed spatial differences to differences in frost-cracking efficacy. Heimsath and McGlynn (2008) used  $^{10}\text{Be}$  bedrock samples from valley ridge crests and sidewalls to derive rockwall erosion rates at a debris-covered glacier in the Himalaya. Yet, due to the spatial limitation, point-samples taken directly from a rock face are representative for only a rockwall section. Potential bias by stochastic erosion may therefore be greater on single rate estimates compared to estimates averaging across the entire rockwall area (Small *et al.*, 1997). Indeed, Heimsath and McGlynn (2008) found a large range of erosion rates within their dataset and related higher erosion rates to recent episodic rockfall. For several steep faces in the Mont Blanc massif, Gallach *et al.* (2018, 2020) reported  $^{10}\text{Be}$ -derived exposure ages from rockfall scars of the same face that date from the LIA back to the Pleistocene. Both examples show that point-measured  $^{10}\text{Be}$  concentrations can exceed several orders of magnitude across a single rock face, indicating pronounced spatial variability and dependence on the sampled area.

To account for such heterogeneities in rockwall surface nuclide concentrations from stochastic rockfall, the average value of many individual erosion rate estimates is considered to best represent the overall average rockwall erosion rate (Small *et al.*, 1997). However, limited access and steep rock faces make the collection of many such bedrock samples difficult and dangerous (e.g., Ward & Anderson, 2011). To facilitate averaging and to mix sources more equally, a small number of studies have quantified rockwall erosion rates indirectly by using  $^{10}\text{Be}$

concentrations within amalgamated samples of supraglacial debris deposits - similar to the approach of sediment amalgamation in river catchments (see Section 1.3.1). Seong *et al.* (2009) estimated basin-wide rockwall erosion rates for an extensive glacier system in the Karakoram by sampling lateral moraines and hummocky glacier surfaces. Sarr *et al.* (2019) combined supraglacial debris samples from variable terminal positions in the Mont Blanc massif with a theoretical rockfall distribution model. Accordingly, samples should statistically amalgamate clasts from more than 30 rockfalls to compensate data variability due to episodic erosion. Ward and Anderson (2011) instead tested active, ice-cored medial moraines as archives of rockwall erosion using the specificity with which the moraines sample delimited supply areas. At regular space, they sampled longitudinal moraine transects at three glaciers in the Alaska Range by amalgamating ~30 debris clasts each, concluding the derived rates to be representative of an erosive glacial climate. This systematic downglacier-interval-sampling was taken up by Scherler and Egholm (2020), who found that  $^{10}\text{Be}$  concentrations in the medial moraine of the Chhota Shigri Glacier in the Himalaya systematically increase downglacier, suggesting recently accelerating rockwall erosion. According to the above studies, the amalgamation approach hence allows to approximate average rockwall surface  $^{10}\text{Be}$  concentrations that account for the stochasticity in glacial landscapes. Nevertheless, deriving rockwall erosion rates from cosmogenic nuclides in supraglacial debris faces challenges, which require future research. Complexities relate particularly to the mechanisms of erosion and to post-depositional debris exposure, addressed in detail in the following.

### 1.3.3 Headwall $^{10}\text{Be}$ in medial moraine debris

Medial moraines may be the most evidently and easily traceable expression of headwall erosion onto valley glaciers (**Figure 1.1c**). Ward and Anderson (2011) and Scherler and Egholm (2020) took advantage of this obvious link between debris source areas and erosion products to derive rockwall erosion rates from  $^{10}\text{Be}$  concentrations in supraglacial medial moraine debris. To illustrate the opportunities and challenges of this approach, the formation of medial moraines and the associated transport pathways of debris through a valley glacier are schematized in **Figure 1.4a** and summarized below from Anderson (2000), Ward and Anderson (2011), and Scherler and Egholm (2020).

Active medial moraines are ice-flow parallel debris bands on a glacier, portraying the surficial downglacier transport routes of debris (**Figure 1.4a**). Their debris largely stems from headwalls eroding onto the ice surface in the headwaters of valley glaciers. Upon deposition, headwall debris is entrained and passively transported along the glacier margins by the moving ice. This debris transport can proceed in two ways: englacially, within the ice, and supraglacially, on the ice surface. The mode depends on the position of the glacier's equilibrium line altitude (ELA), at which annual ice accumulation is in balance with annual ice ablation. In the accumulation zone above the ELA, debris will be progressively buried within the ice as a result of net annual ice accumulation and takes englacial pathways. Due to the laminar flow of ice and the fact that debris deposited further upstream takes deeper englacial pathways, it is unlikely to mix on its way downglacier. In the ablation zone below the ELA, net annual ice ablation causes the debris to re-emerge to the surface where it continues a supraglacial pathway. Where two ice tributaries join, their marginal debris is merged to form a septum of debris between the two ice bodies. If this confluence occurs above the ELA, a medial moraine begins to exhume in the ablation zone.

Below the ELA, a medial moraine directly forms at the confluence. Medial moraines therefore comprise an amalgamation of debris deposits from rockfalls within the debris source area and tend to be older downglacier due to the conveyor belt nature of glacial transport.

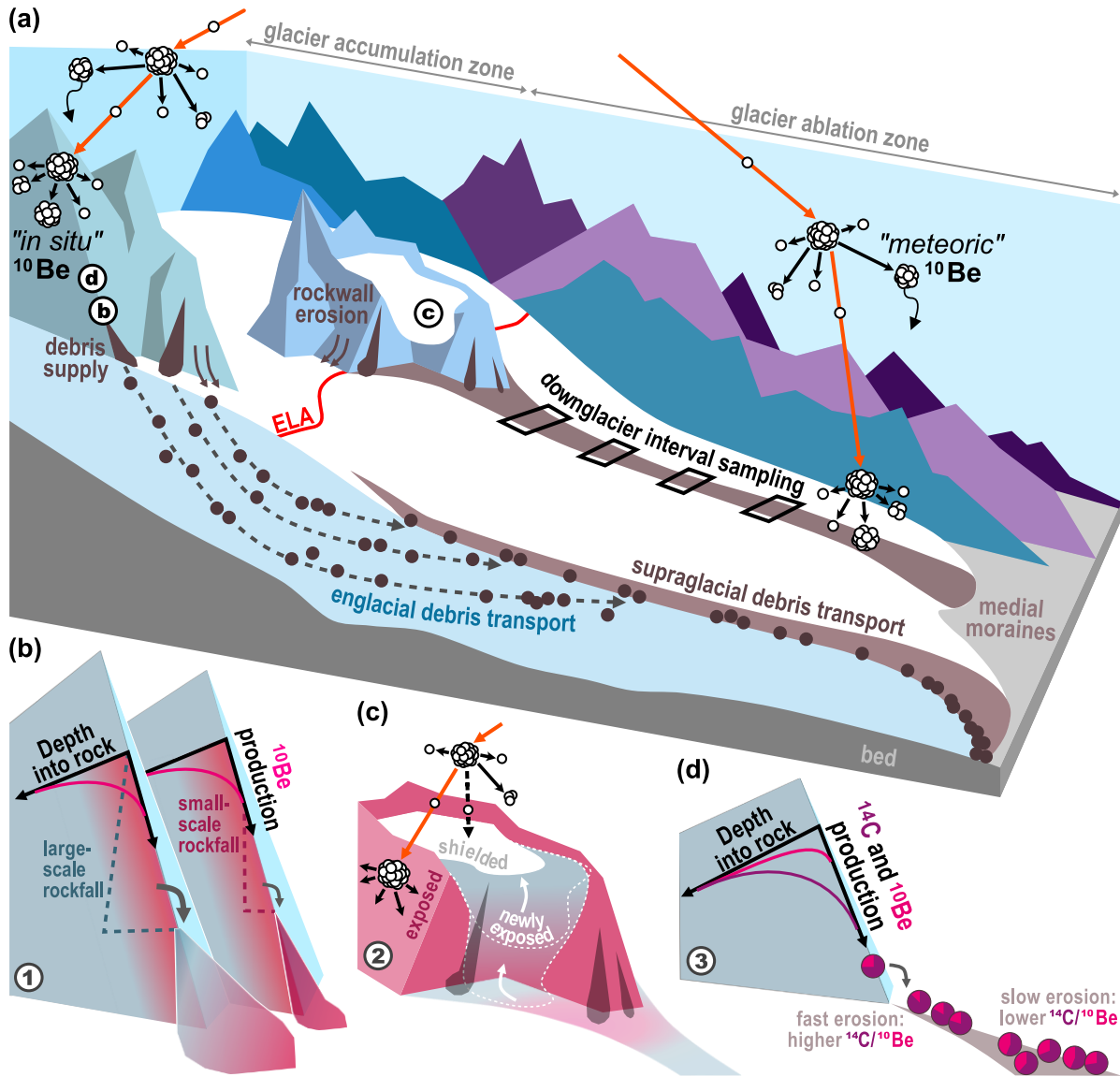


**Figure 1.4:** Schematic of processes and conditions affecting concentrations of *in situ*-produced cosmogenic  $^{10}\text{Be}$  in medial moraine debris. (a) Formation of medial moraines and downglacier transport of debris particles supplied through headwall erosion, in dependence of the equilibrium line altitude (ELA). Above the ELA, debris particles initially take englacial pathways, but remain supraglacial when deposited below the ELA. *In situ*  $^{10}\text{Be}$  production occurs both during headwall erosion and downglacier debris transport. The location of process-close-ups shown below is indicated. (b-d) Process-close-ups, which schematize methodological questions examined in this thesis as outlined in Section 1.4. Numbers 1-3 refer to the respective thesis study from Chapters 2-4, and the pink/turquoise colour in (b) and (c) indicates high/low bedrock  $^{10}\text{Be}$  concentrations. (b) The production of  $^{10}\text{Be}$  decreases exponentially with bedrock depth. Will medial moraine  $^{10}\text{Be}$  concentration records therefore show grain size effects and will stochastic, large-scale rockwall erosion affect the records? (c) The concentration of  $^{10}\text{Be}$  in rockwalls is affected by the bedrock's shielding and re-exposure history. Will deglaciation that exposes newly eroding bedrock surfaces of possibly different  $^{10}\text{Be}$  signatures therefore affect medial moraine  $^{10}\text{Be}$  concentration records? (d) The paired *in situ*  $^{14}\text{C}/^{10}\text{Be}$  ratio is a function of differential nuclide production at depth and decay. Will medial moraine records therefore show deviating ratios indicative for short-term variations in erosion rates and landscape transience?

Consequently, by amalgamating debris samples along medial moraine intervals (Figure 1.4a), Ward and Anderson (2011) assessed surface average  $^{10}\text{Be}$  concentrations across well-definable source areas, and Scherler and Egholm (2020) additionally used the time-line character of

medial moraines to derive rockwall erosion rates through time. As part of their evaluations, Ward and Anderson (2011) further studied the effects of (i) post-depositional debris exposure and (ii) stochastic erosion on medial moraine  $^{10}\text{Be}$  concentrations, and Scherler and Egholm (2020) examined the (iii) temporal variability in medial moraine  $^{10}\text{Be}$  concentrations. Their findings are briefly summarized in the following. (i) Debris exposure after deposition but before sample collection will result in additional nuclide accumulation (**Figure 1.4a**). Due to the general steepness of source rockwalls, long-term storage of debris near the headwaters presumably is low and additional post-depositional  $^{10}\text{Be}$  accumulation is limited to the period of downglacier debris transport. The amount of additional transport accumulation may be comparatively small in case of englacial debris transport.  $^{10}\text{Be}$  production below a ~10 m thick ice cover is ~1% of the surface production and debris particles are well-shielded. Using a simplified analytical model of a stable glacier geometry under constant environmental conditions, Ward and Anderson (2011) found downglacier transport time to have a negligible effect on their measured concentrations (<10%) as shallow transport pathways were short and longer pathways sufficiently deep. However, estimating additional nuclide accumulation during transport may be required if rockwall surface concentrations are overall low due to rapid erosion or where transport distances are long, glaciers are slow, and supraglacial transport dominates. (ii) Nuclide production is a function of depth into the bedrock (see Section 1.3.1), being highest at the rockwall surface (**Figure 1.4b**). The strategy of supraglacial debris amalgamation aims to assess outcrop-scale average  $^{10}\text{Be}$  concentrations in episodically eroding rockwall surfaces (Small *et al.*, 1997). Yet, the stochastic nature of erosion implies that bedrock is scoured to different depths depending on rockfall size. Hence,  $^{10}\text{Be}$  concentrations in medial moraine debris clasts will vary according to their depth below the rockwall surface at the time of erosion. Using Monte Carlo simulations of sample amalgamation and arguing that erosion over a typical centennial residence time of medial moraine debris is commonly dominated by small-scale rockfalls, Ward and Anderson (2011) concluded that the sampling strategy nevertheless reflects the average bedrock surface concentration well. (iii) Along the medial moraine of the Chhota Shigri Glacier, Scherler and Egholm (2020) found the upper four of five samples to reflect an increase in  $^{10}\text{Be}$  concentrations downglacier. Based on a numerical ice flow model with a particle tracking routine, the authors simulated the evolution of  $^{10}\text{Be}$  concentrations in glacial debris during transport to investigate what may cause the observed temporal variability. Imposing climatic scenarios onto the catchment, they studied erosion scenarios as a function of slope, source area changes from fluctuating ice cover, and frost-cracking efficacy. Although their scenarios caused spatial variability in erosion rates, magnitudes were too small to reproduce the observed increase in  $^{10}\text{Be}$  concentrations. Alternatively, the authors suggested increasing destabilization and erosion of recently deglaciated bedrock to be another possible explanation for the observed trend. This, however, will require constraining dominant source area zones and site-specific bedrock exposure histories as part of future investigations.

Despite these promising initial studies by Ward and Anderson (2011) and Scherler and Egholm (2020), the straightforward downglacier-interval-sampling strategy has not yet been pursued further and the archival character of medial moraines - if real and not just incidental - is not yet well understood. Its applicability and the use of medial moraines as timelines of rockwall erosion rates therefore remain to be tested in different glacial areas and for medial moraine records of higher sample-resolution.

## 1.4 Research aims and questions

In this thesis, I investigate the climate sensitivity of glacial landscapes and their dynamics by temporally and spatially studying headwall erosion and debris supply to valley glaciers. This work further aims to pursue the sampling strategies introduced by Ward and Anderson (2011) and Scherler and Egholm (2020), and to increase the number of high-alpine rockwall erosion rate datasets. As the European Alps are one of the most intensively studied mountain ranges in the world (e.g., Haeberli & Beniston, 1998) and there is a particularly large amount of long-term monitoring data on glacier change in the Swiss Alps (GLAMOS, 2023), my focus is on glacial landscapes in the Swiss Alps. Based on three studies, I quantify headwall erosion rates at six Swiss glaciers in the Canton of Valais using downglacier medial moraine  $^{10}\text{Be}$  concentration records (**Figure 1.5**) and address the following research questions:

- Can medial moraines serve as archives of headwall erosion above glaciers?
- Are there temporal trends in headwall erosion above glaciers and, if so, do they correlate with climatic changes?
- Do differences among downglacier medial moraine records relate to spatially distinct headwall morphology?

In the first study (Chapter 2), the archive function of medial moraines and the temporal evolution of headwall erosion are investigated. Initially, the potential of the relatively new sampling strategy is tested in detail to gain a better understanding of the headwall-moraine-system and of how medial moraine  $^{10}\text{Be}$  concentrations reflect erosion rates in glacial landscapes. The study takes a micro-perspective on a single valley glacier, the Glacier d'Otemma, which originates at the Swiss mountain Pigne d'Arolla (**Figure 1.5**). This specific glacier was chosen because of its simple geometry, two pronounced parallel medial moraines, and a well-defined small debris source area. To study temporal variability and exclude the possibility that potential temporal patterns are due to artefacts caused by an insufficient number of samples (Scherler & Egholm, 2020), downglacier-interval-sampling was applied at high resolution. Moreover, as outlined in Section 1.3.3 and simulated by Ward and Anderson (2011), bedrock excavation depth may complicate the interpretation of nuclide inventories in rockfall landscapes due to the depth-dependent nuclide production (**Figure 1.4b**). Fluvial sediments for instance can show grain size-dependent nuclide concentrations (e.g., Puchol *et al.*, 2014; West *et al.*, 2014). To this effect, different debris grain sizes were analysed to test for possible effects by stochastic erosion (**Figure 1.4b**). To further approximate the time of headwall erosion and correct for post-depositional  $^{10}\text{Be}$  production during downglacier transport, a simple 1D debris particle trajectory model was developed, which accounts for site-specific temporal changes in glacier flow from surface velocity and elevation reconstructions.

In the second study (Chapter 3), the focus is widened by examining both temporal and spatial patterns in rockwall erosion and by studying a set of five nearby valley glaciers. As a continuation of the Otemma case study, the same sampling and downglacier modelling approach was applied to four other glaciers in the massif around Pigne d'Arolla, all exposing

debris from rockwalls that differ in their morphology: Glacier du Brenay, Glacier de Cheilon, Glacier de Pièce, and Glacier de Tsijiore Nouve (**Figure 1.5**). This small massif has the advantage of minimizing the likelihood of major lithologic, climatic, or tectonic bias that could arise if the compared sites were not as localized but from various settings spread across the Alps. In addition, areal changes in ice cover across all source rockwalls were evaluated to gauge the likelihood of recent bedrock deglaciation imprinting on the  $^{10}\text{Be}$  signal and spatiotemporal analysis (**Figure 1.4c**).

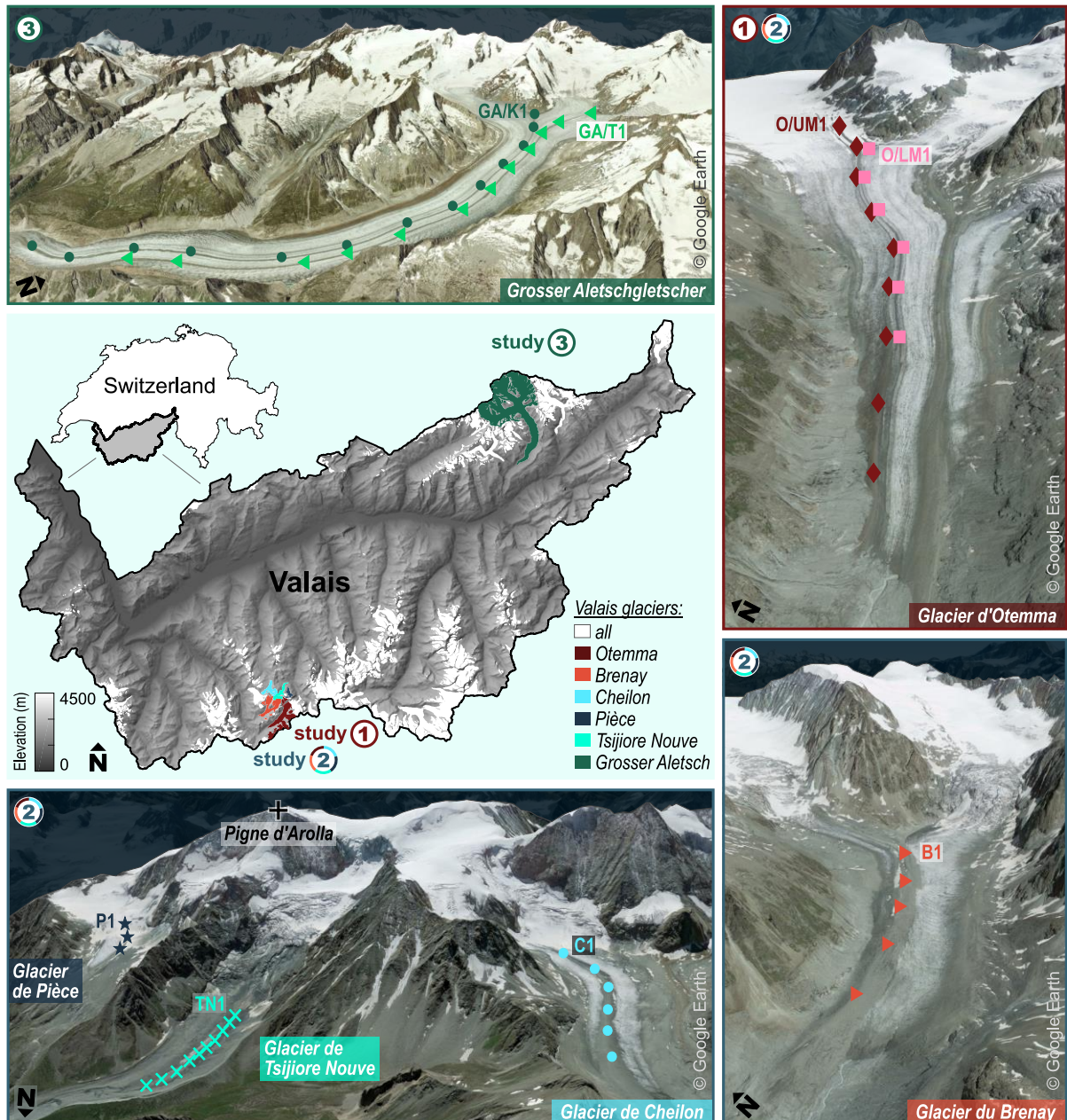


**Figure 1.5:** Overview of the glacier sites in Switzerland investigated as part of this thesis. The locations of the respective study areas are indicated on the DEM of the Canton of Valais (SRTM GL1; NASA Shuttle Radar Topography Mission SRTM, 2013). The six glacier catchments and eight sampled medial moraines are shown as Google Earth views (<https://earth.google.com>, accessed: 2 August 2023). Numbers 1-3 denote the thesis study from Chapters 2-4 for which a dataset was used. Sample locations along the medial moraine profiles are in ascending order downglacier and in the symbol- and colour-codes used in the respective study. Note that the glacier views have different scales and perspectives.

In the third and ongoing study (Chapter 4), the approach previously tested for comparatively small sites is applied to a large-scale glacier catchment, the iconic Grosser Aletschgletscher in Switzerland (**Figure 1.5**). Along with the exceptionally well-monitored catchment, the two long parallel medial moraines allow to study processes within two separate debris source areas in great detail and based on the largest downglacier  $^{10}\text{Be}$  concentration records to date. To investigate erosional transience, the rarely explored paired  $^{14}\text{C}/^{10}\text{Be}$  nuclide analysis is tested for the first time on a small set of samples. The idea is that the fast decay of  $^{14}\text{C}$  and higher subsurface production and the therefore higher sensitivity of  $^{14}\text{C}$  concentrations to recent short-term variations in erosion rates will lead to a deviation of the ratio (**Figure 1.4d**; Hippe, 2017; Mudd, 2017). This third study is still in progress. Therefore, Chapter 4 provides preliminary results and interpretations and concludes with an outlook on further upcoming analyses.

# Temporal evolution of headwall erosion rates derived from cosmogenic nuclide concentrations in the medial moraines of Glacier d'Otemma, Switzerland

*Katharina Wetterauer, Dirk Scherler, Leif S. Anderson & Hella Wittmann*

## Abstract

Climate change affects the stability and erosion of high-alpine rockwalls above glaciers (headwalls) that deliver debris to glacier surfaces. Since supraglacial debris in the ablation zone alters the melt behaviour of the underlying ice, the responses of debris-covered glaciers and of headwalls to climate change may be coupled. In this study, we analyse the  $^{10}\text{Be}$ -cosmogenic nuclide concentration history of glacial headwalls delivering debris to the Glacier d'Otemma in Switzerland. By systematic downglacier-profile-sampling of two parallel medial moraines, we assess changes in headwall erosion through time for small, well-defined debris source areas. We compute apparent headwall erosion rates from  $^{10}\text{Be}$  concentrations ( $[^{10}\text{Be}]$ ), measured in 15 amalgamated medial moraine debris samples. To estimate both the additional  $^{10}\text{Be}$  production during glacial debris transport and the age of our samples we combine our field-based data with a simple model that simulates downglacier debris trajectories. Furthermore, we evaluate additional grain size fractions for 8 samples to test for stochastic mass-wasting effects on  $[^{10}\text{Be}]$ . Our results indicate that  $[^{10}\text{Be}]$  along the medial moraines vary systematically with time and consistently for different grain sizes.  $[^{10}\text{Be}]$  are higher for older debris, closer to the glacier terminus, and lower for younger debris, closer to the glacier head. Computed apparent headwall erosion rates vary between  $\sim 0.6$  and  $10.8 \text{ mm yr}^{-1}$ , increasing over a maximum time span of  $\sim 200$  years towards the present. As ice cover retreats, newly exposed headwall surfaces may become susceptible to enhanced weathering and erosion, expand to lower elevations, and contribute formerly shielded bedrock of likely different  $[^{10}\text{Be}]$ . Hence, we suggest that recently lower  $[^{10}\text{Be}]$  reflect the deglaciation of the debris source areas since the end of the Little Ice Age.

**This chapter is published in:**

*Earth Surface Processes and Landforms*, Volume 47, Pages 2437-2454, 2022

<https://doi.org/10.1002/esp.5386>

## 2.1 Introduction

The sensitivity of high-alpine glacial landscapes to climate change is a matter of growing concern. In the European Alps, one of the world's most populated mountainous regions (Haeberli & Beniston, 1998), rockfalls and slope failures endanger communities, infrastructure, and the tourist economy (e.g., Haeberli *et al.*, 1997; Haeberli & Beniston, 1998; Hartmeyer *et al.*, 2020a, 2020b). Previous studies suggest that enhanced rockfall activities and slope failures during the last three decades are related to permafrost degradation and/or changes in frost weathering (e.g., Gruber *et al.*, 2004; Gruber & Haeberli, 2007; Ravelin & Deline, 2009; Huggel *et al.*, 2010, 2012; Ravelin *et al.*, 2010; Phillips *et al.*, 2016). Increased mass wasting has also been linked to glacial thinning and associated stress changes in the adjacent bedrock (e.g., Ballantyne, 2002b; Cossart *et al.*, 2008; Hartmeyer *et al.*, 2020a, 2020b). At the same time, studies on glaciers from various mountain ranges report an increase in debris cover over decades (e.g., Kirkbride, 1993; Deline, 2005; Bolch *et al.*, 2008; Glasser *et al.*, 2016). This modifies ice ablation and may delay warming-induced glacier retreat and alter regional impacts (e.g., Scherler *et al.*, 2011b; Benn *et al.*, 2012; Rowan *et al.*, 2015; Anderson & Anderson, 2016; Vincent *et al.*, 2016). Therefore, if climate warming induces an increase in debris delivery to glacier surfaces and a thickening of glacial debris cover, climate change-related responses of rockwalls and adjacent glaciers are likely interrelated (Scherler & Egholm, 2020).

Climate variability throughout the Holocene caused glaciers to repeatedly advance and retreat in the European Alps (Holzhauser *et al.*, 2005). Since their maximum Little Ice Age (LIA) extent, typically around 1850 (Ivy-Ochs *et al.*, 2009), Alpine glaciers underwent widespread and pronounced decline (Zemp *et al.*, 2008). Their retreat accounted for about ~50% of Alpine ice cover loss by 2000, despite brief re-advances in the 1890s, 1920s, 1970s, and 1980s (Zemp *et al.*, 2008, and references cited therein); and glacier retreat has accelerated since the 1980s (e.g., Paul *et al.*, 2004; Zemp *et al.*, 2008, 2019; Huss, 2012; GLAMOS, 2019a, 2019b). On several glaciers in the European Alps debris cover extent has substantially expanded since the end of the LIA (e.g., Deline, 2005; Fleischer *et al.*, 2021). Observations of clean-ice glaciers transforming into debris-covered glaciers and rapid expansion of supraglacial debris (Deline, 2005) may be the result of more frequent rockfalls and debris deposition on glaciers, in addition to increasing ablation areas.

Yet, temporal changes in rockwall erosion above glaciers are largely unconstrained. Estimates for the post-LIA deglaciation period are rare and mainly based on records of a few years or decades (e.g., Sass, 2005; Rabatel *et al.*, 2008; Hartmeyer *et al.*, 2020a, 2020b). To quantify long-term ( $>10^2$ - $10^4$  years) erosion rates within glacial catchments recent studies have analysed concentrations of the *in situ*-produced cosmogenic nuclide  $^{10}\text{Be}$  ( $[^{10}\text{Be}]$ , atoms  $\text{g}^{-1}$ ) in supraglacial debris (e.g., Heimsath & McGlynn, 2008; Seong *et al.*, 2009; Guillon *et al.*, 2015; Sarr *et al.*, 2019). For example, Ward and Anderson (2011) measured  $[^{10}\text{Be}]$  in supraglacial debris samples collected along medial moraines on Alaskan glaciers to estimate spatially- and temporally-averaged erosion rates for distinct headwalls. This strategy was revisited by Scherler and Egholm (2020), who combined field-based data with a numerical ice flow model to track  $[^{10}\text{Be}]$  along a medial moraine of the Chhota Shigri Glacier in the Himalaya and to evaluate temporal variations in headwall erosion rates.

However, these previous studies employed a rather widely-spaced or limited sampling scheme and little is known about the processes governing variations in [ $^{10}\text{Be}$ ] along medial moraines. Specifically, low-frequency high-magnitude mass-wasting processes, such as landslides and debris flows, can impact detrital cosmogenic nuclide concentrations, often manifesting themselves in grain size-dependent nuclide concentrations (e.g., Niemi *et al.*, 2005; Kober *et al.*, 2012; Puchol *et al.*, 2014; West *et al.*, 2014). Using a non-representative grain size fraction could therefore bias the quantification of long-term erosion rates.

In this study we quantify headwall erosion rates (i.e., the process of headwall retreat perpendicular to the bedrock surface) from medial moraine debris of a glacier in the European Alps and assess changes thereof through time in a systematic way. For our analysis, we chose Glacier d'Otemma in Switzerland, where the availability of long-term monitoring data sets and historical documents allows for greater in-depth analysis than at glaciers in more remote regions. We sampled two parallel medial moraines that have small and well-defined source areas. Samples were taken at regular intervals and at high spatial density to test for systematic downglacier variations in [ $^{10}\text{Be}$ ]. In addition, we analyse different grain size fractions to identify the potential role of stochastic mass-wasting events. We combine our field-based data with a simple model that simulates debris trajectories through the glacier, allowing us to estimate both the additional production of cosmogenic nuclides during glacial transport and the age of our samples.

## 2.2 Glacial headwalls and medial moraines

Steep ice-free rockwalls are prominent landforms in glacial landscapes. Where they tower at the head of valley glaciers, they are often called glacial headwalls. Being exposed to weathering and erosion, these headwalls retreat and shed bedrock debris onto the ice surface that is eventually transported away from the source by the moving ice. The debris entrainment itself varies with its deposition relative to the equilibrium line altitude (ELA, the elevation where annual ice accumulation balances ablation). In the glacier's accumulation zone above the ELA, debris delivered from headwalls is buried by the accumulating ice. It is first transported downglacier within the ice ("englacial"), before it subsequently re-emerges at the surface below the ELA, and continues to be transported on the ice surface ("supraglacial"). In the glacier's ablation zone below the ELA, debris remains on the ice surface, unless it falls into crevasses or off the glacier (e.g., see summaries in Kirkbride, 1995; Benn & Evans, 1998; Ward & Anderson, 2011).

Medial moraines are the surficial expression of ice-flow parallel debris bands in a glacier's ablation zone. They form where debris that has been deposited in the accumulation zone and entrained englacially is melting out below the ELA, or where two neighbouring glaciers join below the ELA and their supraglacial marginal debris (lateral moraines) merges (e.g., Eyles & Rogerson, 1978a, 1978b; Boulton & Eyles, 1979; Gomez & Small, 1985; Anderson, 2000). Following the laminar flow of ice, this debris is passively transported downglacier and as a result, medial moraine debris deposits tend to be older downglacier. Supraglacial debris has a strong control on melt rates. As shown by Østrem (1959) and numerous subsequent studies

(e.g., Mattson *et al.*, 1993; Nicholson & Benn, 2006; Reid & Brock, 2010; Anderson & Anderson, 2016), sub-debris melt rates below a debris cover thinner than a certain “critical thickness” (often around 2 cm) are higher than clean-ice melt rates but will be reduced underneath a thicker debris cover. Accordingly, the insulating effect of supraglacial debris exponentially reduces sub-debris melt rates as debris cover thickness increases. Therefore, medial moraines often form ridges on the glacier surface because the adjacent bare ice melts faster (e.g., Eyles & Rogerson, 1978a, 1978b; Boulton & Eyles, 1979; Gomez & Small, 1985; Anderson, 2000). For the above reasons, medial moraines may serve as useful and visibly traceable archives to study headwall erosion histories.

## 2.3 Study area

### 2.3.1 Glacier d’Otemma and its catchment

Glacier d’Otemma is a Swiss valley glacier located in the southern part of the Valais, close to the Swiss-Italian border (**Figure 2.1a**). Originating at the southern flank of the Pigne d’Arolla and fed by several smaller tributary glaciers, the main glacier flows southwest into the Haut Val de Bagnes. At present, Glacier d’Otemma has a length of ~6 km and is likely entirely composed of temperate ice (Langhammer *et al.*, 2017). The main trunk ranges from ~3015 m elevation at the ice divide at the Col de Charmotane down to ~2500 m elevation at its terminus (elevations in this paper are stated as metres above mean sea level). Its maximum ice thickness was estimated to be ~290 m close to the ice divide in the year 2009 (Gabbi *et al.*, 2012) and the ice-covered area was ~15.5 km<sup>2</sup> in the year 2013 (GLAMOS, 2019b). From high resolution satellite images of the glacier catchment from the year 2017, we estimate that at present, the ELA is located above ~3100 m elevation.

Systematic long-term monitoring of glacier changes in the Swiss Alps (Glacier Monitoring Switzerland; GLAMOS, 2019a, 2019b) as well as historical maps, orthoimages, and photographs (Federal Office of Topography Swisstopo; Swisstopo, 2021) reveal a continuous recession history of Glacier d’Otemma since the end of the 19th century (Mancini & Lane, 2020), unlike many other Alpine glaciers (Zemp *et al.*, 2008, and references cited therein). The terminus retreated about 2.3 km between 1881 and 2016 (GLAMOS, 2019a). Between 1850 and 2010 the glacier lost ~40% of its surface area and ~60% of its ice volume, while glacier thinning reached ~70 m at the ice divide (Lambiel & Talon, 2019). The geodetic glacier-wide mass balance decreased from ~-0.4 m water equivalent (w.e.) yr<sup>-1</sup> between 1934 and 1983 to ~-1.0 m w.e. yr<sup>-1</sup> between 1983 and 2013 (GLAMOS, 2019b). Thus, Glacier d’Otemma has been losing mass faster than the average glacier in the Swiss Alps (-0.62 m w.e. yr<sup>-1</sup> between 1980 and 2010), implying a high sensitivity to climate change (Fischer *et al.*, 2015). Gabbi *et al.* (2012), who modelled the future evolution of several glaciers in the Haut Val de Bagnes, predict that Glacier d’Otemma will retreat even faster in the future, reducing to some relict ice patches by 2070.

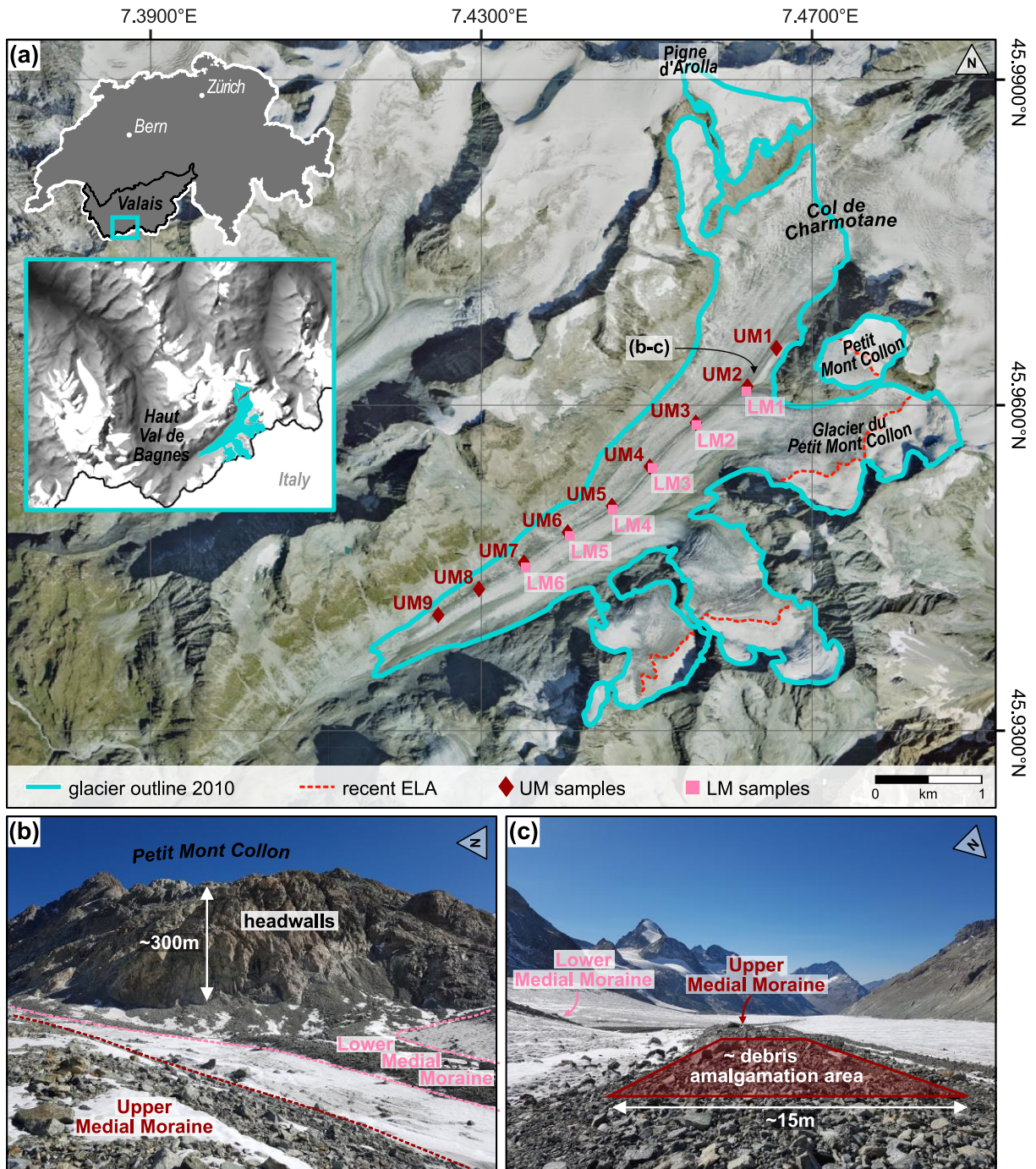


**Figure 2.1:** Glacier d'Otemma, Switzerland. (a) Orthoimage showing the glacier with its catchment, the debris source area Petit Mont Collon, the UM and LM sample locations, and the approximate recent ELA. The upper inset outlines the location of the glaciated Haut Val de Bagnes in Switzerland, the lower inset zooms on the glacier's location in the Haut Val de Bagnes (orthoimage from 2017 by Swisstopo, 2021; glacier outline by Fischer *et al.*, 2014). (b) Field photograph of the headwalls that contribute debris to the LM. (c) Field photograph of the UM downglacier pathway with indicated concept of supraglacial sample amalgamation. Note that UM and LM are separated by an ice septum (photographs taken in October 2018 from an UM position as indicated in (a)). UM/LM: upper/lower medial moraine; ELA: equilibrium line altitude

### 2.3.2 Medial moraines and their source areas

A major bedrock source delivering debris to Glacier d'Otemma is the Petit Mont Collon, a nunatak with a peak at ~3555 m elevation (Figure 2.1a,b). Its west-north-west facing and south-south-west facing headwalls are flanked by the glacier's main trunk and the small

tributary Glacier du Petit Mont Collon, respectively. These headwalls are located in the distribution zone of modelled mountain permafrost in the Swiss Alps (BAFU, 2005). They tower up to ~500 m above the glacier surface, with slopes up to ~60°. While the steeper faces are largely ice-free bedrock, the saddle-like centre of Petit Mont Collon is covered by remnants of a small glacier (**Figure 2.2**). In 1973, this isolated glacier used to flow into Glacier d'Otemma and, before, in 1850, its accumulation zone was connected to Glacier d'Otemma (Swisstopo, 2021). Petit Mont Collon is composed mainly of gneiss and schist (**Figure 2.2**). Only the northernmost and highest flanks are composed of gabbro (Swisstopo, 2021).

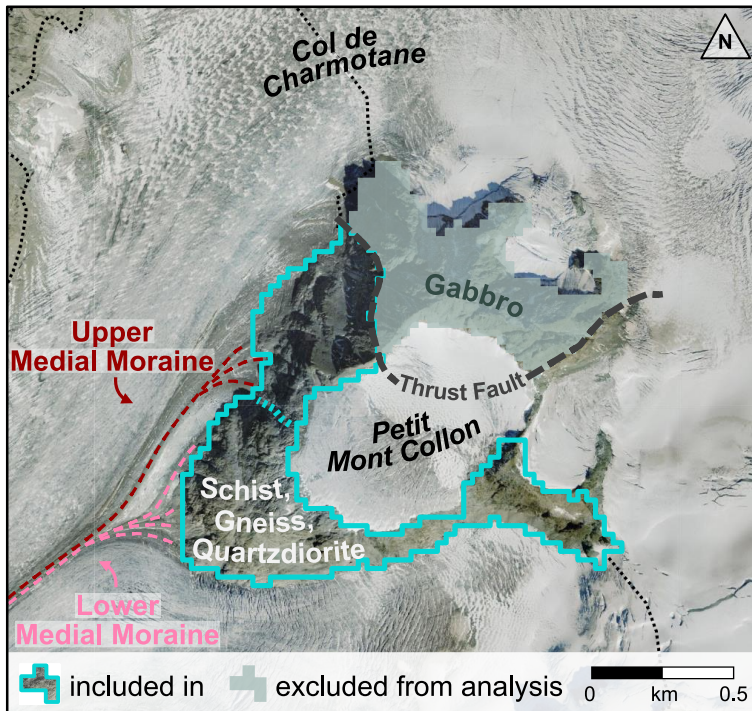


**Figure 2.2:** Debris source area Petit Mont Collon and simplified bedrock lithology of the headwalls. We only consider headwalls which are made of schist, gneiss, or quartzdiorite, and which deposit debris below the ice divide at the Col de Charmotane. The source headwalls are separated from gabbroic areas by a mapped thrust fault (dashed grey line) and differentiated into headwalls to the upper or lower medial moraine (dashed cyan line). Note that the angular course of the headwall outline is the result of superimposing the glacier's 2010 outline onto a 30 m resolution DEM (SRTM GL1; NASA Shuttle Radar Topography Mission SRTM, 2013). The glacier's 2010 outline (black dotted line) and the pathways of the upper/lower medial moraine (dashed red/pink lines) are indicated (orthoimage from 2017 and lithologic mapping by Swisstopo, 2021; glacier outline by Fischer *et al.*, 2014).

Two pronounced medial moraines are nourished from Petit Mont Collon (**Figure 2.1a**, **Figure 2.2**). They are fed by different but adjacent rock faces and from now on we refer to them as the upper medial moraine (UM) and lower medial moraine (LM). Debris input from higher up is prevented by the isolated nature of Petit Mont Collon at the ice divide. Running parallel and mostly 20-40 m apart from each other, UM and LM exist between 3000 and 2650 m elevation. Currently, the UM originates slightly above the 3000 m elevation contour, off the west-north-west facing headwalls, and is clearly traceable over >4 km distance downglacier. The LM starts slightly below 3000 m elevation, off the south-south-west facing headwalls near the recent ice confluence, and is well traceable along a downglacier distance of ~3 km. Close to their source areas (**Figure 2.1b,c**), both moraines have widths of up to ~20 m and a relief of ~3 m, but they narrow down to ~6 m and flatten out in the central part of the glacier. At present, debris deposition and transport in the UM and LM occur entirely in the glacier's ablation zone (**Figure 2.1**, **Figure 2.2**), implying that, except for seasonal snow cover, the debris currently falling on the glacier is permanently exposed.

## 2.4 Material and methods

We provide an accompanying data publication (Wetterauer *et al.*, 2022b) with this study, which comprises the cosmogenic nuclide dataset and detailed descriptions of the sample processing and setup of our model, including its evaluation. As for this thesis, the data publication is included in Appendix A (please note that only the text sections, figures, and tables from Wetterauer *et al.* (2022b) are listed in Appendix A, which contain additional information and data not presented in this Chapter 2 in order to avoid repetition).

### 2.4.1 Medial moraine samples

In October 2018 we collected 15 debris samples from the UM and LM (**Table 2.1**, **Figure 2.1a**). Samples (~7 kg each) were collected downglacier every ~500 m. Nine samples were taken from the UM (UM1 to UM9) along a ~4.2 km long profile, between 2918 and 2547 m elevation. Six samples were taken from the LM (LM1 to LM6) along a ~2.7 km long profile, between 2875 and 2668 m elevation. Samples were mainly composed of schist and gneiss clasts with grain sizes ranging from coarse sand (~1 mm) to pebble (~30 mm) size (**Figure A1**). Clasts were randomly collected (amalgamated) over the moraine surface (**Figure 2.1c**). The collection area for each sample was approximately 10×30 m near the debris source areas and the glacier terminus, and approximately 6×20 m in the central glacier region where the medial moraines are narrower. Over the sampled distance, the moraine topography was relatively smooth and not intersected by open crevasses. We found no obvious indicators for lateral debris input, such as runout deposits from valley side walls traversing onto the ice, or for basal debris input, such as aligned deposits sheared onto the glacier surface by internal ice thrusting or rounded clasts (e.g., Boulton, 1978; Alley *et al.*, 1997).

**Table 2.1:** Data for medial moraine debris samples collected on Glacier d’Otemma.

Sample <sup>a</sup>	Latitude (°N)	Longitude (°E)	Elevation (m)	Downglacier distance <sup>b</sup> (m)	Performed analysis <sup>c</sup>		
					/f	/c	GS
<i>Upper medial moraine (UM)</i>							
UM1	45.9653	7.4657	2918	0	X	X	
UM2	45.9617	7.4622	2882	478	X		X
UM3	45.9584	7.4559	2837	1088	X	X	
UM4	45.9543	7.4504	2789	1712	X	X	
UM5	45.9507	7.4458	2747	2248	X	X	
UM6	45.9483	7.4405	2707	2743	X		
UM7	45.9455	7.4352	2663	3258	X	X	
UM8	45.9431	7.4297	2600	3758	X		
UM9	45.9407	7.4248	2547	4224	X	X	
<i>Lower medial moraine (LM)</i>							
LM1	45.9613	7.4621	2875	0	X		X
LM2	45.9582	7.4560	2835	581	X		
LM3	45.9542	7.4507	2791	1184	X		
LM4	45.9504	7.4459	2749	1745	X		
LM5	45.9480	7.4407	2712	2228	X		
LM6	45.9450	7.4354	2668	2754	X		

<sup>a</sup> Amalgamated supraglacial debris samples. <sup>b</sup> Distance from uppermost sample UM1 and LM1 of upper and lower medial moraine, respectively. <sup>c</sup> /f = fine-grained fraction (0.125-4 mm), /c = coarse-grained fraction (4-22.4 mm), GS = grain size sub-samples (0.125-0.8, 0.8-2, 2-4, 4-8, and 8-16 mm).

Cosmogenic nuclide sample processing was performed according to standard *in situ*-produced <sup>10</sup>Be separation techniques (e.g., von Blanckenburg *et al.*, 2004). Debris samples were sieved into different fractions (**Figure A1**) and processed at the Helmholtz Laboratory for the

Geochemistry of the Earth Surface (HELGES) at the GFZ German Research Centre for Geosciences in Potsdam, Germany. A total of 29  $^{10}\text{Be}/^9\text{Be}$  ratio measurements (**Table 2.2**) were carried out at the accelerator mass spectrometer (AMS) at the University of Cologne, Germany (Dewald *et al.*, 2013), and normalized to the standards KN01-6-2 (nominal  $^{10}\text{Be}/^9\text{Be}$  value:  $5.35 \times 10^{-13}$ ) and KN01-5-3 (nominal  $^{10}\text{Be}/^9\text{Be}$  value:  $6.32 \times 10^{-12}$ ). Details are provided in Section **A1**.

**Table 2.2:** Measured accelerator mass spectrometry (AMS)  $^{10}\text{Be}/^9\text{Be}$  ratios and  $^{10}\text{Be}$  concentrations.

Sample	Grain size (mm)	Qtz mass (g)	Carrier mass (mg)	AMS $^{10}\text{Be}/^9\text{Be}$ $\times 10^{-14}$ $\pm 1\sigma$	$[^{10}\text{Be}]_{\text{measured}}$ $\times 10^3$ (atoms $\text{g}^{-1}$ ) $\pm 1\sigma$	Blank <sup>b</sup>
<i>Upper medial moraine (UM)</i>						
<i>Fine-grained samples</i>						
UM1/f	0.125-4	26.78	0.200	1.47 $\pm$ 0.15	5.53 $\pm$ 0.57	B3
UM2/f <sup>a</sup>	0.125-4	-	-	- - -	7.41 $\pm$ 0.79	-
UM3/f	0.125-4	26.88	0.200	1.73 $\pm$ 0.15	6.52 $\pm$ 0.57	B3
UM4/f	0.125-4	22.82	0.201	8.50 $\pm$ 0.40	38.32 $\pm$ 1.86	B3
UM5/f	0.125-4	23.06	0.201	2.47 $\pm$ 0.17	10.96 $\pm$ 0.78	B3
UM6/f	0.125-4	22.97	0.200	3.48 $\pm$ 0.22	15.52 $\pm$ 0.98	B3
UM7/f	0.125-4	23.39	0.200	6.19 $\pm$ 0.39	26.34 $\pm$ 1.74	B2
UM8/f	0.125-4	22.39	0.201	4.43 $\pm$ 0.26	20.32 $\pm$ 1.23	B3
UM9/f	0.125-4	22.67	0.200	4.12 $\pm$ 0.25	18.59 $\pm$ 1.14	B3
<i>Coarse-grained samples</i>						
UM1/c	4-22.4	32.25	0.200	1.23 $\pm$ 0.15	3.69 $\pm$ 0.47	B4
UM3/c	4-22.4	32.69	0.200	1.03 $\pm$ 0.12	3.01 $\pm$ 0.38	B4
UM4/c	4-22.4	37.09	0.205	1.65 $\pm$ 0.15	4.48 $\pm$ 0.44	B5
UM5/c	4-22.4	25.07	0.200	1.89 $\pm$ 0.18	7.47 $\pm$ 0.76	B4
UM7/c	4-22.4	32.43	0.200	4.19 $\pm$ 0.28	13.06 $\pm$ 0.89	B4
UM9/c	4-22.4	32.69	0.200	5.48 $\pm$ 0.31	17.03 $\pm$ 1.00	B4
<i>Grain size sub-samples</i>						
UM2/0.8	0.125-0.8	21.29	0.206	2.30 $\pm$ 0.22	9.34 $\pm$ 1.18	B1
UM2/2	0.8-2	23.47	0.199	2.12 $\pm$ 0.18	8.30 $\pm$ 0.82	B2
UM2/4	2-4	32.07	0.200	1.78 $\pm$ 0.16	5.47 $\pm$ 0.51	B4
UM2/8	4-8	32.12	0.199	3.12 $\pm$ 0.21	9.70 $\pm$ 0.69	B4
UM2/16	8-16	32.78	0.200	0.65 $\pm$ 0.11	1.80 $\pm$ 0.34	B4
<i>Lower medial moraine (LM)</i>						
<i>Fine-grained samples</i>						
LM1/f <sup>a</sup>	0.125-4	-	-	- - -	17.78 $\pm$ 1.14	-
LM2/f	0.125-4	22.64	0.200	4.94 $\pm$ 0.30	22.37 $\pm$ 1.39	B3
LM3/f	0.125-4	14.54	0.200	2.07 $\pm$ 0.18	13.09 $\pm$ 1.32	B2
LM4/f	0.125-4	20.31	0.199	2.72 $\pm$ 0.21	12.66 $\pm$ 1.10	B2
LM5/f	0.125-4	22.90	0.201	3.28 $\pm$ 0.22	14.68 $\pm$ 0.99	B3
LM6/f	0.125-4	17.11	0.200	5.34 $\pm$ 0.32	30.81 $\pm$ 2.00	B2
<i>Grain size sub-samples</i>						
LM1/0.8	0.125-0.8	26.98	0.206	4.31 $\pm$ 0.31	15.27 $\pm$ 1.26	B1
LM1/2	0.8-2	22.58	0.201	3.58 $\pm$ 0.23	16.28 $\pm$ 1.06	B3
LM1/4	2-4	31.87	0.200	6.56 $\pm$ 0.33	20.97 $\pm$ 1.10	B4
LM1/8	4-8	32.08	0.200	5.75 $\pm$ 0.33	18.22 $\pm$ 1.08	B4
LM1/16	8-16	21.51	0.201	2.83 $\pm$ 0.23	13.23 $\pm$ 1.14	B4

<sup>a</sup>  $[^{10}\text{Be}]$  calculated from corresponding weighted mean of separate measurements of fractions 0.125-0.8, 0.8-2, and 2-4 mm. <sup>b</sup> Process blank used to correct respective sample batches, where corresponding  $^{10}\text{Be}/^9\text{Be}$  ratios are B1 =  $4.43 \times 10^{-15}$ , B2 =  $2.16 \times 10^{-15}$ , B3 =  $2.55 \times 10^{-16}$ , B4 =  $7.65 \times 10^{-16}$ , and B5 =  $1.19 \times 10^{-15}$ .

To ensure comparability, we primarily focused on a fine grain size fraction of 0.125-4 mm for all samples. To explore potential grain size effects, we additionally analysed a coarser grain size fraction of 4-22.4 mm from almost every second sample on the UM. At higher resolution, we separately analysed the five grain size fractions 0.125-0.8, 0.8-2, 2-4, 4-8, and 8-16 mm for the samples UM2 and LM1 (**Table 2.1**, **Table 2.2**).

## 2.4.2 Cosmogenic nuclides in medial moraine debris

Quantifying headwall erosion rates from [ $^{10}\text{Be}$ ] in supraglacial debris relies on knowledge of (i) the  $^{10}\text{Be}$  production rate in the headwall, which allows to quantify [ $^{10}\text{Be}$ ] in the headwall (“[ $^{10}\text{Be}$ ]<sub>headwall</sub>“), and (ii) the  $^{10}\text{Be}$  production rate during downglacier debris transport, which allows to quantify [ $^{10}\text{Be}$ ] accumulated during glacial transport (“[ $^{10}\text{Be}$ ]<sub>transport</sub>“). The sum of these two components is the measured [ $^{10}\text{Be}$ ] in supraglacial debris samples (“[ $^{10}\text{Be}$ ]<sub>measured</sub>“). To disentangle them, we developed a simple 1D model to predict [ $^{10}\text{Be}$ ]<sub>transport</sub> by estimating debris transport trajectories for our samples (see Section 2.4.3). We then subtract [ $^{10}\text{Be}$ ]<sub>transport</sub> from [ $^{10}\text{Be}$ ]<sub>measured</sub> in order to estimate [ $^{10}\text{Be}$ ]<sub>headwall</sub>.

Using the estimated [ $^{10}\text{Be}$ ]<sub>headwall</sub>, Equation 2.1 (Lal, 1991) allows us to determine “apparent“ headwall erosion rates  $E$  (mm yr $^{-1}$ ):

$$[^{10}\text{Be}]_{\text{headwall}}(z) = \frac{P_{sp}(0)}{\lambda + \frac{\rho E}{\Lambda}} e^{-z\left(\frac{\rho}{\Lambda}\right)} \quad (2.1)$$

When assuming a steadily eroding bedrock surface and an initial bedrock concentration of zero, [ $^{10}\text{Be}$ ]<sub>headwall</sub>( $z$ ) is the  $^{10}\text{Be}$  concentration (atoms g $^{-1}$ ) in the headwall as a function of bedrock depth  $z$  (cm),  $P_{sp}(0)$  is the spallogenic surface production rate (atoms g $^{-1}$  yr $^{-1}$ ),  $\lambda$  is the decay constant (yr $^{-1}$ ) (based on a half-life of  $1.387 \pm 0.012$  Myr; Chmeleff *et al.*, 2010; Korschinek *et al.*, 2010),  $\rho$  is the material density (g cm $^{-3}$ ), and  $\Lambda$  is the absorption mean free path (g cm $^{-2}$ ). Building on the steady-state assumption, but being aware that headwalls may inherit nuclide signatures from alternating episodes of exposure and coverage as well as from changing erosion rates during these phases, we consider our rates to be “apparent” headwall erosion rates.

We computed  $^{10}\text{Be}$  production rates for ice-free surfaces using a digital elevation model (DEM) of 30 m resolution (global raster dataset SRTM GL1; NASA Shuttle Radar Topography Mission SRTM, 2013) using MATLAB<sup>®</sup> and TopoToolbox Version 2 (Schwanghart & Scherler, 2014). Gabbroic headwall areas were excluded due to their low quartz content (**Figure 2.2**). We determined mean headwall  $^{10}\text{Be}$  production rates for three different time slices using reconstructed glacier outlines (**Figure 2.3**) that document the ice extent of Glacier d’Otemma for the years 2010 (~recent ice extent; Fischer *et al.*, 2014), 1973 (interim stage; Müller *et al.*, 1976), and 1850 (~final LIA extent; Maisch *et al.*, 2000). We refined the 1850 glacier outline in the headwall region using the first editions of the Dufour and Siegfried Map (Swisstopo, 2021) as well as the 1850 LIA ice extent in the Haut Val de Bagnes as reconstructed by Lambiel and Talon (2019). To examine both moraines individually, we sub-divided the debris source area into UM headwalls and LM headwalls (**Figure 2.2**, **Figure 2.3b-d**), using the DEM and the flow directions following the steepest decent approach.

All  $^{10}\text{Be}$  production rates were calculated with the functions provided by the CRONUS online calculator version 2.3 (Balco *et al.*, 2008), using the constant spallation scaling scheme ‘St’ (Lal, 1991; Stone, 2000) and a sea level high latitude (SLHL) spallation production rate of  $4.01 \pm 0.33$  atoms g $^{-1}$  yr $^{-1}$  (Borchers *et al.*, 2016). We neglected temporal variations in production rates due to paleomagnetic intensity changes as most of our samples are likely younger than ~200 years (see Section 2.5.2). Moreover, we neglected production by muons in

the headwalls as it accounts for <1% of the spallogenic production near the bedrock surface. Effects of topographic shielding on nuclide production rates were estimated following Dunne *et al.* (1999) as implemented in the TopoToolbox Version 2 (Schwanghart & Scherler, 2014). Snow cover shielding of the headwalls was neglected as large bedrock areas seem to remain snow-free during snow cover seasons (Swisstopo, 2021). We assumed a bedrock density  $\rho_r$  of  $2.65 \text{ g cm}^{-3}$  in Equation 2.1 and also considered the surface slope dependency of cosmic ray attenuation in bedrock by calculating the absorption mean free path  $\Lambda$  for each DEM pixel following Masarik *et al.* (2000). Since headwall erosion rates are measured perpendicular to the surface, we applied an area correction using the local slope angle to compute mean production rates.

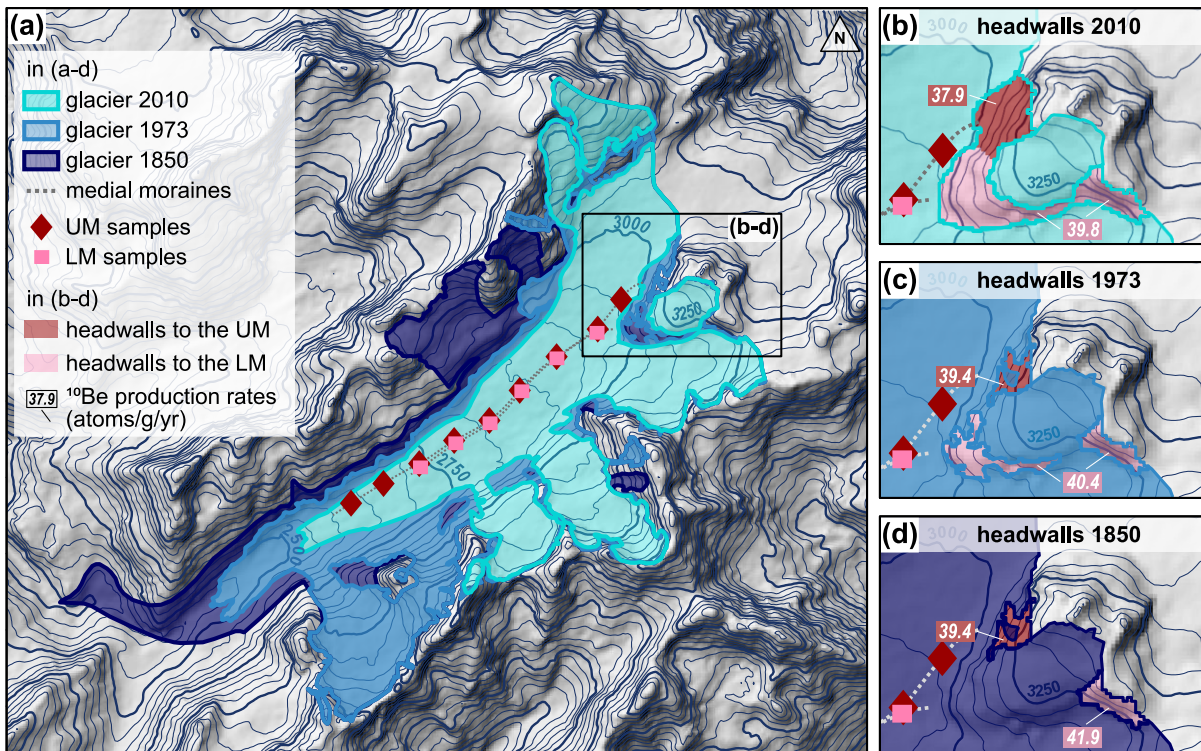


**Figure 2.3:** Glacier d’Otemma and debris source area Petit Mont Collon in 2010, 1973, and 1850 (glacier outlines by Fischer *et al.*, 2014, Müller *et al.*, 1976, and modified from Maisch *et al.*, 2000). (a) Contour grid depicting the three superimposed glacier extents. (b-d) Detail of the ice-covered and ice-free areas of the source headwalls and computed average  $^{10}\text{Be}$  production rates in (b) 2010, (c) 1973, and (d) 1850. The contour line spacing corresponds to 50 m elevation and is based on the recent DEM (SRTM GL1; NASA Shuttle Radar Topography Mission SRTM, 2013) where the glacier extent is smallest. Therefore, contour lines on the glacier body itself are only valid for the most recent glacier extent in 2010. UM/LM: upper/lower medial moraine

### 2.4.3 Computation of downglacier debris transport

The  $[^{10}\text{Be}]_{\text{transport}}$  is small compared to  $[^{10}\text{Be}]_{\text{headwall}}$  in settings where erosion rates are low, glacier transport pathways are short or mainly englacial, glacier surface velocities are high ( $\geq 30 \text{ m yr}^{-1}$ ), and environmental conditions are constant (Ward & Anderson, 2011; Scherler & Egholm, 2020). However,  $[^{10}\text{Be}]_{\text{transport}}$  may be substantial if erosion rates are very high, if transport is far and/or slow, and predominantly supraglacial. Since both glacier velocity and transport depth vary downglacier and through time when the glacier is changing, the relative contribution of  $[^{10}\text{Be}]_{\text{transport}}$  to  $[^{10}\text{Be}]_{\text{measured}}$  must vary in time, too.

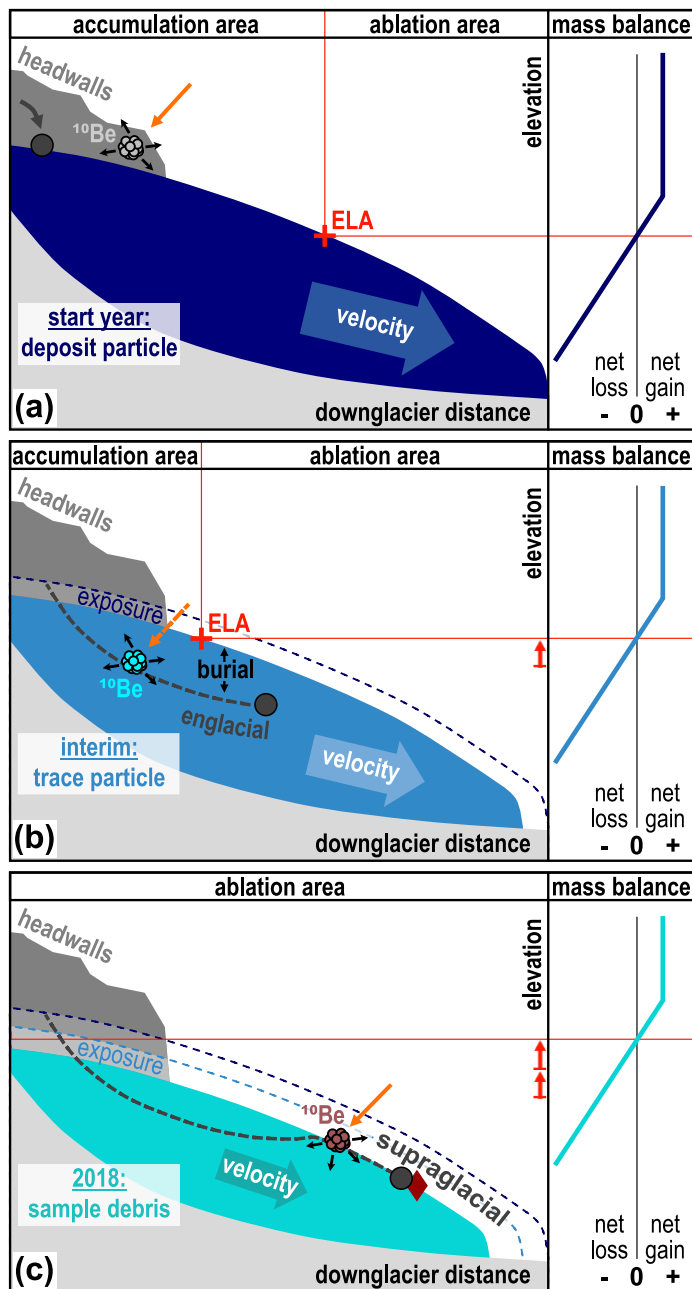


**Figure 2.4:** Schematic of the headwall-glacier system and setup of the debris trajectory model. An exemplary transport scenario illustrates a debris trajectory from headwall to sample location. **(a)** Initially, a debris particle with the  $^{10}\text{Be}$  signature of the headwall ( $^{10}\text{Be}_{\text{headwall}}$ ) is deposited on the ice surface. **(b)** In the accumulation area the debris particle is buried within the ice and transported englacially. During its transport it accumulates additional  $^{10}\text{Be}$  ( $^{10}\text{Be}_{\text{transport}}$ ). **(c)** In the ablation area the debris particle re-emerges and is transported supraglacially until it reaches a sample's 2018 location. It inherits a combined  $^{10}\text{Be}$  signature ( $^{10}\text{Be}_{\text{measured}}$ ). Note the indication of former ice surface elevations (thin dashed lines), new bedrock exposure (highlighted stripes), decreasing glacier velocity (thinning arrows), and ELA rise and shift in mass balance (red arrows) through time. This scenario applies for our older samples (e.g., UM4 to UM9). Younger samples (e.g., UM1, UM2) were deposited in the ablation area and experienced only supraglacial transport. UM/LM: upper/lower medial moraine; ELA: equilibrium line altitude

To estimate both  $^{10}\text{Be}_{\text{transport}}$  and the ages of our samples, we developed a simple 1D model to reconstruct time-depth pathways (**Figure 2.4**). We first derived modern horizontal glacier surface velocities by cross-correlating satellite imagery (**Figure A2c**; Leprince *et al.*, 2007; Scherler *et al.*, 2008), and by tracking boulders on historical aerial images (**Figure A2c**; Swisstopo, 2021). We then calibrated a simple model using the centre-line velocity profile and recent ice thickness and surface slope estimates, by tuning the rate parameter in Glen's flow law (**Figure A2a-c**; Glen, 1952, 1955; Farinotti *et al.*, 2019). Using the model calibrated to present conditions, we then estimated past surface velocities with glacier thicknesses and surface slopes reconstructed for the year 1850 as input (**Figure A2a-c**, **Figure A3**; Lambiel & Talon, 2019). To assess temporal changes in horizontal velocities, we interpolated between the ice thicknesses and slopes from 1850 and the sampling year 2018 in a three-step linear mode (**Figure A2d,e**). To differentiate between englacial and supraglacial transport, and to estimate debris particle burial depth, we also calculated the vertical velocity in the ice. We used a vertical

mass balance profile based on a compilation of glacier mass balances from the European Alps (**Figure A5**; Dyurgerov, 2002). Temporal changes in vertical velocities were estimated by shifting the mass balance profile according to a reconstructed ELA history (**Figure A4**; Kurowski, 1891; Braithwaite, 2015). Finally, we generated particle trajectories through the glacier for all samples, computed sample ages, and estimated  $[^{10}\text{Be}]_{\text{transport}}$  under consideration of seasonal snow cover (**Figure A6**, **Figure A7**). Details are provided in Section A2.

## 2.5 Results

### 2.5.1 Measured $^{10}\text{Be}$ concentrations

The  $[^{10}\text{Be}]_{\text{measured}}$  of our 29 analysed debris sample fractions range between  $2 \times 10^3$  and  $38 \times 10^3$  atoms  $\text{g}^{-1}$  (**Table 2.2**, **Figure 2.5a,b**).

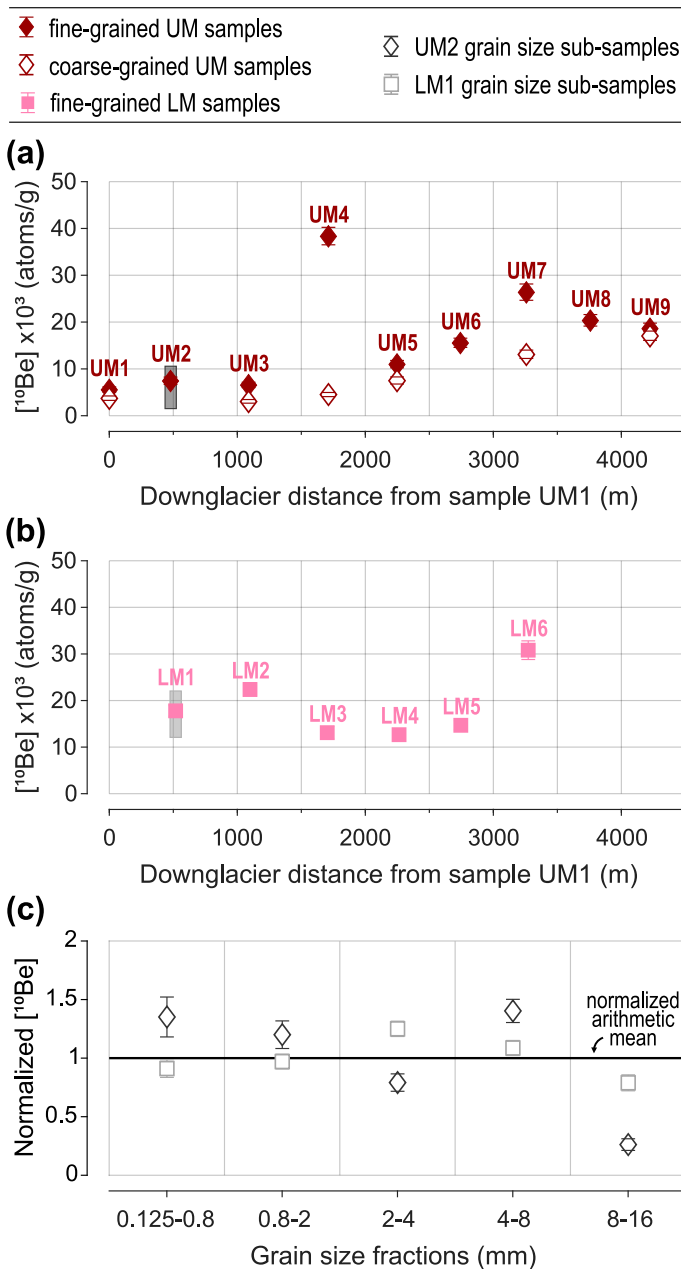


**Figure 2.5:**  $[^{10}\text{Be}]_{\text{measured}}$  ( $\pm 1\sigma$  analytical error) in medial moraine samples along Glacier d’Otemma. **(a)** UM  $[^{10}\text{Be}]$  obtained on a fine grain size fraction (0.125-4 mm) for all nine samples and on a coarse grain size fraction (4-22.4 mm) for every second sample. The grey bar indicates the concentration range of the grain size sub-samples from UM2. **(b)** LM  $[^{10}\text{Be}]$  obtained on a fine grain size fraction (0.125-4 mm) for all six samples. The grey bar indicates the concentration range of the grain size sub-samples from LM1. **(c)** Normalized  $[^{10}\text{Be}]$  of grain size sub-samples from UM2 and LM1. The normalization is based on the arithmetic mean of the five grain size fractions of UM2 and LM1, respectively. Note that symbol sizes are mostly larger than the analytical error and that downglacier distances were measured relative to the uppermost collected sample UM1. UM/LM: upper/lower medial moraine

For the nine fine-grained (0.125-4 mm) UM samples,  $[^{10}\text{Be}]_{\text{measured}}$  range between  $6 \times 10^3$  and  $38 \times 10^3$  atoms  $\text{g}^{-1}$  (**Figure 2.5a**). Overall, samples near the glacier head (younger deposits) have lower concentrations, whereas samples farther downglacier (older deposits) have higher concentrations. Sample UM4/f stands out with an extraordinary high concentration compared to the neighbouring samples. For the six coarse-grained (4-22.4 mm) UM samples,  $[^{10}\text{Be}]_{\text{measured}}$  range between  $3 \times 10^3$  and  $17 \times 10^3$  atoms  $\text{g}^{-1}$  and are thus systematically lower relative to the fine fraction, half of them differing by  $<35\%$  (**Figure 2.5a**). Only sample UM4/c differs by almost 90%. For the six fine-grained (0.125-4 mm) LM samples,  $[^{10}\text{Be}]_{\text{measured}}$  vary between  $13 \times 10^3$  and  $31 \times 10^3$  atoms  $\text{g}^{-1}$  (**Figure 2.5b**). Compared to the UM, LM concentrations are higher and less variable.

**Table 2.3:** Modelled sample ages, burial depth and  $^{10}\text{Be}$  concentrations accumulated during glacial transport ( $[^{10}\text{Be}]_{\text{transport}}$ ), as well as derived  $^{10}\text{Be}$  concentrations in the headwalls ( $[^{10}\text{Be}]_{\text{headwall}}$ ) and apparent headwall erosion rates.

Sample	Age <sup>a</sup> (yrs)	Burial depth <sup>a,b</sup> (m)	$[^{10}\text{Be}]_{\text{transport}}^{\text{a}}$ $\times 10^3$ (atoms $\text{g}^{-1}$ )	$[^{10}\text{Be}]_{\text{transport}}/$ $[^{10}\text{Be}]_{\text{measured}}$ (%)	$[^{10}\text{Be}]_{\text{headwall}}^{\text{c}}$ $\times 10^3$ (atoms $\text{g}^{-1}$ ) $\pm 1\sigma$	Apparent headwall erosion rate <sup>d</sup> (mm $\text{yr}^{-1}$ ) $\pm 1\sigma$
<i>Upper medial moraine (UM)</i>						
<i>Fine-grained samples</i>						
UM1/f	45	0.0	1.37	25	4.16 $\pm$ 0.57	5.1 $\pm$ 0.8
UM2/f	77	0.0	2.36	32	5.04 $\pm$ 0.79	4.2 $\pm$ 0.7
UM3/f	103	-1.2	2.84	44	3.68 $\pm$ 0.57	5.8 $\pm$ 1.0
UM4/f	130	-5.0	2.52	7	35.80 $\pm$ 1.86	0.6 $\pm$ 0.1
UM5/f	148	-9.1	2.35	21	8.61 $\pm$ 0.78	2.5 $\pm$ 0.3
UM6/f	167	-12.4	2.33	15	13.19 $\pm$ 0.98	1.6 $\pm$ 0.2
UM7/f	182	-14.7	2.36	9	23.98 $\pm$ 1.74	0.9 $\pm$ 0.1
UM8/f	199	-16.2	2.43	12	17.89 $\pm$ 1.23	1.2 $\pm$ 0.1
UM9/f	206	-16.7	2.47	13	16.12 $\pm$ 1.14	1.3 $\pm$ 0.1
<i>Coarse-grained samples</i>						
UM1/c	45	0.0	1.37	37	2.32 $\pm$ 0.47	9.1 $\pm$ 2.0
UM3/c	103	-1.2	2.84	94	0.17 $\pm$ 0.38	n.a. <sup>e</sup> $\pm$ n.a. <sup>e</sup>
UM4/c	130	-5.0	2.52	56	1.96 $\pm$ 0.44	10.8 $\pm$ 2.6
UM5/c	148	-9.1	2.35	31	5.12 $\pm$ 0.76	4.1 $\pm$ 0.7
UM7/c	182	-14.7	2.36	18	10.70 $\pm$ 0.89	2.0 $\pm$ 0.2
UM9/c	206	-16.7	2.47	14	14.57 $\pm$ 1.00	1.5 $\pm$ 0.2
<i>Grain size sub-samples</i>						
UM2/0.8	77	0.0	2.36	25	6.98 $\pm$ 1.18	3.0 $\pm$ 0.6
UM2/2	77	0.0	2.36	29	5.93 $\pm$ 0.82	3.6 $\pm$ 0.6
UM2/4	77	0.0	2.36	43	3.10 $\pm$ 0.51	6.8 $\pm$ 1.3
UM2/8	77	0.0	2.36	24	7.34 $\pm$ 0.69	2.9 $\pm$ 0.4
UM2/16	77	0.0	2.36	131	-0.56 $\pm$ 0.34	n.a. <sup>e</sup> $\pm$ n.a. <sup>e</sup>
<i>Lower medial moraine (LM)</i>						
<i>Fine-grained samples</i>						
LM1/f	35	0.0	1.05	6	16.73 $\pm$ 1.14	1.3 $\pm$ 0.1
LM2/f	67	0.0	2.04	9	20.33 $\pm$ 1.39	1.1 $\pm$ 0.1
LM3/f	94	0.0	2.84	22	10.25 $\pm$ 1.32	2.2 $\pm$ 0.3
LM4/f	115	-0.2	3.43	27	9.23 $\pm$ 1.10	2.4 $\pm$ 0.3
LM5/f	134	-1.8	3.46	24	11.23 $\pm$ 0.99	2.0 $\pm$ 0.2
LM6/f	152	-4.2	3.26	11	27.55 $\pm$ 2.00	0.8 $\pm$ 0.1
<i>Grain size sub-samples</i>						
LM1/0.8	35	0.0	1.05	7	14.23 $\pm$ 1.26	1.6 $\pm$ 0.2
LM1/2	35	0.0	1.05	6	15.23 $\pm$ 1.06	1.5 $\pm$ 0.2
LM1/4	35	0.0	1.05	5	19.92 $\pm$ 1.10	1.1 $\pm$ 0.1
LM1/8	35	0.0	1.05	6	17.17 $\pm$ 1.08	1.3 $\pm$ 0.1
LM1/16	35	0.0	1.05	8	12.18 $\pm$ 1.14	1.8 $\pm$ 0.2

<sup>a</sup> Computed using a simple 1D debris particle trajectory model (Wetterauer *et al.*, 2022b). <sup>b</sup> Maximum burial depth modelled for debris particles of a sample. Negative numbers indicate partially englacial transport, 0 indicates exclusively supraglacial transport. <sup>c</sup> Calculated by subtracting  $[^{10}\text{Be}]_{\text{transport}}$  from  $[^{10}\text{Be}]_{\text{measured}}$ .  $1\sigma$  estimates correspond to analytical uncertainties of  $[^{10}\text{Be}]_{\text{measured}}$ . <sup>d</sup> Calculated using spallogenic mean source area production rates of  $P_{sp}(0) = 39.44$  atoms  $\text{g}^{-1} \text{yr}^{-1}$  and  $P_{sp}(0) = 40.43$  atoms  $\text{g}^{-1} \text{yr}^{-1}$  and mean source area absorption mean free paths of  $A = 142.56$  g  $\text{cm}^{-2}$  and  $A = 144.80$  g  $\text{cm}^{-2}$  for UM and LM samples, respectively.  $1\sigma$  estimates are based on the analytical uncertainties of  $[^{10}\text{Be}]_{\text{measured}}$ . <sup>e</sup> Values not available (n.a.) due to unreasonable  $[^{10}\text{Be}]_{\text{headwall}}$  estimates (see Section 2.5.2).

For our grain size sub-samples (0.125-0.8, 0.8-2, 2-4, 4-8, and 8-16 mm) from UM2 and LM1,  $[^{10}\text{Be}]_{\text{measured}}$  vary between  $2 \times 10^3$  and  $10 \times 10^3$  atoms  $\text{g}^{-1}$  and between  $13 \times 10^3$  and  $21 \times 10^3$  atoms  $\text{g}^{-1}$ , respectively (indicated as grey bars in **Figure 2.5a,b**). Notably, variations in  $[^{10}\text{Be}]_{\text{measured}}$  between these grain size fractions are of similar magnitude as variations between fine-grained samples along the first ~2500 and ~3000 m distance downglacier of UM and LM, respectively. To compare grain size-related variations in  $[^{10}\text{Be}]_{\text{measured}}$  between the two samples (UM2 and LM1), we normalized the concentrations of each grain size fraction by the arithmetic mean of all concentrations of the respective sample (**Figure 2.5c**). In both cases, the variations are mostly <50% and no systematic trend is discernible, although the lowest concentrations are found for the coarsest (8-16 mm) grain size sub-sample.

### 2.5.2 Transport and headwall $^{10}\text{Be}$ concentrations, and sample ages

Based on our reconstructed debris trajectories (**Figure A7**), we estimated the age of each sample, which corresponds to the estimated debris transport time from the headwall to the sample location, and the total amount of  $[^{10}\text{Be}]_{\text{transport}}$ . We then derived the  $[^{10}\text{Be}]_{\text{headwall}}$  by correcting  $[^{10}\text{Be}]_{\text{measured}}$  for transport (**Table 2.3, Figure 2.6a**).

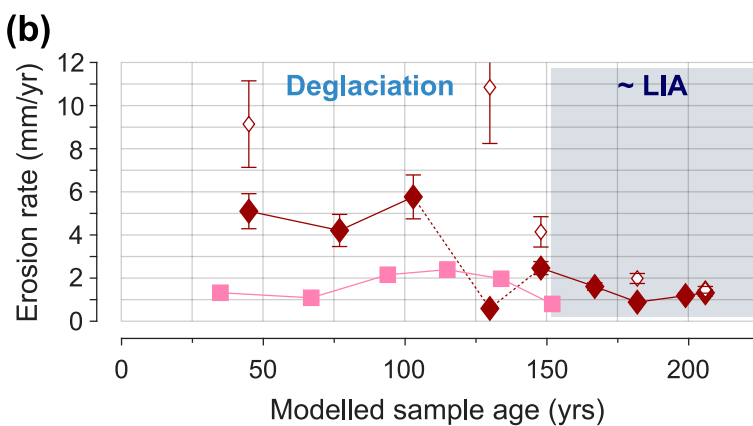
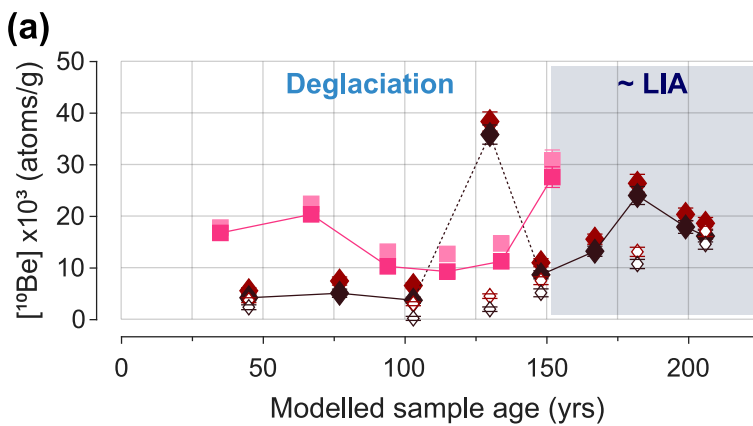
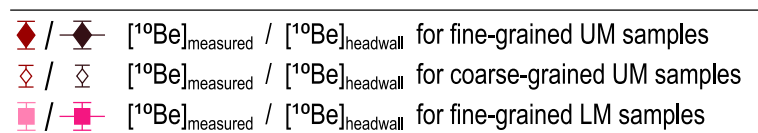


**Figure 2.6:** Medial moraine data of Glacier d’Otemma through time. (a) Comparison of  $[^{10}\text{Be}]_{\text{measured}}$  and transport-corrected  $[^{10}\text{Be}]_{\text{headwall}}$  ( $\pm 1\sigma$  analytical error). (b) Apparent headwall erosion rates ( $\pm 1\sigma$  uncertainty). Concentrations and rates are plotted against modelled sample ages. The end of the LIA and the following deglaciation are indicated. For clarity symbols of coarse-grained UM samples are smaller and unconnected. For fine-grained UM samples, the connecting line to the high concentration outlier UM4/f is dashed (see Section 2.6.2). Note that we did not calculate an erosion rate for the coarse-grained sample UM3 (see Section 2.5.2) and that symbol sizes are often larger than the provided error UM/LM: upper/ lower medial moraine; LIA: Little Ice Age

On the UM, low-concentration samples (UM1 to UM3) yield ages of ~45 to 100 years, whereas high-concentration samples (UM6 to UM9) yield ages of ~170 to 210 years. On the LM, the estimated transport time is shorter, with ages ranging from ~35 to 150 years. Modelled  $^{10}\text{Be}]_{\text{transport}}$  vary between  $\sim 1 \times 10^3$  and  $3 \times 10^3$  atoms  $\text{g}^{-1}$ . For the majority of fine-grained UM and LM samples, this accounts for less than ~25% of our  $^{10}\text{Be}]_{\text{measured}}$  (**Table 2.3**). Overall, subtracting the minor  $^{10}\text{Be}]_{\text{transport}}$  from the dominating  $^{10}\text{Be}]_{\text{measured}}$  does not change downglacier patterns for  $^{10}\text{Be}]_{\text{headwall}}$  (see Section 2.5.1; **Figure 2.5a,b**, **Figure 2.6a**).

We note that for two coarser sample fractions, UM3/c and UM2/16, transport correction yielded very low and even slightly negative  $^{10}\text{Be}]_{\text{headwall}}$  values, respectively (**Table 2.3**). Especially negative concentrations are not possible, suggesting that our modelled  $^{10}\text{Be}]_{\text{transport}}$  are too high. Uncertainties in our model (see Section A2.5) affect particularly samples in which  $^{10}\text{Be}]_{\text{measured}}$  are comparatively low and transport is almost exclusively supraglacial, as in case of these two samples. Since our reconstructions are based on several assumptions (see Section A2.1) it is difficult to verify the model setup or to provide meaningful error estimates. Therefore, we do not calculate apparent headwall erosion rates for UM3/c and UM2/16. Nonetheless, given the continuous retreat history of Glacier d'Otemma (see Section 2.3.1), we consider it unlikely that our model-based estimates are far off the true values, especially for samples older than ~120 years that were most likely quickly buried under snow and ice (**Table 2.3**).

### 2.5.3 Apparent headwall erosion rates

The derived apparent headwall erosion rates are reported in **Table 2.3**; for brevity, these are termed “erosion rates” from now on. They were calculated with mean  $^{10}\text{Be}$  production rates for UM and LM headwalls, respectively (**Table 2.4**). Overall, derived erosion rates range between  $0.6 \pm 0.1$  and  $10.8 \pm 2.6$   $\text{mm yr}^{-1}$  (**Figure 2.6b**). For the fine-grained UM samples, erosion rates range between  $0.6 \pm 0.1$  and  $5.8 \pm 1.0$   $\text{mm yr}^{-1}$ . Younger samples (UM1/f to UM3/f) yield higher erosion rates of  $4.2 \pm 0.7$  to  $5.8 \pm 1.0$   $\text{mm yr}^{-1}$ , whereas erosion rates for older samples (UM6/f to UM9/f) are lower, spanning between  $0.9 \pm 0.1$  and  $1.6 \pm 0.2$   $\text{mm yr}^{-1}$ . Erosion rates for the coarse-grained UM samples decrease from  $10.8 \pm 2.6$  to  $1.5 \pm 0.2$   $\text{mm yr}^{-1}$  downglacier and with increasing age. For the fine-grained LM samples, erosion rates span a narrower range from  $0.8 \pm 0.1$  to  $2.4 \pm 0.3$   $\text{mm yr}^{-1}$ . Among our grain size sub-samples from UM2 and LM1, erosion rates are fairly similar.

## 2.6 Discussion

### 2.6.1 Grain size-dependent $^{10}\text{Be}$ concentrations

Grain size effects in  $^{10}\text{Be}]$  have been observed ever since the first studies have used cosmogenic nuclides for quantifying catchment-average erosion rates (e.g., Brown *et al.*, 1995). In studies of alluvial sediments, coarser sand fractions have frequently lower cosmogenic nuclide concentrations. Such trends are typically related to slope failures and mass-wasting events that excavate larger rocks with lower concentration from greater depth (e.g., Brown *et al.*, 1995, 1998; Belmont *et al.*, 2007; Aguilar *et al.*, 2014; Puchol, *et al.*, 2014; West *et al.*, 2014; Tofelde *et al.*, 2018; van Dongen *et al.*, 2019). Other explanations attribute grain size

dependent nuclide concentrations to differences in source area properties, or to selective and abrasive fluvial transport processes (e.g., Matmon *et al.*, 2003; Carretier *et al.*, 2009; Lukens *et al.*, 2016; van Dongen *et al.*, 2019).

Our analysis of  $[^{10}\text{Be}]_{\text{measured}}$  along the UM reveals consistently lower concentrations for coarse-grained (4-22.4 mm) compared to fine-grained (0.125-4 mm) UM samples (**Figure 2.5a**). Within the finer (<16 mm) grain size sub-samples from UM2 and LM1 we observe no systematic variation (**Figure 2.5c**). Based on findings from fluvial landscapes, we assess below the relevance of (i) variable debris source areas and glacial transport, as well as (ii) erosive processes within glacial landscapes, as potential controls on our grain size effects in  $[^{10}\text{Be}]_{\text{measured}}$  from Glacier d'Otemma.

(i) Differences in headwall lithology, debris origin or transport may result in selective contributions of grains with different  $[^{10}\text{Be}]$ . However, we found no difference in mineral composition and no evidence that debris originated from other source areas such as valley side walls, lateral moraines, or even the glacier bed. The passive nature of debris transport downglacier prevents significant post-depositional mixing and temporal storage, hindering the sorting of supraglacial debris. Moreover, the lack of transport processes that abrade supraglacial debris impedes clast comminution. Therefore, we consider the impact of source area and transport-related processes on our grain size distributions negligible.

(ii) Erosion in high-alpine glacial environments occurs through frequent small-scale rockfalls and by infrequent medium- to large-scale rockfalls or avalanches (e.g., Boulton & Deynoux, 1981; Anderson, 2000; Arsenaault & Meigs, 2005). Large events have the potential to excavate bedrock covering a wide depth range from high  $[^{10}\text{Be}]$  at the surface down to low  $[^{10}\text{Be}]$  at depth (Niemi *et al.*, 2005). Distinguishing between supraglacial sand, pebbles and <30 cm-sized blocks, Sarr *et al.* (2019) found no significant size-dependent variation in  $[^{10}\text{Be}]$ . They argue that the distribution of supraglacial clast sizes from sand to boulders results from numerous rock impacts over long fall distances (Ruiz-Carulla *et al.*, 2017), and thus, is independent of their initial depth within the rockwall. However, their findings are based on only two moraine samples from different glaciers in the Mont Blanc Massif. These samples were taken close to the glacier terminus, one of which actually reveals slightly decreasing  $[^{10}\text{Be}]$  from sand to cobble to blocks. We note that supraglacial debris near termini is generally more susceptible to mixing as debris is compressed due to declining ice surface velocities (Anderson *et al.*, 2021), and basal debris input is also more likely near the terminus (Boulton, 1978). Therefore, termini samples may indeed show grain size  $[^{10}\text{Be}]$  patterns different from our samples. Depending on the magnitude of rockfalls, we actually do think that larger events are also more likely composed of coarser and more deeply anchored material compared to smaller events. Although rocks detaching from headwalls typically shatter upon impact, the resulting clast sizes are partly determined by bedrock properties (e.g., discontinuities, joint patterns, rock strength; see e.g., Ruiz-Carulla *et al.*, 2015, 2017). Moreover, models on frost weathering processes indicate that the magnitude of frost damage decreases with depth into the rockwall (e.g., Rempel *et al.*, 2016) and, hence, relatively fewer fractures may be expected at greater depth than near the surface.

Therefore, we propose that higher  $[^{10}\text{Be}]$  in the fine fraction reflect a higher proportion of fine superficial material frequently chipped off the headwall by near-steady exhumation. The coarse fraction may comprise relatively more coarse material of lower  $[^{10}\text{Be}]$  from greater depth within the bedrock. Importantly, both grain size fractions (0.125-4 and 4-22.4 mm) reproduce a comparable and fairly consistent downglacier  $[^{10}\text{Be}]$  pattern (**Figure 2.5a**), indicating that processes accounting for this effect cannot have changed by much over the transport time invoked here. If our record was affected by extensive rockfalls or rock avalanches, low concentration outliers should be present. Also, outlines of rockfall deposits can often be delineated on glaciers (e.g., Deline, 2009), in the field or from remote sensing products, which we did not observe on UM and LM.

### 2.6.2 Temporal variations in apparent headwall erosion rates

Our  $[^{10}\text{Be}]$  from Glacier d'Otemma show systematic variations downglacier, and thus, variations with time. In particular, along both our fine- and coarse-grained UM records,  $[^{10}\text{Be}]$  generally decrease over the last ~200 years (**Figure 2.6a**), suggesting that erosion rates increased towards the present (**Figure 2.6b**). We consider the fine-grained sample UM4/f as an outlier, given that the coarse-grained sample UM4/c fits the temporal systematics of the record well and that the deviation between the two size fractions is large (**Figure 2.5a**). In the following, we will address the question whether the decreasing nuclide concentrations really reflect an overall acceleration in headwall erosion through time. Below, we (i) inspect the reliability of our derived erosion rates with respect to cosmogenic steady state, and then (ii) focus both on processes modulating headwall erosion in a deglaciating landscape and (iii-iv) on conditions controlling the nuclide history of the rock itself.

(i) Under the assumption implied by Equation 2.1 that headwall surfaces erode steadily and uniformly,  $[^{10}\text{Be}]_{\text{headwall}}$  from UM and LM samples translate into erosion rates between 0.6 and 10.8 mm yr<sup>-1</sup> (**Table 2.3**). With an average attenuation length of ~54 cm for the headwalls of Petit Mont Collon and erosion rates of ~1 to 2 mm yr<sup>-1</sup> it would take at least ~540 to 270 years to reach cosmogenic steady state. However, our estimated sample ages are younger and large parts of the source areas experienced ice cover retreat after the LIA, which argues against cosmogenic steady state. Still, source areas exposed during the LIA were most likely also exposed for centuries before, as glaciers were smaller prior to the LIA (e.g., Holzhauser *et al.*, 2005), making cosmogenic steady state possible. We therefore consider samples older than ~150 years with erosion rates of 0.9 to 2.0 mm yr<sup>-1</sup> (UM6 to UM9) to be the most reliable (**Figure 2.6b**). Samples younger than the LIA, with erosion rates of up to 10.8 mm yr<sup>-1</sup>, should be treated with caution (**Figure 2.6b**). Overall reliability is supported by other studies from the European Alps that derive similar cosmogenic nuclide-based erosion rates for rockwalls close to glacier surfaces (Mont Blanc massif: ~0.1 to 1.1 mm yr<sup>-1</sup>, Sarr *et al.*, 2019; Eiger Mountain: ~1.7 and ~2.6 mm yr<sup>-1</sup>, Mair *et al.*, 2019, 2020) and for glacial catchments (Glacier du Mont Miné: ~1.8 to 6.4 mm yr<sup>-1</sup>, Wittmann *et al.*, 2007). Moreover, our estimates compare well to headwall erosion rates from medial moraine debris in the Alaska Range (~0.5 to 1.3 mm yr<sup>-1</sup>; Ward & Anderson, 2011) and the Indian Himalaya (~0.6 to 1.3 mm yr<sup>-1</sup>; Scherler & Egholm, 2020).

(ii) The tendency towards higher recent erosion rates may be indicative of a transient landscape that responds to deglaciation with faster erosion. Rockfall inventories from the European Alps indicate that periods of higher temperatures after the LIA between 1900 and 2010 coincide with enhanced rockfall activity, particularly in areas of thawing permafrost (Ravanel & Deline, 2009, 2011; Huggel *et al.*, 2012). Enhanced rockfall coincides with summer heat waves (2003 and 2015), likely caused by a warming-related deepening of the active layer (Gruber *et al.*, 2004; Ravanel *et al.*, 2017). At the Kitzsteinhorn, Hartmeyer *et al.* (2020a, 2020b) identified that the majority of rock detachments adjacent to a thinning glacier occur within recently uncovered rockwalls <20 m above the glacier surface. The authors attribute the increased rockfall activity to a combination of thermomechanical stresses and active layer penetration into the rock. Similarly, recently exposed bedrock at Glacier d’Otemma could be prone to enhanced rockfall, since the headwall-ice-contact zone at Petit Mont Collon experienced up to ~50 m of ice loss since 1850 (cf. Figure 4 in Lambiel & Talon, 2019).

(iii) The longer the downglacier debris transport continues, the longer it may be exposed to additional cosmic radiation, and the more additional  $^{10}\text{Be}$  accumulation may contribute to  $[\text{}^{10}\text{Be}]_{\text{measured}}$ . At present, debris transport on Glacier d’Otemma proceeds slowly (**Figure A2**) and exclusively supraglacially (**Figure A7**). Nonetheless, our computation of downglacier debris trajectories through time indicates that debris burial and shielding in the past have been sufficient to keep  $[\text{}^{10}\text{Be}]_{\text{transport}}$  low (**Figure 2.6a**). This is in line with estimates from Ward and Anderson (2011) and Scherler and Egholm (2020). Moreover, downglacier medial moraine samples may be a composite of different debris sources as debris continuously emerges in the ablation zone, and their  $^{10}\text{Be}$  signatures may differ depending on where along the source area debris deposition occurred. Recently, at the UM, debris input appears to be a point source (**Figure 2.2**), as simulated with our model. At the LM, debris delivery may occur along a wider zone (**Figure 2.2**), which cannot be resolved with our model. However, potential differences, at present and in the past, are presumably small as the debris source area is isolated and not very extensive. Therefore, we exclude transport time and other additional debris sources as a possible explanation for the observed systematic temporal variation in  $[\text{}^{10}\text{Be}]_{\text{measured}}$ .

(iv) The steady retreat of Glacier d’Otemma and concurrent deglaciation of Petit Mont Collon uncover headwall sections that presently deliver rocks to the glacier (**Figure 2.7**). Newly exposed debris source areas following the LIA could affect the  $[\text{}^{10}\text{Be}]_{\text{headwall}}$  in our samples in two ways. First, as the glacier surface lowers through time, the debris source area expands towards lower elevations (**Figure 2.4**), where production rates are lower. Therefore, computed mean source area production rates decrease towards the present (**Table 2.4**, **Figure 2.3b-d**).

**Table 2.4:** Computed headwall  $^{10}\text{Be}$  production rates and absorption mean free paths for three different time slices.

Year	Mean $^{10}\text{Be}$ production rate (atoms $\text{g}^{-1} \text{yr}^{-1}$ ) $\pm 1\sigma$	Mean absorption mean free path ( $\text{g cm}^{-2}$ )	Mean slope ( $^{\circ}$ )
<i>Upper medial moraine (UM) headwalls</i>			
2010	37.88 $\pm$ 2.58	144.59	35
1973	39.44 $\pm$ 2.30	142.56	43
1850	39.44 $\pm$ 2.30	142.56	43
<i>Lower medial moraine (LM) headwalls</i>			
2010	39.85 $\pm$ 2.81	146.14	32
1973	40.43 $\pm$ 2.65	144.80	36
1850	41.92 $\pm$ 2.62	142.46	42

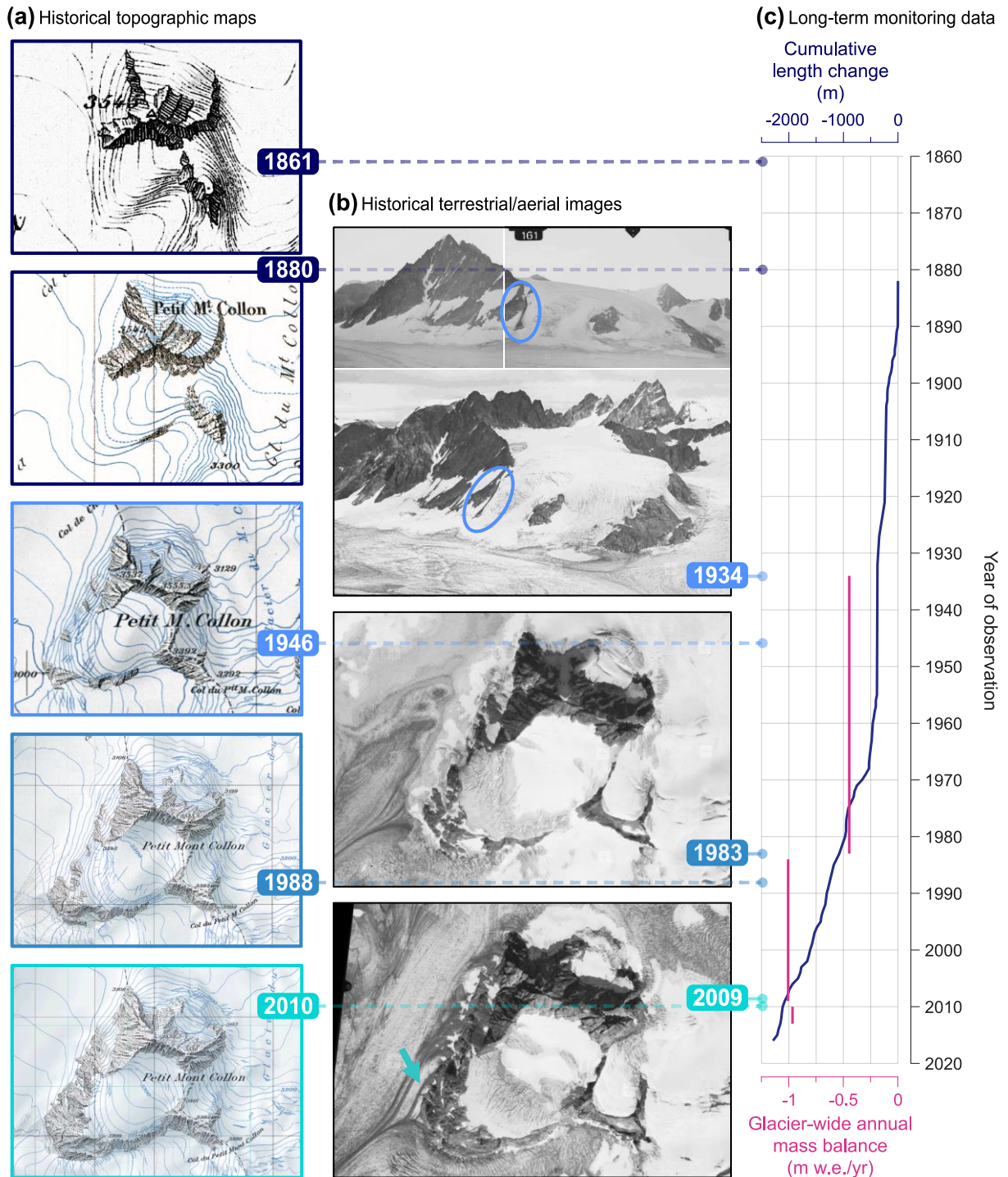


**Figure 2.7:** Chronological overview on available historical datasets from Petit Mont Collon used to assess the deglaciation history of the debris source area and to define the setup of our debris trajectory model. **(a)** Topographic maps of ice cover retreat across the headwalls. Note the disconnection of ice, formerly feeding into the glacier's main trunk and evolving into an isolated glacier in the centre of Petit Mont Collon (topographic maps by Swisstopo, 2021). **(b)** Terrestrial and aerial snapshots picturing the exposure of formerly ice-covered bedrock. The recent uncovering is patchier for headwalls to the lower medial moraine. Note the small-scale rockfall captured on the 1934 photographs (encircled) representative for erosion processes operating frequently in high-alpine glacial environments, and the ice septum separating the two moraines (arrowed) (historical images by Swisstopo, 2021). **(c)** Long-term monitoring records of glacier retreat, and decline in annual glacier-wide mass balance of Glacier d'Otemma (GLAMOS, 2019a, 2019b). m w.e. yr<sup>-1</sup>: metre water equivalent per year

However, since headwall elevation ranges are small, production rates differ by only up to 5%, too low to explain the substantial temporal [<sup>10</sup>Be] changes alone. Second, deglaciation also

exposes bedrock areas previously shielded from cosmic radiation by ice. These areas possibly inherit nuclide signatures from previous episodes of exposure during the Holocene, as the LIA was preceded by periods of major glacier recession (e.g., Holzhauser *et al.*, 2005). If subglacial erosion has removed a substantial amount of bedrock from these areas during the LIA, present-day  $[^{10}\text{Be}]_{\text{headwall}}$  may be lower compared to areas which have been ice-free over centuries. Instead, if subglacial erosion was negligible and if headwall erosion during former ice-free times proceeded slowly,  $[^{10}\text{Be}]_{\text{headwall}}$  at those surfaces may be even higher (e.g., a possible scenario for the high concentration outlier UM4/f, **Figure 2.6a**). As a consequence, continued source area expansion with possibly variable  $[^{10}\text{Be}]_{\text{headwall}}$  may progressively dilute the previous signatures from LIA times and may result in time-dependent  $[^{10}\text{Be}]_{\text{headwall}}$  variations. However, whether this would result in generally higher or lower nuclide concentrations is currently difficult to evaluate.

### 2.6.3 Medial moraines in comparison

When compared through time, UM and LM  $[^{10}\text{Be}]_{\text{headwall}}$  are surprisingly different (**Table 2.3**, **Figure 2.6a**). Overall, LM  $[^{10}\text{Be}]_{\text{headwall}}$  are higher for samples similar in age and the difference to the UM amounts to  $>10^4$  atoms  $\text{g}^{-1}$  for samples younger than  $\sim 80$  years, but no systematic temporal difference is evident. The only obvious difference between the two medial moraines is that they have different source headwalls (see Section 2.3.2; **Figure 2.2**). Yet, lithology is uniform across the source headwalls and average  $^{10}\text{Be}$  production rates vary by only up to 6% and are thus insufficient to explain the observed differences in  $[^{10}\text{Be}]_{\text{headwall}}$  (**Table 2.4**, **Figure 2.3b-d**). Also, the processing of both UM and LM samples has been comparable, and we could not observe any obvious differences in the sampled grain size distribution (**Figure A1**), or in the mineral composition. Hence, below, we inspect (i) differences in solar insolation due to different aspects and (ii) different deglaciation histories as potential causes.

(i) The aspect of rock faces has been used to explain distinct spatial patterns of rockfall and rockwall erosion, as it affects the moisture level and the thermomechanical regime of rockwalls (e.g., Coutard & Francou 1989; Sass, 2005). Gruber *et al.* (2004) associate increased erosive activity during the hot summer of 2003 with an increase of permafrost thawing depth. They explain larger thaw anomalies on north-facing rockwalls with lower inter-annual variability of thawing depth due to less direct solar radiation than south-facing rockwalls. Similarly, studies by Sass (2007, 2010) suggest enhanced Holocene rockwall erosion and present-day rockfalls at northerly oriented rockwalls. At Petit Mont Collon, the west-north-west facing UM headwalls most likely experience different insolation and temperatures than the south-south-west facing LM headwalls. Permafrost is more extensive and thicker at UM headwalls but rather patchy across LM headwalls (BAFU, 2005). In addition, mean slope angles of UM headwalls appear to be steeper, by up to  $\sim 20\%$ , during deglaciation following the LIA (**Table 2.4**). We note, however, that this difference strongly depends on the accuracy of the glacier outlines used. Nonetheless, in this context, recently faster erosion of UM compared to LM headwalls due to northerly exposure and possibly steeper slopes appears reasonable (**Figure 2.6b**).

(ii) Ice cover retreat across Petit Mont Collon has proceeded unequally after the LIA (**Figure 2.7a,b**). It appears that UM headwalls experience a comparatively steady bedrock exposure due to glacier thinning, which may be expressed in the more systematic temporal

[ $^{10}\text{Be}$ ] variation along the UM. In contrast, LM headwalls are additionally affected by the disintegration of a small glacier that separated from Glacier d'Otemma upwards onto Petit Mont Collon. This detachment proceeds unevenly and leads to a rather patchy exposure of previously ice-covered bedrock, which may thus manifest itself in the less distinct [ $^{10}\text{Be}$ ] variation along the LM.

In summary, we attribute the more recent differences in UM and LM [ $^{10}\text{Be}$ ] to a combination of spatial differences in headwall erosion rates and ice cover retreat across Petit Mont Collon. Spatially varying erosion rates across formerly glaciated bedrock surfaces have previously been observed in the Mont Blanc Massif (Lehmann *et al.*, 2020). Further, the presence or absence of ice cover is known to modulate the nuclide concentrations inherited from previous exposure (e.g., Cockburn & Summerfield, 2004). However, due to the centennial coverage of our dataset, whether [ $^{10}\text{Be}$ ]<sub>headwall</sub> prior to the LIA were higher or lower than today, and whether they were preserved throughout ice coverage or reduced or even reset by subglacial erosion (see Section 2.6.2) remain open questions.

#### 2.6.4 Methodological conclusions and future opportunities

Our findings from Glacier d'Otemma show decreasing [ $^{10}\text{Be}$ ] and increasing erosion rates towards the present, in accordance with observations by Scherler and Egholm (2020) from a Himalayan glacier. Systematic instead of random downglacier [ $^{10}\text{Be}$ ] variations in both studies support the notion that medial moraines can be exploited as archives of headwall erosion above glaciers. This is reinforced by the fact that the observed downglacier [ $^{10}\text{Be}$ ] trend is reflected in two different size fractions. Therefore, cosmogenic nuclide-based medial moraine records appear to reflect observations of decadal changes in headwall erosion (e.g., Hartmeyer *et al.*, 2020a, 2020b) on centennial time scales, but encounter limitations on shorter time scales due to the nuclide integration time (see Section 2.6.2). To further elaborate on climate change-related responses of headwalls and adjacent debris-covered glaciers, future analyses may involve various glacial catchments and debris source areas that differ in size, orientation or morphology to check for potential spatial patterns. Besides, consulting additional temporal records on rockwall temperatures or water availability may be of interest, too, since studies indicate that increased melt- and rainwater runoff may enhance the frost weathering efficacy in the contact zone of headwall and glacier (Hartmeyer *et al.*, 2020a, 2020b) and that warmer temperatures after the LIA may have enhanced the frost-cracking efficiency (Mair *et al.*, 2020), both preconditioning rock-fracturing.

Applying our particle trajectory model indicates that the model-based  $^{10}\text{Be}$  corrections due to downglacier transport are in most cases not very substantial (**Figure 2.6a**). Yet, resolving slow supraglacial transport close to the headwalls with a simple 1D model proved to be challenging (see Section A2.1). Whereas older englacially transported samples largely remain unaffected by this, younger almost exclusively supraglacially transported samples may be affected more severely by the assumptions and uncertainties underlying the model (see Section 2.5.2 and Section A2.5). Using a well calibrated 3D glacier model may help to overcome these limitations in future studies, to refine  $^{10}\text{Be}$  corrections and sample age estimates, and to backtrack particles more precisely to specific delivery zones within a source area (e.g., certain elevation windows).

We further suggest that the manual amalgamation of sand-sized supraglacial debris offers the opportunity to obtain representative estimates of headwall erosion rates, as the analysis of [ $^{10}\text{Be}$ ] from various fine-grained sub-samples of UM2 and LM1 revealed no obvious dependency of size fractions <16 mm. However, on a larger scale, systematic grain size differences exist when comparing sand-sized (0.125-4 mm) and pebble-sized (4-22.4 mm) debris fractions of several samples, with the latter having consistently lower [ $^{10}\text{Be}$ ] (see Section 2.6.1). These trends need further investigation by future studies.

Finally, the choice of a glacier with a small catchment, as it is the case for Glacier d'Otemma, holds several advantages. The debris of both medial moraines can be traced to the well-definable headwalls of Petit Mont Collon. The small size and homogeneity of the debris source area reduce complexity. Differences in [ $^{10}\text{Be}$ ] production rates are small, due to the small elevation range, and lithology can be excluded as a primary factor for temporal and spatial variability in headwall erosion. Yet, disentangling cosmogenic signals of headwall erosion from those rooted in the nuclide history of deglaciating bedrock itself, both governing [ $^{10}\text{Be}$ ]<sub>headwall</sub>, remains challenging (see Section 2.6.2 and Section 2.6.3). Field sites with debris source areas that are characterized by a simple bedrock exposure history may help to clarify these issues in the future.

## 2.7 Conclusions

We derived a ~200-year record of headwall erosion rates at Glacier d'Otemma, Switzerland, from combining cosmogenic  $^{10}\text{Be}$  concentration ([ $^{10}\text{Be}$ ]) measurements on medial moraine debris with particle trajectory and age modelling. Our results indicate that downglacier [ $^{10}\text{Be}$ ] vary systematically with time. During the LIA (debris samples older than ~150 years), we find relatively high [ $^{10}\text{Be}$ ] yielding low apparent headwall erosion rates of 0.9 to 2.0 mm yr<sup>-1</sup>. After the LIA (debris samples younger than ~150 years), lower [ $^{10}\text{Be}$ ] result in higher apparent headwall erosion rates of up to 10.8 mm yr<sup>-1</sup>. This decrease in [ $^{10}\text{Be}$ ] from past to present is reflected both in sand-sized and pebble-sized grain size fractions, which suggests that the temporal trends are not affected by large stochastic events that could bias cosmogenic nuclide concentrations.

Computing debris particle trajectories through the glacier from source area to sample location with our model shows that the observed temporal variation in [ $^{10}\text{Be}$ ] still remains after correcting for additional nuclide accumulation during glacial transport. Recently decreasing [ $^{10}\text{Be}$ ] seem to reflect a combination of processes that can be associated with the ongoing ice cover retreat across the source headwalls since the end of the LIA. On the one hand, high-alpine headwalls face increased destabilization and retreat as glaciers degrade and permafrost thaws. On the other hand, they experience profound changes in shielding and exposure to cosmic rays as ice cover disintegrates and debris source areas expand. Temporal differences in [ $^{10}\text{Be}$ ] along two parallel medial moraines suggest that both headwall orientation and their deglaciation history are important factors to consider when interpreting medial moraine cosmogenic nuclide concentrations.

## 2.8 Data availability

The cosmogenic nuclide and model data of this study and a detailed description of the sample processing and debris trajectory modelling are available in the accompanying data publication: Wetterauer *et al.* (2022b) at <https://doi.org/10.5880/GFZ.3.3.2021.007>. These data are freely available under the Creative Commons Attribution 4.0 International (CC BY 4.0) open-access license at GFZ Data Services. When using these data please cite this study.

## 2.9 Acknowledgements

This research was funded from the European Research Council (ERC) under the European Union's Horizon 2020 research and innovation program (grant no. 759639). We are grateful to the “COLD”-project members Donovan Dennis and Deniz Gök for scientific discussions and support during sampling. Stefan Heinze and Steven Binnie from the University of Cologne are thanked for performing AMS measurements. Swisstopo and GLAMOS are acknowledged for giving access to historical datasets. Cathrin Schulz, Nadja Kuhl, and Kristina Krüger are thanked for their help and advice in sample preparation. We also thank two anonymous reviewers and the editors for their constructive and thoughtful feedback that improved this manuscript.



# **Spatial and temporal variations in rockwall erosion rates derived from cosmogenic $^{10}\text{Be}$ in medial moraines at five valley glaciers around Pigne d’Arolla, Switzerland**

*Katharina Wetterauer & Dirk Scherler*

## **Abstract**

Rockwall erosion in high-alpine glacial environments varies both temporally and spatially. Where rockwalls flank glaciers, changes in debris supply and supraglacial cover will modify ice ablation. Yet, quantifying spatiotemporal patterns in erosion across deglaciating rockwalls is not trivial. At five nearby valley glaciers around Pigne d’Arolla in Switzerland, we derived apparent rockwall erosion rates using  $^{10}\text{Be}$  cosmogenic nuclide concentrations ( $^{10}\text{Be}$ ) in medial moraine debris. Systematic downglacier-sampling of six medial moraines that receive debris from rockwalls with differing orientation, slope, and deglaciation histories enabled us to assess rockwall erosion through time and to investigate how distinct spatial source rockwall morphology may express itself in medial moraine  $^{10}\text{Be}$  records. Our dataset combines 24 new samples from medial moraines of Glacier du Brenay, Glacier de Cheilon, Glacier de Pièce, and Glacier de Tsijiore Nouve with 15 published samples from Glacier d’Otemma. For each sample, we simulated the glacial debris transport using a simple debris particle trajectory model to approximate the time of debris erosion and to correct the measured  $^{10}\text{Be}$  for post-depositional  $^{10}\text{Be}$  accumulation. Our derived apparent rockwall erosion rates range between  $\sim 0.6$  and  $10.0 \text{ mm yr}^{-1}$ . Whereas the longest downglacier  $^{10}\text{Be}$  record presumably reaches back to the end of the Little Ice Age and suggests a systematic increase in rockwall erosion rates over the last  $\sim 200$  years, the shorter records only cover the last  $\sim 100$  years from the recent deglaciation period and indicate temporally more stable erosion rates. For the estimated time of debris erosion, ice cover changes across most source rockwalls were small, suggesting that our records are largely unaffected by the contribution of recently deglaciated bedrock of possibly different  $^{10}\text{Be}$ , but admixture of subglacially derived debris cannot be excluded at every site. Comparing our sites suggests that apparent rockwall erosion rates are higher where rockwalls are steep and north-facing, indicating a potential slope and temperature control on rockwall erosion around Pigne d’Arolla.

**This chapter is published in:**

*Earth Surface Dynamics*, Volume 11, Pages 1013-1033, 2023

<https://doi.org/10.5194/esurf-11-1013-2023>

### 3.1 Introduction

Alpine glacial environments are characterized by steep rockwalls near the head of valley glaciers that expose bare rock surfaces to erosion. Erosion in these environments largely proceeds via frequent small-scale rockfalls and infrequent large-scale mass-wasting processes (e.g., Boulton & Deynoux, 1981; Anderson, 2000; Arsenault & Meigs, 2005). On glacier surfaces, rockwall debris is passively entrained, becoming part of the glacial system, for example in the form of medial moraines (e.g., Eyles & Rogerson, 1978a; Gomez & Small, 1985; Anderson, 2000). Where debris is transported on the surface, it alters sub-debris melt rates (Østrem, 1959) and potentially modifies glacier retreat (e.g., Scherler *et al.*, 2011b; Rowan *et al.*, 2015; Vincent *et al.*, 2016). The debris cover thickness and its change are influenced by the rate at which the surrounding rockwalls erode (Scherler & Egholm, 2020). However, rockwall erosion and thus debris supply rates are not spatially uniform, as evidenced by topographic asymmetry across glacial landscapes (e.g., Gilbert, 1904; Tuck, 1935; Naylor & Gabet, 2007). Although such asymmetry is commonly associated with spatial and temporal gradients in erosion, the underlying conditions are still controversial.

In the European Alps, recent temporal and spatial variability in rockwall erosion has been commonly linked to post-Little Ice Age (LIA; approximately post-1850) warming and/or to locally distinct temperature-related conditions. As temperatures increase and permafrost thaws, the stability of alpine rockwalls decreases, promoting rockfalls and slope failures (e.g., Gruber & Haeberli, 2007; Huggel *et al.*, 2010; Raveland *et al.*, 2010; Fischer *et al.*, 2012). Enhanced destabilization is also observed in recently deglaciating bedrock, where glacial thinning and unloading are thought to affect the thermomechanical stress field and frost damage intensity within the adjacent bedrock (e.g., Wegmann *et al.*, 1998; Kenner *et al.*, 2011; Hartmeyer *et al.*, 2020a). Spatial variability in erosion has previously been related to rock face aspect, and higher rockfall activity at north-facing rockwalls has been associated with differences in moisture supply and damage by frost (e.g., Coutard & Francou, 1989; Gruber *et al.*, 2004; Sass, 2005, 2010). Yet, rockfalls are pronounced stochastic processes (e.g., Ward & Anderson, 2011; Sanders *et al.*, 2013), and their observation is typically based on repeated monitoring over comparatively short time periods ( $10^0$ - $10^1$  years). Therefore, the number of quantified rockwall erosion rates and their spatiotemporal analyses are still limited.

An alternative approach for quantifying rockwall erosion rates over longer time periods ( $>10^2$ - $10^4$  years) uses downglacier records of *in situ*-produced cosmogenic  $^{10}\text{Be}$  concentrations ( $[^{10}\text{Be}]$ , atoms  $\text{g}^{-1}$ ) in medial moraines. By interval sampling along medial moraines, rockwall erosion is quantified through time based on the  $[^{10}\text{Be}]$  within the debris that reflects the rockwall erosion products. The approach exploits the conveyor-belt nature of glaciers: passively transported rockwall debris forms medial moraines as it melts out below the equilibrium line altitude (ELA) in the glacier ablation zone or as it is merged from individual glacier branches (e.g., Eyles & Rogerson, 1978a; Gomez & Small, 1985; Anderson, 2000). Thus, medial moraine deposits tend to be older downglacier (for detailed treatments on rockwall  $[^{10}\text{Be}]$  in medial moraine debris see Ward & Anderson, 2011; Scherler & Egholm, 2020; Wetterauer *et al.*, 2022a). Previous work from the Himalaya (Scherler & Egholm, 2020) and the Swiss Alps (Wetterauer *et al.*, 2022a) suggests that medial moraines can indeed act as archives for the

temporal evolution of rockwall erosion. At both sites, downglacier records indicate an acceleration in erosion rates with climate warming, consistent with the aforementioned monitoring observations. However, using [ $^{10}\text{Be}$ ] from supraglacial debris has also proven challenging: medial moraine [ $^{10}\text{Be}$ ] likely reflects a mixed signal of rockwall erosion, rockwall deglaciation, and englacial/supraglacial transport time, and our understanding of how these processes affect erosion rate estimates is still limited.

This study examines patterns of rockwall erosion in a broader context using medial moraine [ $^{10}\text{Be}$ ] records from five valley glaciers surrounding the Pigne d'Arolla, a Swiss mountain peak in the Canton of Valais. We aim to (i) further evaluate the systematics of medial moraine [ $^{10}\text{Be}$ ]-derived estimates of rockwall erosion rates, (ii) check for temporal trends along downglacier medial moraine records, and (iii) test for differences among rockwall erosion rates in relation to spatially distinct geomorphic rockwalls. This study expands the work by Wetterauer *et al.* (2022a) on the Glacier d'Otemma, closely resembling their approach to remain as comparable as possible. As an extension to their previous strategy of assessing the temporal evolution of rockwall erosion rates from downglacier medial moraine [ $^{10}\text{Be}$ ] records, we now additionally integrate the comparison of records from several different glaciers with varied source rockwalls in the same area to capture possible spatial patterns in rockwall erosion. In addition to the records from Glacier d'Otemma, our new rockwall erosion dataset comprises downglacier [ $^{10}\text{Be}$ ] records from four new study sites close by: Glacier du Brenay, Glacier de Cheilon, Glacier de Pièce, and Glacier de Tsijiore Nouve. All glaciers flow down either from the northern or southern flanks of the Pigne d'Arolla and receive debris from rockwalls that differ in their exposure and morphology. We corrected our [ $^{10}\text{Be}$ ] records for englacial/supraglacial transport and derived estimates of apparent rockwall erosion rates using a simple debris particle trajectory model (Wetterauer *et al.*, 2022a, 2022b), for which we generated ~40-year records of glacier surface velocities by manually tracing medial moraine boulders across orthoimages. Finally, we compared the different source rockwalls with respect to their area, elevation, slope, aspect, and deglaciation history based on former glacier outlines and historical photographs.

## 3.2 Study area

### 3.2.1 Pigne d'Arolla massif

The Pigne d'Arolla (3790 m; all elevations stated as metres above sea level) is a mountain in the southern Swiss Alps, near the border with Italy (**Figure 3.1a,b**). The massif surrounding it is part of the Dent Blanch nappe (Austroalpine unit) and consists of crystalline rocks of the Arolla series, mainly orthogneiss and metadiorites (Swisstopo, 2022). The majority of its ice-free slopes are around 3000 m in elevation, with more south- than north-facing slopes in terms of area (**Figure 3.2a,b**). At this elevation and higher, slopes are typically inclined by 30 to 50°, with north faces tending to be steeper than south faces (**Figure 3.2a,c**).

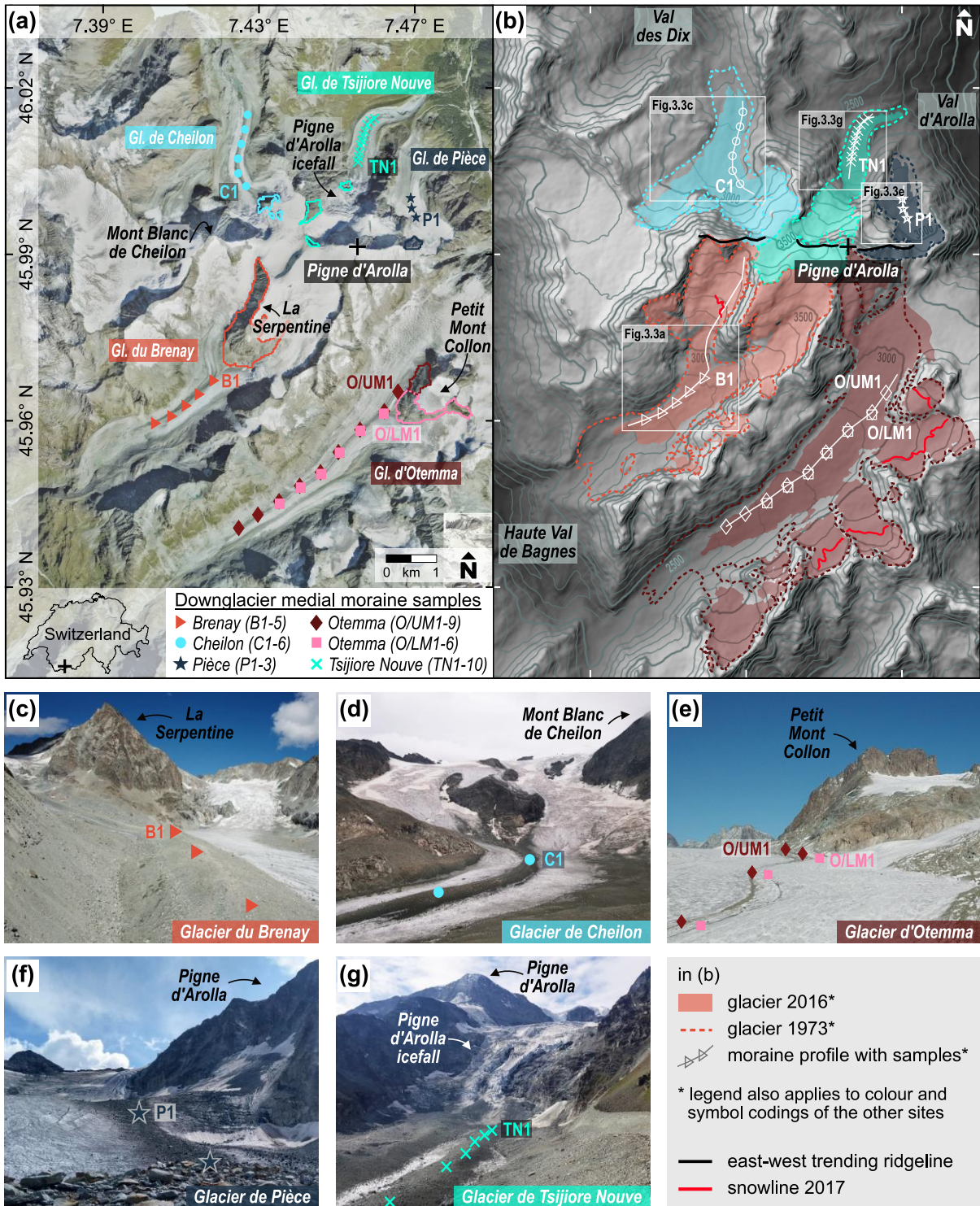


**Figure 3.1:** Pigne d'Arolla massif, Switzerland. (a) Orthoimage showing the five glacier catchments and their downglacier medial moraine sample locations. The respective associated source rockwalls are outlined (orthoimage from 2017 by Swisstopo, 2022). (b) Hillshade image of the same area as in (a) with glacier extents in 2016 and 1973 after Linsbauer *et al.* (2021) and Müller *et al.* (1976), respectively. The snowline of the 2017 orthoimage is indicated as an approximation of the recent equilibrium line altitude. Hillshade and 100 m contour lines are based on the DEM SRTM GL1 (NASA Shuttle Radar Topography Mission SRTM, 2013). White rectangles indicate map extents shown in Figure 3.3. Note the east-west trending ridgeline between Pigne d'Arolla and Mont Blanc de Cheilon closely following the ~3500 m contour line. (c-g) Field photographs showing medial moraines, approximated sample locations, and associated source rockwalls of (c) Glacier du Brenay, (d) Glacier de Cheilon, (e) Glacier d'Otemma (samples from Wetterauer *et al.*, 2022a), (f) Glacier de Pièce, and (g) Glacier de Tsijiore Nouvelle.

At present, the area around Pigne d’Arolla is still glaciated (**Figure 3.1**). Several valley glaciers emerge from the faces of an east-west trending ridgeline, which connects Pigne d’Arolla to the adjacent Mont Blanc de Cheilon, and flow downvalley in a northerly or southerly direction. These include the five study sites: Glacier du Brenay, Glacier de Cheilon, Glacier d’Otemma, Glacier de Pièce, and Glacier de Tsijiore Nouve. From now on, we refer to this set of five glacier catchments as the “Pigne d’Arolla massif” and to the individual glaciers as “Brenay”, “Cheilon”, “Otemma”, “Pièce”, and “Tsijiore Nouve” for brevity.

Throughout the Pigne d’Arolla massif, rockwalls of varying extent and morphology deposit debris on the glacier surfaces, forming distinct medial moraines as the debris is transported downglacier (**Figure 3.1c-g**). At present, these rockwalls are still located within the distribution zone of modelled mountain permafrost in the Swiss Alps (BAFU, 2005). The recent ELA is located above 3000 m (e.g., >3100 m at Otemma between autumn 2019 and 2021; GLAMOS, 2021b). Therefore, where recent debris deposition occurs below 3000 m elevation, in the ablation zone, downglacier debris transport is exclusively supraglacial. However, aerial images from 1983 indicate a lower ELA, debris deposition in the accumulation zone above, and therefore englacial transport in the past (Swisstopo, 2022).

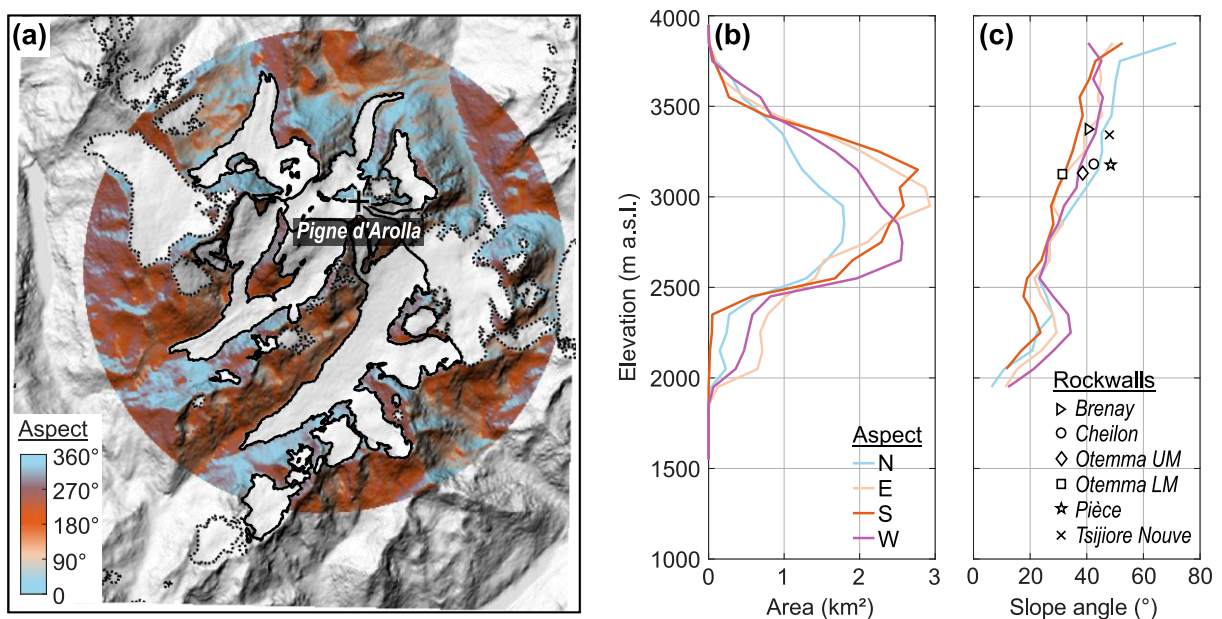


**Figure 3.2:** Morphology of ice-free rock faces and slopes in an area with 6 km radius, centred on the studied glaciers of the Pigne d’Arolla massif. (a) Topographic map indicating the aspect of ice-free areas. Areas covered by glacial ice (dashed black outlines) are excluded from the analysis and the five studied glacier sites (bold black outline) explicitly highlighted (2016 glacier outlines by Linsbauer *et al.*, 2021). (b) Hypsometry and (c) slope angles of ice-free areas in 100 m elevation bins, differentiated by aspect. Symbols denote the mean elevation and mean slope angle of the studied source rockwalls.

In the following, we will introduce each study site separately. Please note the following: (i) glacier areas were assigned according to the latest Swiss Glacier Inventory SGI2016 dataset (Linsbauer *et al.*, 2021); (ii) for simplicity we describe only the medial moraines and associated source rockwalls relevant to this study; and (iii) descriptions below are for the present time, based on the latest datasets available via Swisstopo’s online map viewer (Swisstopo, 2022) unless otherwise noted.

### 3.2.2 Glacier du Brenay

Brenay (**Figure 3.1c**) is the second-largest glacier of the Pigne d’Arolla massif (7.1 km<sup>2</sup> in 2016; Linsbauer *et al.*, 2021), originating from two basins. Its eastern and main tributary emerges from the southern/southwestern flanks of Pigne d’Arolla, while its subparallel western tributary originates at the southern flanks of Mont Blanc de Cheilon. Both join at 2900 m elevation, continuing southwest into the Haut Val de Bagnes. In 2020, the glacier was ~5 km long, ranging from 2640 to >3600 m elevation. On a relatively snow-free 2017 orthoimage, the snowline is located between 3200 and 3300 m elevation within the western tributary (**Figure 3.1a,b**). Between 1881 and 2020, the glacier continuously retreated, by 1.6 km (GLAMOS, 2021a), and between 1850 and 2010, it lost 30% of its surface area and 60% of its ice volume (Lambiel & Talon, 2019). Between 1934 and 2017, the geodetic glacier-wide mass balance decreased from -0.2 to -0.6 m water equivalent (w.e.) yr<sup>-1</sup> (GLAMOS, 2021c). The medial moraine of Brenay originates below 3100 m elevation within the western tributary as a lateral moraine and continues for another ~2 km as a medial moraine from the confluence to the glacier terminus. It is sourced from the rockwalls of La Serpentine (3700 m), a ~2 km long mountain ridge that separates the two tributaries. These rockwalls tower up to 700 m above the glacier surface and are mainly composed of quartzdiorite. Whereas rockwalls to the southeast and main tributary are still largely covered by ice, the southern to northwestern rockwalls are generally ice-free. At present, debris deposition occurs in both the accumulation and ablation zone.

### 3.2.3 Glacier de Cheilon

Cheilon (**Figure 3.1d**) is the third-largest glacier of the Pigne d’Arolla massif (3.5 km<sup>2</sup> in 2016; Linsbauer *et al.*, 2021). An eastern and a western tributary both originate at the northern flanks of Mont Blanc de Cheilon and join at 2900 m elevation, flowing northwards into the Val des Dix. In 2020, the glacier was ~3 km long, ranging from 2700 to 3500 m elevation. Between 1924 and 2020, it was shrinking in a stepwise manner, with its terminus retreating 1.2 km (GLAMOS, 2021a). The medial moraine of Cheilon originates within the eastern tributary and extends for ~2 km towards the glacier terminus. It is nourished from three bedrock knobs that emerge between flanking sectors of an icefall in the centre of the eastern tributary at 3000 m elevation. These rockwalls face north, reach heights of up to 300 m, show remnants of ice cover on their flatter tops, and comprise mainly quartzdiorite. At present, they deposit debris in the glacier ablation zone.

### 3.2.4 Glacier d’Otemma

The study site at Otemma (**Figure 3.1e**) has been described in detail in Wetterauer *et al.* (2022a) and we provide only a brief summary here. Otemma is the largest of the five glaciers (12.6 km<sup>2</sup> in 2016; Linsbauer *et al.*, 2021) and originates at the southern/southeastern flanks of the Pigne d’Arolla, flowing towards the southwest into the Haut Val de Bagnes. In 2020, its main trunk was ~6 km long, extending from 2500 to 3000 m elevation. The ELA was located at 3165 m elevation (GLAMOS, 2021b), indicating that the glacier lost most of its former accumulation basin (**Figure 3.1b**). Between 1881 and 2020, the glacier continuously retreated by 2.5 km (GLAMOS, 2021a), and between 1850 and 2010, it lost 40% of its surface area and 60% of its ice volume (Lambiel & Talon, 2019). Between 1934 and 2017, the geodetic glacier-wide mass

balance decreased from  $-0.4$  to  $-1.3$  m w.e.  $\text{yr}^{-1}$  (GLAMOS, 2021c). Two parallel medial moraines exist below 3000 m elevation. We refer to them as the upper (UM) and lower (LM) medial moraine of Otemma, and they can be traced downglacier for  $>4$  and  $\sim 3$  km, respectively. Both are nourished from adjacent but different rock faces of the isolated nunatak Petit Mont Collon at the glacier head. At present, its northwest-facing rockwalls deliver debris to the UM moraine and are largely ice-free. Its southwest-facing rockwalls supply the LM moraine and are topped by remnants of a small, currently isolated glacier. Overall, these UM and LM rockwalls are up to 500 m high, mainly composed of orthogneiss and schist, and they deposit debris in the ablation zone.

### 3.2.5 Glacier de Pièce

Pièce (**Figure 3.1f**) is the smallest glacier within the massif ( $1.3$  km<sup>2</sup> in 2016; Linsbauer *et al.*, 2021). It originates on the east to northeastern flanks of the Pigne d’Arolla, and its main trunk flows northwards into the Val d’Arolla. In 2020, the main trunk was  $\sim 1.5$  km long, ranging from 2700 to  $>3100$  m elevation. We found no monitoring datasets of the glacier, but historical topographic maps (Swisstopo, 2022) indicate its retreat since the end of the 19th century. The medial moraine of Pièce is comparatively short and can be traced for  $\sim 1$  km downglacier, starting on the easternmost flanks of the Pigne d’Arolla. These rockwalls face northeast, are up to 300 m high, and are mainly composed of orthogneiss and granodiorites. They are largely ice-free, but at their easternmost margin, ice from the southern faces of Pigne d’Arolla reroutes northward into the main trunk. Debris is deposited at 3000 m elevation and currently transported supraglacially.

### 3.2.6 Glacier de Tsijiore Nouve

Tsijiore Nouve (**Figure 3.1g**) is the second-smallest of the five glaciers ( $2.8$  km<sup>2</sup> in 2016; Linsbauer *et al.*, 2021). It originates on the northern flanks of the Pigne d’Arolla and takes a northeastward turn into the Val d’Arolla. In 2020, the glacier was  $\sim 5$  km long, covering a large elevation range from 2300 to  $>3700$  m. The glacier itself can be split into different sections (e.g., Small & Clark, 1974; Small *et al.*, 1979; Small & Gomez, 1981): (i) an upper accumulation basin that spans the upper  $\sim 500$  m elevation and largely comprises partly crevassed clean ice, (ii) the steep and heavily crevassed Pigne d’Arolla icefall that drops across the middle  $\sim 600$  m elevation and hosts the recent ELA, and (iii) a lower and at present heavily debris-covered part in the ablation zone that spans the lower  $\sim 300$  m elevation and is flanked by large lateral moraines. The glacier’s recession history has been discontinuous. Between 1880 and 2020, its terminus retreated by 0.4 km in total; however, this was disrupted by two major periods of re-advance from 1914 to 1921 and 1971 to 1990 (GLAMOS, 2021a). The sampled medial moraine of Tsijiore Nouve is one of two prominent moraines that both extend along the entire lower part, occupying almost the full recent glacier width. They are separated from each other by an ice septum of a few tens of metres of width and are distinguishable by their ridge-like shape. In this study, we focused on the western medial moraine. Unlike the other glaciers, there is no direct apparent continuity to its source rockwalls (Small & Clark, 1974) due to the intervening Pigne d’Arolla icefall and the elongated nature of the accumulation basin. Apparent debris source areas (**Figure 3.1a**) are (i) a 200 m high bedrock face of Pigne d’Arolla that crops out to the north between flanking sectors of a small icefall, (ii) up to 300 m high rockwalls of

an adjacent mountain ridge that flanks the western rim of the accumulation basin and faces east, and (ii) a 200 m sized bedrock patch recently uncovered at the base of the Pigne d’Arolla icefall (Small & Clark, 1974; Small & Gomez, 1981). All three areas comprise mainly quartzdiorites. Where deposited above the Pigne d’Arolla icefall, debris takes englacial pathways.

### 3.3 Material and methods

We provide a supplement as well as an accompanying data publication (Wetterauer & Scherler, 2023b) with this study, the latter comprising the cosmogenic nuclide dataset and derived glacier surface velocities. As for this thesis, both supplement and data publication are included in Appendix B (please note that only the text sections and tables from Wetterauer & Scherler (2023b) are listed in Appendix B, which contain additional information and data not presented in this Chapter 3 in order to avoid repetition).

#### 3.3.1 $^{10}\text{Be}$ -derived rockwall erosion rates from medial moraine debris

Where rockwalls erode in cosmogenic steady state, their “apparent” rockwall erosion rate  $E$  ( $\text{mm yr}^{-1}$ ) is described by Equation 3.1 (Lal, 1991):

$$E = \left( \frac{P_{sp}(0)}{[^{10}\text{Be}]_{\text{rockwall}}} - \lambda \right) \frac{\Lambda}{\rho} \quad (3.1)$$

where  $[^{10}\text{Be}]_{\text{rockwall}}$  is the  $^{10}\text{Be}$  concentration ( $\text{atoms g}^{-1}$ ) at the rockwall surface accumulated during exposure to cosmic rays,  $P_{sp}(0)$  is the spallogenic surface production rate ( $\text{atoms g}^{-1} \text{yr}^{-1}$ ),  $\lambda$  is the decay constant ( $\text{yr}^{-1}$ ) (here based on a half-life of  $1.387 \pm 0.012$  Myr; Chmeleff *et al.*, 2010; Korschinek *et al.*, 2010),  $\Lambda$  is the absorption mean free path ( $\text{g cm}^{-2}$ ), and  $\rho$  is the material density (here  $2.65 \text{ g cm}^{-3}$ ). In our study, we consider rockwall erosion to proceed surface-perpendicular, resulting in lateral rockwall retreat. Moreover, we refer to our rockwall erosion rates as “apparent” because the steady-state assumption precludes nuclide inheritance and erosion rate changes over time, and it implies that the period of rockwall erosion is longer than the nuclide integration time, which, however, may not apply to recently deglaciating rockwalls (Wetterauer *et al.*, 2022a).

In Equation 3.1,  $[^{10}\text{Be}]_{\text{rockwall}}$  is not equal to the actual measured  $^{10}\text{Be}$  concentration ( $[^{10}\text{Be}]_{\text{measured}}$ ) in the medial moraine. During supraglacial transport from rockwall to sample location, debris continues to accumulate  $^{10}\text{Be}$  ( $[^{10}\text{Be}]_{\text{transport}}$ ) (Ward & Anderson, 2011; Scherler & Egholm, 2020; Wetterauer *et al.*, 2022a). Therefore, to obtain  $[^{10}\text{Be}]_{\text{rockwall}}$ , we need to know  $[^{10}\text{Be}]_{\text{transport}}$  and subtract it from  $[^{10}\text{Be}]_{\text{measured}}$ . As supraglacial exposure times and rockwall erosion rates vary for individual glaciers,  $[^{10}\text{Be}]_{\text{transport}}$  and its importance relative to  $[^{10}\text{Be}]_{\text{rockwall}}$  likely vary, too. Therefore, estimating and comparing apparent rockwall erosion rates in the Pigne d’Arolla massif require two independent data acquisitions: (i) quantifying  $[^{10}\text{Be}]_{\text{measured}}$  from debris samples as well as computing rockwall  $^{10}\text{Be}$  production rates (see Section 3.3.1.1) and (ii) estimating glacier flow and debris transport time to correct for  $[^{10}\text{Be}]_{\text{transport}}$  and to approximate the time of rockwall erosion (see Section 3.3.1.2).

### 3.3.1.1 Debris sampling, $^{10}\text{Be}$ measurements, and $^{10}\text{Be}$ production in rockwalls

In autumn 2019, we collected 24 new debris samples along medial moraine profiles in the Pigne d'Arolla massif (**Table 3.1**, **Figure 3.1a**). The new data expand our previously published 15 samples from the Glacier d'Otemma (Wetterauer *et al.*, 2022a, 2022b) by four new glaciers. As rockwalls erode by stochastic processes and individual bedrock samples may have different  $^{10}\text{Be}$ , rockwall erosion rate records should reflect outcrop-scale average rates and thus amalgamate  $^{10}\text{Be}$  across the entire source rockwall area to avoid episodic effects on single measurements (Small *et al.*, 1997). Therefore, each sample is a 3-4 kg amalgamation of supraglacial clasts from coarse sand to pebble size (~1-30 mm), randomly hand-scraped across medial moraine surface areas that cover 5-30 m along a moraine by the entire moraine width. In addition, to minimize subjective selection of sample locations, samples from the same medial moraine were taken at regular downglacier intervals. At each site, sample numbers are in ascending order downglacier. None of the moraines was heavily intersected by open crevasses, and debris contribution from valley sidewalls or lateral moraines was not observed. At Brenay, five samples (B1-5) were collected every ~350 m along a 1.5 km long profile. The moraine topography is pronounced, doubling from ~15 to 30 m in height and increasing from ~70 to 110 m in width downglacier. At Cheilon, six samples (C1-6) were collected every ~300 m along a 1.5 km long profile. Downglacier, the moraine topography gains relief, with heights increasing from <1 to ~20 m and widths increasing from ~50 to 130 m. At Pièce, three samples (P1-3) were collected every ~200 m from a 0.4 km long profile, along which the moraine topography is <1 m and the width remains at ~50 m. At Tsijiore Nouve, 10 samples (TN1-10) were collected every ~100 m from a 1.0 km long profile. Downglacier, the moraine topography varies, with heights between ~10 and 20 m and widths between ~70 and 90 m. At the last three sampling locations, the moraine flanks had distinct ice cliffs. The 15 Otemma samples by Wetterauer *et al.* (2022a) were collected every ~500 m from two medial moraine profiles: nine samples from the UM moraine (O/UM1-9) along 4.2 km and six samples from the LM moraine (O/LM1-6) along 2.7 km. Along both medial moraines, the initial height of ~3 m flattens out in the central part of the glacier and stays low, and the width decreases from ~20 to 6 m.

*In situ*-produced  $^{10}\text{Be}$  separation was performed on grain size fractions of 1-16 mm (B, C, P, and TN samples) and 0.125-4 mm (O/UM and O/LM samples), as described in Section **B3** and Section **A1**, respectively, largely following the procedures of von Blanckenburg *et al.* (2004). All samples were prepared at the Helmholtz Laboratory for the Geochemistry of the Earth Surface (HELGES) at the GFZ German Research Centre for Geosciences in Potsdam, Germany.  $^{10}\text{Be}/^9\text{Be}$  ratios (**Table 3.1**) were measured at the accelerator mass spectrometer (AMS) at the University of Cologne, Germany (Dewald *et al.*, 2013), relative to standards KN01-6-2 and KN01-5-3 (nominal  $^{10}\text{Be}/^9\text{Be}$  ratios:  $5.35 \times 10^{-13}$  and  $6.32 \times 10^{-12}$ , respectively). All ratios were converted into  $^{10}\text{Be}]_{\text{measured}}$  and corrected for co-processed blanks ( $^{10}\text{Be}/^9\text{Be}$  ratios:  $2.16 \times 10^{-15}$ ,  $2.55 \times 10^{-16}$ ,  $1.19 \times 10^{-15}$ ,  $1.56 \times 10^{-15}$ ).

**Table 3.1:** Medial moraine debris samples from the Pigne d’Arolla massif, as well as AMS data with measured  $^{10}\text{Be}/^9\text{Be}$  ratios and  $^{10}\text{Be}$  concentrations ( $[^{10}\text{Be}]_{\text{measured}}$ ).

Sample	Latitude (°N)	Longitude (°E)	Elevation (m a.s.l.)	Distance <sup>b</sup> (m)	Qtz mass (g)	AMS $^{10}\text{Be}/^9\text{Be}$ $\times 10^{-14} \pm 1\sigma$	Blank <sup>c</sup>	$[^{10}\text{Be}]_{\text{measured}}$ $\times 10^3 \pm 1\sigma$ (atoms $\text{g}^{-1}$ )
<i>Glacier du Brenay</i>								
B1	45.9672	7.4181	2880	0	40.95	9.02 $\pm$ 0.45	blk3	23.58 $\pm$ 1.21
B2	45.9648	7.4144	2843	399	34.51	10.63 $\pm$ 0.48	blk3	32.97 $\pm$ 1.56
B3	45.9627	7.4110	2819	746	33.36	10.30 $\pm$ 0.48	blk3	33.05 $\pm$ 1.60
B4	45.9608	7.4074	2755	1099	37.82	10.72 $\pm$ 0.50	blk3	30.39 $\pm$ 1.47
B5	45.9596	7.4032	2698	1454	42.53	13.14 $\pm$ 0.57	blk3	33.33 $\pm$ 1.50
<i>Glacier de Cheilon</i>								
C1	46.0023	7.4267	2882	0	35.55	1.58 $\pm$ 0.13	blk3	4.56 $\pm$ 0.43
C2	46.0046	7.4247	2852	301	38.93	1.29 $\pm$ 0.12	blk3	3.30 $\pm$ 0.36
C3	46.0073	7.4246	2839	598	35.29	1.96 $\pm$ 0.17	blk3	5.69 $\pm$ 0.52
C4	46.0099	7.4255	2799	899	37.47	1.63 $\pm$ 0.16	blk3	4.36 $\pm$ 0.47
C5	46.0125	7.4264	2771	1199	33.15	0.96 $\pm$ 0.13	blk3	2.75 $\pm$ 0.43
C6	46.0152	7.4271	2739	1499	33.64	1.49 $\pm$ 0.14	blk3	4.38 $\pm$ 0.48
<i>Glacier d’Otemma/ upper medial moraine (UM)<sup>a</sup></i>								
O/UM1	45.9653	7.4657	2918	0	26.78	1.47 $\pm$ 0.15	blk2	5.53 $\pm$ 0.57
O/UM2	45.9617	7.4622	2882	478	-	- - -	-	7.41 $\pm$ 0.79
O/UM3	45.9584	7.4559	2837	1088	26.88	1.73 $\pm$ 0.15	blk2	6.52 $\pm$ 0.57
O/UM4	45.9543	7.4504	2789	1712	22.82	8.50 $\pm$ 0.40	blk2	38.32 $\pm$ 1.86
O/UM5	45.9507	7.4458	2747	2248	23.06	2.47 $\pm$ 0.17	blk2	10.96 $\pm$ 0.78
O/UM6	45.9483	7.4405	2707	2743	22.97	3.48 $\pm$ 0.22	blk2	15.52 $\pm$ 0.98
O/UM7	45.9455	7.4352	2663	3258	23.39	6.19 $\pm$ 0.39	blk1	26.34 $\pm$ 1.74
O/UM8	45.9431	7.4297	2600	3758	22.39	4.43 $\pm$ 0.26	blk2	20.32 $\pm$ 1.23
O/UM9	45.9407	7.4248	2547	4224	22.67	4.12 $\pm$ 0.25	blk2	18.59 $\pm$ 1.14
<i>Glacier d’Otemma/ lower medial moraine (LM)<sup>a</sup></i>								
O/LM1	45.9613	7.4621	2875	0	-	- - -	-	17.78 $\pm$ 1.14
O/LM2	45.9582	7.4560	2835	581	22.64	4.94 $\pm$ 0.30	blk2	22.37 $\pm$ 1.39
O/LM3	45.9542	7.4507	2791	1184	14.54	2.07 $\pm$ 0.18	blk1	13.09 $\pm$ 1.32
O/LM4	45.9504	7.4459	2749	1745	20.31	2.72 $\pm$ 0.21	blk1	12.66 $\pm$ 1.10
O/LM5	45.9480	7.4407	2712	2228	22.90	3.28 $\pm$ 0.22	blk2	14.68 $\pm$ 0.99
O/LM6	45.9450	7.4354	2668	2754	17.11	5.34 $\pm$ 0.32	blk1	30.81 $\pm$ 2.00
<i>Glacier de Pièce</i>								
P1	45.9967	7.4703	2859	0	40.45	1.86 $\pm$ 0.17	blk4	4.40 $\pm$ 0.46
P2	45.9983	7.4692	2802	203	32.19	1.50 $\pm$ 0.16	blk4	4.35 $\pm$ 0.53
P3	46.0001	7.4690	2775	406	31.87	1.33 $\pm$ 0.14	blk4	3.83 $\pm$ 0.49
<i>Glacier de Tsjiore Nouve</i>								
TN1	46.0067	7.4554	2530	0	39.91	1.07 $\pm$ 0.14	blk4	2.25 $\pm$ 0.37
TN2	46.0075	7.4556	2526	98	40.84	1.00 $\pm$ 0.13	blk4	2.05 $\pm$ 0.33
TN3	46.0084	7.4558	2509	199	39.70	0.82 $\pm$ 0.11	blk4	1.68 $\pm$ 0.31
TN4	46.0096	7.4561	2491	334	40.78	0.96 $\pm$ 0.13	blk4	2.05 $\pm$ 0.34
TN5	46.0105	7.4565	2480	432	40.63	0.87 $\pm$ 0.11	blk4	1.84 $\pm$ 0.31
TN6	46.0113	7.4568	2466	532	40.64	1.61 $\pm$ 0.15	blk4	3.71 $\pm$ 0.39
TN7	46.0122	7.4572	2458	632	40.71	1.11 $\pm$ 0.15	blk4	2.45 $\pm$ 0.39
TN8	46.0133	7.4578	2457	765	38.20	1.40 $\pm$ 0.14	blk4	3.40 $\pm$ 0.41
TN9	46.0140	7.4586	2433	865	39.72	0.90 $\pm$ 0.13	blk4	1.95 $\pm$ 0.36
TN10	46.0145	7.4597	2431	963	40.67	1.14 $\pm$ 0.13	blk4	2.51 $\pm$ 0.35

<sup>a</sup> Samples O/UM1-9 and O/LM1-6 within this study correspond to published samples UM1-9/f and LM1-6/f in Wetterauer *et al.* (2022a, 2022b). <sup>b</sup> Downglacier distance from the uppermost sample of the respective medial moraine. <sup>c</sup> Process blank used to correct respective sample batches, where corresponding AMS  $^{10}\text{Be}/^9\text{Be}$  ratios are blk1 =  $2.16 \times 10^{-15}$ , blk2 =  $2.55 \times 10^{-16}$ , blk3 =  $1.19 \times 10^{-15}$ , and blk4 =  $1.56 \times 10^{-15}$ .

Mean  $P_{sp}(0)$  and  $A$  per debris source area were computed on a digital elevation model (DEM) for ice-free rockwalls in 1850, 1973, and 2017 (see Section 3.3.2 for details on the DEM and rockwall outlines). To quantify apparent rockwall erosion rates the mean values for the 1973 exposed rockwalls were used. In brief, mean  $P_{sp}(0)$  values are based on the CRONUS functions v2.3 (Balco *et al.*, 2008), the constant spallation scaling model “St” (Lal, 1991; Stone, 2000), and a sea level high latitude (SLHL) production rate of  $4.01 \pm 0.33$  atoms  $\text{g}^{-1} \text{yr}^{-1}$  (Borchers *et al.*, 2016). We considered topographic shielding (Dunne *et al.*, 1999) using the TopoToolbox

v2 function “toposhielding” (Schwanghart & Scherler, 2014) and surface area correction by local slope angles. We neglected temporal variations in production rates (due to young sample ages of  $10^1$ - $10^2$  years; Wetterauer *et al.*, 2022a), production by muons (typically <1% of spallogenic production), and snow cover shielding (as rockwalls remain largely snow-free throughout snow cover seasons; Swisstopo, 2022). Mean  $\lambda$  values were corrected for the surface slope dependency of cosmic-ray attenuation in bedrock (Masarik *et al.*, 2000).

### 3.3.1.2 Debris transport time and additional $^{10}\text{Be}$ production

To assess  $^{10}\text{Be}_{\text{transport}}$  additionally accumulated during debris transport from source rockwalls to the sampling location, we used the simple 1D debris particle trajectory model developed for Otemma and described in detail in Wetterauer *et al.* (2022a, 2022b). For every glacier, we estimated the horizontal and vertical ice velocities along the sampled medial moraine through time using observed surface velocities as well as mass balance-dependent particle burial and re-emergence, respectively. For a given time span, we then fed the glacial conveyor belt with particles and tracked their downglacier and englacial/supraglacial position. For each sample, we estimated its sample age, which corresponds to the time of debris erosion, and  $^{10}\text{Be}_{\text{transport}}$  from the modelled transport duration, by averaging the trajectories of particles that arrived supraglacially within  $\pm 30$  m of the sample location in 2019.

We determined glacier surface velocities and elevations as well as a generalized ELA history for the four new study sites Brenay, Cheilon, Pièce, and Tsijiore Nouve. Unfortunately, recent surface velocities obtained from cross-correlation of satellite imagery tend to be poorly resolved for the relatively small and slow glaciers of the Pigne d’Arolla massif. Especially close to the rockwalls, uncertainties are typically similar to the derived velocities (**Figure 3.3b,d,f,h**; Millan *et al.*, 2022). Therefore, we estimated horizontal glacier surface velocities by manually tracing the displacement of medial moraine boulders across orthoimages of the last ~40 years (Swisstopo, 2022). Boulder displacements were measured between successive orthoimages from the years 1977, 1983, 1988, 1995, 1999, 2005, 2007, 2010, 2013, 2017, and 2020 (**Figure 3.3a,c,e,g**). We considered boulder displacements parallel to profiles of the respective medial moraine and averaged boulder velocities over the respective time period between two orthoimages. Although exact acquisition dates were unavailable, the orthoimages presumably stem from a similar time during the summer season, as the snowline was located high, and the medial moraines were largely snow-free, except during the period 1995-1999. The positional accuracy for the orthoimages increases from 1 m before 1999 to 0.1 m at present (Swisstopo, 2022). Due to the increasing orthoimage resolution, we were able to identify and track more boulders during more recent periods, which allowed us to obtain continuous downglacier velocity profiles. For earlier periods, this was hampered by fewer velocity estimates with greater uncertainties. To nevertheless obtain temporally continuous velocity profiles, we fitted the most recent tracking period 2017-2020 using Shape Language Modeling tools (D’Errico, 2022) and shifted this fit vertically to the higher velocities during earlier periods using least squares (**Figure 3.3b,d,f,h**). Velocity changes over the entire period 1977-2020 were obtained by linear interpolation between the individual periods (**Figure 3.4b**). For the years 1880-1977, velocity changes were approximated by aligning the gradient of velocity change with the linear gradient of the respective glacier’s length change for the same period, obtained from long-term glacier length monitoring records (**Figure 3.4**, GLAMOS, 2021a).

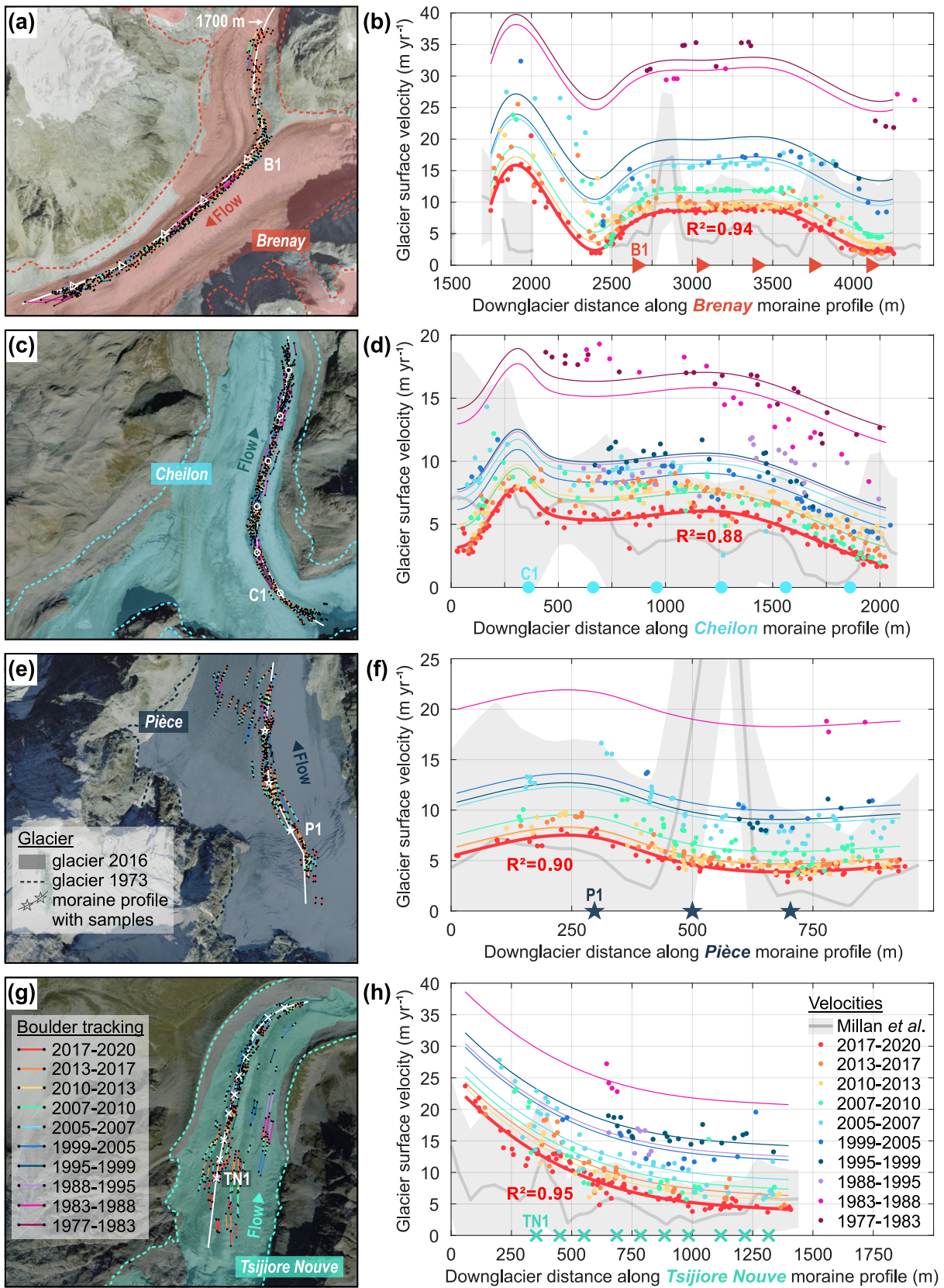


**Figure 3.3:** Glacier surface velocities along the four newly sampled medial moraines, reconstructed from 10 boulder-tracking periods between the years 1977 and 2020. (a, c, e, g) Tracked boulder displacements along downglacier profiles, which trace the sampled medial moraines. Where a boulder could be followed across several tracking periods colour-coded lines are connected. Note that boulder displacements at Brenay could only be tracked after a profile distance of ~1700 m due to englacial transport along the first half of the profile (2017 orthoimage by Swisstopo, 2022; glacier extents by Linsbauer *et al.*, 2021, and Müller *et al.*, 1976). (b, d, f, h) Glacier surface velocities through time derived

from the mapped boulder tracks. The solid red line and  $R^2$  indicate the fit of the velocities obtained for the most recent tracking period 2017–2020, and thin coloured lines reflect the same fit applied to the nine older tracking periods. For reference, remotely sensed velocities ( $\pm$  uncertainties) by Millan *et al.* (2022) are shown in grey in the background, and downglacier sample locations are indicated on the  $x$  axis. All datasets indicate a systematic slowdown of glacier flow towards the present. For reconstructions of Glacier d’Otemma see Wetterauer *et al.* (2022b).

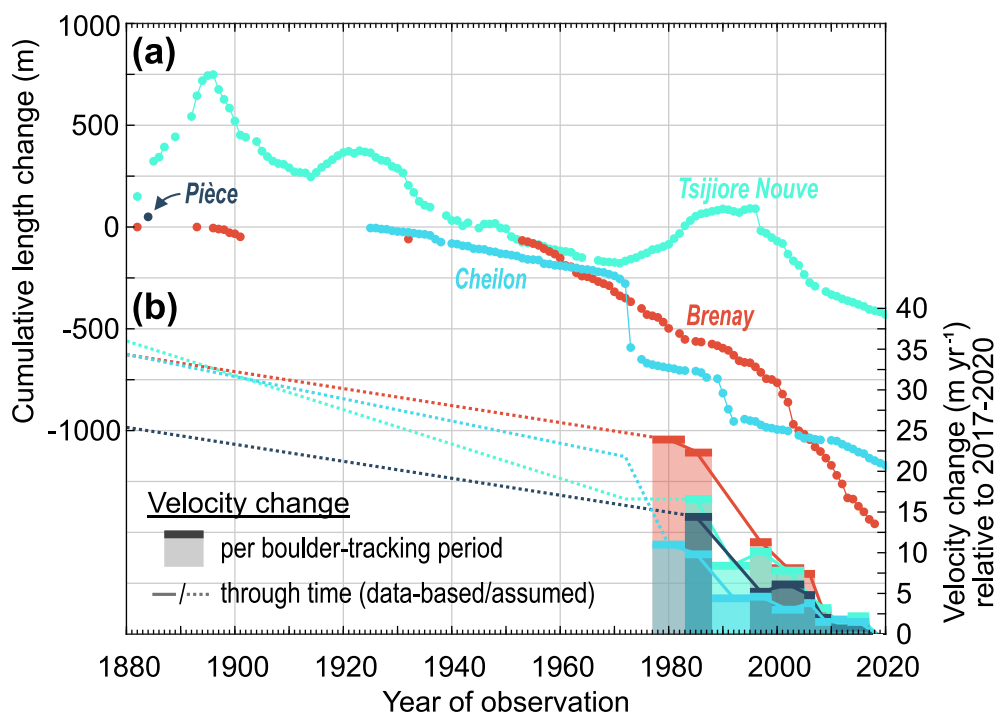


**Figure 3.4:** Glacier change at the four new study sites since 1880. **(a)** Long-term monitoring records of glacier length change (GLAMOS, 2021a). Note that markers from consecutive years are connected and that no length change record exists for Glacier de Pièce. **(b)** Reconstructed temporal changes in glacier surface velocity relative to the most recent boulder-tracking period 2017–2020. Per boulder-tracking period, the velocity change corresponds to the y-axis shift of its fit line to the solid red fit line in **Figure 3.3b,d,f,h**. On a year-to-year basis, velocity changes are based on linear interpolation between the velocity changes of the different tracking periods. Pre-1977 changes in velocities were approximated with reference to the linear gradient of the glacier’s length change in **(a)**. Due to a lack of length data at Glacier de Pièce, pre-1977 assumptions there align with Glacier du Brenay. For reconstructions of Glacier d’Otemma see Wetterauer *et al.* (2022b).

To constrain ice surface lowering along the four new moraine profiles through time, we interpolated between contour lines for the year 1880 extracted from the Siegfried Map (first edition 1870–1926) and a topographic map from 2016 (Swisstopo, 2022) using a three-step linear decline (Wetterauer *et al.*, 2022b). ELA elevations through time were adopted from a recent ELA reconstruction dataset for this region (Žebre *et al.*, 2021). Model settings of a generalized vertical mass balance profile (gradient: 0.7 m w.e. yr<sup>-1</sup> per 100 m elevation, maximum snow accumulation above the ELA: 0.75 m w.e. yr<sup>-1</sup>) and the computation of <sup>10</sup>Be production rates as a function of transport time, downglacier distance, and burial depth were adopted from Wetterauer *et al.* (2022b). At Brenay, where the elongated source rockwalls of La Serpentine lead to debris deposition along the first 2.3 km of the profile (**Figure 3.1**), we additionally considered the mixing of debris particles of different age and  $[^{10}\text{Be}]_{\text{transport}}$  at a sample location. There, particle trajectories were modelled from various source locations and weighted according to the above rockwall area, which we defined by flow directions using the steepest decent approach (**Figure B2**). At the other sites, where debris deposition occurs approximately at the profile’s head, trajectories were modelled from the profile head as a single point source.

We acknowledge that our reconstruction of glacier surface velocities and elevations contains several sources of unquantified uncertainties. On average, our uncertainty estimates for the velocities derived from boulder tracking are small (see Section **B1**). However, properly modelling these glaciers and the particle transport (e.g., Scherler & Egholm, 2020) requires even more empirical constraints that are currently unavailable, and, as we will show in Section **3.5.2**, our findings are largely insensitive to the  $[^{10}\text{Be}]_{\text{transport}}$ .

### 3.3.2 Source rockwall analysis

To compare the different medial moraine debris source areas in the Pigne d’Arolla massif and quantitatively assess the extent to which they are affected by deglaciation, we obtained source rockwall outlines for a recent (2017) and two past time slices (1973, 1850). Recent outlines were defined manually by mapping the ice-free rockwalls on a 2017 orthoimage (Swisstopo, 2022). Former outlines of ice-free rockwalls are based on reconstructed glacier outlines from the years 1973 and 1850 (Müller *et al.*, 1976; modified from Maisch *et al.*, 2000). Across the defined rockwalls (**Figure B1**), area, elevation, slope, and aspect were determined for each pixel in a 30 m resolution digital elevation model (DEM; global raster dataset SRTM GL1; NASA Shuttle Radar Topography Mission SRTM, 2013). The surface area covered per pixel was corrected for its local slope angle. To visualize changes in ice cover across the source rockwalls, we further compiled historical photographs from the online archives of Swisstopo (2022) and the ETH Library (2022).

## 3.4 Results

Below, the four new datasets of Brenay, Cheilon, Pièce, and Tsijiore Nouve are presented in summary form and in context with the two published Otemma datasets (Wetterauer *et al.*, 2022a, 2022b). Details on  $[^{10}\text{Be}]$  measurement results (**Table 3.1**), model-based corrections, and derived apparent rockwall erosion rates (**Table 3.2**) of individual medial moraine samples as well as on distinct debris source area properties (**Table 3.3**) are provided in the data tables as indicated.

### 3.4.1 Glacier surface velocities, estimated $^{10}\text{Be}$ transport concentrations, and sample ages

The tracked boulder displacements resulted in well-defined glacier surface velocities along our four new sampled medial moraines for the most recent period (**Figure 3.3b,d,f,h**). The further back in time, the more fragmented the records. Our approach to fit the most recent tracking period and shift the velocity fit vertically appears to yield reasonable fits to velocity estimates from earlier tracking periods. However, observations prior to 1995 are scarce, especially for Pièce and Tsijiore Nouve, and the shifted fit does not agree very well with the pre-1988 estimates for Cheilon.

Based on the modelled debris trajectories at Brenay, Cheilon, Pièce, and Tsijiore Nouve, transport occurred supraglacial over most of the downglacier distance, in part even exclusively (**Figure B3**, **Figure B4**). The resulting  $[^{10}\text{Be}]_{\text{transport}}$  values reach up to  $3 \times 10^3$  atoms  $\text{g}^{-1}$

(Table 3.2). The estimated sample ages overlap and are generally younger than 100 years (Table 3.2, Figure 3.5). In contrast, sample ages at the Otemma UM and LM moraine cover the last 200 and 150 years, respectively (Wetterauer *et al.*, 2022a).

**Table 3.2:** Model results of downglacier debris transport with sample ages, burial depth, and additional  $^{10}\text{Be}$  accumulation ( $[^{10}\text{Be}]_{\text{transport}}$ ), as well as transport-corrected  $^{10}\text{Be}$  concentrations ( $[^{10}\text{Be}]_{\text{rockwall}}$ ) and derived minimum and maximum apparent rockwall erosion rates.

Sample	Age <sup>b</sup> (yrs)	Burial <sup>b,c</sup> / max (m)	$[^{10}\text{Be}]_{\text{transport}}^{\text{b}}$ $\times 10^3$ (atoms $\text{g}^{-1}$ )	$[^{10}\text{Be}]_{\text{rockwall}}^{\text{d}}$ $\times 10^3$ (atoms $\text{g}^{-1}$ ) $\pm 1\sigma$	Apparent rockwall erosion rate <sup>e,f</sup>	
					min (uncorr.) (mm $\text{yr}^{-1}$ ) $\pm 1\sigma$	max (transport-corr.) (mm $\text{yr}^{-1}$ ) $\pm 1\sigma$
<i>Glacier du Brenay</i>						
B1	52	-13.4	0.7	22.9 $\pm$ 1.2	1.0 $\pm$ 0.1	1.0 $\pm$ 0.1
B2	63	-13.5	0.9	32.1 $\pm$ 1.6	0.7 $\pm$ 0.1	0.7 $\pm$ 0.1
B3	72	-10.2	1.1	32.0 $\pm$ 1.6	0.7 $\pm$ 0.1	0.7 $\pm$ 0.1
B4	83	-7.8	1.5	28.8 $\pm$ 1.5	0.8 $\pm$ 0.1	0.8 $\pm$ 0.1
B5	96	-9.9	1.9	31.5 $\pm$ 1.5	0.7 $\pm$ 0.1	0.7 $\pm$ 0.1
<i>Glacier de Cheilon</i>						
C1	36	-0.2	1.0	3.5 $\pm$ 0.4	3.9 $\pm$ 0.5	5.1 $\pm$ 0.7
C2	50	-1.8	1.3	2.0 $\pm$ 0.4	5.5 $\pm$ 0.8	8.9 $\pm$ 1.8
C3	61	-0.2	1.7	4.0 $\pm$ 0.5	3.2 $\pm$ 0.4	4.5 $\pm$ 0.7
C4	70	0.0	2.0	2.4 $\pm$ 0.5	4.1 $\pm$ 0.6	7.6 $\pm$ 1.6
C5	80	0.0	2.3	0.5 $\pm$ 0.4	6.6 $\pm$ 1.2	36.7 <sup>g</sup> $\pm$ 32.3 <sup>g</sup>
C6	92	0.0	2.6	1.8 $\pm$ 0.5	4.1 $\pm$ 0.6	10.0 $\pm$ 2.8
<i>Glacier d'Otemma/ upper medial moraine (UM)<sup>a</sup></i>						
O/UM1	45	0.0	1.4	4.2 $\pm$ 0.6	3.8 $\pm$ 0.5	5.1 $\pm$ 0.8
O/UM2	77	0.0	2.4	5.0 $\pm$ 0.8	2.9 $\pm$ 0.4	4.2 $\pm$ 0.7
O/UM3	103	-1.2	2.8	3.7 $\pm$ 0.6	3.3 $\pm$ 0.4	5.8 $\pm$ 1.0
O/UM4	130	-5.0	2.5	35.8 $\pm$ 1.9	0.6 $\pm$ 0.1	0.6 $\pm$ 0.1
O/UM5	148	-9.1	2.3	8.6 $\pm$ 0.8	1.9 $\pm$ 0.2	2.5 $\pm$ 0.3
O/UM6	167	-12.4	2.3	13.2 $\pm$ 1.0	1.4 $\pm$ 0.1	1.6 $\pm$ 0.2
O/UM7	182	-14.7	2.4	24.0 $\pm$ 1.7	0.8 $\pm$ 0.1	0.9 $\pm$ 0.1
O/UM8	199	-16.2	2.4	17.9 $\pm$ 1.2	1.0 $\pm$ 0.1	1.2 $\pm$ 0.1
O/UM9	206	-16.7	2.5	16.1 $\pm$ 1.1	1.1 $\pm$ 0.1	1.3 $\pm$ 0.1
<i>Glacier d'Otemma/ lower medial moraine (LM)<sup>a</sup></i>						
O/LM1	35	0.0	1.0	16.7 $\pm$ 1.1	1.2 $\pm$ 0.1	1.3 $\pm$ 0.1
O/LM2	67	0.0	2.0	20.3 $\pm$ 1.4	1.0 $\pm$ 0.1	1.1 $\pm$ 0.1
O/LM3	94	0.0	2.8	10.3 $\pm$ 1.3	1.7 $\pm$ 0.2	2.2 $\pm$ 0.3
O/LM4	115	-0.2	3.4	9.2 $\pm$ 1.1	1.7 $\pm$ 0.2	2.4 $\pm$ 0.3
O/LM5	134	-1.8	3.5	11.2 $\pm$ 1.0	1.5 $\pm$ 0.2	2.0 $\pm$ 0.2
O/LM6	152	-4.2	3.3	27.6 $\pm$ 2.0	0.7 $\pm$ 0.1	0.8 $\pm$ 0.1
<i>Glacier de Pièce</i>						
P1	27	0.0	0.8	3.6 $\pm$ 0.5	4.5 $\pm$ 0.6	5.5 $\pm$ 0.8
P2	39	-1.1	1.0	3.3 $\pm$ 0.5	4.5 $\pm$ 0.7	5.9 $\pm$ 1.1
P3	50	-1.6	1.2	2.6 $\pm$ 0.5	5.1 $\pm$ 0.8	7.6 $\pm$ 1.6
<i>Glacier de Tsijiore Nouve</i>						
TN1	16	0.0	0.4	1.9 $\pm$ 0.4	8.8 $\pm$ 1.6	10.6 $\pm$ 2.3
TN2	21	0.0	0.5	1.6 $\pm$ 0.3	9.7 $\pm$ 1.7	12.7 $\pm$ 2.9
TN3	27	0.0	0.6	1.1 $\pm$ 0.3	11.8 $\pm$ 2.4	18.7 $\pm$ 5.8
TN4	34	0.0	0.8	1.3 $\pm$ 0.3	9.7 $\pm$ 1.8	15.6 $\pm$ 4.4
TN5	40	0.0	0.9	0.9 $\pm$ 0.3	10.8 $\pm$ 2.0	21.3 $\pm$ 7.3
TN6	45	0.0	1.0	2.7 $\pm$ 0.4	5.3 $\pm$ 0.7	7.4 $\pm$ 1.2
TN7	50	0.0	1.1	1.3 $\pm$ 0.4	8.1 $\pm$ 1.5	15.1 $\pm$ 4.7
TN8	56	0.0	1.3	2.1 $\pm$ 0.4	5.8 $\pm$ 0.9	9.3 $\pm$ 1.9
TN9	61	0.0	1.4	0.6 $\pm$ 0.4	10.2 $\pm$ 2.1	34.5 $\pm$ 21.7
TN10	65	0.0	1.5	1.1 $\pm$ 0.3	7.9 $\pm$ 1.3	18.9 $\pm$ 6.5

<sup>a</sup> Samples O/UM1-9 and O/LM1-6 within this study correspond to published samples UM1-9/f and LM1-6/f in Wetterauer *et al.* (2022a, 2022b). <sup>b</sup> Computed using a simple 1D debris particle trajectory model (Wetterauer *et al.*, 2022b). <sup>c</sup> Maximum burial depth modelled for debris particles of a sample. Negative numbers indicate partially englacial transport, and 0 indicates exclusively supraglacial transport. <sup>d</sup> Calculated by subtracting  $[^{10}\text{Be}]_{\text{transport}}$  from  $[^{10}\text{Be}]_{\text{measured}}$ .  $1\sigma$  estimates correspond to analytical uncertainties of  $[^{10}\text{Be}]_{\text{measured}}$ . <sup>e</sup> Calculated using the mean spallogenic production rates and absorption mean free paths of the respective 1973 exposed source rockwalls listed in Table 3.3.  $1\sigma$  estimates are based on the analytical uncertainties of  $[^{10}\text{Be}]_{\text{measured}}$ . <sup>f</sup> Minimum rates were derived from  $[^{10}\text{Be}]_{\text{measured}}$ , uncorrected for downglacier transport. Maximum rates were derived from  $[^{10}\text{Be}]_{\text{rockwall}}$ , corrected for downglacier transport. <sup>g</sup> Value excluded from any erosion rate-based analysis due to unreasonable  $[^{10}\text{Be}]_{\text{rockwall}}$  estimate (see Section 3.5.1).

### 3.4.2 Measured $^{10}\text{Be}$ and estimated $^{10}\text{Be}$ rockwall concentrations

The  $[^{10}\text{Be}]_{\text{measured}}$  values of our 24 new medial moraine debris samples range between  $2 \times 10^3$  and  $33 \times 10^3$  atoms  $\text{g}^{-1}$  (**Table 3.1, Figure 3.5**). At Brenay, Cheilon, Pièce, and Tsijiore Nouve,  $[^{10}\text{Be}]_{\text{measured}}$  values are rather uniform along the medial moraine, averaging at  $31 \times 10^3$ ,  $4 \times 10^3$ ,  $4 \times 10^3$ , and  $2 \times 10^3$  atoms  $\text{g}^{-1}$ , respectively. Correcting  $[^{10}\text{Be}]_{\text{measured}}$  for  $[^{10}\text{Be}]_{\text{transport}}$  results in overall lower  $[^{10}\text{Be}]_{\text{rockwall}}$  (**Table 3.2, Figure 3.5**). At Brenay, where  $[^{10}\text{Be}]_{\text{measured}}$  is high,  $[^{10}\text{Be}]_{\text{transport}}$  is only a small fraction of the concentration (3-6%). For samples with low  $[^{10}\text{Be}]_{\text{measured}}$  at Cheilon, Pièce, and Tsijiore Nouve, the correction can account for up to half (17-49%) and in individual cases even more (58-82%). Still, the general tendency of the individual  $[^{10}\text{Be}]_{\text{measured}}$  records towards temporal consistency is maintained in  $[^{10}\text{Be}]_{\text{rockwall}}$ . The concentration ranges are comparable to the Otemma datasets (**Figure 3.5**); however, medial moraine  $[^{10}\text{Be}]$  at Otemma was found to be more variable and to systematically increase downglacier at the Otemma UM moraine (Wetterauer *et al.*, 2022a).

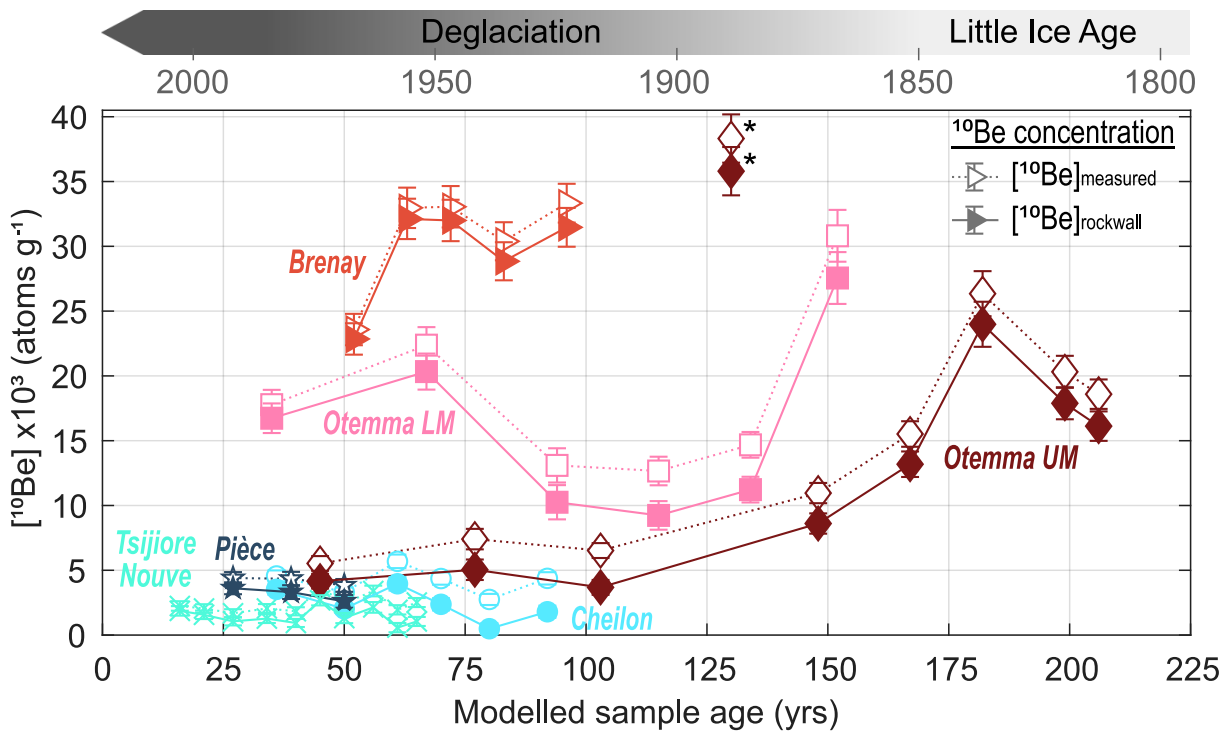


**Figure 3.5:** Comparison of uncorrected ( $[^{10}\text{Be}]_{\text{measured}}$ ) and transport-corrected ( $[^{10}\text{Be}]_{\text{rockwall}}$ ) medial moraine  $[^{10}\text{Be}]$  records of the Pigne d’Arolla massif through time (data from Glacier d’Otemma by Wetterauer *et al.*, 2022a). Concentrations ( $\pm 1\sigma$  analytical error) are plotted against modelled sample ages, reflecting the timing of rockwall erosion either during the Little Ice Age or the following deglaciation period, as indicated by the timeline above. Note that a re-measurement of a high-concentration outlier at the Otemma UM moraine (\*) at a slightly coarser grain size fraction fits the temporal trend well (see **Figure 2.6a**; Wetterauer *et al.*, 2022a).

### 3.4.3 Apparent rockwall erosion rates

We provide two estimates of apparent rockwall erosion rates: based on the uncorrected  $[^{10}\text{Be}]_{\text{measured}}$  and on the transport-corrected  $[^{10}\text{Be}]_{\text{rockwall}}$  (**Table 3.2**). At Brenay, the mean uncorrected/corrected rate estimates ( $\pm 1\sigma$ ) both round to  $0.8 \pm 0.1$   $\text{mm yr}^{-1}$ . For Cheilon and Pièce, mean uncorrected/corrected rate estimates deviate more strongly and are comparatively higher with  $4.6 \pm 1.2$  /  $7.2 \pm 2.4$  and  $4.7 \pm 0.4$  /  $6.3 \pm 1.1$   $\text{mm yr}^{-1}$ , respectively. Mean

uncorrected/corrected rate estimates are much higher at Tsijiore Nouve with  $8.8 \pm 2.1 / 16.4 \pm 7.8 \text{ mm yr}^{-1}$ , which we consider to be unreasonable for reasons discussed in Section 3.5.1. For comparison, mean uncorrected/corrected rate estimates at the Otemma UM and LM rockwalls are  $1.9 \pm 1.2 / 2.6 \pm 2.0$  and  $1.3 \pm 0.4 / 1.6 \pm 0.6 \text{ mm yr}^{-1}$ , respectively (Wetterauer *et al.*, 2022a). We note that our erosion rate analyses are based on the ice-free rockwall areas of 1973 because debris deposition and thus rockwall erosion presumably occurred largely between 1850 and 1973 (Figure 3.5).

### 3.4.4 Source rockwall morphology

We compare the debris source areas in the Pigne d’Arolla massif by area, aspect, and mean slope of the ice-free rockwall areas in the years 1850, 1973, and 2017 (Table 3.3). Overall, rockwalls are located between 3100 and 3400 m elevation. While the rockwalls at Brenay represent by far the largest debris source area, the other rockwalls are comparatively small. Southwest-facing rockwalls at Brenay in 1973 were inclined by  $43^\circ$  on average. At the northwest- to east-facing rockwalls of Cheilon, Pièce, and Tsijiore Nouve mean slope angles were steeper, ranging between  $48$  and  $51^\circ$ . These observations are consistent with mean slope angles at Otemma, which in 1973 were steeper at the northwest-facing UM rockwalls ( $43^\circ$ ) than at the southwest-facing LM rockwalls ( $36^\circ$ ; Wetterauer *et al.*, 2022a).

**Table 3.3:** Geomorphic parameters of source rockwalls in the years 1850, 1973, and 2017, as well as  $^{10}\text{Be}$  production rates and absorption mean free paths.

Rockwalls	Lithology <sup>a</sup>	Area <sup>b</sup>		Elevation		Slope	Aspect	$P_{sp}(0)$	$\lambda$
		(km <sup>2</sup> )	$\pm \Delta^c$	(m a.s.l.)	$\pm \Delta^d$	( $^\circ$ )	( $^\circ$ )	(atoms g <sup>-1</sup> yr <sup>-1</sup> )	(g cm <sup>-2</sup> )
<i>Glacier du Brenay</i>									
1850	QD	1.26		3387		43	238 SW	43	141
1973	QD	1.27	1%	3385	-2 m	43	238 SW	43	141
2017	QD	1.53	20%	3374	-11 m	41	230 SW	44	142
<i>Glacier de Cheilon</i>									
1850	QD	0.08		3131		52	317 NW	35	136
1973	QD	0.08	3%	3138	7 m	51	316 NW	35	137
2017	QD	0.15	86%	3181	43 m	42	311 NW	38	141
<i>Glacier d'Otemma/ upper medial moraine</i>									
1850	OG + S	0.10		3174		43	293 NW	39	143
1973	OG + S	0.10	0%	3174	0 m	43	293 NW	39	143
2017	OG + S	0.23	129%	3131	-43 m	39	292 W	38	144
<i>Glacier d'Otemma/ lower medial moraine</i>									
1850	OG + S	0.11		3283		41	214 SW	42	142
1973	OG + S	0.27	151%	3162	-121 m	36	229 SW	40	145
2017	OG + S	0.51	87%	3126	-36 m	31	236 SW	40	146
<i>Glacier de Pièce</i>									
1850	OG + GD	0.08		3175		49	26 NE	37	140
1973	OG + GD	0.08	0%	3175	0 m	49	26 NE	37	140
2017	OG + GD	0.10	16%	3177	2 m	48	27 NE	38	140
<i>Glacier de Tsijiore Nouve</i>									
1850	QD	0.21		3339		48	90 E	39	136
1973	QD	0.21	0%	3339	0 m	48	90 E	39	136
2017	QD	0.26	23%	3247	-92 m	47	78 E	38	137

<sup>a</sup> Crystalline rocks of the Arolla series, where GD: granodiorite, OG: orthogneiss, QD: quartzdiorite, S: schist. <sup>b</sup> Corrected for slope. <sup>c</sup> Area expansion (%) between 1850 and 1973 and between 1973 and 2017, respectively. <sup>d</sup> Mean elevation gain or loss (m) between 1850 and 1973 and between 1973 and 2017, respectively, indicating predominant direction of area expansion.

Source rockwall deglaciation in the Pigne d’Arolla massif after 1850 differs locally. Ice-free areas at Brenay, Cheilon, the Otemma UM rockwalls, Pièce, and Tsijiore Nouve expanded by <5% between 1850 and 1973, resulting in minimal changes in mean rockwall elevation. At the

Otemma LM rockwalls, however, ice-free areas expanded by ~150%, and the mean elevation markedly dropped. Brenay, Pièce, and Tsijiore Nouve rockwalls seem to have expanded by only ~20% between 1973 and 2017. Thus, shifts in mean elevations have again remained small, except at Tsijiore Nouve, where recent bedrock exposure at the Pigne d'Arolla icefall reduced the mean rockwall elevation. In contrast, ice-free areas at Cheilon and the Otemma UM and LM rockwalls approximately doubled since 1973, expanding by 86 to 129%. Whereas at Cheilon mean rockwall elevation has shifted upward, Otemma UM and LM rockwalls have expanded predominantly downward. Visually, the degree of rockwall deglaciation is also evident on historical photographs (**Figure 3.6**), particularly the significant ice cover changes across Otemma LM rockwalls.

## 3.5 Discussion

### 3.5.1 How “apparent” are the rockwall erosion rate estimates?

The medial moraine records of the Pigne d'Arolla massif - including the Otemma datasets (Wetterauer *et al.*, 2022a) - cover a wide range of apparent rockwall erosion rates (**Table 3.2**), largely spanning between 0.6 and 10.0 mm yr<sup>-1</sup> and presumably covering the last 200 years. Our particle trajectory modelling suggests that our new samples from Brenay, Cheilon, Pièce, and Tsijiore Nouve cover the post-LIA deglaciation period, and their [<sup>10</sup>Be] values indicate relatively stable apparent erosion rates (**Figure 3.5**). In contrast, [<sup>10</sup>Be] values in the longer Otemma UM moraine record were found to decrease after the end of the LIA (Wetterauer *et al.*, 2022a). Our estimates are broadly consistent with previous estimates of rockwall erosion rates in glacial landscapes in the Alps. Other studies using cosmogenic nuclides, albeit from different sources, report comparable erosion rates ranging from 0.1 to 6.4 mm yr<sup>-1</sup> (Wittmann *et al.*, 2007; Mair *et al.*, 2019, 2020; Sarr *et al.*, 2019). Similarly, erosion rates derived from optically stimulated luminescence reach values up to 4.3 mm yr<sup>-1</sup> over the last ~100 years (Lehmann *et al.*, 2020), whereas erosion rates derived from terrestrial laser scanning between the years 2005 and 2010 reach values as high as 6.5 and 8.4 mm yr<sup>-1</sup> (Rabatel *et al.*, 2008; Kenner *et al.*, 2011). Despite the similarity of our and previously estimated erosion rates, we emphasize that estimating apparent rockwall erosion rates from medial moraine [<sup>10</sup>Be]<sub>measured</sub> involves uncertainties that are not easy to quantify (Wetterauer *et al.*, 2022a).

Apart from the assumption of isotopic steady state that underlies our calculation (see Section **3.3.1**), the range of our erosion rate estimates depends on whether we account for post-depositional <sup>10</sup>Be accumulation during downglacier debris transport (transport-corrected [<sup>10</sup>Be]<sub>rockwall</sub>), or not (uncorrected [<sup>10</sup>Be]<sub>measured</sub>). The differences are negligible for samples with high [<sup>10</sup>Be]<sub>measured</sub> but noticeable where [<sup>10</sup>Be]<sub>measured</sub> values are low (**Table 3.2**). Overall, our particle trajectory model involves generalized assumptions and thus sample ages and [<sup>10</sup>Be]<sub>transport</sub> should be considered approximations. Our temporal assignment seems to be quite robust because even if we assume half or twice the velocity changes for years before 1977, for which we lack boulder-tracking data, the modelled sample ages are mostly <5 years older or younger (**Table B1**). Yet, we note here that the model is not capable of simulating debris transport through an icefall and that debris trajectories at Tsijiore Nouve start at the base of the Pigne d'Arolla icefall and therefore probably underestimate the overall debris transport time.

Assuming fast surface velocities across the Pigne d’Arolla icefall of up to  $\sim 70 \text{ m yr}^{-1}$  (Millan *et al.*, 2022), sample ages at Tsijiore Nouve would be a few decades older ( $< 40$  years) than estimated and would thus still fall into the post-LIA deglaciation period.

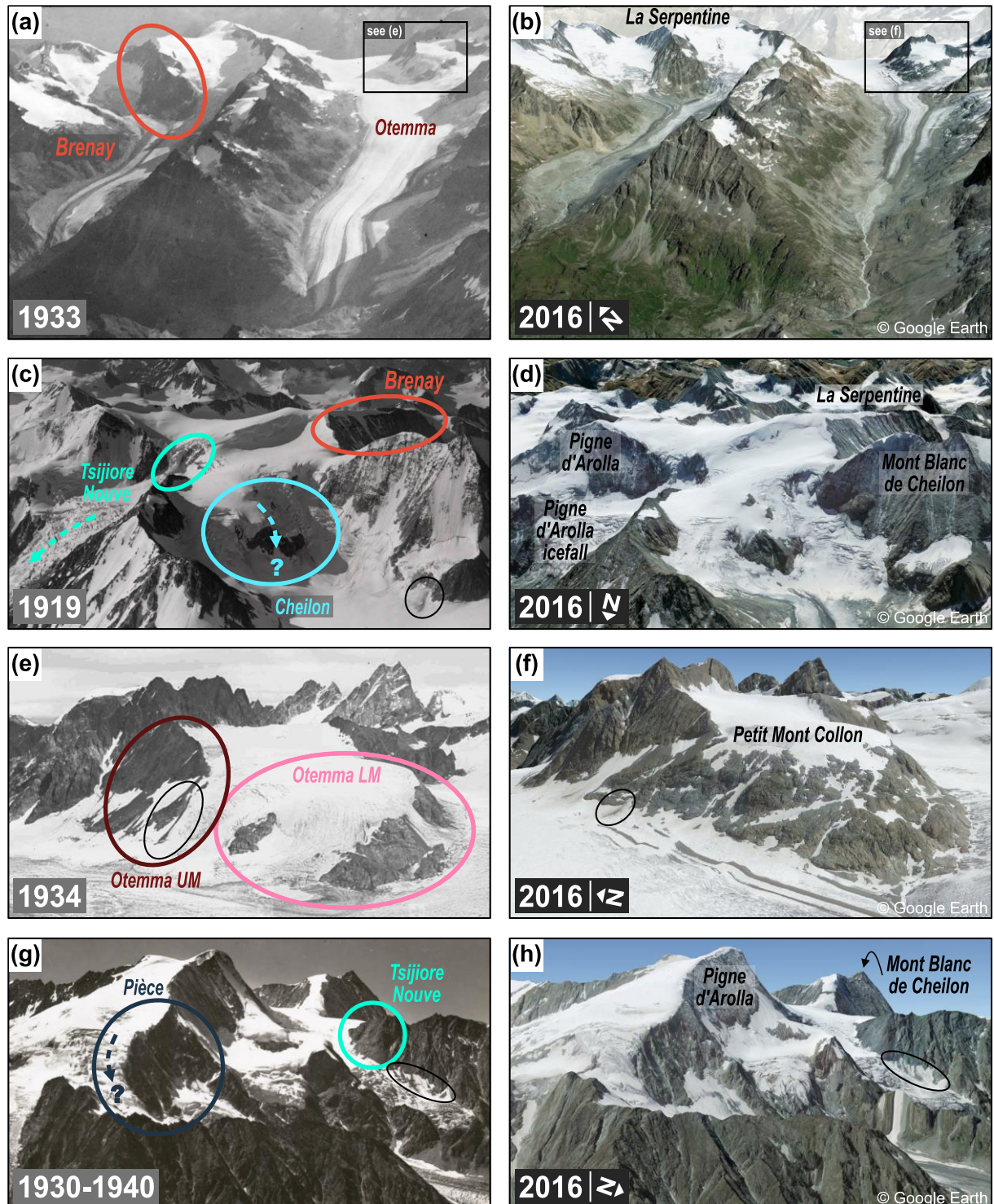


**Figure 3.6:** Ice cover changes across deglaciating source rockwalls in the Pigne d’Arolla massif between the beginning of the (a, c, e, g) 20th and (b, d, f, h) 21st century. For each historical photograph on the left, approximately the same view from Google Earth (<https://earth.google.com>, accessed: 5 December 2022) is shown on the right. The years shown are indicated (historical photographs by the ETH Library, 2022, Swisstopo, 2022). For clarity, debris source areas are only indicated on the left (coloured circles), and mountain peaks or ridges mentioned in the text are only labelled on the right. Areas where subglacial erosion may bias our medial moraine records are indicated (dashed arrows). Note the examples of small-scale rockfalls representative of rockwall erosion (black circles).

Our estimates of supraglacial transport paths largely agree with historical photographs. At Brenay, our modelled trajectories (**Figure B3**) indicate supraglacial transport below the confluence of both tributaries at all times. This is consistent with historical photographs (**Figure 3.6a**) and reconstructions of the glacier in 1850, which indicate that the medial moraine was already at the surface at the end of the LIA (Lambiel & Talon, 2019). At Pièce, burial and englacial transport of debris deposited before or around 1980, as suggested by our modelled trajectories (**Figure B4b**), also appear to be consistent with aerial images taken in September 1983 (**Figure B5**), which indicate a low ELA and re-emergence of debris further downglacier. However, exceptionally high erosion rate estimates for Cheilon sample C5, which result from very low calculated  $[^{10}\text{Be}]_{\text{rockwall}}$ , suggest that the model may overestimate  $[^{10}\text{Be}]_{\text{transport}}$  at this glacier. Specifically, the simulated transport of C5 is exclusively supraglacial (**Figure B4a**), with its modelled trajectory always being slightly below the assumed ELA. We note that it is possible that the local ELA history may well differ from the assumed one, which we adopted from a regional, large-scale record (Žebre *et al.*, 2021). In fact, samples deposited subsequently to C5 have been buried and aerial images from 1983 (**Figure B5**) indicate debris deposition in the accumulation zone (at the time of image acquisition), suggesting that it is unlikely that C5 was never buried. Also, at Tsijiore Nouve,  $[^{10}\text{Be}]_{\text{transport}}$  values seem to be maximum estimates, as our model does not incorporate englacial transport through the Pigne d’Arolla icefall. There, modelled debris particles experience supraglacial transport only (**Figure B4c**), even though early observations (Small & Clark, 1974) and aerial images from 1983 (**Figure B5**) suggest englacial transport in the past, downglacier of the icefall base. However, in the absence of better-resolved ELA, mass balance, and pre-1977 glacier velocity data, it is difficult to obtain more reliable estimates of  $[^{10}\text{Be}]_{\text{transport}}$ . Therefore, we consider the provided uncorrected erosion rate estimates to be minimum values, whereas our transport-corrected estimates may instead be considered maximum values if we overestimate supraglacial transport time, as indicated by the C5 and TN samples. Nevertheless, given the mostly rather narrow ranges, except for C5 and TN samples, any trend that we observe in our apparent erosion rates is likely real and not an artefact of downglacier transport.

In addition to  $^{10}\text{Be}$  accumulation during transport, the possible contribution of subglacially derived debris challenges the direct interpretation of our apparent rockwall erosion rates as actual rockwall erosion rates. Subglacially eroded debris probably has a low  $[^{10}\text{Be}]$  and, if admixed with supraglacially eroded debris, would tend to reduce the concentration signal in medial moraine debris (Wetterauer *et al.* 2022a), especially where  $[^{10}\text{Be}]$  signals of rockwall erosion are low. At Tsijiore Nouve, the two medial moraines do not directly detach from their source rockwalls but are separated from them by the upper accumulation basin and the Pigne d’Arolla icefall (**Figure 3.1g**). Samples therefore possibly combine rockwall debris buried and transported englacially in the upper accumulation basin, as well as debris from subglacially eroded bedrock brought up by the icefall, both melting out and mixing in the ablation zone below the icefall (Small *et al.*, 1979; Small & Gomez, 1981; Gomez & Small, 1983). Still, supraglacial sources have been suggested to be dominant based on a higher proportion of angular medial moraine clasts (Small & Gomez, 1981). This is supported by the ridge-like topography of both moraines and their separation by an ice septum (**Figure 3.1g**), which indicate locally enhanced supply from rockwall debris. If subglacial supply along the icefall were dominant, we would expect a more continuous debris cover over the entire ablation zone

width, which is not the case. At Pièce and Cheilon, ice moving along the rockwall margin may also contribute subglacial material. Whether such material would lower the  $[^{10}\text{Be}]$  of the debris by much is difficult to assess. However, rockwall debris deposition at Pièce occurs over  $\sim 200$  m of distance, while potential subglacial input seems to be confined to a single local point source at the easternmost rockwall margin (**Figure 3.6g**). In contrast, at Cheilon, the emergence of rockwalls within the glacier tributary (**Figure 3.6c**) could allow for subglacial input along larger sections of the rockwall margin, which may explain the low concentrations measured in sample C5 (**Table 3.1**).

Since the end of the LIA, glaciers around the Pigne d’Arolla massif have been retreating, exposing bedrock surfaces formerly shielded from cosmic radiation, which are now probably eroding. However, the expansion of ice-free areas is not uniform across the study sites (**Table 3.3, Figure 3.6**), raising the question of whether our samples with low  $[^{10}\text{Be}]$  may be due to the erosion of recently uncovered bedrock with a potentially low concentration (Scherler & Egholm, 2020; Wetterauer *et al.*, 2022a). At the Otemma LM rockwalls, Wetterauer *et al.* (2022a) have found that the ice cover has shrunk significantly in patches since 1850, so the associated patchy rockwall expansion could be the reason why  $[^{10}\text{Be}]$  here shows the comparatively largest spread among the deglaciation records from the massif. In contrast, between 1850 and 1973, the reconstructed rockwall expansion due to shrinking ice cover was small ( $<5\%$ ) at Brenay, Cheilon, Pièce, and Tsijiore Nouve, as well as at the Otemma UM rockwalls (**Figure B1c**). Since 1973, the ice-free rockwall areas have changed only slightly ( $\sim 20\%$ ) at Brenay, Pièce, and Tsijiore Nouve but more significantly at Cheilon and the Otemma UM rockwalls, where the areas have doubled (**Figure B1b**). Our modelled sample ages suggest that erosion at Brenay, Cheilon, and the Otemma UM rockwalls presumably occurred before 1973, and thus we expect that the associated erosion rate estimates are largely unaffected by ice cover changes. Similarly, in the younger records of Pièce and Tsijiore Nouve, post-1973 deglaciation effects should be comparatively small as rockwall areas varied only marginally. Even if our modelled age estimates were too old by a few years, it is not straightforward to provide estimates of the relative amounts of debris eroded from surfaces newly exposed since 1973 that are included in medial moraine debris and what their actual  $[^{10}\text{Be}]$  is. However, we would expect continuous ice surface lowering to have notable effects, probably reflected by temporal trends, which is only observed for the long Otemma UM moraine record. If we assume that the temporal trend in the Otemma UM moraine record since 1850 reflects a pure deglaciation signal, due to the addition of debris from formerly subglacial surfaces with a  $[^{10}\text{Be}]$  of zero atoms  $\text{g}^{-1}$  at the same erosion rate as before, the medial moraine would require a contribution of 75% of such debris to lower the mean  $[^{10}\text{Be}]_{\text{rockwall}}$  of the pre-1860 LIA value ( $\sim 18 \times 10^3$  atoms  $\text{g}^{-1}$  for O/UM6-9) to the mean  $[^{10}\text{Be}]_{\text{rockwall}}$  of the post-1900 deglaciation value ( $\sim 4 \times 10^3$  atoms  $\text{g}^{-1}$  for O/UM1-3). This would correspond to a quadrupling of the debris source area and supply. Such an increase in the debris supply should also be visible in the amount of material exposed in the medial moraine. Yet, our source rockwall analysis indicates no changes in ice-free areas at Otemma UM rockwalls from 1850 to 1973 (**Table 3.3, Figure B1c**), and the downglacier narrowing of the UM moraine between sample locations O/UM3 and O/UM8 is most probably due to the acceleration of flow velocities at the ice confluence below Petit Mont Collon (**Figure A2c**).

Based on the above assessments, we assume that the actual  $^{10}\text{Be}$ -derived rockwall erosion rates lie somewhere between our apparent minimum and maximum rockwall erosion rate estimates. The fact that within these bounds, the records are either trending or stable, rather than being randomly scattered, suggests that the operating erosion processes (see Section 3.5.2) are characterized by continuity. Source rockwall expansion into formerly glaciated terrain is small at Brenay, Cheilon, Pièce, Otemma UM rockwalls, and Tsijiore Nouve but can be problematic at Otemma LM rockwalls, where deglaciation is most pronounced and complex. At Cheilon and Pièce, the contribution of subglacially derived debris of low concentration is possible, probably with a greater chance of bias at Cheilon, as subglacial input could occur along larger rockwall sections. The icefall at Tsijiore Nouve likely introduces subglacial material that may lower  $[\text{}^{10}\text{Be}]_{\text{measured}}$ , suggesting that actual  $^{10}\text{Be}$ -derived rockwall erosion rates are lower. Nevertheless, the temporal consistency of its record and the continuity of its medial moraine indicate that erosion rates remained fairly stable through time, as is the case for most other post-LIA records, too.

### 3.5.2 Spatial trends in apparent rockwall erosion

The source rockwalls of the Pigne d'Arolla massif differ in their morphology (**Table 3.3**), and comparison with our apparent rockwall erosion rates, averaged over the deglaciation period, indicates some spatial trends: mean erosion rate estimates appear to be higher for smaller rockwall areas (**Figure 3.7a**) and for steeper slopes (**Figure 3.7d**) but vary independently of mean rockwall elevation (**Figure 3.7b**). Differentiating by aspect, mean erosion rate estimates are higher at northwest- to northeast-facing rockwalls but lower at southwest faces (**Figure 3.7c**). These trends are the same for apparent minimum and maximum rockwall erosion rates. We note that aspect and slope angle appear to be related in the area around Pigne d'Arolla: at the approximate elevation range of the studied debris source areas, ice-free north faces are the steepest, while south faces are the shallowest (**Figure 3.2c**).

At mountain ridges where asymmetry between north and south slopes has been observed, cirque erosion has been suggested to be the dominant process promoting retreat of glaciated north slopes at the expense of unglaciated south slopes during glacial periods (Oskin & Burbank, 2005; Naylor & Gabet, 2007). Our datasets indicate that asymmetry may also be observed where both north and south faces are glaciated. North of the east-west trending ridgeline between Pigne d'Arolla and Mont Blanc de Cheilon, steeper rockwalls tower above smaller glaciers, while to the south, shallower rockwalls tower above larger glaciers (**Figure 3.1a,b**). It appears that steeper north-facing rockwalls, although smaller in area, have higher erosion rates than the more extensive shallower south-facing rockwalls, where larger bedrock areas are exposed (**Figure 3.7a**). In the following, we will address the relevance of (i) rockwall area, (ii) slope, and (iii) aspect as potential controls on the observed spatial trends in our apparent rockwall erosion rates.

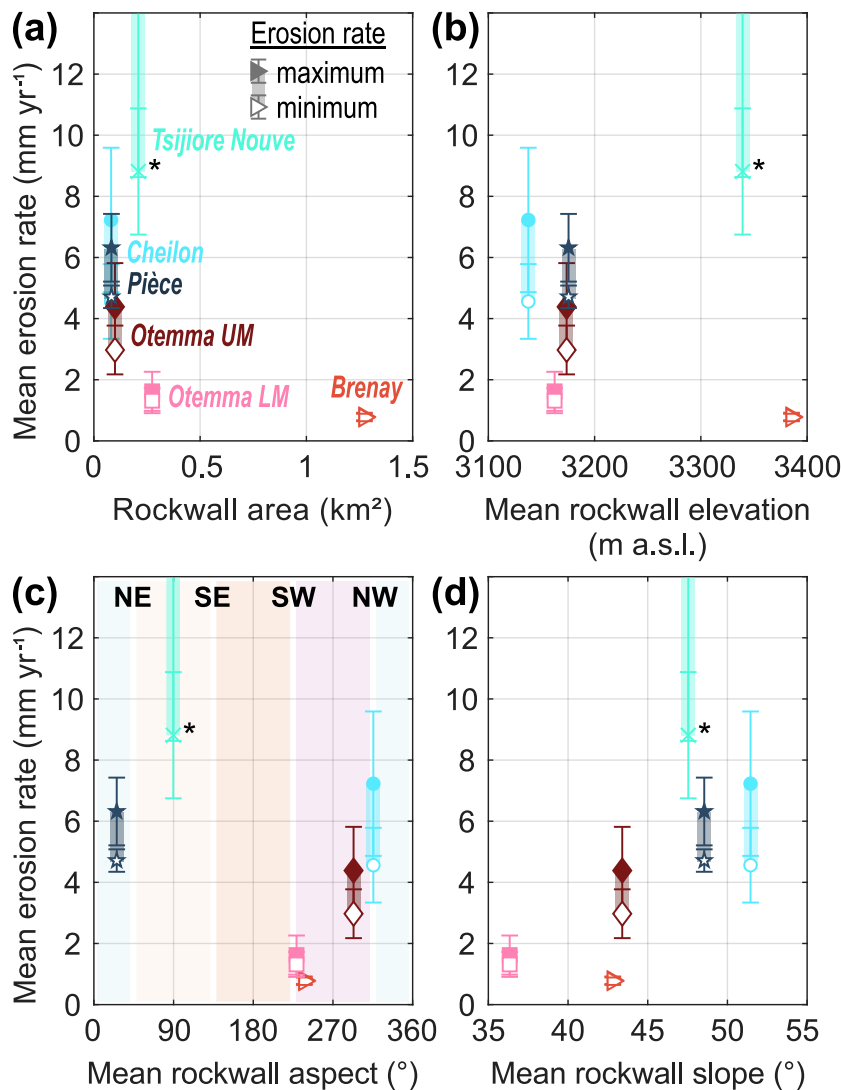


**Figure 3.7:** Comparison of apparent mean rockwall erosion rates with respect to (a) area, (b) mean elevation, (c) mean aspect, and (d) mean slope of the 1973 exposed source rockwalls. Apparent mean erosion rates ( $\pm 1\sigma$ ) are depicted as shaded ranges from minimum (uncorrected) to maximum (transport-corrected) estimates. For comparison, mean erosion rates here include only samples associated with the recent deglaciation period (Figure 3.5) but exclude samples from the Little Ice Age (O/UM6-9). The high-concentration outlier at Glacier d’Otemma (O/UM4, Figure 3.5) is also excluded but would not change the overall pattern if included. Note that mean erosion rates at Glacier de Tsijiore Nouve (\*) should be treated with caution and are likely overestimated due to an unquantified subglacial bias (see Section 3.5.1) and that Glacier de Cheilon sample C5 was excluded from the maximum estimate due to its unreasonably high erosion rate (see Section 3.5.1).

(i) The larger a source area, the more likely it is to capture and average a variety of erosive events. In smaller areas, however, large individual events may represent a larger portion of the total area and may result in overall higher erosion rates. Nevertheless, recent rockfalls in the Pigne d’Arolla massif seem small enough (Figure 3.6) not to dominate an entire area or sample. According to studies that examine the size of recent rockfalls in the Alps, large-volume rockfalls of 100 to 1000 m<sup>3</sup> are rare, though measured over short recent time periods (e.g., Strunden *et al.*, 2015; Hartmeyer *et al.*, 2020a), and would still only represent a fraction of our source rockwall areas (Table 3.3). Moreover, we could not delineate massive deposits of debris instantly released onto the ice on any of the orthoimages of the last ~40 years (Swisstopo, 2022) that we used for our boulder tracking.

(ii) Erosion is typically considered a slope-dependent process (Gilbert, 1877). According to nonlinear transport laws, erosion rates linearly increase with steepening hillslopes at shallow gradients but rapidly increase when reaching a critical hillslope angle (e.g., Roering *et al.*, 1999, 2001). This positive correlation has been widely recognized across fluvial landscapes, where catchment-wide erosion rates derived from cosmogenic nuclides suggest a broad linear trend up to a critical angle, often around 30° (e.g., Granger *et al.*, 1996; Binnie *et al.*, 2007; Ouimet *et al.*, 2009; DiBiase *et al.*, 2012; Delunel *et al.*, 2020). Ice-free rockwalls in glacial landscapes,

however, are much steeper and considered to be at their threshold angle (Scherler, 2014), and a similarly clear correlation may be complicated by the stochastic nature of rockfalls. Still, our erosion rate estimates suggest a positive correlation with rockwall slope in the Pigne d’Arolla massif, as do erosion rates from rockwalls flanking the Mer de Glace in the Mont Blanc massif (Lehmann *et al.*, 2020).

(iii) In alpine landscapes, spatial variability in rockwall stability and erosion is often suggested to be temperature-driven (e.g., Sass, 2005; Gruber & Haeberli, 2007; Hales & Roering, 2009; Delunel *et al.*, 2010; Mair *et al.*, 2020). At north faces, higher rockfall activity has been associated with higher moisture supply and deeper continued freezing, favouring damage by frost on shaded versus sunny faces (Coutard & Francou, 1989; Sass, 2005). In addition, recent rockwall destabilization has also been related to climate-induced permafrost degradation (Gruber & Haeberli, 2007), with thaw anomalies and rockfall activity appearing to be particularly pronounced at north faces, which are accustomed to a lower inter-annual thawing depth variability due to less direct solar radiation (Gruber *et al.*, 2004; Sass, 2010). Furthermore, frost-cracking models predict rockwall erosion to be higher where rockwalls reach into the frost-cracking window, an elevation-dependent temperature range of high frost-cracking efficiency (e.g., Walder & Hallet, 1985; Anderson, 1998; Hales & Roering, 2007), typically near the base of steep rockwalls (Hales & Roering, 2005; Sanders *et al.*, 2012; Scherler, 2014). Overall higher apparent rockwall erosion rates at north faces in the Pigne d’Arolla massif could hence also be related to distinct aspect-related temperature conditions. Permafrost is still most extensive at the shaded north faces of the ridgeline (**Figure B6**; BAFU, 2005) and probably more susceptible to post-LIA warming than the discontinuous permafrost occurrence to the south. Moreover, where rockwall base elevations are similar (~3000 m at all sites except Tsijiore Nouve, **Figure 3.1b**), temperature conditions at north faces may be more favourable for frost cracking. It is noteworthy that, although Brenay rockwalls partially also face northwest, erosion rate estimates are much lower than at the other north-facing sites. Here, elevation could play a role as the northwest faces at Brenay are located high (3400-3700 m; **Figure 3.1b**) and may experience less permafrost degradation and/or different altitudinal controls on frost cracking compared to the other slightly lower north-facing sites (3000-3400 m).

Based on the above assessments, we do not expect spatial trends in rockwall erosion among our study sites to be dominated by an area effect. Rather, higher mean apparent erosion rates at steeper northwest-facing rockwalls may indicate a potential slope and aspect control, which could be related to distinct temperature-driven destabilization conditions. Yet, as our studied sites are overall very steep and cover only a narrow range of slope gradients, it is not easy to resolve slope dependency in rockwall erosion more precisely or even to generalize patterns. Moreover, it is difficult to judge whether the aspect-related differences in permafrost and frost-cracking conditions suggested above were already as pronounced at the estimated time of rockwall erosion. Future studies following this approach may therefore examine datasets that cover a wider range of rockwall gradients and incorporate temporal records of land surface temperatures or frost-cracking models to further assess the role of aspect and temperature.

### 3.6 Conclusions

We derived apparent rockwall erosion rates around Pigne d’Arolla in Switzerland from [ $^{10}\text{Be}$ ] in medial moraine debris at five nearby valley glaciers. The total of six medial moraine records largely span 0.6 to 10.0  $\text{mm yr}^{-1}$  and cover the recent deglaciation period (Glacier du Brenay, Glacier de Cheilon, Glacier de Pièce, Glacier de Tsijiore Nouve), back to the end of the LIA (Glacier d’Otemma). Our analyses lead us to the following main findings.

(i) Although glacial landscapes typically erode stochastically, which could make random variability along temporal records likely, our medial moraine [ $^{10}\text{Be}$ ] records are temporally consistent for the deglaciation period and decrease systematically from the end of the LIA towards deglaciation. Whereas large-volume rockfalls are typically identifiable by the additional volume of rock delivered to the glacier, the morphology of the studied medial moraines varies only gradually and is more likely to reflect gradual variations in ice dynamics or rockwall erosion. This suggests that the medial moraines from the Pigne d’Arolla massif indeed act as archives of rockwall erosion.

(ii) Post-depositional debris exposure during downglacier transport, ice cover changes across deglaciating rockwalls, and subglacially derived material introduce uncertainties that complicate the conversion of measured medial moraine [ $^{10}\text{Be}$ ] to rockwall erosion rates directly and require high-resolution datasets on the temporal evolution of the studied glaciers. For the majority of samples, the transport corrections derived from our boulder-tracking velocities and debris trajectory modelling seem reasonable when compared to historical photographs. They are overall negligible where the measured [ $^{10}\text{Be}$ ] values are high but more significant for lower values, yet without affecting any observed systematic consistency or variability. Quantifying ice cover changes across the source rockwalls indicates that source area changes have been small, except for one site. Yet, the contribution of recently deglaciated bedrock and/or subglacially derived material remains difficult to quantify, may affect some of the sites, and requires further analysis.

(iii) Temporally, [ $^{10}\text{Be}$ ] records at Glacier du Brenay, Glacier de Cheilon, Glacier de Pièce, and Glacier de Tsijiore Nouve appear comparatively stable over the last  $\sim 100$  years, as do their debris source areas for the estimated time of rockwall erosion. This may indicate that source area changes, which are reflected in the decrease in [ $^{10}\text{Be}$ ] in the  $\sim 200$ -year-long record from the Glacier d’Otemma, are transient processes related to the transition from the LIA to the following deglaciation period. The absence of similar trends at the other sites may suggest that changes in source area either play a minor role or have stabilized again after a short time period.

(iv) The choice of the small and localized massif around Pigne d’Arolla, with its similar rockwall lithology, facilitates the relative spatial comparison of its debris source areas without major bias arising from comparing sites with different tectonic or climatic settings or pronounced lithological differences. Around Pigne d’Arolla, higher mean apparent erosion rates at overall steeper north-facing compared to shallower southwest-facing rockwalls indicate a potential slope and aspect control on our records and may be related to rockwall erosion and destabilization affected by temperature conditions.

### **3.7 Data availability**

The cosmogenic nuclide dataset and derived glacier surface velocities of this study are available in the accompanying data publication: Wetterauer and Scherler (2023b) at <https://doi.org/10.5880/GFZ.3.3.2023.002>. These data are freely available under the Creative Commons Attribution 4.0 International (CC BY 4.0) open-access license at GFZ Data Services. When using these data please cite this study.

### **3.8 Acknowledgements**

This research received funding from the European Research Council (ERC) under the European Union's Horizon 2020 research and innovation program (grant no. 759639). We are grateful to Leif Anderson and Deniz Gök for support during sampling and fieldwork. Stefan Heinze and Steven Binnie from the University of Cologne are thanked for performing AMS measurements. Hella Wittmann, Cathrin Schulz, and Kristina Krüger are thanked for their help and advice in sample preparation. We also thank the editors and the two reviewers, Neil Glasser and one anonymous referee, for their constructive feedback on the paper.

# Two different histories of headwall erosion at Grosser Aletschgletscher, Switzerland: first insights from medial moraine cosmogenic nuclides

*Katharina Wetterauer & Dirk Scherler*

## Abstract

Rates of debris supply to glaciers are still poorly constrained. In particular, the variability with which debris delivering rockwalls erode through space and time is not well understood, limiting the simulation of debris cover evolution in future glacier retreat scenarios. Yet, increasing supraglacial debris cover can significantly reduce glacial melt and may slow down glacier retreat. Lately, downglacier records of *in situ*-produced cosmogenic  $^{10}\text{Be}$  concentrations ( $[^{10}\text{Be}]$ ) in medial moraine debris have revealed promising systematics to study spatiotemporal changes in headwall erosion above glaciers. So far, however, studies predominately focused on small-scale glacier catchments and short-length medial moraines. Here, we present 25 new  $[^{10}\text{Be}]$  sampled along the Kranzberg and Trugberg medial moraine of Grosser Aletschgletscher in Switzerland to investigate headwall erosion at larger scale at two separate but nearby debris source areas. We further present additional *in situ*-produced cosmogenic  $^{14}\text{C}$  concentrations ( $[^{14}\text{C}]$ ) measured for five samples from the Trugberg medial moraine to resolve erosional transience by paired  $^{14}\text{C}/^{10}\text{Be}$  analysis. Preliminary analyses on minimum headwall erosion rates at Kranzberg and Trugberg (i.e.,  $^{10}\text{Be}$ -derived erosion rate estimates that are uncorrected for post-depositional debris exposure) reveal two contrasting histories of headwall erosion at Grosser Aletschgletscher. At Trugberg, erosion rate estimates peak at up to  $5 \text{ mm yr}^{-1}$ , in line with increased  $^{14}\text{C}/^{10}\text{Be}$  ratios, indicating a pulse in headwall erosion. This could relate to a pronounced ice surface lowering across the headwalls since the end of the Little Ice Age, possibly exposing highly erosive bedrock surfaces. At Kranzberg instead, consistently low erosion rate estimates  $<1 \text{ mm yr}^{-1}$  imply temporally stable headwall erosion, which may be due to major debris supply from headwalls that experienced comparatively less bedrock deglaciation. We conclude our preliminary studies by discussing further steps that we consider suitable to obtain additional information from this dataset on the origin of medial moraine debris and the control of its supply at Grosser Aletschgletscher, but which are not part of the present work.

**This chapter is in manuscript preparation**

## 4.1 Introduction

Where rockwalls deposit debris onto glacier surfaces, changes in rockwall erosion and in the evolution of adjacent glaciers due to climate change are likely linked (Scherler & Egholm, 2020). Since the end of the Little Ice Age (LIA) around 1850, glacierized areas in the European Alps experience pronounced deglaciation (Haeberli & Hoelzle, 1995; Haeberli & Beniston, 1998). Along with rising temperatures, the shrinkage of glacier area accelerates (e.g., Zemp *et al.*, 2008, 2019; Huss, 2012) and mountain permafrost degrades (e.g., Gruber & Haeberli, 2007). Associated glacial uncovering and unloading as well as changing permafrost and frost-damage conditions are thought to increasingly destabilize rockwalls next to glaciers (e.g., Wegmann *et al.*, 1998; Kenner *et al.*, 2011; Raveland & Deline, 2011; Fischer *et al.*, 2012; Huggel *et al.*, 2012; Hartmeyer *et al.*, 2020a). Changing debris supply rates to glaciers will in turn modify glacial debris cover (Scherler & Egholm, 2020), where ice ablation is reduced as debris cover thickens (e.g., Østrem, 1959; Mattson *et al.*, 1993; Kayastha *et al.*, 2000).

Future projections of the largest glacier in the European Alps - Grosser Aletschgletscher in Switzerland - suggest that under recent climate scenarios the glacier's volume and length could at least be half of the present values by the end of the 21st century (Jouvet *et al.*, 2011; Jouvet & Huss, 2019). Simulations that integrate the insulating effect of glacial debris cover with a simple debris development model also suggest that supraglacial debris, however, may significantly retard the retreat of Grosser Aletschgletscher (Jouvet *et al.*, 2011). Yet, accounting for spatiotemporal debris cover changes in glacier models often involves assumptions on how much debris is supplied to glacier surfaces by the adjacent rockwalls. The number of field-based quantifications of debris supply rates, respectively of rockwall erosion rates, is still small. In particular, resolving the temporal evolution of headwall erosion (i.e., rockwall erosion at the head of valley glaciers) under changing climate since the end of the LIA is still challenging (Scherler & Egholm, 2020; Wetterauer *et al.*, 2022a; Wetterauer & Scherler, 2023a).

Lately, assessing headwall erosion rates from concentrations of *in situ*-produced cosmogenic  $^{10}\text{Be}$  (integrating over  $>10^2$ - $10^4$  years) in medial moraine debris through downglacier-interval-sampling has shown the potential to resolve systematic temporal changes in debris supply rates archived within the downglacier aging moraine deposits (Ward & Anderson, 2011; Scherler & Egholm, 2020; Wetterauer *et al.*, 2022a; Wetterauer & Scherler, 2023a). For hitherto comparatively small ( $<16\text{ km}^2$ ) glacier catchments, one in the Himalayas (Scherler & Egholm, 2020) and five in the Swiss Alps (Wetterauer *et al.*, 2022a; Wetterauer & Scherler, 2023a), downglacier records of medial moraine  $^{10}\text{Be}$  concentrations either suggest a systematic acceleration of erosion towards the present or fairly stable erosion rates through time. However, recent medial moraine debris on Swiss glaciers appears to have been deposited over relatively short time periods since the end of the LIA ( $\sim 200$  years), and thus in a landscape changing under deglaciation. Yet, applying single nuclide analyses commonly requires steady-state conditions (Lal, 1991). To assess erosion transience in landscapes instead, few studies have applied paired *in situ*  $^{14}\text{C}/^{10}\text{Be}$  nuclide analysis (e.g., Skov *et al.*, 2019; Hippe *et al.*, 2021), using the combination of the different decay time times of the short-lived  $^{14}\text{C}$  and long-lived  $^{10}\text{Be}$  to resolve short-term changes in erosion rates (Hippe, 2017; Mudd, 2017).

This study combines downglacier medial moraine  $^{10}\text{Be}$  and  $^{14}\text{C}$  concentrations ( $[^{10}\text{Be}]$  and  $[^{14}\text{C}]$ , atoms  $\text{g}^{-1}$ ) at Grosser Aletschgletscher in Switzerland to derive headwall erosion rates for a well-monitored large-scale glacier catchment, and in the hope to resolve longer time scales. As a first part of the still ongoing study, we here present and compare downglacier  $[^{10}\text{Be}]$  measured along the parallel Kranzberg and Trugberg medial moraine at Grosser Aletschgletscher. With a total of 25 samples, the two new records are the longest downglacier medial moraine  $[^{10}\text{Be}]$  records so far and enable to study headwall erosion at the two separate debris source areas Kranzberg and Trugberg at high resolution. For five Trugberg medial moraine samples, additional  $[^{14}\text{C}]$  were quantified to evaluate for the first time in this context combined  $^{14}\text{C}/^{10}\text{Be}$  ratios as indicator for recent short-term erosion rate changes. Preliminary minimum headwall erosion rate estimates (i.e., estimates derived from the measured  $[^{10}\text{Be}]$ , but uncorrected for  $^{10}\text{Be}$  accumulation during downglacier debris transport) are considered together with topographic analyses for Kranzberg and Trugberg since 1850 to assess the evolution of the debris source areas with recent deglaciation. As this work is in progress, we conclude with an outlook on upcoming analyses to verify our preliminary explanations.

## 4.2 Study area

### 4.2.1 Grosser Aletschgletscher

The Grosser Aletschgletscher in the Swiss Canton of Valais (**Figure 4.1a**) is the longest and largest valley glacier in the European Alps, measuring 23.5 km in length and 78.5 km<sup>2</sup> in area (data from 2017; Linsbauer *et al.*, 2021). It is located within the Bernese Alps, which are part of the crystalline Aare Massif. Framed by three of their highest peaks, the Aletschhorn (4190 m; all elevations stated as metres above sea level), Jungfrau (4160 m), and Mönch (4110 m), the glacier extends south from about 4000 m elevation down to recently 1700 m. Grosser Aletschgletscher originates within three accumulation basins: the western Grosser Aletschfirn north of Aletschhorn and south of Gletscherhorn (3980 m), the central Jungfraufirn southeast of Jungfrau and southwest of Mönch, and the eastern Ewigschneefeld southeast of Mönch. The three tributaries converge at the Konkordiaplatz, which is a zone of confluence at approximately 2700 m elevation where the present glacier still reaches maximum ice thicknesses of almost 800 m (Grab *et al.*, 2021; Jouvét, 2023). Downglacier of Konkordiaplatz, a ~12 km long and >1 km wide main trunk continues southeast, before bending and terminating in a large southwest curve towards the Rhône valley. At present, the glacier still flows over wide areas at fast velocities of 100 to 150 m yr<sup>-1</sup> and exceeds even 200 m yr<sup>-1</sup> in Ewigschneefeld (Millan *et al.*, 2022; Jouvét, 2023). Over the last two decades, the equilibrium line altitude (ELA) varied between 2900 and 3200 m elevation (GLAMOS, 2021b).

Throughout the LIA, Grosser Aletschgletscher experienced three periods of advance: in the 1370s, the 1670s, and around 1860. Since its last maximum extent at the end of the LIA (**Figure 4.1a**), the glacier has been continuously receding (Holzhauser *et al.*, 2005). Between 1870 and 2020, the terminus retreated by 3.4 km (GLAMOS, 2021a), and between 1880 and 2017, the geodetic glacier-wide mass balance decreased from -0.3 to -1.3 m water equivalent (w.e.) yr<sup>-1</sup> (GLAMOS, 2021c). In the 20th century, the ice surface at Konkordiaplatz lowered

by ~100 m (Wegmann *et al.*, 1998) and by the end of the 21st century, the glacier is projected to lose 60% or more of its ice volume (Jouvet *et al.*, 2011; Jouvet & Huss, 2019).

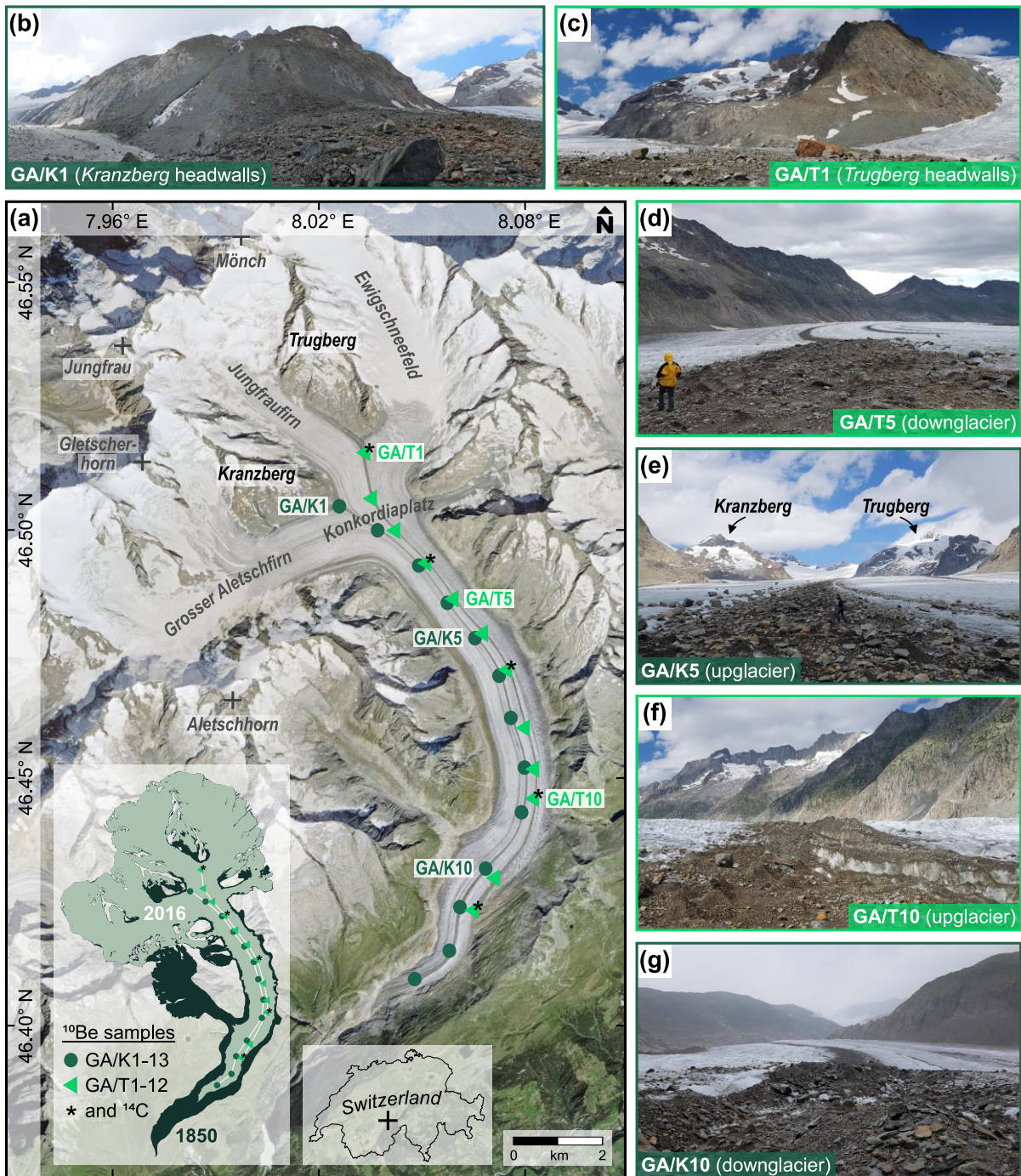


**Figure 4.1:** Grosser Aletschgletscher, Switzerland. (a) Orthoimage from 2020 showing the glacier catchment with the 25 sample locations at the Kranzberg (GA/K) and Trugberg (GA/T) medial moraine. Sample locations to which one of the field photographs depicted in (b-g) belongs are labelled. The left inset outlines the changes between the extent of the glacier in 1850 (at the end of the Little Ice Age) and in 2016, as well as the associated changes in ice cover across the two debris source areas Kranzberg and Trugberg (orthoimage by Swisstopo, 2023; 2016 and 1850 glacier extent after Linsbauer *et al.*, 2021, and Maisch *et al.*, 2000). (b-g) Field photographs from (b,e,g) Kranzberg and (c,d,f) Trugberg medial moraine as well as from their debris source areas. The sample locations where the respective photographs were taken and the direction of view as up- or downglacier are indicated.

## 4.2.2 Kranzberg and Trugberg medial moraine

At present, debris cover on Grosser Aletschgletscher accounts for 4% of the surface area (Jouvet *et al.*, 2011). Due to the confluence of the three glacier tributaries, two pronounced medial moraines form at Konkordiaplatz: the Kranzberg and Trugberg medial moraine (**Figure 4.1**). Running parallel in the centre of the glacier main trunk and more than 200 m apart from each other, they extend down to the terminus. For most of their downglacier distance, they are 350 m or more from the respective glacier margin and valley sidewalls. Along both medial moraines, crevassed sections alternate with crevasse-free sections.

The Kranzberg medial moraine is the more western medial moraine of Grosser Aletschgletscher (**Figure 4.1a,b,e,g**), forming at the confluence of Grosser Aletschfirn and Jungfraufirn at 2700 m elevation. Over a length of 14.3 km it extends down to the glacier terminus at 1700 m elevation. It receives debris from the headwalls of the Kranzberg (3740 m; **Figure 4.1a,b**), an east-southeast running and 4.2 km long mountain ridge between the two glacier tributaries. These headwalls tower up to ~700 m above the glacier surface and are composed of gneisses and shists from the Altkristallin of the Aare Massif. While the northeast faces of Kranzberg are still largely covered by ice, the bedrock of the south faces is largely exposed. Recent debris is deposited both in the glacier's accumulation and ablation zone.

The Trugberg medial moraine is the more eastern medial moraine of Grosser Aletschgletscher (**Figure 4.1a,c,d,f**). It originates at the confluence of Jungfraufirn and Ewigschneefeld at 2740 m elevation and continues for 12.5 km downglacier to 2000 m elevation. The moraine is supplied by the headwalls of the Trugberg (3930 m; **Figure 4.1a,c**), a south-southeast running mountain ridge that separates the two glacier tributaries over a length of also 4.2 km. The Trugberg headwalls are up to ~600 m high and composed of the same gneiss and shist complex. The east faces are still fully covered by glacier ice, but large areas at south to west faces are recently ice-free. Debris deposition occurs both in the accumulation and ablation zone (recent descriptions in this subchapter refer to the Swisstopo online map viewer, Swisstopo, 2023).

## 4.3 Material and methods

### 4.3.1 Sample collection and processing

In August 2019, we collected a total of 25 medial moraine debris samples from Grosser Aletschgletscher (**Table 4.1**, **Figure 4.1**): 13 samples from the Kranzberg medial moraine (GA/K1-13) along a 13.0 km long profile and 12 samples from the Trugberg medial moraine (GA/T1-12) along an 11.8 km long profile. At both sites, samples were taken every ~1 km in ascending order downglacier and at approximately the same elevation. Each sample is an amalgamation of clasts from coarse sands to pebbles (~1-30 mm) collected randomly over surface areas that span a moraine length of 10-30 m and the entire moraine width. In 2019 and along the first ~9 km of the Kranzberg and Trugberg profile, the moraine topography was flat (<1 m) with relative constant moraine widths of 10-20 m and 20-30 m, respectively (e.g., **Figure 4.1b-f**). Towards the terminus, where the glacier's main trunk narrows, both moraines gained a wave-like relief (e.g., **Figure 4.1g**), in parts up to ~5 m high, and widened up to ~70 m.

Open crevasses were cutting the moraines predominately profile-perpendicular at sample locations immediately downglacier the confluence at Konkordiaplatz and below 2300 m elevation, where the glacier bends and narrows towards the southwest (e.g., **Figure 4.1f**). Due to a high crevasse density at ~2200 m elevation in 2019, the sampling interval could not be adhered to between GA/K9 and GAK/10, respectively GA/T10 and GA/T11. Lateral debris contribution from the glacier margins to the medial moraines was not observed.

Cosmogenic  $^{10}\text{Be}$  analysis was performed on all GA/K and GA/T samples (**Table 4.1**), while  $^{14}\text{C}$  analysis was applied for the first time on five GA/T samples at every third profile kilometre (**Table 4.2**). For both analyses, quartz separates from a grain size fraction of 1-16 mm were purified at the Helmholtz Laboratory for the Geochemistry of the Earth Surface (HELGES) at GFZ Potsdam, Germany, by crushing, magnetic separation, hydrochloric acid leaches, froth flotation (skipped for  $^{14}\text{C}$  quartz separates as it introduces contaminant  $^{14}\text{C}$ ; Nichols & Goehring, 2019), as well as repeatedly hydrofluoric acid and orthophosphoric acid leaches. *In situ*-produced  $^{10}\text{Be}$  was extracted from ~30-40 g of pure quartz (spiked with 0.2 g 770 ppm  $^9\text{Be}$  carrier) at HELGES by quartz decomposition in hydrofluoric acid, ion exchange chromatography, alkaline precipitation, and oxidation (e.g., von Blanckenburg *et al.*, 2004).  $^{10}\text{Be}/^9\text{Be}$  ratios (**Table 4.1**) were measured at the accelerator mass spectrometer (AMS) at the University of Cologne, Germany (Dewald *et al.*, 2013), relative to standards KN01-6-2 and KN01-5-3 (nominal  $^{10}\text{Be}/^9\text{Be}$  ratios:  $5.35 \times 10^{-13}$  and  $6.32 \times 10^{-12}$ , respectively), and converted into  $[\text{}^{10}\text{Be}]_{\text{measured}}$  correcting for the corresponding process blank.

**Table 4.1:** Medial moraine samples from Grosser Aletschgletscher and AMS  $^{10}\text{Be}$  data.

Sample	Latitude (°N)	Longitude (°E)	Elevation (m a.s.l.)	Distance <sup>b</sup> (m)	Qtz mass (g)	AMS $^{10}\text{Be}/^9\text{Be}$ $\times 10^{-14} \pm 1\sigma$	Blank <sup>c</sup>	$[\text{}^{10}\text{Be}]_{\text{measured}}$ $\times 10^4 \pm 1\sigma$ (atoms $\text{g}^{-1}$ )
<i>Kranzberg medial moraine</i>								
GA/K1	46.5040	8.0253	2693	0	40.61	21.68 ± 0.87	blk1	5.41 ± 0.23
GA/K2	46.4991	8.0364	2667	1010	40.90	22.01 ± 0.86	blk1	5.46 ± 0.22
GA/K3	46.4920	8.0483	2610	2221	41.09	24.27 ± 0.94	blk1	5.90 ± 0.24
GA/K4	46.4844	8.0565	2533	3275	40.69	21.32 ± 0.84	blk1	5.24 ± 0.21
GA/K5	46.4772	8.0644	2457	4278	40.18	19.01 ± 0.75	blk1	4.72 ± 0.19
GA/K6	46.4696	8.0714	2414	5278	40.87	16.05 ± 0.66	blk1	3.96 ± 0.17
GA/K7	46.4611	8.0747	2366	6258	41.09	22.30 ± 1.03	blk1	5.49 ± 0.26
GA/K8	46.4510	8.0786	2296	7413	41.15	19.95 ± 0.85	blk1	4.90 ± 0.22
GA/K9	46.4420	8.0776	2246	8417	40.44	17.69 ± 0.78	blk1	4.41 ± 0.20
GA/K10	46.4307	8.0671	2142	9912	41.13	21.76 ± 0.92	blk1	5.36 ± 0.24
GA/K11	46.4230	8.0595	2054	10950	40.50	17.47 ± 0.73	blk1	4.35 ± 0.19
GA/K12	46.4142	8.0563	1944	11955	40.33	17.30 ± 0.73	blk1	4.33 ± 0.19
GA/K13	46.4086	8.0462	1839	12955	40.91	13.95 ± 0.77	blk1	3.44 ± 0.20
<i>Trugberg medial moraine</i>								
GA/T1 <sup>a</sup>	46.5148	8.0330	2705	0	29.18	5.80 ± 0.33	blk2	1.98 ± 0.12
GA/T2	46.5055	8.0348	2691	1041	32.17	5.76 ± 0.35	blk2	1.78 ± 0.12
GA/T3	46.4990	8.0415	2655	1927	29.19	2.19 ± 0.19	blk2	0.71 ± 0.07
GA/T4 <sup>a</sup>	46.4925	8.0505	2605	2932	29.51	2.63 ± 0.20	blk2	0.86 ± 0.07
GA/T5	46.4852	8.0583	2538	3938	29.65	3.24 ± 0.24	blk2	1.07 ± 0.09
GA/T6	46.4782	8.0668	2448	4955	28.97	2.16 ± 0.17	blk2	0.70 ± 0.07
GA/T7 <sup>a</sup>	46.4708	8.0738	2415	5934	29.21	1.37 ± 0.16	blk2	0.43 ± 0.06
GA/T8	46.4590	8.0788	2347	7296	28.81	3.57 ± 0.25	blk2	1.22 ± 0.09
GA/T9	46.4507	8.0815	2296	8242	31.49	8.12 ± 0.44	blk2	2.59 ± 0.15
GA/T10 <sup>a</sup>	46.4448	8.0813	2262	8900	29.61	4.50 ± 0.30	blk2	1.51 ± 0.11
GA/T11	46.4288	8.0698	2136	10882	27.19	8.17 ± 0.42	blk2	3.03 ± 0.16
GA/T12 <sup>a</sup>	46.4223	8.0635	2069	11751	34.53	14.43 ± 0.61	blk2	4.24 ± 0.19

<sup>a</sup> GA/T samples with additional  $^{14}\text{C}$  measurement (**Table 4.2**). <sup>b</sup> Downglacier distance from the uppermost sample of the respective medial moraine. <sup>c</sup> Process blank used to correct respective sample batches, with corresponding AMS  $^{10}\text{Be}/^9\text{Be}$  ratios of blk1 =  $1.95 \times 10^{-15}$  and blk2 =  $1.59 \times 10^{-15}$ .

*In situ*-produced  $^{14}\text{C}$  was extracted from ~4-5 g of pure quartz at ETH Zürich, Switzerland, using the *in situ*  $^{14}\text{C}$  extraction line (Hippe *et al.*, 2009; Lupker *et al.*, 2019).  $^{14}\text{C}/^{12}\text{C}$  ratios (Table 4.2) were measured with the gas ion source of the MICADAS AMS system at ETH Zürich (Ruff *et al.*, 2007; Synal *et al.*, 2007; Wacker *et al.*, 2010), and converted into  $[\text{}^{14}\text{C}]_{\text{measured}}$  correcting for a mean process blank (Hippe & Lifton, 2014).

**Table 4.2:** AMS  $^{14}\text{C}$  data and derived  $^{14}\text{C}/^{10}\text{Be}$  ratios.

Sample	Qtz mass (g)	CO <sub>2</sub> yield ( $\mu\text{g}$ )	Fraction modern $\text{F}^{14}\text{C}^{\text{a}}$ $\pm 1\sigma$	$\delta^{13}\text{C}$ (‰)	$^{14}\text{C}/^{12}\text{C}_{\text{total}}^{\text{b}}$ $\times 10^{-14}$	$^{14}\text{C}_{\text{total}}^{\text{b,c}}$ $\times 10^4 \pm 1\sigma$ (atoms)	$[\text{}^{14}\text{C}]_{\text{measured}}$ $\times 10^4 \pm 1\sigma$ (atoms $\text{g}^{-1}$ )	$^{14}\text{C}/^{10}\text{Be}$
<i>Trugberg medial moraine</i>								
GA/T1	4.62	60.22	0.078 $\pm$ 0.002	-15.77	9.15 $\pm$ 0.23	26.34 $\pm$ 0.97	5.70 $\pm$ 0.21	2.87
GA/T4	4.93	65.17	0.034 $\pm$ 0.001	-15.51	3.95 $\pm$ 0.17	11.61 $\pm$ 0.89	2.36 $\pm$ 0.18	2.75
GA/T7	4.18	68.87	0.022 $\pm$ 0.001	-18.18	2.58 $\pm$ 0.15	7.61 $\pm$ 0.86	1.82 $\pm$ 0.21	4.27
GA/T10	4.40	66.05	0.045 $\pm$ 0.002	-17.37	5.23 $\pm$ 0.19	16.02 $\pm$ 0.94	3.64 $\pm$ 0.21	2.41
GA/T12	4.65	117.66	0.046 $\pm$ 0.002	-21.18	5.28 $\pm$ 0.19	29.86 $\pm$ 1.30	6.43 $\pm$ 0.28	1.51

<sup>a</sup> Normalized to  $\delta^{13}\text{C}$  of -25‰ VPDB and AD 1950. <sup>b</sup> Calculated according to the equations in Hippe and Lifton (2014). <sup>c</sup> Corrected for the mean process blank of  $1.30 \pm 0.69 \times 10^4$   $^{14}\text{C}$  atoms from 9 measurements between February-May 2022.

### 4.3.2 Principles of paired $^{14}\text{C}/^{10}\text{Be}$ analysis

Recently, paired *in situ*  $^{14}\text{C}/^{10}\text{Be}$  analysis is used more frequently to evaluate the erosional transience of landscapes (e.g., Hippe, 2017; Mudd, 2017). The emerging application is based on the sensitivity of  $^{14}\text{C}$  to recent short-term changes in surface erosion. Due to the significantly faster decay of  $^{14}\text{C}$  (half-life 5.7 kyr) compared to  $^{10}\text{Be}$  (half-life 1.4 Myr; Chmeleff *et al.*, 2010; Korschinek *et al.*, 2010), the concentrations of the two nuclides, respectively their ratio, evolve differently as a function of exposure changes and differential decay (Hippe, 2017; Mudd, 2017). At complete exposure, the ratio of the spallogenic production rate (St scaling) at sea level high latitude (SLHL) of  $^{14}\text{C}$  (12.24 atoms  $\text{g}^{-1} \text{yr}^{-1}$ ) to  $^{10}\text{Be}$  (4.01 atoms  $\text{g}^{-1} \text{yr}^{-1}$ ) in quartz approximates ~3 at the bedrock surface (Borchers *et al.*, 2016). Both nuclides are produced predominantly through spallogenic reaction processes and to a lesser extent by muons. However, whereas muonic contribution to the total  $^{10}\text{Be}$  surface production in quartz accounts for <2% (Balco, 2017), muonic contribution to total  $^{14}\text{C}$  surface production is at ~20% (Lupker *et al.*, 2015). Therefore, the production of  $^{14}\text{C}$  below the subsurface by deeper penetrating muons is relatively higher than that of  $^{10}\text{Be}$  and the  $^{14}\text{C}/^{10}\text{Be}$  ratio changes with depth into the bedrock (Lupker *et al.*, 2015).

At steadily eroding surfaces under constant conditions, the surficial  $^{14}\text{C}/^{10}\text{Be}$  ratio is expected to remain the same, its magnitude defined by the strength of erosion. Where bedrock erodes slowly (<0.1 mm  $\text{yr}^{-1}$ ), the  $^{14}\text{C}/^{10}\text{Be}$  ratio is lower than the surface production rate ratio due to the comparatively fast decay of  $^{14}\text{C}$ . Where bedrock erodes fast (>10 mm  $\text{yr}^{-1}$ ), the  $^{14}\text{C}/^{10}\text{Be}$  ratio is higher than the surface production rate ratio, as bedrock enriched in  $^{14}\text{C}$  by muogenic production at depth is quickly advected to the surface (cf. Figure 1b in Dennis & Scherler, 2022). Perturbations to uniform erosion, however, will result in  $^{14}\text{C}/^{10}\text{Be}$  ratios deviating from the ratio that is expected under a constant erosion rate. This offset is expected to reflect the depth of erosion as a result of depth-dependent nuclide production (cf. Figure 1b in Dennis & Scherler, 2022). With increasing depth into the subsurface, the  $^{14}\text{C}/^{10}\text{Be}$  ratio initially rises above the surficial ratio for the first ~2 m depth, before decreasing again towards greater depth.

If bedrock was constantly exposed, a  $^{14}\text{C}/^{10}\text{Be}$  ratio higher than the one expected under uniform erosion would therefore imply deeper bedrock excavation due to faster erosion. Consequently, with rapid changes in erosion, bedrock surface  $^{14}\text{C}/^{10}\text{Be}$  ratios will fluctuate with time as a function of the magnitude and frequency of change, and because  $^{14}\text{C}$  responds more rapidly to erosional changes than does  $^{10}\text{Be}$  (cf. Figure 9b in Dennis & Scherler, 2022). The type of deviation may be indicative for the style of erosion, where for instance non-uniform random offsets may indicate stochastic erosion events. Deviations in  $^{14}\text{C}/^{10}\text{Be}$  records therefore seem promising to detect short-term erosional transience (Dennis & Scherler, 2022).

### 4.3.3 Topographic analysis

Topographic analyses across the source headwalls at Kranzberg and Trugberg were computed on a 30 m resolution digital elevation model (DEM, global raster dataset SRTM GL1; NASA Shuttle Radar Topography Mission SRTM, 2013). Based on a set of reconstructed glacier outlines, ice-free headwall outlines were defined for the years 2016 (Linsbauer *et al.*, 2021), 1973 (Müller *et al.*, 1976), and 1850 (Maisch *et al.*, 2000). For all three time slices, elevation, slope, aspect, and surface area (slope-corrected) were determined for each DEM pixel to assess the post-LIA evolution of both debris supply areas.

## 4.4 Results

### 4.4.1 Measured $^{10}\text{Be}$ and $^{14}\text{C}$ concentrations

The 25  $[^{10}\text{Be}]_{\text{measured}}$  from the two medial moraines of Grosser Aletschgletscher span between  $0.4 \times 10^4$  and  $5.9 \times 10^4$  atoms  $\text{g}^{-1}$  (**Table 4.1, Figure 4.2a**). For the Kranzberg medial moraine,  $[^{10}\text{Be}]_{\text{measured}}$  vary between  $3.4 \times 10^4$  and  $5.9 \times 10^4$  atoms  $\text{g}^{-1}$  and slightly decrease downglacier. For the Trugberg medial moraine,  $[^{10}\text{Be}]_{\text{measured}}$  are comparatively lower with  $0.4 \times 10^4$  to  $4.2 \times 10^4$  atoms  $\text{g}^{-1}$ . While concentrations are low in the upper half of the profile, they increase systematically downglacier (please note that preliminary minimum headwall erosion rates are derived in Section 4.5.1 in the following discussion).

The five  $[^{14}\text{C}]_{\text{measured}}$  from the Trugberg medial moraine span  $1.8 \times 10^4$  to  $6.4 \times 10^4$  atoms  $\text{g}^{-1}$  (**Table 4.2, Figure 4.2a**). Except for the first sample GA/T1,  $[^{14}\text{C}]_{\text{measured}}$  reflect the same systematic downglacier increase in concentration as indicated by  $[^{10}\text{Be}]_{\text{measured}}$ , although at overall higher concentrations and based on a lower sample-resolution. The resulting  $^{14}\text{C}/^{10}\text{Be}$  ratios increase from almost 3 for the uppermost deposits to  $\sim 4$  at the profile centre before decreasing down to 1.5 for the terminal deposits (**Table 4.2, Figure 4.2b**).

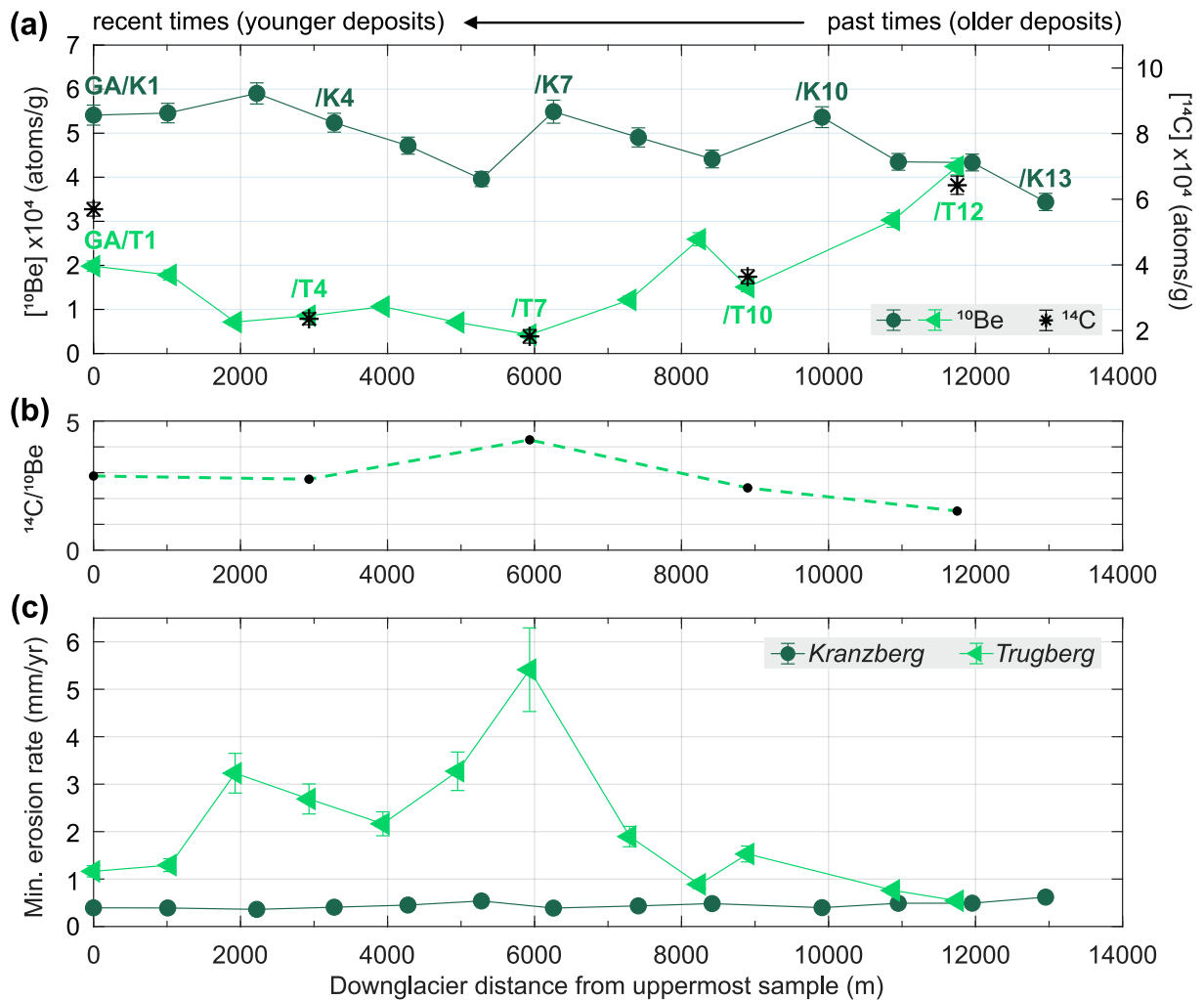


**Figure 4.2:**  $^{10}\text{Be}$  and  $^{14}\text{C}$  records along the Kranzberg and Trugberg medial moraine at Grosser Aletschgletscher. (a) Downglacier  $^{10}\text{Be}$ <sub>measured</sub> and  $^{14}\text{C}$ <sub>measured</sub> ( $\pm 1\sigma$  analytical error). With increasing downglacier distance, debris deposits are getting older. Note the different y axes of the respective nuclide. (b) Downglacier  $^{14}\text{C}/^{10}\text{Be}$  ratios based on the measured nuclide concentrations along the Trugberg medial moraine. (c) Preliminary downglacier erosion rate estimates. Note that these are minimum estimates based on  $^{10}\text{Be}$ <sub>measured</sub> and thus not yet corrected for post-depositional nuclide accumulation during downglacier transport. Preliminary calculations were carried out as described in Wetterauer *et al.* (2022a) and Wetterauer and Scherler (2023a). As previous studies suggest, the upcoming transport corrections will presumably lead to higher rate estimates, but preserve the overall downglacier patterns (Figure 3.5; Wetterauer & Scherler, 2023a).

#### 4.4.2 Debris source area characteristics

The two major debris source areas at Grosser Aletschgletscher, Kranzberg and Trugberg, morphologically differ. Recently, ice-free headwalls at Kranzberg cover an area of 3.8 km<sup>2</sup> at an average elevation of ~3100 m (Figure 4.3a). At a mean slope angle of 31° (Figure 4.3b) they predominately face southeast (Figure 4.3c). At Trugberg, ice-free headwalls measure 3.3 km<sup>2</sup> at an overall higher average elevation of ~3200 m (Figure 4.3a). The headwalls are inclined by 36° (Figure 4.3b) and are predominantly exposed southwest (Figure 4.3c). Since the end of the LIA, both mountain ridges have experienced pronounced ice cover retreat and their source headwalls have expanded towards lower elevation (Figure 4.3a). Between 1850 and 1973, the areal expansion at Kranzberg and Trugberg accounted for 41 and 22%, respectively. Since then, source headwalls enlarged by 59 and 57%, respectively. Throughout time, ice-free Trugberg headwalls appear comparatively steeper (Figure 4.3b).

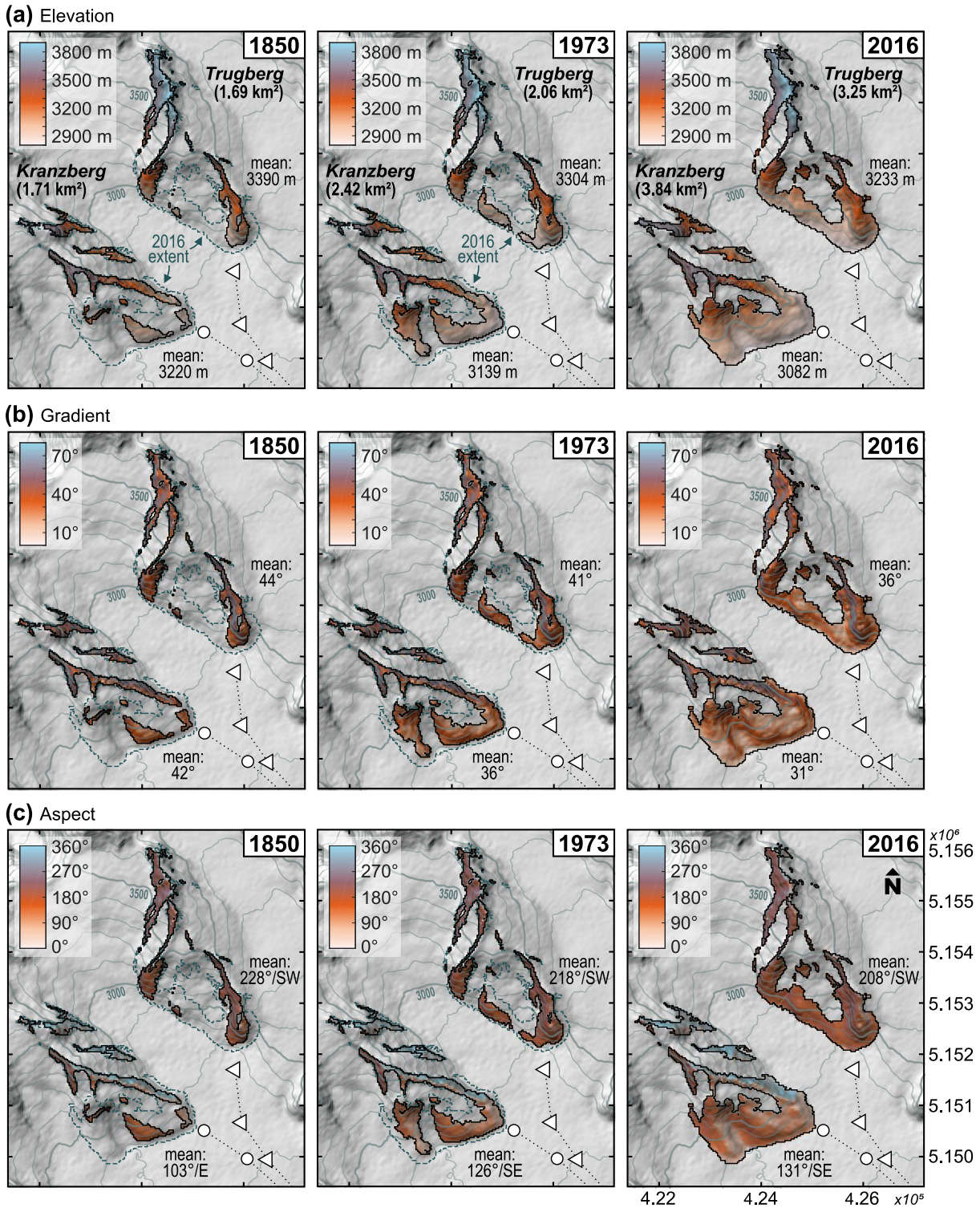


**Figure 4.3:** Headwall morphology at Kranzberg and Trugberg in 1850, 1973, and 2016. Shown are the (a) elevation, (b) gradient, and (c) aspect for the ice-free bedrock surfaces of both debris source areas (outlines based on glacier extents after Maisch *et al.*, 2000, Müller *et al.*, 1976, and Linsbauer *et al.*, 2021). 2019 sample locations are indicated. Areal extents of the ice-free headwalls are exemplarily listed in (a). For comparison, the 2016 ice-free headwall extents are indicated in the 1850 and 1973 panels. Hillshade and 100 m spaced contour lines are based on the recent DEM SRTM GL1 (NASA Shuttle Radar Topography Mission SRTM, 2013).

## 4.5 Discussion and implications

### 4.5.1 Preliminary assessment of minimum headwall erosion rates

At Grosser Aletschgletscher,  $[^{10}\text{Be}]_{\text{measured}}$  from the Kranzberg and Trugberg medial moraine markedly differ through time (**Figure 4.2a**), and so will headwall erosion rates. For younger deposits, concentrations of the GA/K samples are  $3\text{--}5 \times 10^4$  atoms  $\text{g}^{-1}$  higher than for GA/T samples at approximately the same elevation. For older deposits, GA/K and GA/T samples approach similar concentrations. Towards the present (upglacier), concentrations at the Kranzberg medial moraine increase only slightly, while they systematically and pronouncedly decrease for the Trugberg medial moraine. In the following, we address the deviating patterns observed for the two records and derive preliminary minimum headwall erosion rates for the Kranzberg and Trugberg headwalls (please note that this is ongoing work, that estimates on the time of headwall erosion and on post-depositional  $^{10}\text{Be}$  accumulated during downglacier debris transport are still pending, and that final numbers therefore may change somewhat).

According to Wetterauer and Scherler (2023a), deriving headwall erosion rates directly from  $[^{10}\text{Be}]_{\text{measured}}$  without correcting these values for post-depositional  $^{10}\text{Be}$  accumulation during downglacier debris transport (i.e.,  $[^{10}\text{Be}]_{\text{transport}}$ ) provides minimum erosion rate estimates. We may assume that the two medial moraine records at Grosser Aletschgletscher cover an erosion time span from the end of the LIA to the present, similar to Glacier d'Otemma in Switzerland (**Figure 2.6**; Wetterauer *et al.*, 2022a), possibly somewhat longer. Even though the Kranzberg and Trugberg medial moraine are about three times as long as the medial moraines of Glacier d'Otemma, ice flow at Grosser Aletschgletscher is much faster. Thus, as done for Glacier d'Otemma and following the methodological steps by Wetterauer and Scherler (2023a), we may assess uncorrected headwall erosion rates at Grosser Aletschgletscher based on the mean  $^{10}\text{Be}$  production rates across the 1973 ice-free headwalls of Kranzberg and Trugberg (40 and 43 atoms  $\text{g}^{-1} \text{yr}^{-1}$ , respectively; **Figure 4.4**). The resulting preliminary minimum headwall erosion rates at Grosser Aletschgletscher range between 0.4 and 5.4  $\text{mm yr}^{-1}$  (**Figure 4.2c**).

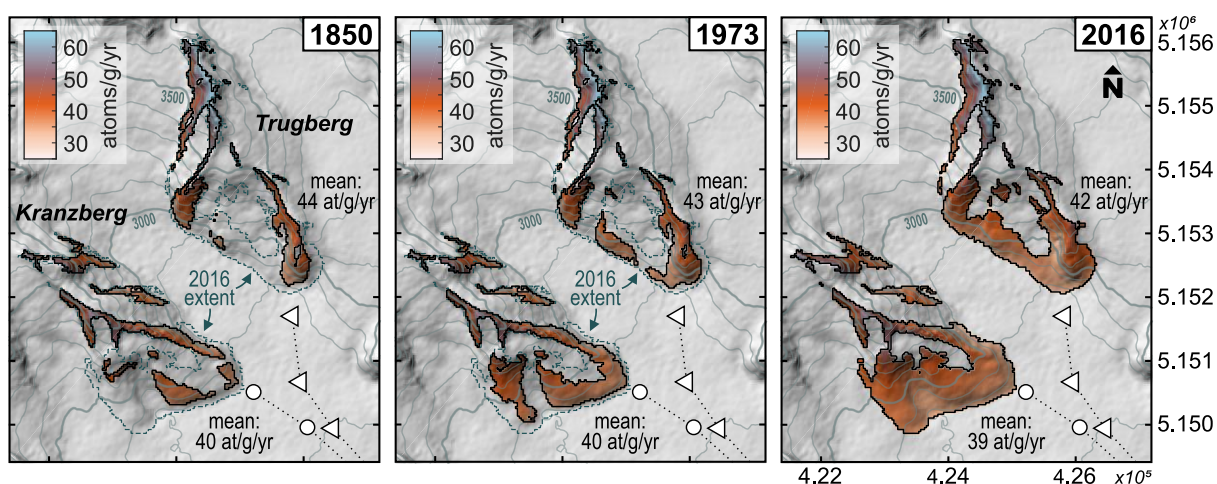


**Figure 4.4:**  $^{10}\text{Be}$  production rates across ice-free source headwalls of Kranzberg and Trugberg in 1850, 1973, and 2016 (outlines based on glacier extents after Maisch *et al.*, 2000, Müller *et al.*, 1976, and Linsbauer *et al.*, 2021). 2019 sample locations are indicated. For comparison, the 2016 ice-free headwall extents are indicated in the 1850 and 1973 panels. Rates were computed as described in Wetterauer *et al.* (2022a) and Wetterauer and Scherler (2023a). Hillshade and 100 m contour lines are based on the recent DEM SRTM GL1 (NASA Shuttle Radar Topography Mission SRTM, 2013).

The analyses of Wetterauer and Scherler (2023a) indicate further that correcting  $[^{10}\text{Be}]_{\text{measured}}$  for  $[^{10}\text{Be}]_{\text{transport}}$  ultimately leads to higher erosion rate estimates, but does not change the overall spatial and temporal patterns among the different records by much. In particular, where  $[^{10}\text{Be}]_{\text{measured}}$  are high, differences between corrected and uncorrected values appear negligible. For example at Glacier du Brenay in Switzerland, where  $[^{10}\text{Be}]_{\text{measured}}$  are on the order of  $\sim 30 \times 10^3$  atoms  $\text{g}^{-1}$ , modelled  $[^{10}\text{Be}]_{\text{transport}}$  accounts for only 3-6% of  $[^{10}\text{Be}]_{\text{measured}}$  (Wetterauer & Scherler, 2023a). Therefore, the still pending transport corrections at Grosser Aletschgletscher may change our preliminary erosion rate estimates only slightly for Kranzberg, as  $[^{10}\text{Be}]_{\text{measured}}$  of all GA/K samples are consistently higher, but likely result in overall higher estimates for Trugberg, where  $[^{10}\text{Be}]_{\text{measured}}$  are lower. Consequently, we expect the divergence of the two trends (**Figure 4.2c**) to be maintained, possibly even strengthened, by future transport corrections. Since we find a systematically changing trend but also a fairly constant trend from two nearby moraines that experience similar glacial dynamics, we assume that downglacier changes in ice and crevasse dynamics, which occur particularly where the glacier trunk bends (**Figure 4.1**), are not decisive for the variability among GA/T samples.

#### 4.5.2 Contrasting histories of headwall erosion at two nearby source areas

Preliminary minimum erosion rate estimates thus suggest overall different headwall erosion rates as well as two different histories of headwall erosion at Grosser Aletschgletscher (**Figure 4.2c**). In the past, headwall erosion at Kranzberg and Trugberg has been similar low, indicated by the oldest deposits of both medial moraine records. However, while erosion at Kranzberg has remained stable and  $< 1$   $\text{mm yr}^{-1}$  through time, Trugberg appears to have experienced a phase of enhanced erosion towards the present, indicated by higher minimum rates of 2 to 5  $\text{mm yr}^{-1}$  for samples GA/T3-8. Although estimates on the time of headwall erosion are still pending, it is likely that the two medial moraine records cover similar time periods. As both moraines develop from similar elevations and locations on the glacier and evolve parallel along most of the glacier, they experience similar velocity fields in the glacier main trunk downglacier of Konkordiaplatz. This implies both temporal and spatial variability in debris supply rates at Grosser Aletschgletscher. The erosion history appears rather simple for Kranzberg and more complex for Trugberg, despite their proximity and hence comparable climatic, lithological, and tectonic conditions. Therefore, the observed variability may be due to distinct spatial morphological differences between the two debris source areas and to spatial variability in the location of major debris origin within each area.

Since the end of the LIA, the debris source areas at Kranzberg and Trugberg have changed through time, their source headwalls experiencing pronounced changes in areal bedrock exposure (**Figure 4.3**). Ice-free areas were rather disconnected and predominantly located at higher elevations in the past, but expanded towards lower elevation through both ice surface lowering and ice cover retreat upward the source headwalls. At both sites, mean headwall elevation lowered by around -150 m since 1850 (**Figure 4.3a**). At the Austrian Kitzsteinhorn, such recently deglaciating areas above glacier surfaces have been found to be particularly active and to erode at increased rates (Hartmeyer *et al.*, 2020a, 2020b). This observation has been associated with freshly exposed bedrock surfaces that adjust to new subaerial environmental conditions, after having been preconditioned in the *randkluft* between rockwall and glacier. At a Canadian glacier, Sanders *et al.* (2012) demonstrated that conditions favourable for rock

fracturing through frost damage particularly occur at the base of headwalls and the glacier randkluft. Following this line of argumentation, the observed increase in erosion at Trugberg (**Figure 4.2c**) could relate to changes in frost-driven destabilizing effects at recently deglaciating surfaces. A slowdown in turn may indicate a depletion of the glacially-conditioned sources. Contrastingly, erosion at Kranzberg appears stable at presumably similar times and despite comparable pronounced ice cover changes (**Figure 4.3a**). If one compares historical orthoimages of the ice confluences at Kranzberg and Trugberg and traces the two medial moraines upglacier, debris supply from the three glacier tributaries seems to vary (**Figure 4.5**). Over time, the Trugberg medial moraine mainly received debris from the Jungfraufirn (**Figure 4.5**), where major changes in ice-free areas at Trugberg occurred (**Figure 4.3**). Similarly, the marked shape of the Kranzberg medial moraine body predominantly leads into the Jungfraufirn, both in the past and recently (**Figure 4.5**). This observation could indicate major debris supply by the eastern Kranzberg flanks, which deposit debris to the Jungfraufirn, but a smaller contribution by the western Kranzberg flanks, which deposit debris to Grosser Aletschfirn. Since 1850, these eastern and western Kranzberg flanks have experienced different deglaciation. Whereas ice-free areas across the western flanks are expanding, headwalls at the eastern flanks have been exposed already in 1850 and since have changed less (**Figure 4.3**).

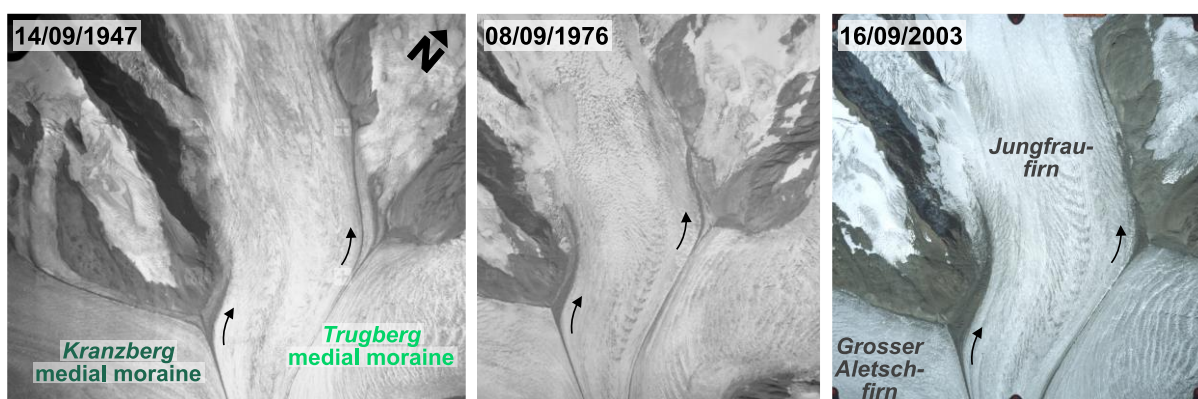


**Figure 4.5:** Historical images of the ice confluences at Kranzberg and Trugberg from the years 1947, 1976, and 2003. Arrows suggest major debris supply from source headwalls depositing debris to the Jungfraufirn, based on the respective medial moraine morphology. Note the relatively more pronounced deglaciation history of Trugberg headwalls and the temporally more variable shape of the Trugberg medial moraine close to its source headwalls (orthoimages from Swisstopo, 2023).

If this idea of predominantly eastern debris supply at Kranzberg holds true, despite its recent western areal expansion towards Grosser Aletschfirn, the post-1850 areal changes across the supplying Kranzberg headwalls as well as the related changes in elevation and gradient would be much smaller when compared to those at the supplying Trugberg headwalls. As a result, the erosion history of Kranzberg may be less variable (**Figure 4.2c**). In this context, particularly also the aspect of Kranzberg and Trugberg headwalls would markedly differ (**Figure 4.3c**), which has been shown to be a possible controlling factor within the Swiss massif around Pigne d’Arolla. In the small massif, steeper north faces apparently erode faster, which could relate to distinct temperature-sensitive conditions, such as permafrost degradation and/or frost-cracking intensity, both affecting rockwall stability (Wetterauer & Scherler, 2023a). However, in order to make similarly precise statements on distinct headwall morphology at the much larger debris source areas at Grosser Aletschgletscher, a more detailed spatial knowledge on the location of major debris origin is required.

Although  $^{14}\text{C}/^{10}\text{Be}$  ratios have primarily been used to detect catchment-average erosional transience (e.g., Skov *et al.*, 2019; Hippe *et al.*, 2021), hypothetical rockwall modelling has shown that paired  $^{14}\text{C}/^{10}\text{Be}$  also serves to study spatially constrained short-term erosion rate changes in stochastically eroding high-alpine landscapes (Dennis & Scherler, 2022). At Grosser Aletschgletscher, the changing  $^{14}\text{C}/^{10}\text{Be}$  ratios along the Trugberg medial moraine, which peak towards the middle of the record (**Figure 4.2b**), may indicate erosional changes at the Trugberg headwalls. Given the depth-dependent nuclide production and given that headwall surfaces were constantly exposed (see Section 4.3.2; cf. Figure 1b in Dennis & Scherler, 2022), the changing  $^{14}\text{C}/^{10}\text{Be}$  ratios could reflect different headwall excavation depths and thus changes in the magnitude of erosion. The high  $^{14}\text{C}/^{10}\text{Be}$  ratio of sample GA/T7 may result from the supply of debris relatively more enriched in muogenically produced  $^{14}\text{C}$ . This could imply that bedrock comprised in GA/T7 was more rapidly advected from depth to the surface, as a result of faster erosion. The lower ratios obtained for the other samples instead, would then reflect shallower bedrock excavation due to slower erosion. Accordingly, Trugberg may have experienced a phase of enhanced headwall erosion, consistent with the increase in  $^{10}\text{Be}$ -derived erosion rate estimates (**Figure 4.2c**). It is unlikely that the increased  $^{14}\text{C}/^{10}\text{Be}$  ratio is the result of a single large erosional event, as this would presumably lead to a stronger deflection and offset of the ratio (cf. Figure 9b in Dennis & Scherler, 2022). Moreover, we could not delineate any voluminous debris deposits in this moraine section, either in the field or on satellite images (Swisstopo, 2023), typical for single infrequent rockfall. More likely and as suggested above, an increased erosional activity at Trugberg may relate to the exposure of new, highly erosive bedrock surfaces at the time that debris comprised in samples GA/T3-8 was deposited (**Figure 4.2c**). However, temporal changes in the exposure of headwalls due to changes in ice cover complicate the interpretation of medial moraine and headwall nuclide inventories, as addressed in the following.

In transient glacial landscapes, medial moraine samples may not share the same bedrock exposure history, and  $^{10}\text{Be}$  inheritance can introduce bias if the exposure of surfaces changes through repeated cycles of ice cover retreat and advance (Scherler & Egholm, 2020; Wetterauer *et al.*, 2022a; Wetterauer & Scherler, 2023a). In the massif around Pigne d'Arolla, Wetterauer and Scherler (2023a) addressed the impact of recent deglaciation on downglacier  $^{10}\text{Be}$  records by quantifying post-LIA area expansion of ice-free source rockwalls, suggesting that the majority of their records is only marginally affected. At Grosser Aletschgletscher, the areal expansion at Trugberg headwalls between 1850 and 1973 proceeded relatively slow, accounting for 22%. At Kranzberg, the ice retreated faster and headwalls expanded by 41%. Since 1973, ice cover retreat has accelerated significantly at both sites, and headwalls have now expanded by almost 60% relative to 1973 (**Figure 4.3a**). As previously discussed, recent ice retreat may thus have led to enhanced erosion of newly exposed areas above the headwall-glacier contact zone (Hartmeyer *et al.*, 2020a), potentially explaining the reduction in  $^{10}\text{Be}$  in the Trugberg record. However, these areas could also contribute debris of lower  $^{10}\text{Be}$  due to former shielding by the glacier body (Wetterauer *et al.*, 2022a). At Trugberg, both processes may play a role and it is difficult to disentangle their relative importance. At Kranzberg instead, the lack of variability in its  $^{10}\text{Be}$  record, despite the overall pronounced ice cover retreat and thus source headwall expansion, may suggest that the addition of recently deglaciated bedrock of possibly different  $^{10}\text{Be}$  may play a minor role. Similar questions on the nuclide history in

downglacier medial moraine records and the role of changes in bedrock exposure arise for [ $^{14}\text{C}$ ], however, with additional challenges: the comparatively faster decay of  $^{14}\text{C}$  and its pronounced depth production by muons. For example, where a headwall surface was completely shielded from cosmic radiation for  $\sim 40$  kyr by a non-erosive ice cover, inherited  $^{14}\text{C}$  from previous bedrock exposure would have decayed by  $\sim 99\%$  but inherited  $^{10}\text{Be}$  only by  $\sim 2\%$  (Hippe, 2017). In addition, the muon-induced production of  $^{14}\text{C}$  in glacially-shielded rock is relatively larger than that of  $^{10}\text{Be}$ , with the muonic component being a function of the duration and thickness of ice coverage. While an ice cover thickness of only  $\sim 13$  m reduces the production of  $^{10}\text{Be}$  to 1% of its surface production rate, at least a  $\sim 70$  m thick ice column is required to reduce  $^{14}\text{C}$  production to 1% (Hippe, 2017). This dependency becomes particularly important when recently exposed areas previously shielded by a comparatively thin ice cover begin to contribute debris to medial moraines, and when post-depositional debris transport proceeds englacially but close to the glacier surface. Consequently, where headwall surfaces or debris were covered or buried by ice,  $^{14}\text{C}/^{10}\text{Be}$  ratios will also change depending on the duration and thickness of coverage or burial. Therefore,  $^{14}\text{C}/^{10}\text{Be}$  analysis in glacial landscapes requires to carefully consider the duration and effectivity of shielding and the origin of the muonic component.

### 4.5.3 Outlook

The above preliminary assessment of headwall erosion at Grosser Aletschgletscher has shown that different processes can cause the observed trends and patterns in [ $^{10}\text{Be}$ ] and [ $^{14}\text{C}$ ]. At present, however, it is difficult to separate these processes and test their probable importance in a physically meaningful way. Although the additional  $^{14}\text{C}$  data provide additional constraints on the samples, the sensitivity of  $^{14}\text{C}$  to multiple processes operating in the transient landscape of Grosser Aletschgletscher make quantitative interpretations difficult. To move forward, we suggest to employ a numerical glacier model for accurately reconstructing debris particle trajectories from source headwalls to sample locations that allows us to (i) correct our measured nuclide concentrations for additional nuclide accumulation during downglacier debris transport, (ii) assess the time span of headwall erosion at Kranzberg and Trugberg, and (iii) test the above initial interpretations on why the trends from the two parallel medial moraine [ $^{10}\text{Be}$ ] records diverge and what may cause the apparent phase of enhanced Trugberg erosion. Previous simulations of debris particle transport with a simple 1D glacier model (Wetterauer *et al.*, 2022b) in the Swiss massif around Pigne d'Arolla and with a coupled ice and landscape evolution model (iSOSIA; Egholm *et al.*, 2011) at the Chhota Shigri Glacier in the Himalayas under imposed climatic scenarios highlight the need to well constrain local model boundary conditions such as the recent evolution of both glacier and source headwalls (Scherler & Egholm, 2020; Wetterauer & Scherler, 2023a). Particularly, at the comparatively small and less-well studied Swiss sites, modelling debris particle trajectories through the glaciers required assumptions about past conditions as well as glacier reconstructions that are associated with unquantified uncertainties (Wetterauer & Scherler, 2023a).

For Grosser Aletschgletscher and in continuation of this work, we initiated a collaboration with Guillaume Juvet to use the Instructed Glacier Model (IGM; Juvet *et al.*, 2022; Juvet, 2023; Juvet & Cordonnier, 2023; <https://github.com/juvetg/igm>, last access: 31 October 2023) for simulating 3D debris particle transport. The planned IGM simulations will hold several

advantages. IGM has been trained to learn ice mechanics from a set of mountain glaciers with state-of-the-art ice flow physical models, and its accuracy has been validated particularly on Grosser Aletschgletscher as forcing case (Jouvet *et al.*, 2022; Jouvet, 2023; Jouvet & Cordonnier, 2023). Simulations of the glacier's evolution already exist from the end of the LIA until today and consider climatic datasets of the region as well as topographic data and glaciological reports on the glacier since 1880 (e.g., Jouvet *et al.*, 2011; Jouvet & Huss, 2019). With the Lagrangian particle tracking routine of IGM, which is currently tested and updated (<https://github.com/jouvetg/igm>, last access: 31 October 2023), thousands of particles can be seeded at different frequencies across the source headwalls and will be advected by the velocity field in 3D, to simulate debris trajectories at low computational cost. Therefore, in addition to more accurately estimating the time of headwall erosion,  $[^{10}\text{Be}]_{\text{transport}}$ , and associated modelling uncertainties, we hope to backtrack/assign particles to distinct surface zones at Kranzberg and Trugberg accounting for the temporal evolution of ice coverage at their deglaciating headwalls. This would allow us to make more precise statements on predominating debris origin, and to verify for example the suggested predominant debris supply by eastern headwalls at Kranzberg (see Section 4.5.2). In this context, also morphological conditions such as dominant source elevation, aspect, and gradient at which headwall erosion preferably occurred at a given time will be better delineated. The upcoming modelling will further help to evaluate possible nuclide inheritance. Specifically, the muonic  $^{14}\text{C}$  component within medial moraine debris acquired during englacial transport time can be estimated from the modelled IGM trajectories and particle burial depths below the ice surface, to help interpreting  $^{14}\text{C}/^{10}\text{Be}$  ratios.

#### 4.5.4 Preliminary conclusions

In this study, we assessed headwall erosion at Kranzberg and Trugberg at Grosser Aletschgletscher, based on the two longest downglacier medial moraine  $[^{10}\text{Be}]$  records to date and for the first time in combination with an additional downglacier  $^{14}\text{C}/^{10}\text{Be}$  record. The results reveal that the magnitude and temporal variability of the two  $[^{10}\text{Be}]$  records markedly differ, despite the proximity of the two major debris source areas at the glacier head. Concluding from our preliminary analyses of  $^{10}\text{Be}$ -derived minimum headwall erosion rates, the erosion history appears simple at Kranzberg but comparatively complex at Trugberg. At Trugberg, preliminary erosion rate estimates reflect an apparent pulse in headwall erosion, and concurrently increasing  $^{14}\text{C}/^{10}\text{Be}$  ratios may relate to a deepening of bedrock excavation, both of which may indicate erosional transience. This contrasts with temporally steady and low erosion rate estimates at Kranzberg. The two variant erosion histories imply that different spatiotemporal conditions are operating and/or dominating across the two nearby source areas. For instance, the exposure of highly erosive surfaces due to more pronounced deglaciation (Hartmeyer *et al.*, 2020a) across Trugberg headwalls may serve as a possible explanation for the enhanced erosive phase, which exceeds concurrent Kranzberg erosion by almost an order of magnitude (**Figure 4.2c**). Spatiotemporal patterns of rockwall erosion have also been observed by previous studies on six medial moraine  $[^{10}\text{Be}]$  records in the Swiss massif around Pigne d'Arolla. There, accelerating rockwall erosion appears to be temporally limited to the transition from the LIA to the following deglaciation period, suggesting a short-term increase in erosion rates in response to transient source area changes (Wetterauer *et al.*, 2022a; Wetterauer & Scherler, 2023a).

With 0.4 to 5.4 mm yr<sup>-1</sup>, our preliminary <sup>10</sup>Be-derived minimum headwall erosion rates compare well with previous estimates of rockwall erosion rates in the massif around Pigne d'Arolla (0.6-10.0 mm yr<sup>-1</sup>; Wetterauer *et al.*, 2022a; Wetterauer & Scherler, 2023a). However, these former studies consider <sup>10</sup>Be-derived headwall erosion rates in deglaciating landscapes to be “apparent” estimates and thus approximations. Where ice cover is retreating, the interpretation of these rates requires to carefully consider small-scale dynamics that relate to site-specific headwall deglaciation and possible contribution of formerly shielded bedrock, as well as to correct medial moraine cosmogenic nuclide concentrations for additional nuclide accumulation during post-depositional debris exposure, both of which is challenging (Wetterauer *et al.*, 2022a; Wetterauer & Scherler, 2023a). Therefore, and especially with respect to the sensitivity of paired <sup>14</sup>C/<sup>10</sup>Be due to both differential decay and depth-dependent muogenic production in glacially-shielded bedrock and debris, we consider it necessary to model the transport of medial moraine debris through Grosser Aletschgletscher and trace its origin in detail in a next step to refine our preliminary estimates and verify our explanations above.

Eventually, the medial moraine records from Grosser Aletschgletscher comprise on average twice as much <sup>10</sup>Be data points as previous downglacier records (Scherler & Egholm, 2020; Wetterauer *et al.*, 2022a; Wetterauer & Scherler, 2023a) and the source headwalls at Kranzberg (3.8 km<sup>2</sup>) and Trugberg (3.3 km<sup>2</sup>) are by far larger in area than the previously studied Swiss sites (mostly ≤0.5 km<sup>2</sup>; Wetterauer *et al.*, 2022a; Wetterauer & Scherler, 2023a). Although one might assume that these large-scale records could be more susceptible to random single outliers in stochastically eroding landscapes, we also observe clear temporal systematics along the two downglacier [<sup>10</sup>Be] records and distinct spatiotemporal patterns for the inferred headwall erosion rate estimates. In combination with the upcoming transport modelling, this not only promises the most comprehensive <sup>10</sup>Be-derived headwall erosion rate analyses so far, but also reinforces the utility to continue studying downglacier medial moraine [<sup>10</sup>Be] records as archives of headwall erosion.

## 4.6 Data availability

The cosmogenic nuclide dataset presented here will be made freely available via GFZ Data Services once our study has been completed and submitted to a scientific journal. When using the preliminary data presented in this chapter please cite this thesis.

## 4.7 Acknowledgements

This research received funding from the European Research Council (ERC) under the European Union's Horizon 2020 research and innovation program (grant no. 759639). We are grateful to Leif Anderson, Donovan Dennis, Deniz Gök, and Julian Wahl for support during sampling. Stefan Heinze and Steven Binnie from the University of Cologne are thanked for performing AMS <sup>10</sup>Be measurements. Anne Sofie Søndergaard from the ETH Zurich is thanked for performing AMS <sup>14</sup>C measurements and calculating <sup>14</sup>C concentrations. Hella Wittmann and Cathrin Schulz are thanked for their help and advice in sample preparation. We further thank Guillaume Juvet for his efforts in testing and updating IGM for the upcoming collaboration.



## Synthesis and conclusions

The aim of this thesis was to study the evolution of cold mountain regions with recent climate change by deriving spatiotemporal records of rockwall erosion rates in glacial landscapes. These landscapes experience pronounced warming, and recently increasing rockfall has been attributed particularly to climate-induced rockwall destabilization. Yet, these observations are largely based on short-term monitoring datasets from the 21st century (e.g., Gruber *et al.*, 2004; Ravanel *et al.*, 2010; Hartmeyer *et al.*, 2020a). To obtain longer time records of rockwall erosion, I quantified headwall erosion rates at six Swiss glaciers from downglacier  $^{10}\text{Be}$  concentrations in medial moraine debris, pursuing the promising but little tested downglacier-interval-sampling strategy by Ward and Anderson (2011) and Scherler and Egholm (2020). As such, this thesis is the first to integrate combined  $^{10}\text{Be}$  analyses, glacier velocity reconstructions and transport modelling, and source rockwall deglaciation histories from a detailed small-scale case study (Glacier d'Otemma; Chapter 2) to a small mountain massif (Pigne d'Arolla massif; Chapter 3) to the largest glacier in the European Alps (Grosser Aletschgletscher; Chapter 4). Below, I will conclude on the findings of the three studies presented by reflecting on the initial research questions (see Section 1.4) and the potential and current challenges the approach entails.

The fundamental question underlying this thesis was whether downglacier  $^{10}\text{Be}$  concentration records can provide systematic information on headwall erosion and debris supply in glacial landscapes, or whether temporal records will randomly scatter as a result of sampling stochastic erosion events. With this work, eight new downglacier  $^{10}\text{Be}$  concentration records were obtained for the Swiss Alps (Chapters 2-4). Considered together with the first dataset from the Himalayas (Scherler & Egholm, 2020), these records are either temporally constant or vary systemically through time (**Figure 5.1**), partly even with similar trends in both mountain ranges (**Figure 5.1a,b**). Detailed grain size analyses for Glacier d'Otemma (Chapter 2) showed that sand-sized and pebble-sized debris fractions reflect the same downglacier trend, indicating that temporal variations in  $^{10}\text{Be}$  concentrations are preserved throughout different grain size classes of the same record (**Figure 5.1b**). This systematic behaviour and the gradually varying moraine morphologies without the usually well-delineated voluminous deposits attributed to major rockfalls suggest that the analysed records reflect gradual temporal variations in the source area, largely unaffected by episodic large-scale erosion. Overall, these observations confirm the potential of the downglacier-interval-sampling strategy and debris amalgamation approach to derive meaningful records to estimate erosion rates at average outcrop-scale (Small *et al.*,

1997). Consequently, medial moraines indeed serve as archives of headwall erosion, where the observed systematic downglacier variability reflects distinct source area processes that have changed or remained stable over time.

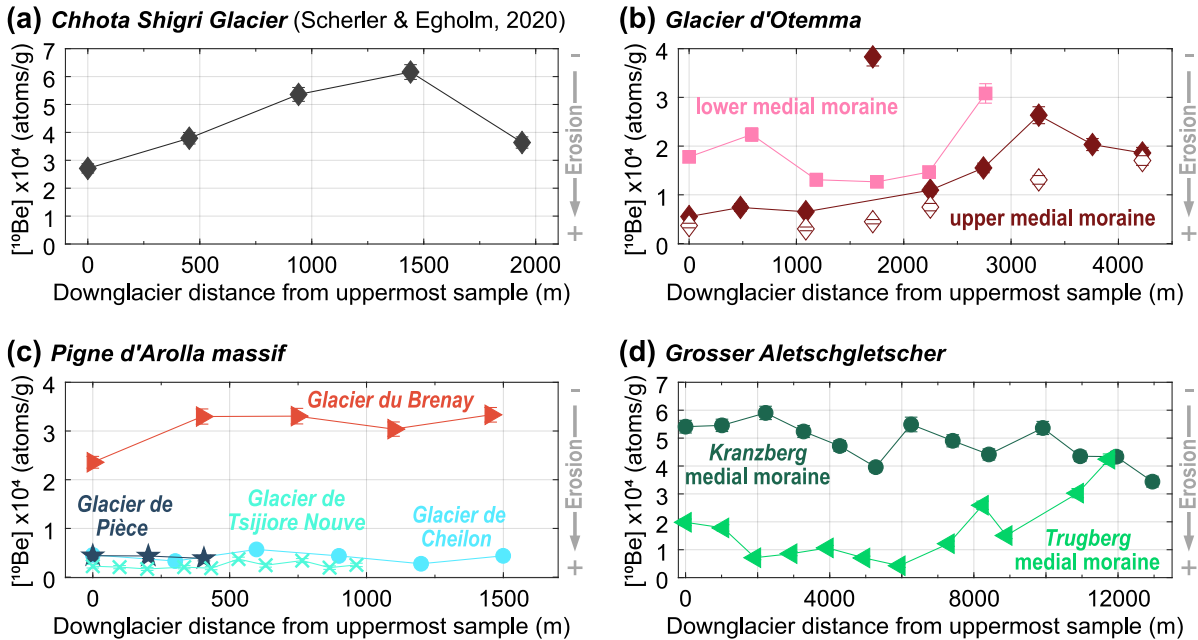


**Figure 5.1:** Systematic temporal variability in all currently existing medial moraine records, with measured downglacier  $^{10}\text{Be}$  concentrations ( $\pm 1\sigma$  analytical error) from (a) Chhota Shigri Glacier, Himalayas (Scherler & Egholm, 2020), (b) Glacier d'Otemma in the Pigne d'Arolla massif, Swiss Alps (Chapter 2), (c) Glacier du Brenay, de Cheilon, de Pièce, and de Tsjiore Nouve in the Pigne d'Arolla massif, Swiss Alps (Chapter 3), and (d) Grosser Aletschgletscher, Swiss Alps (Chapter 4). Open symbols in (b) show additional measurements on a coarser debris fraction.

Rockwall erosion is known to be a dynamic process, varying through space and time. The systematic variability along and among the presented medial moraine records implies distinct temporal and spatial patterns for rockwall erosion over the last two centuries (Chapters 2-4). Apparently increasing headwall erosion rates from the end of the LIA towards deglaciation seem to reflect a climate-sensitive response of debris source areas to glacial landscape transience (**Figure 2.6b**; Chapter 2). The underlying processes, however, either quickly re-stabilize after the transition or are less relevant at others sites as suggested by comparatively more stable records throughout the deglaciation (**Figure 3.5**; Chapter 3). Consequently, distinct temporal trends in headwall erosion may indeed relate to climatic changes. From the studies on Glacier d'Otemma, the Pigne d'Arolla massif, and Grosser Aletschgletscher (Chapters 2-4) it can be further concluded that considering the individual evolution of each debris source area is crucial to study rockwall erosion in glacial landscapes. Even within the same glacier catchment, small-scale dynamics among different debris source areas vary as preliminary analyses at Grosser Aletschgletscher suggested (Chapter 4). Conditions that caused an apparent pulse in erosion in one of two nearby debris source areas apparently are absent or minor in the other (**Figure 4.2c**). Studying the Pigne d'Arolla massif further revealed distinct asymmetric spatial patterns in the magnitude of erosion among different records (Chapter 3). Increased erosion rates at steeper north-facing rockwalls suggest a possible aspect and slope control on rockwall erosion in the massif (**Figure 3.7**). In particular, the correlation with rockwall aspect seems to be in line with the observation that temperature-driven rockwall destabilization particularly affects north faces due to pronounced permafrost thaw (Gruber *et al.*, 2004; Sass, 2010) and

frost damage (Coutard & Francou, 1989; Sass, 2005). Likewise, medial moraine  $^{10}\text{Be}$ -derived rockwall erosion rates in the Alaska Range seem significantly higher for northerly exposed debris source areas compared to those of southern aspect (Ward & Anderson, 2011). Consequently, differences among downglacier medial moraine records indeed seem to relate to spatially distinct headwall morphology.

Although the eight new downglacier  $^{10}\text{Be}$  concentration records are either stable or trending, this work also demonstrates that deriving and interpreting temporal records of rockwall erosion rates from medial moraine  $^{10}\text{Be}$  concentrations faces considerable methodological challenges. Where rapid changes in erosion occur, downglacier cosmogenic nuclide records may not accurately quantify the actual headwall erosion rate as source area changes may be too fast to ensure isotopic cosmogenic steady state (see Section 2.6.2; Chapter 2). Moreover, the effect of post-depositional transport time and additional nuclide production on the measured concentrations should not be neglected per se, but should better be assessed individually for each glacier. Modelling debris particle trajectories with a simple 1D glacier transport model (**Figure 2.4**) has proven useful to approximate additional nuclide production and the time of rockwall erosion in the small Pigne d'Arolla massif (Chapter 2, Chapter 3). Transport corrections appear to be minor for samples with overall high measured concentrations and short transport durations, and do not skew the observed temporal (**Figure 3.5**) and spatial (**Figure 3.7**) patterns. Yet, where sample concentrations are generally low, transport corrections can affect estimating erosion rates (**Table 3.2**). Using a simple model setup further demonstrated that generalizations of glacier-specific parameters, due to the lack of historical datasets on glacier velocities and the ELA for less-well studied glaciers, lead to uncertainties that are difficult to quantify. Where the glacier architecture is more complex, for instance due to icefalls, reconstructing debris particle transport further can be less intuitive (see Glacier de Tsijiore Nouve, **Figure 3.1**; Chapter 3). Hence, and especially in the case of low-concentration samples and extensive debris source areas, sophisticated glacier models may allow for more precise transport corrections and backtracking of debris particles to their source (Scherler & Egholm, 2020). The planned 3D modelling of debris trajectories at Grosser Aletschgletscher (Chapter 4), will be a next step to gain a better control over glacial transport and different source regions across eroding rockwalls based on a well-researched glacier evolution history. Still, even if model simulations and transport corrections were as accurate as possible, the temporal variability in downglacier  $^{10}\text{Be}$  concentrations likely reflects different processes that relate to the post-LIA deglaciation of debris source areas (Chapters 2-4). On the one hand, rockfall inventories from terrestrial laser scans indicate enhanced erosion of recently deglaciated rockwalls above the glacier surface, presumably induced by thermomechanical forcing in the formerly perennial frozen bedrock (Hartmeyer *et al.*, 2020a). Retreating ice cover thus seems to trigger phases of enhanced rockwall erosion and debris supply, possibly also reflected by the records at Glacier d'Otemma (**Figure 2.6b**; Chapter 2), Grosser Aletschgletscher (**Figure 4.2c**; Chapter 4), and the Chhota Shigri Glacier (Scherler & Egholm, 2020). On the other hand, rockwall deglaciation exposes newly eroding surfaces that may inherit nuclide signals that are non-representative of the current pace of erosion due to shielding effects by formerly overlying ice (Chapters 2-4). Debris supply by these rockwalls may progressively dilute previous nuclide signals from the LIA. This could cause temporal variability in  $^{10}\text{Be}$  concentrations, too. Source rockwall analyses revealed that rockwall deglaciation locally can differ significantly, even at

adjacent debris source areas (**Figure 2.7, Figure 3.6, Figure 4.3**). Where areal changes in ice-free surfaces were small and/or rather gradual, temporal records were found to vary more consistently and are presumably less affected by shielding effects. Instead, for temporally more variable records, source rockwall deglaciation appeared more pronounced and complex (**Table 3.3, Figure 3.6**), increasing the likelihood of varied nuclide signatures. The above considerations show that the analysis of medial moraine  $^{10}\text{Be}$  concentration records therefore requires to study the geometry and deglaciation history for each study site individually. Downglacier cosmogenic nuclide records likely reflect a variety of different processes, which to disentangle remains a major challenge. Consequently, headwall erosion rates derived from medial moraine  $^{10}\text{Be}$  concentrations should be considered “apparent” rate estimates in landscapes that experience significant deglaciation.

Future studies can build on the findings discussed in the three studies of this thesis. For example, the grain size analyses on Glacier d’Otemma (Chapter 2) were the first to show that  $^{10}\text{Be}$  concentrations in pebble-sized fractions of supraglacial debris are systematically lower compared to sand-sized fractions (**Figure 2.5a**). This probably indicates that coarse material originates from greater rockwall depths. Such observations were made repeatedly within fluvial landscapes (e.g., Puchol *et al.*, 2014; West *et al.*, 2014), and future studies in glacial landscapes may continue to analyse grain size variations through time to analyse temporal changes in source area processes and/or provenance (e.g., Kapannusch *et al.*, 2020). In the study on the Pigne d’Arolla massif (Chapter 3), first attempts were made to evaluate possible effects of rockwall deglaciation and nuclide inheritance on erosion rate estimates by quantifying source area expansion since 1850 (**Table 3.3**). Still, this does not provide any information about the actual nuclide concentration within rockwall surfaces, for example whether concentrations in recently exposed bedrock are generally lower compared to bedrock unshielded over centuries, as is often assumed. In this context, pairs of rockwall samples may be taken from adjacent surfaces, one of which was exposed throughout the LIA and one of which got recently deglaciated, to assess by how much their  $^{10}\text{Be}$  concentrations vary. The study on the massif (Chapter 3) further suggested that, among other factors, aspect and related distinct temperature-conditions affect the magnitude of rockwall erosion (**Figure 3.7, Figure B6**). As continuation, additional bedrock temperature analyses based on satellite-derived temporal records of land surface temperature, frost-cracking models (e.g., Scherler, 2014; Mair *et al.*, 2020), or  $^3\text{He}$  paleothermometry (e.g., Dennis & Scherler, 2022) may help to investigate the sensitivity of high-alpine rockwall erosion to bedrock temperature. For the three studies of this thesis (Chapters 2-4), medial moraines with gradual morphology and no evidence of large-scale instantaneous deposition were deliberately selected to minimize stochastic effects on the datasets (**Figure 2.1, Figure 3.1, Figure 4.1**). Nevertheless, for comparison, it would be interesting to sample an obviously inhomogeneous medial moraine to test whether its record would be dominated by more scatter. The medial moraine of Glacier d’Arolla close to Pigne d’Arolla, for example, would lend itself to such a test. Both in the field (**Figure 1.2b**) and on satellite imagery (Swisstopo, 2023), it appears as a conglomerate of different-sized rockfall events, possibly due to pronounced episodic debris supply. Eventually, further analyses such as those proposed will be beneficial not only for this specific young approach but also more generally for studies that estimate rockwall erosion rates from cosmogenic nuclides in glaciated, episodically eroding high-alpine terrain.

Finally, the eight new records on headwall erosion in the European Alps over the last ~200 years help to fill a temporal gap that is difficult to assess with modern monitoring capabilities. For the eight studied Swiss sites, erosion rate estimates largely range between 0.6 and 10 mm yr<sup>-1</sup> (**Table 3.2**, **Figure 4.2c**). Thus, although they are considered to be “apparent” estimates (Chapters 2-4), the derived rates are well in line with estimates from previous studies on high-alpine rockwall erosion using the same, similar, or different approaches (**Table 1.1**). Even the comparatively high rate estimates, where intermixing of nuclide signals due to deglaciation cannot be excluded, still appear reasonable when compared to the mostly high recent rates from terrestrial laser scanning (>5-10 mm yr<sup>-1</sup>; **Table 1.1**). The archival potential of the eight medial moraines to study rockwall erosion, the systematic temporal and spatial variability in their nuclide concentrations and derived erosion rate estimates, as well as the apparent link to distinct climatic changes and spatial conditions motivate further work. In particular, recent catastrophic climate-related rockfalls, such as the summit failure of the Fluchthorn in Austria in 2023 (**Figure 1.2f**), highlight the need of future studies that continue to quantify rate changes in high-alpine regions and analyse patterns and driving forces to assess the sensitivity of cold mountain landscapes to climate change.



## References

- Aguilar, G., Carretier, S., Regard, V., Vassallo, R., Riquelme, R. & Martinod, J. (2014) Grain size-dependent  $^{10}\text{Be}$  concentrations in alluvial stream sediment of the Huasco Valley, a semi-arid Andes region. *Quaternary Geochronology*, 19, 163-172. <https://doi.org/10.1016/j.quageo.2013.01.011>
- Alley, R.B., Cuffey, K.M., Evenson, E.B., Strasser, J.C., Lawson, D.E. & Larson, G.J. (1997) How glaciers entrain and transport basal sediment: physical constraints. *Quaternary Science Reviews*, 16, 1017-1038. [https://doi.org/10.1016/S0277-3791\(97\)00034-6](https://doi.org/10.1016/S0277-3791(97)00034-6)
- Anderson, R.S. (1998) Near-surface thermal profiles in alpine bedrock: implications for the frost weathering of rock. *Arctic and Alpine Research*, 30, 362-372. <https://doi.org/10.2307/1552008>
- Anderson, R.S. (2000) A model of ablation-dominated medial moraines and the generation of debris-mantled glacier snouts. *Journal of Glaciology*, 46, 459-469. <https://doi.org/10.3189/172756500781833025>
- Anderson, R.S. & Anderson, S.P. (2010) *Geomorphology: the mechanics and chemistry of landscapes*. Cambridge: Cambridge University Press.
- Anderson, L.S. & Anderson, R.S. (2016) Modeling debris-covered glaciers: response to steady debris deposition. *The Cryosphere*, 10, 1105-1124. <https://doi.org/10.5194/tc-10-1105-2016>
- Anderson, R.S., Anderson, L.S., Armstrong, W.H., Rossi, M.W. & Crump, S.E. (2018) Glaciation of alpine valleys: the glacier - debris-covered glacier - rock glacier continuum. *Geomorphology*, 311, 127-142. <https://doi.org/10.1016/j.geomorph.2018.03.015>
- Anderson, L.S., Armstrong, W.H., Anderson, R.S., Scherler, D. & Petersen, E. (2021) The Causes of debris-covered glacier thinning: evidence for the importance of ice dynamics from Kennicott Glacier, Alaska. *Frontiers in Earth Science*, 9, 1-19. <https://doi.org/10.3389/feart.2021.680995>
- André, M.-F. (1986) Dating slope deposits and estimating rates of rock wall retreat in northwest Spitsbergen by lichenometry. *Geografiska Annaler: Series A, Physical Geography*, 68, 65-75. <https://doi.org/10.1080/04353676.1986.11880159>
- Antoniazza, G. & Lane, S.N. (2021) Sediment yield over glacial cycles: a conceptual model. *Progress in Physical Geography: Earth and Environment*, 45, 842-865. <https://doi.org/10.1177/0309133321997292>
- Arsenault, A.M. & Meigs, A.J. (2005) Contribution of deep-seated bedrock landslides to erosion of a glaciated basin in southern Alaska. *Earth Surface Processes and Landforms*, 30, 1111-1125. <https://doi.org/10.1002/esp.1265>
- BAFU Bundesamt für Umwelt (2005) Hinweiskarte der potenziellen Permafrostverbreitung, <https://map.geo.admin.ch> (last access: 14 November 2022).
- Balco, G. (2011) Contributions and unrealized potential contributions of cosmogenic-nuclide exposure dating to glacier chronology, 1990-2010. *Quaternary Science Reviews*, 30, 3-27. <https://doi.org/10.1016/j.quascirev.2010.11.003>
- Balco, G. (2017) Production rate calculations for cosmic-ray-muon-produced  $^{10}\text{Be}$  and  $^{26}\text{Al}$  benchmarked against geological calibration data. *Quaternary Geochronology*, 39, 150-173. <https://doi.org/10.1016/j.quageo.2017.02.001>

- Balco, G., Stone, J.O., Lifton, N.A. & Dunai, T.J. (2008) A complete and easily accessible means of calculating surface exposure ages or erosion rates from  $^{10}\text{Be}$  and  $^{26}\text{Al}$  measurements. *Quaternary Geochronology*, 3, 174-195. <https://doi.org/10.1016/j.quageo.2007.12.001>
- Ballantyne, C.K. (2002a) Paraglacial geomorphology. *Quaternary Science Reviews*, 21, 1935-2017. [https://doi.org/10.1016/S0277-3791\(02\)00005-7](https://doi.org/10.1016/S0277-3791(02)00005-7)
- Ballantyne, C.K. (2002b) A general model of paraglacial landscape response. *The Holocene*, 12, 371-376. <https://doi.org/10.1191/0959683602hl553fa>
- Ballantyne, C.K., Wilson, P., Gheorghiu, D. & Rodés, À. (2014a) Enhanced rock-slope failure following ice-sheet deglaciation: timing and causes. *Earth Surface Processes and Landforms*, 39, 900-913. <https://doi.org/10.1002/esp.3495>
- Ballantyne, C.K., Sandeman, G.F., Stone, J.O. & Wilson, P. (2014b) Rock-slope failure following Late Pleistocene deglaciation on tectonically stable mountainous terrain. *Quaternary Science Reviews*, 86, 144-157. <https://doi.org/10.1016/j.quascirev.2013.12.021>
- Banerjee, A. & Wani, B.A. (2018) Exponentially decreasing erosion rates protect the high-elevation crests of the Himalaya. *Earth and Planetary Science Letters*, 497, 22-28. <https://doi.org/10.1016/j.epsl.2018.06.001>
- Barrows, T.T., Stone, J.O., Fifield, L.K. & Cresswell, R.G. (2002) The timing of the Last Glacial Maximum in Australia. *Quaternary Science Reviews*, 21, 159-173. [https://doi.org/10.1016/S0277-3791\(01\)00109-3](https://doi.org/10.1016/S0277-3791(01)00109-3)
- Belmont, P., Pazzaglia, F.J. & Gosse, J.C. (2007) Cosmogenic  $^{10}\text{Be}$  as a tracer for hillslope and channel sediment dynamics in the Clearwater River, western Washington State. *Earth and Planetary Science Letters*, 264, 123-135. <https://doi.org/10.1016/j.epsl.2007.09.013>
- Benn, D.I. & Evans, D.J.A. (1998) *Glaciers and glaciation*. London: Arnold.
- Benn, D.I., Bolch, T., Hands, K., Gulley, J., Luckman, A., Nicholson, L.I., Quincey, D., Thompson, S., Toumi, R. & Wiseman, S. (2012) Response of debris-covered glaciers in the Mount Everest region to recent warming, and implications for outburst flood hazards. *Earth-Science Reviews*, 114, 156-174. <https://doi.org/10.1016/j.earscirev.2012.03.008>
- Binnie, S.A., Phillips, W.M., Summerfield, M.A. & Fifield, L.K. (2007) Tectonic uplift, threshold hillslopes, and denudation rates in a developing mountain range. *Geology*, 35, 743-746. <https://doi.org/10.1130/G23641A.1>
- Bolch, T., Buchroithner, M., Pieczonka, T. & Kunert, A. (2008) Planimetric and volumetric glacier changes in the Khumbu Himal, Nepal, since 1962 using Corona, Landsat TM and ASTER data. *Journal of Glaciology*, 54, 592-600. <https://doi.org/10.3189/002214308786570782>
- Borchers, B., Marrero, S., Balco, G., Caffee, M., Goehring, B., Lifton, N., Nishiizumi, K., Phillips, F., Schaefer, J. & Stone, J. (2016) Geological calibration of spallation production rates in the CRONUS-Earth project. *Quaternary Geochronology*, 31, 188-198. <https://doi.org/10.1016/j.quageo.2015.01.009>
- Boulton, G.S. (1978) Boulder shapes and grain size distributions of debris as indicators of transport paths through a glacier and till genesis. *Sedimentology*, 25, 773-799. <https://doi.org/10.1111/j.1365-3091.1978.tb00329.x>
- Boulton, G.S. & Deynoux, M. (1981) Sedimentation in glacial environments and the identification of tills and tillites in ancient sedimentary sequences. *Precambrian Research*, 15, 397-422. [https://doi.org/10.1016/0301-9268\(81\)90059-0](https://doi.org/10.1016/0301-9268(81)90059-0)
- Boulton, G.S. & Eyles, N. (1979) Sedimentation by valley glaciers: a model and genetic classification. In: Schlüchter, C. (Ed.) *Moraines and Varves*. Balkema, pp.11-23.
- Braithwaite, R.J. (2015) From Doktor Kurowski's Schneegrenze to our modern glacier equilibrium line altitude (ELA). *The Cryosphere*, 9, 2135-2148. <https://doi.org/10.5194/tc-9-2135-2015>
- Briner, J.P., Kaufman, D.S., Manley, W.F., Finkel, R.C. & Caffee, M.W. (2005) Cosmogenic exposure dating of late Pleistocene moraine stabilization in Alaska. *Geological Society of America Bulletin*, 117, 1108-1120. <https://doi.org/10.1130/B25649.1>
- Brown, E.T., Stallard, R.F., Larsen, M.C., Raisbeck, G.M. & Yiou, F. (1995) Denudation rates determined from the accumulation of in situ-produced  $^{10}\text{Be}$  in the luquillo experimental forest, Puerto Rico. *Earth and Planetary Science Letters*, 129, 193-202. [https://doi.org/10.1016/0012-821X\(94\)00249-X](https://doi.org/10.1016/0012-821X(94)00249-X)

- Brown, E.T., Stallard, R.F., Larsen, M.C., Bourlès, D.L., Raisbeck, G.M. & Yiou, F. (1998) Determination of predevelopment denudation rates of an agricultural watershed (Cayaguás River, Puerto Rico) using in-situ-produced  $^{10}\text{Be}$  in river-borne quartz. *Earth and Planetary Science Letters*, 160, 723-728. [https://doi.org/10.1016/S0012-821X\(98\)00123-X](https://doi.org/10.1016/S0012-821X(98)00123-X)
- Caltech (2021) California Institute of Technology Tectonics Observatory, <http://www.tectonics.caltech.edu> (last access: 21 May 2021).
- Carreter, S., Regard, V. & Soual, C. (2009) Theoretical cosmogenic nuclide concentration in river bed load clasts: does it depend on clast size? *Quaternary Geochronology*, 4, 108-123. <https://doi.org/10.1016/j.quageo.2008.11.004>
- Chmeleff, J., von Blanckenburg, F., Kossert, K. & Jakob, D. (2010) Determination of the  $^{10}\text{Be}$  half-life by multicollector ICP-MS and liquid scintillation counting. *Nuclear Instruments and Methods in Physics Research B: Beam Interactions with Materials and Atoms*, 268, 192-199. <https://doi.org/10.1016/j.nimb.2009.09.012>
- Church, M. & Ryder, J.M. (1972) Paraglacial sedimentation: a consideration of fluvial processes conditioned by glaciation. *Geological Society of America Bulletin*, 83, 3059-3072. [https://doi.org/10.1130/0016-7606\(1972\)83\[3059:PSACOF\]2.0.CO;2](https://doi.org/10.1130/0016-7606(1972)83[3059:PSACOF]2.0.CO;2)
- Cockburn, H.A.P. & Summerfield, M.A. (2004) Geomorphological applications of cosmogenic isotope analysis. *Progress in Physical Geography: Earth and Environment*, 28, 1-42. <https://doi.org/10.1191/0309133304pp395oa>
- Cossart, E., Braucher, R., Fort, M., Bourlès, D.L. & Carcaillet, J. (2008) Slope instability in relation to glacial debuttressing in alpine areas (Upper Durance catchment, southeastern France): evidence from field data and  $^{10}\text{Be}$  cosmic ray exposure ages. *Geomorphology*, 95, 3-26. <https://doi.org/10.1016/j.geomorph.2006.12.022>
- Coutard, J.-P. & Francou, B. (1989) Rock temperature measurements in two alpine environments: implications for frost shattering. *Arctic and Alpine Research*, 21, 399-416. <https://doi.org/10.2307/1551649>
- Curry, A.M. (2021) Paraglacial rock-slope failure following deglaciation in Western Norway. In: Beylich, A.A. (Ed.) *Landscapes and Landforms of Norway*. Springer, Cham, pp. 97-130.
- Deline, P. (2005) Change in surface debris cover on Mont Blanc massif glaciers after the 'Little Ice Age' termination. *The Holocene*, 15, 302-309. <https://doi.org/10.1191/0959683605hl809rr>
- Deline, P. (2009) Interactions between rock avalanches and glaciers in the Mont Blanc massif during the late Holocene. *Quaternary Science Reviews*, 28, 1070-1083. <https://doi.org/10.1016/j.quascirev.2008.09.025>
- Delunel, R., van der Beek, P.A., Carcaillet, J., Bourlès, D.L. & Valla, P.G. (2010) Frost-cracking control on catchment denudation rates: insights from *in situ* produced  $^{10}\text{Be}$  concentrations in stream sediments (Ecrins-Pelvoux massif, French Western Alps). *Earth and Planetary Science Letters*, 293, 72-83. <https://doi.org/10.1016/j.epsl.2010.02.020>
- Delunel, R., Schlunegger, F., Valla, P.G., Dixon, J., Glotzbach, C., Hippe, K., Kober, F., Molliex, S., Norton, K.P., Salcher, B., Wittmann, H., Akçar, N. & Christl, M. (2020) Late-Pleistocene catchment-wide denudation patterns across the European Alps. *Earth-Science Reviews*, 211, 103407. <https://doi.org/10.1016/j.earscirev.2020.103407>
- Dennis, D.P. & Scherler, D. (2022) A combined cosmogenic nuclides approach for determining the temperature-dependence of erosion. *Journal of Geophysical Research: Earth Surface*, 127, e2021JF006580. <https://doi.org/10.1029/2021JF006580>
- D'Errico, J. (2022) SLM - Shape Language Modeling, MATLAB Central File Exchange, <https://www.mathworks.com/matlabcentral/fileexchange/24443-slm-shape-language-modeling> (last access: 20 July 2022).
- Dewald, A., Heinze, S., Jolie, J., Zilges, A., Dunai, T., Rethemeyer, J., Melles, M., Staubwasser, M., Kuczewski, B., Richter, J., Radtke, U., von Blanckenburg, F. & Klein, M. (2013) CologneAMS, a dedicated center for accelerator mass spectrometry in Germany. *Nuclear Instruments and Methods in Physics Research Section B: Beam Interactions with Materials and Atoms*, 294, 18-23. <https://doi.org/10.1016/j.nimb.2012.04.030>
- DiBiase, R.A., Whipple, K.X., Heimsath, A.M. & Ouimet, W.B. (2010) Landscape form and millennial erosion rates in the San Gabriel Mountains, CA. *Earth and Planetary Science Letters*, 289, 134-144. <https://doi.org/10.1016/j.epsl.2009.10.036>

- DiBiase, R.A., Heimsath, A.M. & Whipple, K.X. (2012) Hillslope response to tectonic forcing in threshold landscapes. *Earth Surface Processes and Landforms*, 37, 855-865. <https://doi.org/10.1002/esp.3205>
- Dunai, T.J. (2010) *Cosmogenic nuclides: principles, concepts and applications in the Earth surface sciences*. Cambridge: Cambridge University Press.
- Dunne, J., Elmore, D. & Muzikar, P. (1999) Scaling factors for the rates of production of cosmogenic nuclides for geometric shielding and attenuation at depth on sloped surfaces. *Geomorphology*, 27, 3-11. [https://doi.org/10.1016/S0169-555X\(98\)00086-5](https://doi.org/10.1016/S0169-555X(98)00086-5)
- Dyrgerov, M.B. (2002) Glacier mass balance and regime: data of measurements and analysis. In: Meier, M. & Armstrong, R. (Eds.) *Institute of Arctic and Alpine Research Occasional Paper No. 55*. Boulder, CO, USA: University of Colorado.
- Dyrgerov, M.B. & Meier, M.F. (2000) Twentieth century climate change: evidence from small glaciers. *Proceedings of the National Academy of Sciences*, 97, 1406-1411. <https://doi.org/10.1073/pnas.97.4.1406>
- Egholm, D.L., Knudsen, M.F., Clark, C.D. & Lesemann, J.E. (2011) Modeling the flow of glaciers in steep terrains: the integrated second-order shallow ice approximation (iSOSIA). *Journal of Geophysical Research*, 116, F02012. <https://doi.org/10.1029/2010JF001900>
- ETH Library (2022) e-pics Image Archive Online, ETH Library, Zürich, [https://www.e-pics.ethz.ch/en/home\\_en/](https://www.e-pics.ethz.ch/en/home_en/) (last access: 15 August 2022).
- Evans, S.G. & Clague, J.J. (1994) Recent climatic change and catastrophic geomorphic processes in mountain environments. *Geomorphology*, 10, 107-128. [https://doi.org/10.1016/0169-555X\(94\)90011-6](https://doi.org/10.1016/0169-555X(94)90011-6)
- Evans, S.G. & Clague, J.J. (1999) Rock avalanches on glaciers in the Coast and St. Elias Mountains, British Columbia. (Symposium at Vancouver - *Proceedings of the 13th annual Vancouver Geotechnical Society Symposium*), 115-123.
- Eyles, N. & Rogerson, R.J. (1978a) A framework for the investigation of medial moraines formation: Austerdalsbreen, Norway, and Berendon Glacier, British Columbia, Canada. *Journal of Glaciology*, 20, 99-113. <https://doi.org/10.3189/S0022143000021249>
- Eyles, N. & Rogerson, R.J. (1978b) Sedimentology of medial moraines on Berendon Glacier, British Columbia, Canada: implications for debris transport in a glacierized basin. *Geological Society of America Bulletin*, 89, 1688-1693. [https://doi.org/10.1130/0016-7606\(1978\)89<1688:SOMMOB>2.0.CO;2](https://doi.org/10.1130/0016-7606(1978)89<1688:SOMMOB>2.0.CO;2)
- Fabel, D., Harbor, J., Dahms, D., James, A., Elmore, D., Horn, L., Daley, K. & Steele, C. (2004) Spatial patterns of glacial erosion at a valley scale derived from terrestrial cosmogenic  $^{10}\text{Be}$  and  $^{26}\text{Al}$  concentrations in rock. *Annals of the Association of American Geographers*, 94, 241-255. <https://doi.org/10.1111/j.1467-8306.2004.09402001.x>
- Farinotti, D., Huss, M., Fürst, J.J., Landmann, J., Machguth, H., Maussion, F. & Pandit, A. (2019) A consensus estimate for the ice thickness distribution of all glaciers on Earth. *Nature Geoscience*, 12, 168-173. <https://doi.org/10.1038/s41561-019-0300-3>
- Farinotti, D., Immerzeel, W.W., de Kok, R.J., Quincey, D.J. & Dehecq, A. (2020) Manifestations and mechanisms of the Karakoram glacier anomaly. *Nature Geoscience*, 13, 8-16. <https://doi.org/10.1038/s41561-019-0513-5>
- Fischer, L., Käab, A., Huggel, C. & Noetzli, J. (2006) Geology, glacier retreat and permafrost degradation as controlling factors of slope instabilities in a high-mountain rock wall: the Monte Rosa east face. *Natural Hazards and Earth System Sciences*, 6, 761-772. <https://doi.org/10.5194/nhess-6-761-2006>
- Fischer, L., Purves, R.S., Huggel, C., Noetzli, J. & Haerberli, W. (2012) On the influence of topographic, geological and cryospheric factors on rock avalanches and rockfalls in high-mountain areas. *Natural Hazards and Earth System Sciences*, 12, 241-254. <https://doi.org/10.5194/nhess-12-241-2012>
- Fischer, L., Huggel, C., Käab, A. & Haerberli, W. (2013) Slope failures and erosion rates on a glacierized high-mountain face under climatic changes. *Earth Surface Processes and Landforms*, 38, 836-846. <https://doi.org/10.1002/esp.3355>
- Fischer, M., Huss, M., Barboux, C. & Hoelzle, M. (2014) The new Swiss Glacier Inventory SGI2010: relevance of using high-resolution source data in areas dominated by very small glaciers. *Arctic, Antarctic, and Alpine Research*, 46, 933-945. <https://doi.org/10.1657/1938-4246-46.4.933>

- Fischer, M., Huss, M. & Hoelzle, M. (2015) Surface elevation and mass changes of all Swiss glaciers 1980-2010. *The Cryosphere*, 9, 525-540. <https://doi.org/10.5194/tc-9-525-2015>
- Fleischer, F., Otto, J.-C., Junker, R.R. & Hölbling, D. (2021) Evolution of debris cover on glaciers of the Eastern Alps, Austria, between 1996 and 2015. *Earth Surface Processes and Landforms*, 46, 1673-1691. <https://doi.org/10.1002/esp.5065>
- Gabbi, J., Farinotti, D., Bauder, A. & Maurer, H. (2012) Ice volume distribution and implications on runoff projections in a glacierized catchment. *Hydrology and Earth System Sciences*, 16, 4543-4556. <https://doi.org/10.5194/hess-16-4543-2012>
- Ganti, V., von Hagke, C., Scherler, D., Lamb, M.P., Fischer, W.W. & Avouac, J.-P. (2016) Time scale bias in erosion rates of glaciated landscapes. *Science Advances*, 2, e1600204. <https://doi.org/10.1126/sciadv.1600204>
- Gallach, X., Ravel, L., Egli, M., Brandova, D., Schaepman, M., Christl, M., Gruber, S., Deline, P., Carcaillet, J. & Pallandre, F. (2018) Timing of rockfalls in the Mont Blanc massif (Western Alps): evidence from surface exposure dating with cosmogenic  $^{10}\text{Be}$ . *Landslides*, 15, 1991-2000. <https://doi.org/10.1007/s10346-018-0999-8>
- Gallach, X., Carcaillet, J., Ravel, L., Deline, P., Ogier, C., Rossi, M., Malet, E. & Garcia-Sellés, D. (2020) Climatic and structural controls on Late-glacial and Holocene rockfall occurrence in high-elevated rock walls of the Mont Blanc massif (Western Alps). *Earth Surface Processes and Landforms*, 45, 3071-3091. <https://doi.org/10.1002/esp.4952>
- Gilbert, G.K. (1877) *Geology of the Henry Mountains*. Washington, D.C.: Government Printing Office.
- Gilbert, G.K. (1904) Systematic asymmetry of crest lines in the High Sierra of California. *The Journal of Geology*, 12, 579-588.
- GLAMOS (2019a) Swiss Glacier Length Change, release 2019, Glacier Monitoring Switzerland. <https://doi.org/10.18750/lengthchange.2019.r2019>
- GLAMOS (2019b) Swiss Glacier Volume Change, release 2019, Glacier Monitoring Switzerland. <https://doi.org/10.18750/volumechange.2019.r2019>
- GLAMOS (2019c) Swiss Glacier Mass Balance, release 2019, Glacier Monitoring Switzerland. <https://doi.org/10.18750/massbalance.2019.r2019>
- GLAMOS (2021a) Swiss glacier length change, release 2021, Glacier Monitoring Switzerland. <https://doi.org/10.18750/lengthchange.2021.r2021>
- GLAMOS (2021b) Swiss glacier mass balance, release 2021, Glacier Monitoring Switzerland. <https://doi.org/10.18750/massbalance.2021.r2021>
- GLAMOS (2021c) Swiss glacier volume change, release 2021, Glacier Monitoring Switzerland. <https://doi.org/10.18750/volumechange.2021.r2021>
- GLAMOS (2023) Glacier Monitoring Switzerland, <https://www.glamos.ch> (last access: 16 October 2023).
- Glasser, N.F., Holt, T.O., Evans, Z.D., Davies, B.J., Pelto, M. & Harrison, S. (2016) Recent spatial and temporal variations in debris cover on Patagonian glaciers. *Geomorphology*, 273, 202-216. <https://doi.org/10.1016/j.geomorph.2016.07.036>
- Glen, J.W. (1952) Experiments on the deformation of ice. *Journal of Glaciology*, 2, 111-114. <https://doi.org/10.3189/S0022143000034067>
- Glen, J.W. (1955) The creep of polycrystalline ice. *Proceedings of the Royal Society of London. Series A. Mathematical and Physical Sciences*, 228, 519-538.
- Glotzbach, C., van Der Beek, P.A. & Spiegel, C. (2011) Episodic exhumation and relief growth in the Mont Blanc massif, Western Alps from numerical modelling of thermochronology data. *Earth and Planetary Science Letters*, 304, 417-430. <https://doi.org/10.1016/j.epsl.2011.02.020>
- Godard, V., Burbank, D.W., Bourlès, D.L., Bookhagen, B., Braucher, R. & Fisher, G.B. (2012) Impact of glacial erosion on  $^{10}\text{Be}$  concentrations in fluvial sediments of the Marsyandi catchment, central Nepal. *Journal of Geophysical Research: Earth Surface*, 117, F03013. <https://doi.org/10.1029/2011JF002230>

- Goehring, B.M., Schaefer, J.M., Schluechter, C., Lifton, N.A., Finkel, R.C., Jull, A.J.T., Akçar, N. & Alley, R.B. (2011) The Rhone Glacier was smaller than today for most of the Holocene. *Geology*, 39, 679-682. <https://doi.org/10.1130/G32145.1>
- Goehring, B.M., Muzikar, P. & Lifton, N.A. (2013) An *in situ*  $^{14}\text{C}$ - $^{10}\text{Be}$  Bayesian isochron approach for interpreting complex glacial histories. *Quaternary Geochronology*, 15, 61-66. <https://doi.org/10.1016/j.quageo.2012.11.007>
- Gomez, B. & Small, R.J. (1983) Genesis of englacial debris within the lower Glacier de Tsidjiore Nouve, Valais, Switzerland, as revealed by scanning electron microscopy. *Geografiska Annaler: Series A, Physical Geography*, 65, 45-51. <https://doi.org/10.1080/04353676.1983.11880073>
- Gomez, B. & Small, R.J. (1985) Medial moraines of the Haut Glacier d'Arolla, Valais, Switzerland: debris supply and implications for moraine formation. *Journal of Glaciology*, 31, 303-307. <https://doi.org/10.3189/S002214300006638>
- Gosse, J.C. & Phillips, F.M. (2001) Terrestrial *in situ* cosmogenic nuclides: theory and application. *Quaternary Science Reviews*, 20, 1475-1560. [https://doi.org/10.1016/S0277-3791\(00\)00171-2](https://doi.org/10.1016/S0277-3791(00)00171-2)
- Gosse, J.C., Klein, J., Lawn, B., Middleton, R. & Evenson, E.B. (1995) Beryllium-10 dating of the duration and retreat of the last Pinedale glacial sequence. *Science*, 268, 1329-1333. <https://doi.org/10.1126/science.268.5215.1329>
- Grab, M., Mattea, E., Bauder, A., Huss, M., Rabenstein, L., Hodel, E., Linsbauer, A., Langhammer, L., Schmid, L., Church, G., Hellmann, S., Délèze, K., Schaer, P., Lathion, P., Farinotti, D. & Maurer, H. (2021) Ice thickness distribution of all Swiss glaciers based on extended ground-penetrating radar data and glaciological modeling. *Journal of Glaciology*, 67, 1074-1092. <https://doi.org/10.1017/jog.2021.55>
- Granger, D.E. & Riebe, C.S. (2014) Cosmogenic nuclides in weathering and erosion. In: Holland, H.D. & Turekian, K.K. (Eds.) *Treatise on Geochemistry, Second Edition*. Elsevier, pp. 401-436. <https://doi.org/10.1016/B978-0-08-095975-7.00514-3>
- Granger, D.E., Kirchner, J.W. & Finkel, R. (1996) Spatially averaged long-term erosion rates measured from *in situ*-produced cosmogenic nuclides in alluvial sediment. *The Journal of Geology*, 104, 249-257. <https://doi.org/10.1086/629823>
- Gruber, S. & Haeberli, W. (2007) Permafrost in steep bedrock slopes and its temperature-related destabilization following climate change. *Journal of Geophysical Research: Earth Surface*, 112, F02S18. <https://doi.org/10.1029/2006JF000547>
- Gruber, S., Hoelzle, M. & Haeberli, W. (2004) Permafrost thaw and destabilization of Alpine rock walls in the hot summer of 2003. *Geophysical Research Letters*, 31, L13504. <https://doi.org/10.1029/2004GL020051>
- Guillon, H., Mugnier, J.-L., Buoncristiani, J.-F., Carcaillet, J., Godon, C., Prud'homme, C., van der Beek, P. & Vassallo, R. (2015) Improved discrimination of subglacial and periglacial erosion using  $^{10}\text{Be}$  concentration measurements in subglacial and supraglacial sediment load of the Bossons glacier (Mont Blanc massif, France). *Earth Surface Processes and Landforms*, 40, 1202-1215. <https://doi.org/10.1002/esp.3713>
- Haeberli, W. & Beniston, M. (1998) Climate change and its impacts on glaciers and permafrost in the Alps. *Ambio: A Journal of the Human Environment*, 27, 258-265.
- Haeberli, W. & Hoelzle, M. (1995) Application of inventory data for estimating characteristics of and regional climate-change effects on mountain glaciers: a pilot study with the European Alps. *Annals of Glaciology*, 21, 206-212. <https://doi.org/10.1017/S0260305500015834>
- Haeberli, W., Wegmann, M. & Vonder Mühll, D. (1997) Slope stability problems related to glacier shrinkage and permafrost degradation in the Alps. *Eclogae Geologicae Helvetiae*, 90, 407-414. <https://doi.org/10.5169/seals-168172>
- Haeberli, W., Frauenfelder, R., Hoelzle, M. & Maisch, M. (1999) On rates and acceleration trends of global glacier mass changes. *Geografiska Annaler: Series A, Physical Geography*, 81, 585-591.
- Hales, T.C. & Roering, J.J. (2005) Climate-controlled variations in scree production, Southern Alps, New Zealand. *Geology*, 33, 701-704. <https://doi.org/10.1130/G21528.1>

- Hales, T.C. & Roering, J.J. (2007) Climatic controls on frost cracking and implications for the evolution of bedrock landscapes. *Journal of Geophysical Research: Earth Surface*, 112, F02033. <https://doi.org/10.1029/2006JF000616>
- Hales, T.C. & Roering, J.J. (2009) A frost “buzzsaw” mechanism for erosion of the eastern Southern Alps, New Zealand. *Geomorphology*, 107, 241-253. <https://doi.org/10.1016/j.geomorph.2008.12.012>
- Hallet, B., Walder, J.S. & Stubbs, C.W. (1991) Weathering by segregation ice growth in microcracks at sustained subzero temperatures: verification from an experimental study using acoustic emissions. *Permafrost and Periglacial Processes*, 2, 283-300. <https://doi.org/10.1002/ppp.3430020404>
- Hallet, B., Hunter, L. & Bogen, J. (1996) Rates of erosion and sediment evacuation by glaciers: a review of field data and their implications. *Global and Planetary Change*, 12, 213-235. [https://doi.org/10.1016/0921-8181\(95\)00021-6](https://doi.org/10.1016/0921-8181(95)00021-6)
- Harris, C., Arenson, L.U., Christiansen, H.H., Etzelmüller, B., Frauenfelder, R., Gruber, S., Haerberli, W., Hauck, C., Hölzle, M., Humlum, O., Isaksen, K., Kääb, A., Kern-Lütschg, M.A., Lehning, M., Matsuoka, N., Murton, J.B., Nötzli, J., Phillips, M., Ross, N., Seppälä, M., Springman, S.M., & Vonder Mühll, D. (2009) Permafrost and climate in Europe: monitoring and modelling thermal, geomorphological and geotechnical responses. *Earth-Science Reviews*, 92, 117-171. <https://doi.org/10.1016/j.earscirev.2008.12.002>
- Hartmeyer, I., Delleske, R., Keuschnig, M., Krautblatter, M., Lang, A., Schrott, L. & Otto, J.-C. (2020a) Current glacier recession causes significant rockfall increase: the immediate paraglacial response of deglaciating cirque walls. *Earth Surface Dynamics*, 8, 729-751. <https://doi.org/10.5194/esurf-8-729-2020>
- Hartmeyer, I., Keuschnig, M., Delleske, R., Krautblatter, M., Lang, A., Schrott, L., Prasicek, G. & Otto, J.-C. (2020b) A 6-year lidar survey reveals enhanced rockwall retreat and modified rockfall magnitudes/frequencies in deglaciating cirques. *Earth Surface Dynamics*, 8, 753-768. <https://doi.org/10.5194/esurf-8-753-2020>
- Heimsath, A.M. & McGlynn, R. (2008) Quantifying periglacial erosion in the Nepal high Himalaya. *Geomorphology*, 97, 5-23. <https://doi.org/10.1016/j.geomorph.2007.02.046>
- Herman, F., Seward, D., Valla, P.G., Carter, A., Kohn, B., Willett, S.D. & Ehlers, T.A. (2013) Worldwide acceleration of mountain erosion under a cooling climate. *Nature*, 504, 423-426. <https://doi.org/10.1038/nature12877>
- Heyman, J., Stroeven, A.P., Harbor, J.M. & Caffee, M.W. (2011) Too young or too old: evaluating cosmogenic exposure dating based on an analysis of compiled boulder exposure ages. *Earth and Planetary Science Letters*, 302, 71-80. <https://doi.org/10.1016/j.epsl.2010.11.040>
- Hippe, K. (2017) Constraining processes of landscape change with combined *in situ* cosmogenic  $^{14}\text{C}$ - $^{10}\text{Be}$  analysis. *Quaternary Science Reviews*, 173, 1-19. <https://doi.org/10.1016/j.quascirev.2017.07.020>
- Hippe, K. & Lifton, N.A. (2014) Calculating isotope ratios and nuclide concentrations for *in situ* cosmogenic  $^{14}\text{C}$  analyses. *Radiocarbon*, 56, 1167-1174. <https://doi.org/10.2458/56.17917>
- Hippe, K., Kober, F., Baur, H., Ruff, M., Wacker, L. & Wieler, R. (2009) The current performance of the *in situ*  $^{14}\text{C}$  extraction line at ETH. *Quaternary Geochronology*, 4, 493-500. <https://doi.org/10.1016/j.quageo.2009.06.001>
- Hippe, K., Ivy-Ochs, S., Kober, F., Zasadni, J., Wieler, R., Wacker, L., Kubik, P.W. & Schlüchter, C. (2014) Chronology of Lateglacial ice flow reorganization and deglaciation in the Gotthard Pass area, Central Swiss Alps, based on cosmogenic  $^{10}\text{Be}$  and *in situ*  $^{14}\text{C}$ . *Quaternary Geochronology*, 19, 14-26. <https://doi.org/10.1016/j.quageo.2013.03.003>
- Hippe, K., Jansen, J.D., Skov, D.S., Lupker, M., Ivy-Ochs, S., Kober, F., Zeilinger, G., Capriles, J.M., Christl, M., Maden, C., Vockenhuber, C. & Egholm, D.L. (2021) Cosmogenic *in situ*  $^{14}\text{C}$ - $^{10}\text{Be}$  reveals abrupt Late Holocene soil loss in the Andean Altiplano. *Nature Communications*, 12, 2546. <https://doi.org/10.1038/s41467-021-22825-6>
- Hock, R., Rasul, G., Adler, C., Cáceres, B., Gruber, S., Hirabayashi, Y., Jackson, M., Kääb, A., Kang, S., Kutuzov, S., Milner, A., Molau, U., Morin, S., Orlove, B. & Steltzer, H. (2019) High mountain areas. In: Pörtner, H.-O., Roberts, D.C., Masson-Delmotte, V., Zhai, P., Tignor, M., Poloczanska, E., Mintenbeck, K., Alegría, A., Nicolai, M., Okem, A., Petzold, J., Rama, B. & Weyer, N.M. (Eds.) *IPCC Special Report on the Ocean and Cryosphere in a Changing Climate*. pp. 131-202. <https://doi.org/10.1017/9781009157964.004>

- Hoffmann, T. & Schrott, L. (2002) Modelling sediment thickness and rockwall retreat in an Alpine valley using 2D-seismic refraction (Reintal, Bavarian Alps). *Zeitschrift für Geomorphologie / Supplementary Issues*, 153-173.
- Holm, K., Bovis, M. & Jakob, M. (2004) The landslide response of alpine basins to post-Little Ice Age glacial thinning and retreat in southwestern British Columbia. *Geomorphology*, 57, 201-216. [https://doi.org/10.1016/S0169-555X\(03\)00103-X](https://doi.org/10.1016/S0169-555X(03)00103-X)
- Holzhauser, H., Magny, M. & Zumbühl, H.J. (2005) Glacier and lake-level variations in west-central Europe over the last 3500 years. *The Holocene*, 15, 789-801. <https://doi.org/10.1191/0959683605hl853ra>
- Hubbard, A., Willis, I., Sharp, M., Mair, D., Nienow, P., Hubbard, B. & Blatter, H. (2000) Glacier mass-balance determination by remote sensing and high-resolution modelling. *Journal of Glaciology*, 46, 491-498. <https://doi.org/10.3189/172756500781833016>
- Huggel, C. (2009) Recent extreme slope failures in glacial environments: effects of thermal perturbation. *Quaternary Science Reviews*, 28, 1119-1130. <https://doi.org/10.1016/j.quascirev.2008.06.007>
- Huggel, C., Salzmann, N., Allen, S., Caplan-Auerbach, J., Fischer, L., Haeberli, W., Larsen, C., Schneider, D. & Wessels, R. (2010) Recent and future warm extreme events and high-mountain slope stability. *Philosophical Transactions of the Royal Society A*, 368, 2435-2459. <https://doi.org/10.1098/rsta.2010.0078>
- Huggel, C., Allen, S., Deline, P., Fischer, L., Noetzli, J. & Ravelin, L. (2012) Ice thawing, mountains falling - are alpine rock slope failures increasing? *Geology Today*, 28, 98-104. <https://doi.org/10.1111/j.1365-2451.2012.00836.x>
- Humlum, O. (2000) The geomorphic significance of rock glaciers: estimates of rock glacier debris volumes and headwall recession rates in West Greenland. *Geomorphology*, 35, 41-67. [https://doi.org/10.1016/S0169-555X\(00\)00022-2](https://doi.org/10.1016/S0169-555X(00)00022-2)
- Huss, M. (2012) Extrapolating glacier mass balance to the mountain-range scale: the European Alps 1900-2100. *The Cryosphere*, 6, 713-727. <https://doi.org/10.5194/tc-6-713-2012>
- IPCC (2022) Climate change 2022: impacts, adaptation and vulnerability. Contribution of Working Group II to the Sixth Assessment Report of the Intergovernmental Panel on Climate Change. [Pörtner, H.-O., Roberts, D.C., Tignor, M., Poloczanska, E.S., Mintenbeck, K., Alegría, A., Craig, M., Langsdorf, S., Lösschke, S., Möller, V., Okem, A. & Rama, B. (Eds.)] Cambridge University Press. Cambridge University Press, Cambridge, UK and New York, NY, USA, 3056 pp. <https://doi.org/10.1017/9781009325844>
- Ivy-Ochs, S. & Kober, F. (2008) Surface exposure dating with cosmogenic nuclides. *E&G Quaternary Science Journal*, 57, 179-209. <https://doi.org/10.3285/eg.57.1-2.7>
- Ivy-Ochs, S., Schlüchter, C., Kubik, P.W. & Denton, G.H. (1999) Moraine exposure dates imply synchronous Younger Dryas glacier advances in the European Alps and in the Southern Alps of New Zealand. *Geografiska Annaler: Series A, Physical Geography*, 81, 313-323.
- Ivy-Ochs, S., Kerschner, H., Reuther, A., Maisch, M., Sailer, R., Schaefer, J., Kubik, P.W., Synal, H.-A. & Schlüchter, C. (2006) The timing of glacier advances in the northern European Alps based on surface exposure dating with cosmogenic  $^{10}\text{Be}$ ,  $^{26}\text{Al}$ ,  $^{36}\text{Cl}$ , and  $^{21}\text{Ne}$ . In: Siame, L.L., Bourlès, D.L. & Brown, E.T. (Eds.) *In Situ-Produced Cosmogenic Nuclides and Quantification of Geological Processes*. Geological Society of America Special Paper, pp. 43-60. [https://doi.org/10.1130/2006.2415\(04\)](https://doi.org/10.1130/2006.2415(04))
- Ivy-Ochs, S., Kerschner, H., Maisch, M., Christl, M., Kubik, P.W. & Schlüchter, C. (2009) Latest Pleistocene and Holocene glacier variations in the European Alps. *Quaternary Science Reviews*, 28, 2137-2149. <https://doi.org/10.1016/j.quascirev.2009.03.009>
- Jonas, T., Marty, C. & Magnusson, J. (2009) Estimating the snow water equivalent from snow depth measurements in the Swiss Alps. *Journal of Hydrology*, 378, 161-167. <https://doi.org/10.1016/j.jhydrol.2009.09.021>
- Jouvet, G. (2023) Inversion of a Stokes glacier flow model emulated by deep learning. *Journal of Glaciology*, 69, 13-26. <https://doi.org/10.1017/jog.2022.41>
- Jouvet, G. & Cordonnier, G. (2023) Ice-flow model emulator based on physics-informed deep learning. *Journal of Glaciology*, 1-15. <https://doi.org/10.1017/jog.2023.73>
- Jouvet, G. & Huss, M. (2019) Future retreat of Great Aletsch Glacier. *Journal of Glaciology*, 65, 869-872. <https://doi.org/10.1017/jog.2019.52>

- Jouvet, G., Huss, M., Funk, M. & Blatter, H. (2011) Modelling the retreat of Grosser Aletschgletscher, Switzerland, in a changing climate. *Journal of Glaciology*, 57, 1033-1045. <https://doi.org/10.3189/002214311798843359>
- Jouvet, G., Cordonnier, G., Kim, B., Lüthi, M., Vieli, A. & Aschwanden, A. (2022) Deep learning speeds up ice flow modelling by several orders of magnitude. *Journal of Glaciology*, 68, 651-664. <https://doi.org/10.1017/jog.2021.120>
- Kamb, B. & Echelmeyer, K.A. (1986) Stress-gradient coupling in glacier flow: I. longitudinal averaging of the influence of ice thickness and surface slope. *Journal of Glaciology*, 32, 267-284. <https://doi.org/10.1017/S0022143000015604>
- Kapannusch, R., Scherler, D., King, G. & Wittmann, H. (2020) Glacial influence on late Pleistocene <sup>10</sup>Be-derived paleo-erosion rates in the north-western Himalaya, India. *Earth and Planetary Science Letters*, 547, 116441. <https://doi.org/10.1016/j.epsl.2020.116441>
- Kayastha, R.B., Takeuchi, Y., Nakawo, M. & Ageta, Y. (2000) Practical prediction of ice melting beneath various thickness of debris cover on Khumbu Glacier, Nepal, using a positive degree-day factor. *IAHS Publication*, 264 (Symposium at Seattle, 2000 - *Debris-Covered Glaciers*), 71-81.
- Kenner, R., Phillips, M., Danioth, C., Denier, C., Thee, P. & Zraggen, A. (2011) Investigation of rock and ice loss in a recently deglaciated mountain rock wall using terrestrial laser scanning: Gemsstock, Swiss Alps. *Cold Regions Science and Technology*, 67, 157-164. <https://doi.org/10.1016/j.coldregions.2011.04.006>
- Kirkbride, M.P. (1993) The temporal significance of transitions from melting to calving termini at glaciers in the central Southern Alps of New Zealand. *Holocene*, 3, 232-240. <https://doi.org/10.1177/095968369300300305>
- Kirkbride, M.P. (1995) Processes of transportation. In: Menzies, J. (Ed.) *Modern glacial environments: processes, dynamics and sediments*. Butterworth-Heinemann, pp. 261-292.
- Kober, F., Hippe, K., Salcher, B., Ivy-Ochs, S., Kubik, P.W., Wacker, L. & Hähnen, N. (2012) Debris-flow-dependent variation of cosmogenically derived catchment-wide denudation rates. *Geology*, 40, 935-938. <https://doi.org/10.1130/G33406.1>
- Korschinek, G., Bergmaier, A., Faestermann, T., Gerstmann, U.C., Knie, K., Rugel, G., Wallner, A., Dillmann, I., Dollinger, G., Lierse von Gostomski, Ch., Kossert, K., Maiti, M., Poutivtsev, M. & Remmert, A. (2010) A new value for the half-life of <sup>10</sup>Be by Heavy-Ion Elastic Recoil Detection and liquid scintillation counting. *Nuclear Instruments and Methods in Physics Research B: Beam Interactions with Materials and Atoms*, 268, 187-191. <https://doi.org/10.1016/j.nimb.2009.09.020>
- Krautblatter, M., Moser, M., Schrott, L., Wolf, J. & Morche, D. (2012) Significance of rockfall magnitude and carbonate dissolution for rock slope erosion and geomorphic work on Alpine limestone cliffs (Reintal, German Alps). *Geomorphology*, 167-168, 21-34. <https://doi.org/10.1016/j.geomorph.2012.04.007>
- Krautblatter, M., Funk, D. & Günzel, F.K. (2013) Why permafrost rocks become unstable: a rock-ice-mechanical model in time and space. *Earth Surface Processes and Landforms*, 38, 876-887. <https://doi.org/10.1002/esp.3374>
- Kurowski, L. (1891) Die Höhe der Schneegrenze mit besonderer Berücksichtigung der Finsteraarhorn-Gruppe. *Penck's Geographische Abhandlungen*, 5, 119-160.
- Lal, D. (1991) Cosmic ray labeling of erosion surfaces: in situ nuclide production rates and erosion models. *Earth and Planetary Science Letters*, 104, 424-439. [https://doi.org/10.1016/0012-821X\(91\)90220-C](https://doi.org/10.1016/0012-821X(91)90220-C)
- Lambiel, C. & Talon, P. (2019) Les glaciers du haut val de Bagnes au Petit Age glaciaire. *Annales valaisannes. Actes du colloque Giétro 1818 sous la loupe des sciences*, 63-75.
- Langhammer, L., Rabenstein, L., Bauder, A. & Maurer, H. (2017) Ground-penetrating radar antenna orientation effects on temperate mountain glaciers. *Geophysics*, 82, H15-H24. <https://doi.org/10.1190/geo2016-0341.1>
- Lease, R.O. (2018) Pliocene erosional pulse and glacier-landscape feedbacks in the western Alaska Range. *Earth and Planetary Science Letters*, 497, 62-68. <https://doi.org/10.1016/j.epsl.2018.06.009>
- Lehmann, B., Herman, F., Valla, P.G., King, G.E., Biswas, R.H., Ivy-Ochs, S., Steinemann, O. & Christl, M. (2020) Postglacial erosion of bedrock surfaces and deglaciation timing: new insights from the Mont Blanc massif (western Alps). *Geology*, 48, 139-144. <https://doi.org/10.1130/G46585.1>

- Lehmann, B., Anderson, R.S., Bodin, X., Cusicanqui, D., Valla, P.G. & Carcaillet, J. (2022) Alpine rock glacier activity over Holocene to modern timescales (western French Alps). *Earth Surface Dynamics*, 10, 605-633. <https://doi.org/10.5194/esurf-10-605-2022>
- Leprince, S., Barbot, S., Ayoub, F. & Avouac, J.-P. (2007) Automatic and precise orthorectification, coregistration, and subpixel correlation of satellite images, application to ground deformation measurements. *IEEE Transactions on Geoscience and Remote Sensing*, 45, 1529-1558. <https://doi.org/10.1109/TGRS.2006.888937>
- Linsbauer, A., Huss, M., Hodel, E., Bauder, A., Fischer, M., Weidmann, Y., Bärtschi, H. & Schmassmann, E. (2021) The new Swiss Glacier Inventory SGI2016: from a topographical to a glaciological dataset. *Frontiers in Earth Science*, 9, 1-22. <https://doi.org/10.3389/feart.2021.704189>
- Lukens, C.E., Riebe, C.S., Sklar, L.S. & Shuster, D.L. (2016) Grain size bias in cosmogenic nuclide studies of stream sediment in steep terrain. *Journal of Geophysical Research: Earth Surface*, 121, 978-999. <https://doi.org/10.1002/2016JF003859>
- Lupker, M., Hippe, K., Wacker, L., Kober, F., Maden, C., Braucher, R., Bourlès, D., Vidal Romani, J.R. & Wieler, R. (2015) Depth-dependence of the production rate of *in situ*  $^{14}\text{C}$  in quartz from the Leymon High core, Spain. *Quaternary Geochronology*, 28, 80-87. <https://doi.org/10.1016/j.quageo.2015.04.004>
- Lupker, M., Hippe, K., Wacker, L., Steinemann, O., Tikhomirov, D., Maden, C., Haghipour, N. & Synal, H.-A. (2019) In-situ cosmogenic  $^{14}\text{C}$  analysis at ETH Zürich: characterization and performance of a new extraction system. *Nuclear Instruments and Methods in Physics Research Section B: Beam Interactions with Materials and Atoms*, 457, 30-36. <https://doi.org/10.1016/j.nimb.2019.07.028>
- Magnin, F., Josnin, J.-Y., Ravanel, L., Pergaud, J., Pohl, B. & Deline, P. (2017) Modelling rock wall permafrost degradation in the Mont Blanc massif from the LIA to the end of the 21st century. *The Cryosphere*, 11, 1813-1834. <https://doi.org/10.5194/tc-11-1813-2017>
- Mair, D., Lechmann, A., Yeşilyurt, S., Tikhomirov, D., Delunel, R., Vockenhuber, C., Akçar, N. & Schlunegger, F. (2019) Fast long-term denudation rate of steep alpine headwalls inferred from cosmogenic  $^{36}\text{Cl}$  depth profiles. *Scientific Reports*, 9, 1-15. <https://doi.org/10.1038/s41598-019-46969-0>
- Mair, D., Lechmann, A., Delunel, R., Yeşilyurt, S., Tikhomirov, D., Vockenhuber, C., Christl, M., Akçar, N. & Schlunegger, F. (2020) The role of frost cracking in local denudation of steep Alpine rockwalls over millennia (Eiger, Switzerland). *Earth Surface Dynamics*, 8, 637-659. <https://doi.org/10.5194/esurf-8-637-2020>
- Maisch, M., Wipf, A., Denneler, B., Battaglia, J. & Benz, C. (2000) Die Gletscher der Schweizer Alpen: Gletscherhochstand 1850, Aktuelle Vergletscherung, Gletscherschwund-Szenarien, Schlussbericht NFP 31, 2 Auflage, vdf Hochschulverlag an der ETH Zürich, 373 pp.
- Mancini, D. & Lane, S.N. (2020) Changes in sediment connectivity following glacial debuitressing in an Alpine valley system. *Geomorphology*, 352, 106987. <https://doi.org/10.1016/j.geomorph.2019.106987>
- Mann, M.E., Bradley, R.S. & Hughes, M.K. (1999) Northern hemisphere temperatures during the past millennium: inferences, uncertainties, and limitations. *Geophysical Research Letters*, 26, 759-762. <https://doi.org/10.1029/1999GL900070>
- Masarik, J., Kollar, D. & Vanya, S. (2000) Numerical simulation of in situ production of cosmogenic nuclides: effects of irradiation geometry. *Nuclear Instruments and Methods in Physics Research Section B: Beam Interactions with Materials and Atoms*, 172, 786-789. [https://doi.org/10.1016/S0168-583X\(00\)00121-X](https://doi.org/10.1016/S0168-583X(00)00121-X)
- Matmon, A., Bierman, P.R., Larsen, J., Southworth, S., Pavich, M., Finkel, R. & Caffee, M. (2003) Erosion of an ancient mountain range, the Great Smoky Mountains, North Carolina and Tennessee. *American Journal of Science*, 303, 817-855. <https://doi.org/10.2475/ajs.303.9.817>
- Matsuoka, N. & Murton, J. (2008) Frost weathering: recent advances and future directions. *Permafrost and Periglacial Processes*, 19, 195-210. <https://doi.org/10.1002/ppp.620>
- Matsuoka, N. & Sakai, H. (1999) Rockfall activity from an alpine cliff during thawing periods. *Geomorphology*, 28, 309-328. [https://doi.org/10.1016/S0169-555X\(98\)00116-0](https://doi.org/10.1016/S0169-555X(98)00116-0)
- Mattson, L.E., Gardner, J.S. & Young, G.J. (1993) Ablation on debris covered glaciers: an example from the Rakhiot Glacier, Punjab, Himalaya. *IAHS Publication*, 218 (Symposium at Kathmandu, Nepal 1992 - *Snow and Glacier Hydrology*), 289-296.

- McCarthy, M., Miles, E., Kneib, M., Buri, P., Fugger, S. & Pellicciotti, F. (2022) Supraglacial debris thickness and supply rate in High-Mountain Asia. *Communications Earth & Environment*, 3, 269. <https://doi.org/10.1038/s43247-022-00588-2>
- McCull, S.T. (2012) Paraglacial rock-slope stability. *Geomorphology*, 153-154, 1-16. <https://doi.org/10.1016/j.geomorph.2012.02.015>
- Menounos, B., Clague, J.J., Clarke, G.K.C., Marcott, S.A., Osborn, G., Clark, P.U., Tennant, C. & Novak, A.M. (2013) Did rock avalanche deposits modulate the late Holocene advance of Tiedemann Glacier, southern Coast Mountains, British Columbia, Canada? *Earth and Planetary Science Letters*, 384, 154-164. <https://doi.org/10.1016/j.epsl.2013.10.008>
- Millan, R., Mouginot, J., Rabatel, A. & Morlighem, M. (2022) Ice velocity and thickness of the world's glaciers. *Nature Geoscience*, 15, 124-129. <https://doi.org/10.1038/s41561-021-00885-z>
- Monnier, S. & Kinnard, C. (2015) Reconsidering the glacier to rock glacier transformation problem: new insights from the central Andes of Chile. *Geomorphology*, 238, 47-55. <https://doi.org/10.1016/j.geomorph.2015.02.025>
- Moore, J.R., Sanders, J.W., Dietrich, W.E. & Glaser, S.D. (2009) Influence of rock mass strength on the erosion rate of alpine cliffs. *Earth Surface Processes and Landforms*, 34, 1339-1352. <https://doi.org/10.1002/esp.1821>
- Mudd, S.M. (2017) Detection of transience in eroding landscapes. *Earth Surface Processes and Landforms*, 42, 24-41. <https://doi.org/10.1002/esp.3923>
- Müller, F., Caflisch, T. & Müller, G. (1976) Firn und Eis der Schweizer Alpen (Gletscherinventar), Publ. Nr. 57/57a, Geographisches Institut, ETH Zürich, 2 Vol.
- Murton, J.B., Peterson, R. & Ozouf, J.-C. (2006) Bedrock fracture by ice segregation in cold regions. *Science*, 314, 1127-1129. <https://doi.org/10.1126/science.1132127>
- NASA Shuttle Radar Topography Mission SRTM (2013) Shuttle Radar Topography Mission (SRTM) Global. OpenTopography. <https://doi.org/10.5069/G9445JDF>
- Naylor, S. & Gabet, E.J. (2007) Valley asymmetry and glacial versus nonglacial erosion in the Bitterroot Range, Montana, USA. *Geology*, 35, 375-378. <https://doi.org/10.1130/G23283A.1>
- Nichols, K.A. & Goehring, B.M. (2019) Isolation of quartz for cosmogenic in situ <sup>14</sup>C analysis. *Geochronology*, 1, 43-52. <https://doi.org/10.5194/gchron-1-43-2019>
- Nicholson, L. & Benn, D.I. (2006) Calculating ice melt beneath a debris layer using meteorological data. *Journal of Glaciology*, 52, 463-470. <https://doi.org/10.3189/172756506781828584>
- Niemi, N.A., Oskin, M., Burbank, D.W., Heimsath, A.M. & Gabet, E.J. (2005) Effects of bedrock landslides on cosmogenically determined erosion rates. *Earth and Planetary Science Letters*, 237, 480-498. <https://doi.org/10.1016/j.epsl.2005.07.009>
- Nye, J.F. (1952) The mechanics of glacier flow. *Journal of Glaciology*, 2, 82-93. <https://doi.org/10.3189/S0022143000033967>
- Nye, J.F. (1956) The distribution of stress and velocity in glaciers and ice-sheets. *Proceedings of the Royal Society of London, Series A: Mathematical and Physical Sciences*, 239, 113-133. <https://doi.org/10.1098/rspa.1957.0026>
- Olyphant, G.A. (1983) Analysis of the factors controlling cliff burial by talus within Blanca Massif, Southern Colorado, U.S.A. *Arctic and Alpine Research*, 15, 65-75. <https://doi.org/10.2307/1550982>
- Oskin, M. & Burbank, D.W. (2005) Alpine landscape evolution dominated by cirque retreat. *Geology*, 33, 933-936. <https://doi.org/10.1130/G21957.1>
- Østrem, G. (1959) Ice melting under a thin layer of moraine, and the existence of ice cores in moraine ridges. *Geografiska Annaler*, 41, 228-230. <https://doi.org/10.1080/20014422.1959.11907953>
- Quimet, W.B., Whipple, K.X. & Granger, D.E. (2009) Beyond threshold hillslopes: channel adjustment to base-level fall in tectonically active mountain ranges. *Geology*, 37, 579-582. <https://doi.org/10.1130/G30013A.1>

- Owen, L.A., Finkel, R.C., Barnard, P.L., Haizhou, M., Asahi, K., Caffee, M.W. & Derbyshire, E. (2005) Climatic and topographic controls on the style and timing of Late Quaternary glaciation throughout Tibet and the Himalaya defined by  $^{10}\text{Be}$  cosmogenic radionuclide surface exposure dating. *Quaternary Science Reviews*, 24, 1391-1411. <https://doi.org/10.1016/j.quascirev.2004.10.014>
- Paul, F., Kääb, A., Maisch, M., Kellenberger, T. & Haeberli, W. (2004) Rapid disintegration of Alpine glaciers observed with satellite data. *Geophysical Research Letters*, 31, L21402. <https://doi.org/10.1029/2004GL020816>
- Pepin, N., Bradley, R.S., Diaz, H.F., Baraer, M., Caceres, E.B., Forsythe, N., Fowler, H., Greenwood, G., Hashmi, M.Z., Liu, X.D., Miller, J.R., Ning, L., Ohmura, A., Palazzi, E., Rangwala, I., Schöner, W., Severskiy, I., Shahgedanova, M., Wang, M.B., Williamson, S.N. & Yang, D.Q. (2015) Elevation-dependent warming in mountain regions of the world. *Nature Climate Change*, 5, 424-430. <https://doi.org/10.1038/nclimate2563>
- Phillips, M., Wolter, A., Lüthi, R., Amann, F., Kenner, R. & Bühler, Y. (2016) Rock slope failure in a recently deglaciated permafrost rock wall at Piz Kesch (Eastern Swiss Alps), February 2014. *Earth Surface Processes and Landforms*, 42, 426-438. <https://doi.org/10.1002/esp.3992>
- Prager, C., Zangerl, C., Patzelt, G. & Brandner, R. (2008) Age distribution of fossil landslides in the Tyrol (Austria) and its surrounding areas. *Natural Hazards and Earth System Sciences*, 8, 377-407. <https://doi.org/10.5194/nhess-8-377-2008>
- Puchol, N., Lavé, J., Lupker, M., Blard, P.-H., Gallo, F. & France-Lanord, C. (2014) Grain size dependent concentration of cosmogenic  $^{10}\text{Be}$  and erosion dynamics in a landslide-dominated Himalayan watershed. *Geomorphology*, 224, 55-68. <https://doi.org/10.1016/j.geomorph.2014.06.019>
- Putkonen, J. & Swanson, T. (2003) Accuracy of cosmogenic ages for moraines. *Quaternary Research*, 59, 255-261. [https://doi.org/10.1016/S0033-5894\(03\)00006-1](https://doi.org/10.1016/S0033-5894(03)00006-1)
- Rabatel, A., Deline, P., Jaillet, S. & Ravanel, L. (2008) Rock falls in high-alpine rock walls quantified by terrestrial lidar measurements: a case study in the Mont Blanc area. *Geophysical Research Letters*, 35, L10502. <https://doi.org/10.1029/2008GL033424>
- Rapp, A. (1960) Recent development of mountain slopes in Kärkevagge and surroundings, Northern Scandinavia. *Geografiska Annaler*, 42, 65-200. <https://doi.org/10.1080/20014422.1960.11880942>
- Ravanel, L. & Deline, P. (2009) La face ouest des Drus (massif du Mont-Blanc): évolution de l'instabilité d'une paroi rocheuse dans la haute montagne alpine depuis la fin du petit âge glaciaire. *Géomorphologie: Relief, Processus, Environnement*, 4, 261-272. <https://doi.org/10.4000/geomorphologie.7444>
- Ravanel, L. & Deline, P. (2011) Climate influence on rockfalls in high-Alpine steep rockwalls: the north side of the Aiguilles de Chamonix (Mont Blanc massif) since the end of the 'Little Ice Age'. *The Holocene*, 21, 357-365. <https://doi.org/10.1177/0959683610374887>
- Ravanel, L., Allignol, F., Deline, P., Gruber, S. & Ravello, M. (2010) Rock falls in the Mont Blanc Massif in 2007 and 2008. *Landslides*, 7, 493-501. <https://doi.org/10.1007/s10346-010-0206-z>
- Ravanel, L., Magnin, F. & Deline, P. (2017) Impacts of the 2003 and 2015 summer heatwaves on permafrost-affected rock-walls in the Mont Blanc massif. *Science of the Total Environment*, 609, 132-143. <https://doi.org/10.1016/j.scitotenv.2017.07.055>
- Reid, T.D. & Brock, B.W. (2010) An energy-balance model for debris-covered glaciers including heat conduction through the debris layer. *Journal of Glaciology*, 56, 903-916. <https://doi.org/10.3189/002214310794457218>
- Rempel, A.W., Marshall, J.A. & Roering, J.J. (2016) Modeling relative frost weathering rates at geomorphic scales. *Earth and Planetary Science Letters*, 453, 87-95. <https://doi.org/10.1016/j.epsl.2016.08.019>
- Roering, J.J., Kirchner, J.W. & Dietrich, W.E. (1999) Evidence for nonlinear, diffusive sediment transport on hillslopes and implications for landscape morphology. *Water Resources Research*, 35, 853-870. <https://doi.org/10.1029/1998WR900090>
- Roering, J.J., Kirchner, J.W. & Dietrich, W.E. (2001) Hillslope evolution by nonlinear, slope-dependent transport: steady state morphology and equilibrium adjustment timescales. *Journal of Geophysical Research: Solid Earth*, 106, 16499-16513. <https://doi.org/10.1029/2001JB000323>
- Rounce, D.R., Hock, R., Maussion, F., Hugonnet, R., Kochtitzky, W., Huss, M., Berthier, E., Brinkerhoff, D., Compagno, L., Copland, L., Farinotti, D., Menounos, B. & McNabb, R.W. (2023) Global glacier change in

- the 21st century: every increase in temperature matters. *Science*, 379, 78-83. <https://doi.org/10.1126/science.abo1324>
- Rowan, A.V., Egholm, D.L., Quincey, D.J. & Glasser, N.F. (2015) Modelling the feedbacks between mass balance, ice flow and debris transport to predict the response to climate change of debris-covered glaciers in the Himalaya. *Earth and Planetary Science Letters*, 430, 427-438. <https://doi.org/10.1016/j.epsl.2015.09.004>
- Ruff, M., Wacker, L., Gäggeler, H.W., Suter, M., Synal, H.-A. & Szidat, S. (2007) A gas ion source for radiocarbon measurements at 200 kV. *Radiocarbon*, 49, 307-314. <https://doi.org/10.1017/S0033822200042235>
- Ruiz-Carulla, R., Corominas, J. & Mavrouli, O. (2015) A methodology to obtain the block size distribution of fragmental rockfall deposits. *Landslides*, 12, 815-825. <https://doi.org/10.1007/s10346-015-0600-7>
- Ruiz-Carulla, R., Corominas, J. & Mavrouli, O. (2017) A fractal fragmentation model for rockfalls. *Landslides*, 14, 875-889. <https://doi.org/10.1007/s10346-016-0773-8>
- Sanders, J.W., Cuffey, K.M., Moore, J.R., MacGregor, K.R. & Kavanaugh, J.L. (2012) Periglacial weathering and headwall erosion in cirque glacier bergschrunds. *Geology*, 40, 779-782. <https://doi.org/10.1130/G33330.1>
- Sanders, J.W., Cuffey, K.M., MacGregor, K.R. & Collins, B.D. (2013) The sediment budget of an alpine cirque. *Geological Society of America Bulletin*, 125, 229-248. <https://doi.org/10.1130/B30688.1>
- Sarr, A.-C., Mugnier, J.-L., Abrahams, R., Carcaillet, J. & Ravanel, L. (2019) Sidewall erosion: insights from in situ-produced <sup>10</sup>Be concentrations measured on supraglacial clasts (Mont Blanc massif, France). *Earth Surface Processes and Landforms*, 44, 1930-1944. <https://doi.org/10.1002/esp.4620>
- Sass, O. (2005) Spatial patterns of rockfall intensity in the northern Alps. *Zeitschrift für Geomorphologie Supplementband*, 138, 51-65.
- Sass, O. (2007) Bedrock detection and talus thickness assessment in the European Alps using geophysical methods. *Journal of Applied Geophysics*, 62, 254-269. <https://doi.org/10.1016/j.jappgeo.2006.12.003>
- Sass, O. (2010) Spatial and temporal patterns of talus activity - a lichenometric approach in the Stubai Alps, Austria. *Geografiska Annaler: Series A, Physical Geography*, 92, 375-391. <https://doi.org/10.1111/j.1468-0459.2010.00402.x>
- Schaefer, J.M., Denton, G.H., Barrell, D.J.A., Ivy-Ochs, S., Kubik, P.W., Andersen, B.G., Phillips, F.M., Lowell, T.V. & Schluchter, C. (2006) Near-synchronous interhemispheric termination of the Last Glacial Maximum in mid-latitudes. *Science*, 312, 1510-1513. <https://doi.org/10.1126/science.1122872>
- Schaller, M., von Blanckenburg, F., Hovius, N. & Kubik, P.W. (2001) Large-scale erosion rates from in situ-produced cosmogenic nuclides in European river sediments. *Earth and Planetary Science Letters*, 188, 441-458. [https://doi.org/10.1016/S0012-821X\(01\)00320-X](https://doi.org/10.1016/S0012-821X(01)00320-X)
- Scherler, D. (2014) Climatic limits to headwall retreat in the Khumbu Himalaya, eastern Nepal. *Geology*, 42, 1019-1022. <https://doi.org/10.1130/G35975.1>
- Scherler, D. & Egholm, D.L. (2020) Production and transport of supraglacial debris: insights from cosmogenic <sup>10</sup>Be and numerical modeling, Chhota Shigri Glacier, Indian Himalaya. *Journal of Geophysical Research: Earth Surface*, 125, e2020JF005586. <https://doi.org/10.1029/2020JF005586>
- Scherler, D., Leprince, S. & Strecker, M.R. (2008) Glacier-surface velocities in alpine terrain from optical satellite imagery - Accuracy improvement and quality assessment. *Remote Sensing of Environment*, 112, 3806-3819. <https://doi.org/10.1016/j.rse.2008.05.018>
- Scherler, D., Bookhagen, B. & Strecker, M.R. (2011a) Hillslope-glacier coupling: the interplay of topography and glacial dynamics in High Asia. *Journal of Geophysical Research: Earth Surface*, 116, F02019. <https://doi.org/10.1029/2010JF001751>
- Scherler, D., Bookhagen, B. & Strecker, M.R. (2011b) Spatially variable response of Himalayan glaciers to climate change affected by debris cover. *Nature Geoscience*, 4, 156-159. <https://doi.org/10.1038/NGEO1068>
- Schimmelpfennig, I., Schaefer, J.M., Lamp, J., Godard, V., Schwartz, R., Bard, E., Tuna, T., Akçar, N., Schlüchter, C., Zimmerman, S. & ASTER Team (2022) Glacier response to Holocene warmth inferred from in situ <sup>10</sup>Be and <sup>14</sup>C bedrock analyses in Steingletscher's forefield (central Swiss Alps). *Climate of the Past*, 18, 23-44. <https://doi.org/10.5194/cp-18-23-2022>

- Schwanghart, W. & Scherler, D. (2014) Short Communication: TopoToolbox 2 - MATLAB-based software for topographic analysis and modeling in Earth surface sciences. *Earth Surface Dynamics*, 2, 1-7. <https://doi.org/10.5194/esurf-2-1-2014>
- Seong, Y.B., Owen, L.A., Caffee, M.W., Kamp, U., Bishop, M.P., Bush, A., Copland, L. & Shroder, J.F. (2009) Rates of basin-wide rockwall retreat in the K2 region of the Central Karakoram defined by terrestrial cosmogenic nuclide  $^{10}\text{Be}$ . *Geomorphology*, 107, 254-262. <https://doi.org/10.1016/j.geomorph.2008.12.014>
- Shuster, D.L., Ehlers, T.A., Rusmoren, M.E. & Farley, K.A. (2005) Rapid glacial erosion at 1.8 Ma revealed by  $^4\text{He}/^3\text{He}$  thermochronometry. *Science*, 310, 1668-1670. <https://doi.org/10.1126/science.1118519>
- Siewert, M.B., Krautblatter, M., Christiansen, H.H. & Eckerstorfer, M. (2012) Arctic rockwall retreat rates estimated using laboratory-calibrated ERT measurements of talus cones in Longyeardalen, Svalbard. *Earth Surface Processes and Landforms*, 37, 1542-1555. <https://doi.org/10.1002/esp.3297>
- Skov, D.S., Egholm, D.L., Jansen, J.D., Sandiford, M. & Knudsen, M.F. (2019) Detecting landscape transience with in situ cosmogenic  $^{14}\text{C}$  and  $^{10}\text{Be}$ . *Quaternary Geochronology*, 54, 101008. <https://doi.org/10.1016/j.quageo.2019.101008>
- Slymaker, O. (2011) Criteria to distinguish between periglacial, proglacial and paraglacial environments. *Quaestiones Geographicae*, 30, 85-94. <https://doi.org/10.2478/v10117-011-0008-y>
- SLF (2021) Swiss Federal Institute for Snow and Avalanche Research, <https://www.slf.ch/de/index.html> (last access: 21 May 2021).
- Small, R.J. & Clark, M.J. (1974) The medial moraines of the lower Glacier de Tsidjiore Nouve, Valais, Switzerland. *Journal of Glaciology*, 13, 255-263. <https://doi.org/10.3189/S0022143000023066>
- Small, R.J. & Gomez, B. (1981) The nature and origin of debris layers within Glacier de Tsidjiore Nouve, Valais, Switzerland. *Annals of Glaciology*, 2, 109-113. <https://doi.org/10.3189/172756481794352414>
- Small, R.J., Clark, M.J. & Cawse, T.J.P. (1979) The formation of medial moraines on Alpine glaciers. *Journal of Glaciology*, 22, 43-52. <https://doi.org/10.3189/S0022143000014040>
- Small, E.E., Anderson, R.S., Repka, J.L. & Finkel, R. (1997) Erosion rates of alpine bedrock summit surfaces deduced from in situ  $^{10}\text{Be}$  and  $^{26}\text{Al}$ . *Earth and Planetary Science Letters*, 150, 413-425. [https://doi.org/10.1016/S0012-821X\(97\)00092-7](https://doi.org/10.1016/S0012-821X(97)00092-7)
- Smith, S.L., O'Neill, H.B., Isaksen, K., Noetzli, J. & Romanovsky, V.E. (2022) The changing thermal state of permafrost. *Nature Reviews Earth & Environment*, 3, 10-23. <https://doi.org/10.1038/s43017-021-00240-1>
- Stone, J.O. (2000) Air pressure and cosmogenic isotope production. *Journal of Geophysical Research: Solid Earth*, 105, 23753-23759. <https://doi.org/10.1029/2000JB900181>
- Strunden, J., Ehlers, T.A., Brehm, D. & Nettesheim, M. (2015) Spatial and temporal variations in rockfall determined from TLS measurements in a deglaciated valley, Switzerland. *Journal of Geophysical Research: Earth Surface*, 120, 1251-1273. <https://doi.org/10.1002/2014JF003274>
- Swisstopo (2021) Federal Office of Topography Swisstopo, online map viewer, <https://map.geo.admin.ch> (last access: 21 May 2021).
- Swisstopo (2022) Federal Office of Topography Swisstopo, online map viewer, <https://map.geo.admin.ch> (last access: 14 November 2022).
- Swisstopo (2023) Federal Office of Topography Swisstopo, online map viewer, <https://map.geo.admin.ch> (last access: 11 October 2023).
- Synal, H.-A., Stocker, M. & Suter, M. (2007) MICADAS: a new compact radiocarbon AMS system. *Nuclear Instruments and Methods in Physics Research Section B: Beam Interactions with Materials and Atoms*, 259, 7-13. <https://doi.org/10.1016/j.nimb.2007.01.138>
- Tofelde, S., Duesing, W., Schildgen, T.F., Wickert, A.D., Wittmann, H., Alonso, R.N. & Strecker, M. (2018) Effects of deep-seated versus shallow hillslope processes on cosmogenic  $^{10}\text{Be}$  concentrations in fluvial sand and gravel. *Earth Surface Processes and Landforms*, 43, 3086-3098. <https://doi.org/10.1002/esp.4471>
- Tovar, D.S., Shulmeister, J. & Davies, T.R. (2008) Evidence for a landslide origin of New Zealand's Waiho Loop moraine. *Nature Geoscience*, 1, 524-526. <https://doi.org/10.1038/ngeo249>

- Tuck, R. (1935) Asymmetrical topography in high latitudes resulting from alpine glacial erosion. *The Journal of Geology*, 43, 530-538. <https://doi.org/10.1086/624333>
- Vacco, D.A., Alley, R.B. & Pollard, D. (2010) Glacial advance and stagnation caused by rock avalanches. *Earth and Planetary Science Letters*, 294, 123-130. <https://doi.org/10.1016/j.epsl.2010.03.019>
- Valla, P.G., van der Beek, P.A., Shuster, D.L., Braun, J., Herman, F., Tassan-Got, L. & Gautheron, C. (2012) Late Neogene exhumation and relief development of the Aar and Aiguilles Rouges massifs (Swiss Alps) from low-temperature thermochronology modeling and  $^4\text{He}/^3\text{He}$  thermochronometry. *Journal of Geophysical Research: Earth Surface*, 117, F01004. <https://doi.org/10.1029/2011JF002043>
- van Dongen, R., Scherler, D., Wittmann, H. & von Blanckenburg, F. (2019) Cosmogenic  $^{10}\text{Be}$  in river sediment: where grain size matters and why. *Earth Surface Dynamics*, 7, 393-410. <https://doi.org/10.5194/esurf-7-393-2019>
- Vincent, C., Wagnon, P., Shea, J.M., Immerzeel, W.W., Kraaijenbrink, P., Shrestha, D., Soruco, A., Arnaud, Y., Brun, F., Berthier, E. & Sherpa, S.F. (2016) Reduced melt on debris-covered glaciers: investigations from Changri Nup Glacier, Nepal. *The Cryosphere*, 10, 1845-1858. <https://doi.org/10.5194/tc-10-1845-2016>
- von Blanckenburg, F. (2005) The control mechanisms of erosion and weathering at basin scale from cosmogenic nuclides in river sediment. *Earth and Planetary Science Letters*, 237, 462-479. <https://doi.org/10.1016/j.epsl.2005.06.030>
- von Blanckenburg, F. & Willenbring, J.K. (2014) Cosmogenic nuclides: dates and rates of Earth-Surface change. *Elements*, 10, 341-346. <https://doi.org/10.2113/gselements.10.5.341>
- von Blanckenburg, F., Hewawasam, T. & Kubik, P.W. (2004) Cosmogenic nuclide evidence for low weathering and denudation in the wet, tropical highlands of Sri Lanka. *Journal of Geophysical Research: Earth Surface*, 109, F03008. <https://doi.org/10.1029/2003JF000049>
- Wacker, L., Bonani, G., Friedrich, M., Hajdas, I., Kromer, B., Nĕmec, M., Ruff, M., Suter, M., Synal, H.-A. & Vockenhuber, C. (2010) MICADAS: routine and high-precision radiocarbon dating. *Radiocarbon*, 52, 252-262. <https://doi.org/10.1017/s0033822200045288>
- Walder, J. & Hallet, B. (1985) A theoretical model of the fracture of rock during freezing. *Geological Society of America Bulletin*, 96, 336-346. [https://doi.org/10.1130/0016-7606\(1985\)96<336:ATMOTF>2.0.CO;2](https://doi.org/10.1130/0016-7606(1985)96<336:ATMOTF>2.0.CO;2)
- Ward, D.J. & Anderson, R.S. (2011) The use of ablation-dominated medial moraines as samplers for  $^{10}\text{Be}$ -derived erosion rates of glacier valley walls, Kichatna Mountains, AK. *Earth Surface Processes and Landforms*, 36, 495-512. <https://doi.org/10.1002/esp.2068>
- Wegmann, M., Gudmundsson, G.H. & Haeberli, W. (1998) Permafrost changes in rock walls and the retreat of alpine glaciers: a thermal modelling approach. *Permafrost and Periglacial Processes*, 9, 23-33. [https://doi.org/10.1002/\(SICI\)1099-1530\(199801/03\)9:1<23::AID-PPP274>3.0.CO;2-Y](https://doi.org/10.1002/(SICI)1099-1530(199801/03)9:1<23::AID-PPP274>3.0.CO;2-Y)
- West, A.J., Hetzel, R., Li, G., Jin, Z., Zhang, F., Hilton, R.G. & Densmore, A.L. (2014) Dilution of  $^{10}\text{Be}$  in detrital quartz by earthquake-induced landslides: implications for determining denudation rates and potential to provide insights into landslide sediment dynamics. *Earth and Planetary Science Letters*, 396, 143-153. <https://doi.org/10.1016/j.epsl.2014.03.058>
- Wetterauer, K. & Scherler, D. (2023a) Spatial and temporal variations in rockwall erosion rates derived from cosmogenic  $^{10}\text{Be}$  in medial moraine at five valley glaciers around Pigne d'Arolla, Switzerland. *Earth Surface Dynamics*, 11, 1013-1033. <https://doi.org/10.5194/esurf-11-1013-2023>
- Wetterauer, K. & Scherler, D. (2023b) Medial moraine cosmogenic  $^{10}\text{Be}$  data and glacier surface velocities from four Swiss valley glaciers around Pigne d'Arolla. *GFZ Data Services*. <https://doi.org/10.5880/GFZ.3.3.2023.002>
- Wetterauer, K., Scherler, D., Anderson, L.S. & Wittmann, H. (2022a) Temporal evolution of headwall erosion rates derived from cosmogenic nuclide concentrations in the medial moraines of Glacier d'Otemma, Switzerland. *Earth Surface Processes and Landforms*, 47, 2437-2454. <https://doi.org/10.1002/esp.5386>
- Wetterauer, K., Scherler, D., Anderson, L.S. & Wittmann, H. (2022b) Sample and modelling data for cosmogenic  $^{10}\text{Be}$  in medial moraine debris of Glacier d'Otemma, Switzerland. *GFZ Data Services*. <https://doi.org/10.5880/GFZ.3.3.2021.007>

- Whalley, W.B. (1974) Origin of rock glaciers. *Journal of Glaciology*, 13, 323-324. <https://doi.org/10.3189/S0022143000023145>
- Wirsig, C., Ivy-Ochs, S., Akçar, N., Lupker, M., Hippe, K., Wacker, L., Vockenhuber, C. & Schlüchter, C. (2016) Combined cosmogenic  $^{10}\text{Be}$ , in situ  $^{14}\text{C}$  and  $^{36}\text{Cl}$  concentrations constrain Holocene history and erosion depth of Grueben glacier (CH). *Swiss Journal of Geosciences*, 109, 379-388. <https://doi.org/10.1007/s00015-016-0227-2>
- Wirsig, C., Ivy-Ochs, S., Reitner, J.M., Christl, M., Vockenhuber, C., Bichler, M. & Reindl, M. (2017) Subglacial abrasion rates at Goldbergkees, Hohe Tauern, Austria, determined from cosmogenic  $^{10}\text{Be}$  and  $^{36}\text{Cl}$  concentrations. *Earth Surface Processes and Landforms*, 42, 1119-1131. <https://doi.org/10.1002/esp.4093>
- Wittmann, H., von Blanckenburg, F., Kruesmann, T., Norton, K.P. & Kubik, P.W. (2007) Relation between rock uplift and denudation from cosmogenic nuclides in river sediment in the Central Alps of Switzerland. *Journal of Geophysical Research: Earth Surface*, 112, F04010. <https://doi.org/10.1029/2006JF000729>
- Žebre, M., Colucci, R.R., Giorgi, F., Glasser, N.F., Racoviteanu, A.E. & Del Gobbo, C. (2021) 200 years of equilibrium-line altitude variability across the European Alps (1901- 2100). *Climate Dynamics*, 56, 1183-1201. <https://doi.org/10.1007/s00382-020-05525-7>
- Zemp, M., Paul, F., Hoelzle, M. & Haeberli, W. (2008) Glacier fluctuations in the European Alps, 1850-2000: an overview and spatio-temporal analysis of available data. In: Orlove, B., Wiegandt, E. & Luckman, B.H. (Eds.) *Darkening Peaks: Glacier Retreat, Science, and Society*. University of California Press, pp. 152-167. <https://doi.org/10.5167/uzh-9024>
- Zemp, M., Huss, M., Thibert, E., Eckert, N., McNabb, R., Huber, J., Barandun, M., Machguth, H., Nussbaumer, S.U., Gärtner-Roer, I., Thomson, L., Paul, F., Maussion, F., Kutuzov, S. & Cogley, J.G. (2019) Global glacier mass changes and their contributions to sea-level rise from 1961 to 2016. *Nature*, 568, 382-386. <https://doi.org/10.1038/s41586-019-1071-0>

## Appendix A: supplement of Chapter 2

**Sections A1-A2 are part of the accompanying data publication:**

Wetterauer, K., Scherler, D., Anderson, L.S. & Wittmann, H. (2022b)

Sample and modelling data for cosmogenic  $^{10}\text{Be}$  in medial moraine debris of Glacier  
d'Otemma, Switzerland.

*GFZ Data Services.*

<https://doi.org/10.5880/GFZ.3.3.2021.007>

To avoid repetition, only the text sections, figures and tables of the data publication are listed that contain additional information and data not presented in Chapter 2.

## A1 Sample data

Cosmogenic nuclide sample processing was performed according to standard *in situ*-produced  $^{10}\text{Be}$  separation techniques (e.g., von Blanckenburg *et al.*, 2004) and carried out in the Helmholtz Laboratory for the Geochemistry of the Earth Surface (HELGES) at the GFZ German Research Centre for Geosciences in Potsdam, Germany. Debris samples were dried and sieved into different fractions (**Figure A1**). Individual size fractions were then crushed down to the 0.125-1 mm fraction for further analysis. By means of physical (involving magnetic separator) and chemical (involving weak leaching procedures with hydrochloric acid, and repeatedly with hydrofluoric acid and orthophosphoric acid) separation, the quartz minerals were isolated and purified. *Meteoritic*  $^{10}\text{Be}$  was removed with an additional hydrofluoric acid leach. ~22-32 g of pure quartz were spiked with 0.2 g  $^9\text{Be}$  carrier (770 ppm) before being decomposed in concentrated hydrofluoric acid. Cosmogenic  $^{10}\text{Be}$  was extracted using ion exchange chromatography, precipitated from the eluted solution, oxidized, and pressed into targets.

A total of 29  $^{10}\text{Be}/^9\text{Be}$  ratio measurements (**Table 2.2**) were carried out at the accelerator mass spectrometer (AMS) at the University of Cologne, Germany (Dewald *et al.*, 2013), normalized to the standards KN01-6-2 (nominal  $^{10}\text{Be}/^9\text{Be}$  value:  $5.35 \times 10^{-13}$ ) and KN01-5-3 (nominal  $^{10}\text{Be}/^9\text{Be}$  value:  $6.32 \times 10^{-12}$ ).  $^{10}\text{Be}/^9\text{Be}$  ratios were converted into  $[\text{Be}]_{\text{measured}}$  and corrected for co-processed blanks with  $^{10}\text{Be}/^9\text{Be}$  ratios of  $4.43 \times 10^{-15}$ ,  $2.16 \times 10^{-15}$ ,  $2.55 \times 10^{-16}$ ,  $7.65 \times 10^{-16}$ , and  $1.19 \times 10^{-15}$  according to the respective sample batches. A fine grain size fraction (0.125-4 mm) was measured for 13 samples, an additional coarse grain size fraction (4-22.4 mm) for 6 samples, and five grain size sub-samples (0.125-0.8, 0.8-2, 2-4, 4-8, and 8-16 mm) for 2 samples (**Table 2.2**).

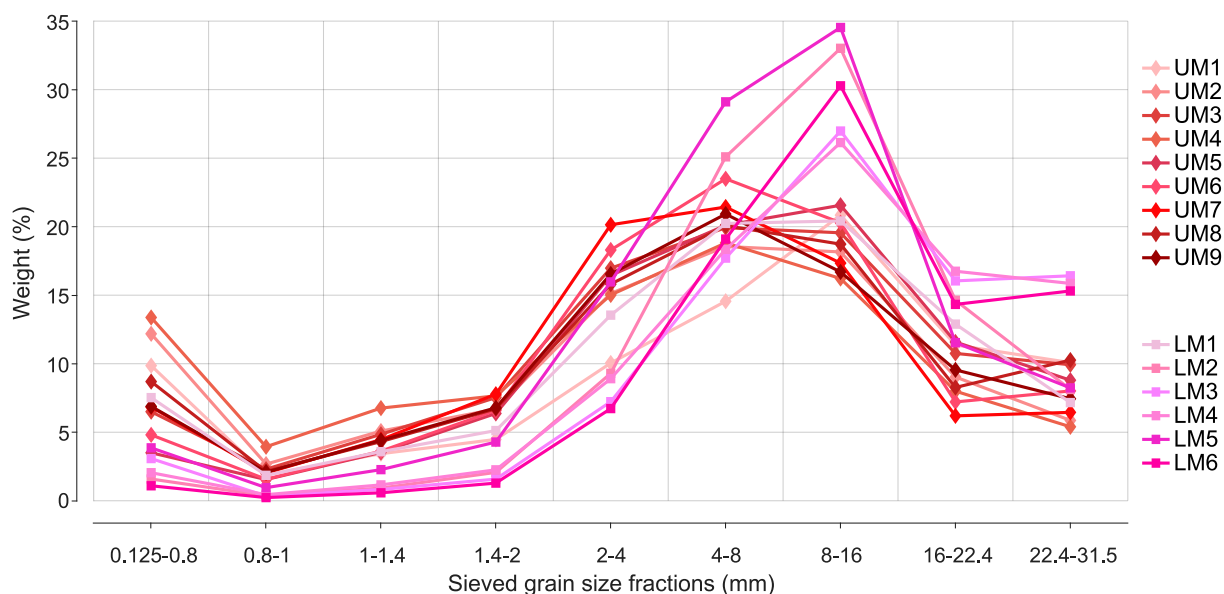


**Figure A1:** Grain size spectra of the 15 amalgamated medial moraine samples from Glacier d'Otemma. All samples are normalized to their bulk sample weight and presented in % for each sieved fraction. UM/LM: upper/lower medial moraine

## A2 Modelling data

$[^{10}\text{Be}]_{\text{measured}}$  from medial moraine debris are composed of  $[^{10}\text{Be}]_{\text{headwall}}$  accumulated during headwall exhumation/erosion and  $[^{10}\text{Be}]_{\text{transport}}$  accumulated during downglacier debris transport (see Section 2.4.2). To derive  $[^{10}\text{Be}]_{\text{headwall}}$  and sample ages we used a simple 1D model to correct  $[^{10}\text{Be}]_{\text{measured}}$  for  $[^{10}\text{Be}]_{\text{transport}}$ . The model computes debris trajectories and nuclide accumulation from source headwalls to sample locations through the glacier and through time, as a function of transport distance, glacier surface velocity and mass balance, and surface  $^{10}\text{Be}$  production rates (**Figure 2.4**).

### A2.1 Computation of horizontal transport

We are not aware of any recent or past velocity measurements on Glacier d’Otemma. Therefore, the assessment of horizontal debris transport is based on a threefold computation of glacier surface velocity, combining (i) satellite imagery correlation, (ii) Glen’s flow law, and (iii) hand-tracing of boulder displacements across historical aerial images (**Figure A2a-c**).

(i) We produced new, recent remotely sensed glacier surface velocities (**Figure A2c**) from Landsat 8, band 8, 15 m resolution satellite imagery from the year 2015 to 2020, using the software package COSI-Corr (Co-registration of Optically Sensed Images and Correlation; Leprince *et al.*, 2007; Caltech, 2021) and following the approach implemented in Scherler *et al.* (2008).

(ii) We reconstructed past glacier surface velocities with Glen’s flow law (Glen, 1952, 1955) after tuning the flow law parameter  $A$  with recent surface velocities and ice thickness estimates (**Figure A2a-c**). Recent and past surface velocities  $U_s$  ( $\text{m yr}^{-1}$ ) are based on ice transfer by internal deformation only and were calculated according to the mathematical description in Anderson and Anderson (2010):

$$U_s = A [\rho_i g \sin(\theta)]^n \left[ \frac{H^{n+1}}{n+1} \right] \quad (\text{A1})$$

where  $A$  is the flow law parameter ( $\text{Pa}^{-3} \text{s}^{-1}$ ),  $\rho_i$  is the density of ice ( $\text{kg m}^{-3}$ ),  $g$  is the gravity constant ( $\text{m s}^{-2}$ ),  $n$  is an exponent (approximately 3 for ice; Glen, 1952),  $\theta$  is the ice surface slope, and  $H$  is the ice thickness (m) (for parameter values used see **Table A1**). Information on recent and past conditions of Glacier d’Otemma were compiled from different sources: Recent ice thicknesses (**Figure A2a**) stem from the global ice thickness distribution dataset by Farinotti *et al.* (2019). Past ice thicknesses (**Figure A2a**) were estimated from contour lines of vertical glacier change between 1850 and 2009 by a reconstruction study (**Figure A3a**; cf. Figure 4 in Lambiel & Talon, 2019). Since our model path follows the UM, which largely follows the central glacier flowline, we linearly interpolated between contour lines (**Figure A3b**). Recent ice surface slopes (**Figure A2b**) were derived from a digital elevation model (DEM) of 30 m resolution (global raster dataset SRTM GL1; NASA Shuttle Radar Topography Mission SRTM, 2013), past ice surface slopes (**Figure A2b**) from the reconstructed ice surface elevations in 1850, all being smoothed by applying filters. We calibrated  $A$  by fitting the recent surface velocities from Glen’s flow law to the recent remotely sensed surface velocities (**Figure A2c**).

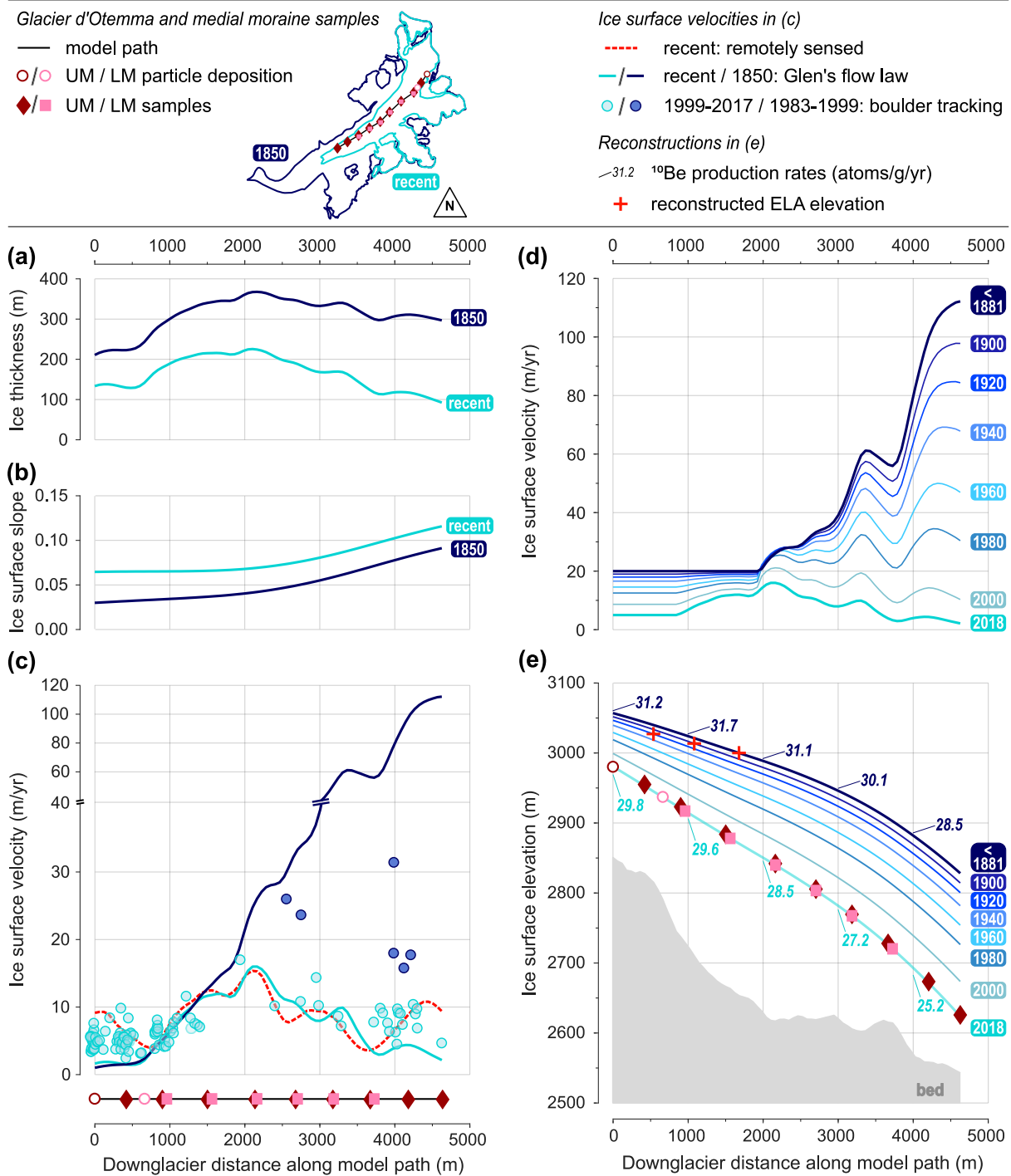


**Figure A2:** Data used to simulate medial moraine debris transport on Glacier d'Otemma through time. **(a)** Ice thicknesses along the medial moraines used with Glen's flow law (recent data by Farinotti *et al.*, 2019; 1850 data by Lambiel & Talon, 2019). **(b)** Ice surface slopes along the medial moraines used with Glen's flow law. **(c)** Ice surface velocity data along the medial moraines derived from remote sensing techniques, boulder tracking, and Glen's flow law. Note the y-axis break and indicated downglacier sample distances. **(d)** Reconstructed ice surface velocities along the medial moraines through time, shown exemplarily for ~20-year intervals. **(e)** Reconstructed ice surface elevations and ELA along the medial moraines through time, shown exemplarily for ~20-year intervals, and <sup>10</sup>Be production rates. Note the reconstructed ELA rising above the displayed range for younger times. UM/LM: upper/lower medial moraine; ELA: equilibrium line altitude

**Table A1:** List of parameters used within the 1D debris particle trajectory model.

Parameter	Definition	Unit	Value used
$A$	Flow law parameter	$\text{Pa}^{-3} \text{s}^{-1}$	$3.33 \times 10^{-24}$
$r_i$	Density of ice	$\text{g cm}^{-3}$	0.917
$g$	Gravity constant	$\text{m s}^{-2}$	9.81
$n$	Exponent of Glen's flow law	-	3
$U_s$ min (1850)	Minimum velocity close to headwalls for 1850	$\text{m yr}^{-1}$	20
$U_s$ min (recent)	Minimum velocity close to headwalls for 2018	$\text{m yr}^{-1}$	5
ELA (1850)	Average ELA elevation for 1850	m	3000
ELA (recent)	Average ELA elevation for 2018	m	3200
Mass balance gradient	Change with elevation	m w.e. $100 \text{ m}^{-1} \text{ yr}^{-1}$	0.7
Mass balance max	Maximum accumulation above ELA	m w.e. $\text{yr}^{-1}$	0.75
$\lambda$	$^{10}\text{Be}$ decay constant	$\text{yr}^{-1}$	$4.997 \times 10^{-7}$
$L$	Absorption mean free path	$\text{g cm}^{-2}$	160
$r_w$	Density of water	$\text{g cm}^{-3}$	1.0
$r_s$	Density of snow	$\text{g cm}^{-3}$	0.3
$r_d$	Density of debris	$\text{g cm}^{-3}$	2.0
$z_s$	Average snow cover thickness	cm	100
$z_d$	Average debris cover thickness	cm	5

Both the datasets used with Glen's flow law and the recent (2018) and reconstructed (1850) glacier surface velocities are provided in **Table A2**. Whereas approximations for recent surface velocities from Glen's flow law and from recent remotely sensed surface velocities agree well in the central part of the downglacier profile, larger deviations appear close to the glacier head and terminus (**Figure A2c**). These marginal areas yield unlikely low surface velocities, particularly for 1850. However, especially close to the headwalls a good velocity estimate is needed, as it will set the pace of environmental changes and ultimately the shape of debris trajectories through the glacier.

(iii) Therefore, we additionally tracked boulders across historical aerial images (Swisstopo, 2021) of both medial moraines to better constrain upper glacier velocities (**Figure A2c**). Only boulder pathways were chosen where a boulder obviously moved parallel to the glacier flowline. On this basis, recent surface velocities close to the headwalls were set to a minimum of  $5 \text{ m yr}^{-1}$  (**Figure A2d**). Unfortunately, photogrammetry could not be applied further back in time than 1983 and boulder tracking close to the headwall proved difficult for the 20th century. Yet, boulder velocities from the 21st century turned out to be similar, close to the glacier head and terminus (**Figure A2c**). We therefore used velocities  $>15 \text{ m yr}^{-1}$  tracked closer to the terminus in the 1980s and 1990s as indicators to set surface velocities of 1850, when the ice was significantly thicker, to a minimum of  $20 \text{ m yr}^{-1}$  (**Figure A2d**). Further, the presently isolated small glacier in the saddle-like centre of Petit Mont Collon, which used to be connected to the glacier's main trunk in 1850 (**Figure 2.7a,b**), served as an indicator for us to define higher past minimum velocities than today. This additional and steeply inclined ice tributary presumably will have accelerated past glacier flow close to the headwalls.

The reconstructed glacier changes along the model path through time are depicted in **Figure A2d,e**. Based on an imposed three-fold linear lowering of the ice surface through time (see Section A2.3; **Figure A2e**), modelled glacier surface velocities decline towards today (**Figure A2d**). For years before 1881, glacier surface velocities increase downglacier from the pre-defined minimum velocity of  $20 \text{ m yr}^{-1}$  close to the headwalls to a maximum of  $\sim 120 \text{ m yr}^{-1}$  at the lowermost sample location. At present, minimum velocities of  $5 \text{ m yr}^{-1}$  close to the

headwalls increase up to  $\sim 16 \text{ m yr}^{-1}$  halfway downglacier, before they decrease to low velocities of  $\sim 2 \text{ m yr}^{-1}$  at the lowermost sample location close to the current glacier terminus.

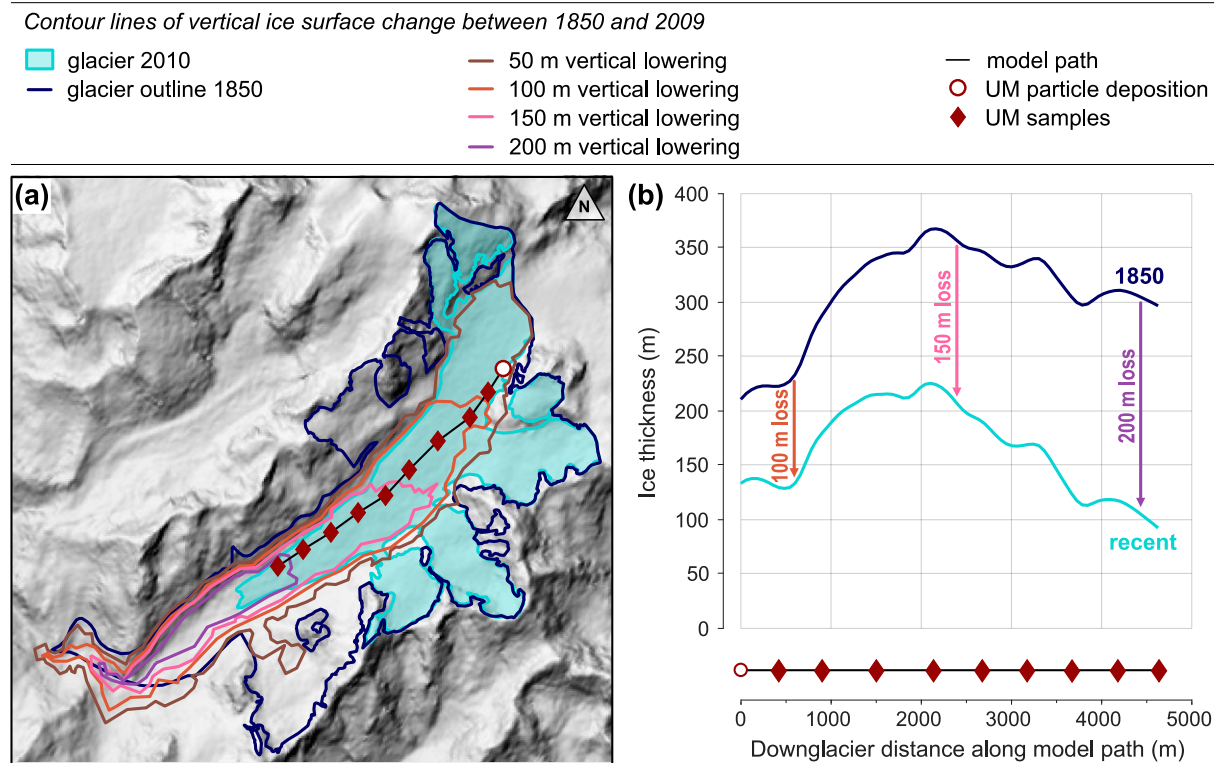


**Figure A3:** Vertical ice surface change of Glacier d'Otemma. **(a)** Contour lines of vertical ice surface lowering between 1850 and 2009 with UM samples being indicated (2010 and 1850 glacier outlines by Fischer *et al.*, 2014, and modified from Maisch *et al.*, 2000; contour lines extracted from Figure 4 in Lambiel & Talon, 2019). **(b)** Ice thicknesses along the model path for recent times and reconstructed for 1850. The arrows indicate the magnitude of vertical lowering at locations where contour lines intersect the model path (recent ice thicknesses by Farinotti *et al.*, 2019). UM: upper medial moraine

We acknowledge that applying Glen's flow law in a shallow-ice-approximation fashion, may be too simplified for small valley glaciers that are confined by steep walls. Especially for the year 1850, glacier flow velocities retrieved with Glen's flow law are likely too low close to the headwalls (**Figure A2c**). In our model we do not account for longitudinal stress-gradient coupling, which, for glaciers flowing over beds of varying slope, can considerably modify their flow (Nye 1952, 1956; Kamb & Echelmeyer, 1986). At Glacier d'Otemma, bed topography close to the headwalls is marked by pronounced downglacier steepening (**Figure A2e**), and thus accelerating downglacier velocities may have a dragging effect on glacier flow higher up. Besides, Glen's flow law is highly sensitive to both ice surface slope and ice thickness. Although glacier ice used to be thicker in the past, past velocity estimates remain slow due to the shallowing of the reconstructed ice surface slopes (**Figure A2b**). In their 2019 study, Lambiel and Talon point out that in a glacier's accumulation area evidence of past ice cover is more difficult to define due to the lack of geomorphic markers (e.g., moraines). Additionally, the presence of an ice divide at the head of Glacier d'Otemma (**Figure 2.1a**) complicates the reconstruction of its 1850 surface.

**Table A2:** Recent and past glacier surface velocities at Glacier d'Otemma from Glen's flow law.

Profile points <sup>a</sup>	X	Y	Distance (m)	Elevation	Thickness	Slope	Velocity	Elevation	Thickness	Slope	Velocity
	UTM	UTM		1850 <sup>b</sup>	1850 <sup>b</sup>	1850 <sup>b</sup>	1850 <sup>c</sup>	2018 <sup>d</sup>	2018 <sup>e</sup>	2018 <sup>d</sup>	2018 <sup>c</sup>
				(m)	(m)		(m yr <sup>-1</sup> )	(m)	(m)		(m yr <sup>-1</sup> )
1	381353	5091693	0	3057	211	0.03	1.01	2981	134	0.06	1.63
2	381320	5091642	60	3055	216	0.03	1.15	2977	137	0.06	1.80
3	381288	5091592	120	3053	220	0.03	1.26	2973	138	0.06	1.87
4	381255	5091541	180	3052	222	0.03	1.35	2969	138	0.06	1.88
5	381223	5091491	240	3050	223	0.03	1.42	2965	137	0.06	1.82
6	381190	5091440	300	3048	223	0.03	1.46	2961	134	0.06	1.71
7	381158	5091390	361	3046	223	0.03	1.48	2957	132	0.06	1.58
8	381125	5091339	421	3044	223	0.03	1.52	2953	130	0.07	1.48
9	381091	5091290	481	3042	224	0.03	1.60	2949	129	0.07	1.45
10	381055	5091241	541	3040	227	0.03	1.73	2945	130	0.07	1.48
11	381020	5091192	601	3038	234	0.03	1.97	2941	134	0.07	1.67
12	380985	5091144	661	3036	243	0.03	2.37	2937	141	0.07	2.11
13	380950	5091095	721	3034	256	0.03	3.00	2933	153	0.07	2.89
14	380915	5091046	781	3032	270	0.03	3.75	2929	165	0.07	3.87
15	380880	5090997	841	3030	280	0.03	4.46	2925	173	0.07	4.76
16	380845	5090949	901	3028	288	0.03	5.12	2921	180	0.07	5.52
17	380798	5090912	961	3025	295	0.03	5.79	2917	185	0.07	6.25
18	380749	5090876	1021	3023	303	0.03	6.55	2913	191	0.07	7.09
19	380701	5090840	1082	3021	310	0.03	7.33	2909	197	0.07	7.91
20	380652	5090805	1142	3019	316	0.03	8.09	2905	201	0.07	8.62
21	380604	5090769	1202	3017	321	0.04	8.80	2901	204	0.07	9.19
22	380556	5090733	1262	3015	325	0.04	9.53	2897	207	0.07	9.73
23	380507	5090698	1322	3013	330	0.04	10.36	2893	210	0.07	10.37
24	380459	5090662	1382	3011	334	0.04	11.23	2890	213	0.07	11.00
25	380411	5090626	1442	3008	338	0.04	12.03	2886	215	0.07	11.46
26	380362	5090591	1502	3006	340	0.04	12.71	2882	215	0.07	11.67
27	380318	5090550	1562	3004	342	0.04	13.37	2878	215	0.07	11.78
28	380276	5090507	1622	3002	344	0.04	14.09	2874	216	0.07	11.94
29	380233	5090465	1682	3000	345	0.04	14.76	2870	215	0.07	11.96
30	380191	5090422	1742	2998	345	0.04	15.28	2867	214	0.07	11.75
31	380149	5090380	1803	2996	345	0.04	15.78	2863	212	0.07	11.48
32	380106	5090337	1863	2994	347	0.04	16.79	2859	212	0.07	11.74
33	380064	5090295	1923	2991	353	0.04	18.52	2855	216	0.07	12.73
34	380021	5090252	1983	2989	359	0.04	20.80	2851	221	0.07	14.20
35	379979	5090209	2043	2987	365	0.04	22.99	2848	225	0.07	15.40
36	379936	5090167	2103	2985	367	0.04	24.75	2844	226	0.07	15.99
37	379895	5090124	2163	2983	368	0.04	26.06	2840	224	0.07	15.99
38	379854	5090079	2223	2980	367	0.04	27.07	2836	222	0.07	15.61
39	379814	5090035	2283	2978	364	0.04	27.75	2832	218	0.07	14.89
40	379773	5089991	2343	2976	361	0.04	28.04	2828	212	0.07	13.82
41	379732	5089946	2404	2973	356	0.05	28.18	2824	206	0.07	12.67
42	379692	5089902	2464	2971	352	0.05	28.45	2820	201	0.07	11.72
43	379651	5089858	2524	2968	350	0.05	29.29	2816	197	0.07	11.18
44	379611	5089813	2584	2966	349	0.05	30.67	2812	194	0.07	10.97
45	379570	5089769	2644	2963	348	0.05	32.16	2808	192	0.07	10.79
46	379525	5089731	2703	2960	346	0.05	33.32	2804	188	0.08	10.35
47	379474	5089699	2764	2958	342	0.05	34.02	2799	183	0.08	9.65
48	379423	5089667	2824	2955	338	0.05	34.60	2795	178	0.08	8.91
49	379372	5089635	2884	2952	335	0.05	35.45	2790	173	0.08	8.31
50	379321	5089603	2944	2949	333	0.05	36.91	2786	170	0.08	7.98
51	379270	5089572	3004	2946	333	0.06	39.19	2781	168	0.08	7.96
52	379219	5089540	3064	2943	334	0.06	42.43	2777	168	0.08	8.24
53	379168	5089508	3124	2940	336	0.06	46.39	2772	168	0.08	8.71
54	379117	5089475	3184	2936	338	0.06	51.02	2767	169	0.08	9.32
55	379069	5089440	3244	2933	340	0.06	55.64	2763	170	0.09	9.81
56	379020	5089405	3304	2930	340	0.06	59.48	2758	168	0.09	9.92
57	378971	5089369	3365	2926	337	0.06	61.17	2753	164	0.09	9.27
58	378923	5089334	3425	2922	331	0.06	61.00	2748	156	0.09	8.12
59	378874	5089299	3485	2919	325	0.07	59.88	2742	148	0.09	6.83
60	378825	5089263	3545	2915	318	0.07	58.76	2737	140	0.09	5.70
61	378777	5089228	3605	2911	311	0.07	57.56	2732	132	0.09	4.71
62	378728	5089193	3665	2907	305	0.07	56.42	2726	124	0.09	3.86
63	378678	5089160	3725	2903	300	0.07	55.94	2720	118	0.10	3.23
64	378627	5089128	3785	2898	297	0.07	57.44	2714	114	0.10	2.95

Profile points <sup>a</sup>	X UTM	Y UTM	Distance (m)	Elevation 1850 <sup>b</sup> (m)	Thickness 1850 <sup>b</sup> (m)	Slope 1850 <sup>b</sup>	Velocity 1850 <sup>c</sup> (m yr <sup>-1</sup> )	Elevation 2018 <sup>d</sup> (m)	Thickness 2018 <sup>e</sup> (m)	Slope 2018 <sup>d</sup>	Velocity 2018 <sup>c</sup> (m yr <sup>-1</sup> )
65	378576	5089097	3845	2894	299	0.07	61.70	2709	113	0.10	3.02
66	378524	5089065	3905	2889	302	0.08	68.34	2703	115	0.10	3.38
67	378473	5089034	3965	2885	306	0.08	75.69	2696	117	0.10	3.78
68	378422	5089003	4026	2880	308	0.08	82.55	2690	118	0.10	4.08
69	378371	5088971	4086	2875	310	0.08	88.88	2684	119	0.10	4.28
70	378319	5088940	4146	2870	311	0.08	94.80	2678	118	0.11	4.38
71	378269	5088908	4206	2866	311	0.08	99.89	2671	117	0.11	4.36
72	378219	5088874	4266	2860	310	0.08	103.60	2665	115	0.11	4.17
73	378169	5088841	4326	2855	309	0.09	106.41	2658	112	0.11	3.89
74	378119	5088808	4386	2850	307	0.09	108.38	2652	108	0.11	3.54
75	378069	5088774	4446	2845	304	0.09	109.78	2645	104	0.11	3.18
76	378019	5088741	4506	2839	302	0.09	110.87	2638	100	0.11	2.82
77	377969	5088708	4566	2834	299	0.09	111.78	2631	97	0.11	2.48
78	377919	5088674	4627	2828	297	0.09	112.18	2624	92	0.12	2.15

<sup>a</sup> Note that the downglacier profile follows the upper medial moraine (UM) sample locations, but is divided into 78 profile points to enhance profile resolution. <sup>b</sup> 1850 data based on a reconstruction study of vertical glacier change between 1850 and 2009 by Lambiel and Talon (2019). <sup>c</sup> Computed with Glen's flow law. <sup>d</sup> Based on a 30 m resolution DEM (SRTM GL1; NASA Shuttle Radar Topography Mission SRTM, 2013). <sup>e</sup> Based on the global ice thickness distribution dataset by Farinotti *et al.* (2019).

## A2.2 Computation of vertical transport

To simulate debris burial and re-emergence at the glacier surface, the relative position of a debris particle to the equilibrium line altitude (ELA) needs to be determined through time (**Figure 2.4**). As we cannot refer to observational data on the ELA of Glacier d'Otemma or to ablation stake monitoring, we approximated the recent ELA to be at ~3200 m altitude. This estimate is based on manually tracing the snowline across the glacier's catchment on a satellite image from the year 2017 with a high lying snowline (**Figure 2.1a**), which yielded a mean elevation of ~3160 m. In comparison, recent ELA records of the nearby Glacier du Giéto and Glacier de Corbassière were found to average at ~3300 m over the last two decades (**Figure A4a**; GLAMOS, 2019c), and glacier mass balance records at the neighbouring Glacier d'Arolla indicate the ELA of the early 1990s to be located at ~3100 m elevation (Hubbard *et al.*, 2000). We approximated the elevation of the past ELA to ~3000 m, applying the mean altitude method by Kurowski (1891) to the reconstructed glacier surface in 1850 (**Figure A4b**; Braithwaite, 2015).

We further used a generalized vertical mass balance profile, which is based on a compilation of glacier mass balances of several Alpine glaciers (Dyurgerov, 2002). Maximum accumulation of snow above the ELA was limited to 0.75 m water equivalent (w.e.) yr<sup>-1</sup>, declining by a gradient of 0.7 m w.e. yr<sup>-1</sup> per 100 m decreasing elevation (**Table A1**, **Figure A5**; generalized numbers courtesy of Jürgen Mey).

## Recent ELA elevations

- recent ELA of Glacier du Giétro
- recent ELA of Glacier de Corbassière
- 2017 ELA of Glacier d'Otemma

## Reconstructed ice surface elevation and ELA in 1850

- 50 m above recent
- 100 m above recent
- 150 m above recent
- 200 m above recent
- glacier outline 1850
- - - reconstructed mean ELA

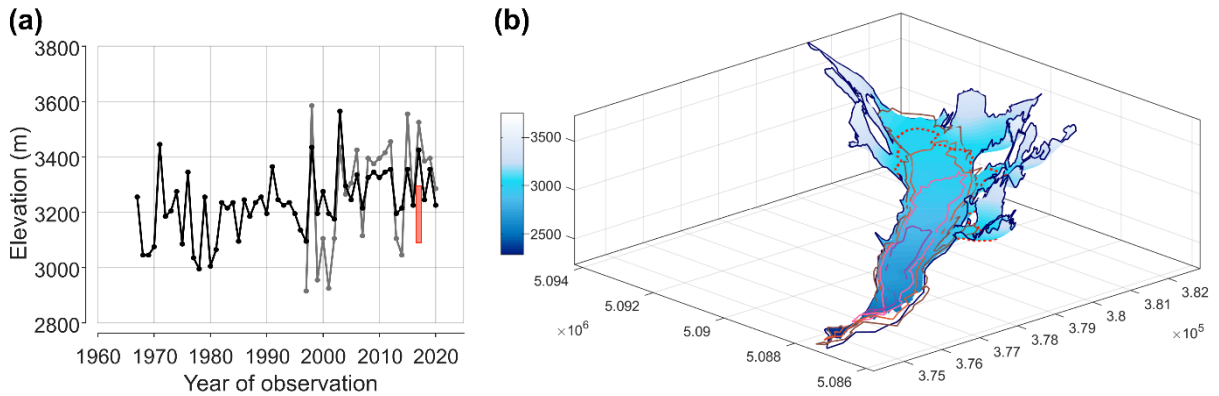


**Figure A4:** ELA estimates for Glacier d'Otemma. **(a)** Approximation of the mean recent ELA elevation. The red box indicates the range of ELA elevations manually traced on a 2017 satellite image displayed in **Figure 2.1a** (datasets of Glacier du Giétro and de Corbassière by GLAMOS, 2019c). **(b)** Reconstruction of the mean past ELA elevation according to the mean altitude method by Kurowski (1891). Glacier surface reconstruction was done by fitting a surface on a 2D grid using the glacier outline from 1850 and contour lines of ice surface elevation estimated from **Figure A3** (1850 glacier outline modified from Maisch *et al.*, 2000; contour lines derived from Lambiel & Talon, 2019). ELA: equilibrium line altitude

## Mass balance records of glaciers in the Alps

- Gries (1962-1995)
- Limmern (1976-1985)
- Silvretta (1960-1995)
- Jamtalferner (1989-1995)
- Vermuntferner (1991-1995)
- Ochsentalferner (1991-1995)
- Kesselwandferner (1967-1995)
- Vernagtferner (1966-1995)
- Nord. Schneeferner (1967-1968)
- Langtalferner (1963-1970)
- Hintereisferner (1964-1995)
- Careser (1967-1995)
- Wurtenkees (1983-1995)
- mean mass balance
- ELA

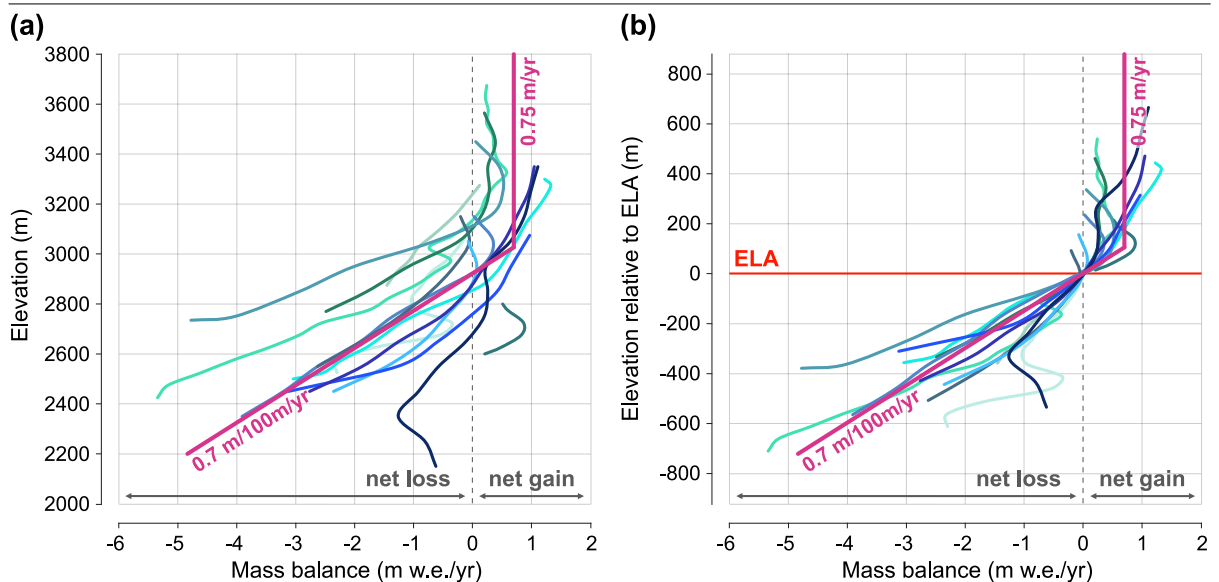


**Figure A5:** Glacier mass balance records from the European Alps. Mass balances in relation to **(a)** elevation and **(b)** elevation above or below the respective ELA. Note the generalized mean mass balance profile. Years in brackets refer to the observation period (glacier mass balances by Dyurgerov, 2002; generalized numbers and figure template courtesy of Jürgen Mey). ELA: equilibrium line altitude; m w.e. yr<sup>-1</sup>: metre water equivalent per year

### A2.3 Computation through time

We computed changes in surface velocities and ELA through time by interpolating between past and recent ice thicknesses and surface slopes, but kept the shape of the vertical mass balance profile constant. For years before 1881, surface velocities and ELA were set to the reconstructed values from 1850. This is due to the fact that historical observations of glacier length (**Figure 2.7c**; GLAMOS, 2019a) and ice cover extent (**Figure 2.7a**; Swisstopo, 2021) noticeably started to change after 1880. We did not account for changes before 1850, since we are lacking any information on earlier glacier extents during the Little Ice Age. However, other reconstructions of glacier fluctuations in the Swiss Alps indicate that, aside from small short-term advances, glacier extents remained fairly stable from the 17th to the mid-19th century (e.g., Lower Grindelwald Glacier; Holzhauser *et al.*, 2005). Interpolation was performed from 1881 onwards to the sampling year 2018 in a three-step linear mode (**Figure A2d,e**), with a simple decline for a first period (1881-1933), a doubled decline for a second period (1934-1982), and a quadrupled decline for a third period (1983-2018). We defined this succession based on datasets from Glacier d'Otemma that record the decline in its length and geodetic glacier-wide mass balance (**Figure 2.7c**; GLAMOS, 2019a, 2019b). Whereas glacier length was found to decrease since ~1885, accelerating towards the present, negative geodetic mass balance records from 1934 onwards doubled after the year 1983. We found no mass balance estimates before 1934, but given the ongoing decrease in glacier length since ~1885, we assume that the glacial mass balance has been negative already, though less severe.

Our simple model itself iterates the horizontal and vertical transport of debris particles from a given start year until the sampling year 2018 on a year-to-year basis (**Figure 2.4**). **Figure A6** depicts the downglacier transport distances of debris particles through time for a given sample. The corresponding reconstructed particle trajectories through the glacier are shown in **Figure A7**, revealing the proportion of englacial and supraglacial particle transport along the changing glacier through time for a given sample. Eventually, the age of a sample equals the mean age of the transport time of those debris particles that arrived at the glacier surface within a 30 m buffer zone around the sample location in the year 2018. Note that the model path is defined by the UM sample locations. We did not generate a separate flow path for the LM as the two moraines are very close, but chose different start locations for the respective medial moraine.

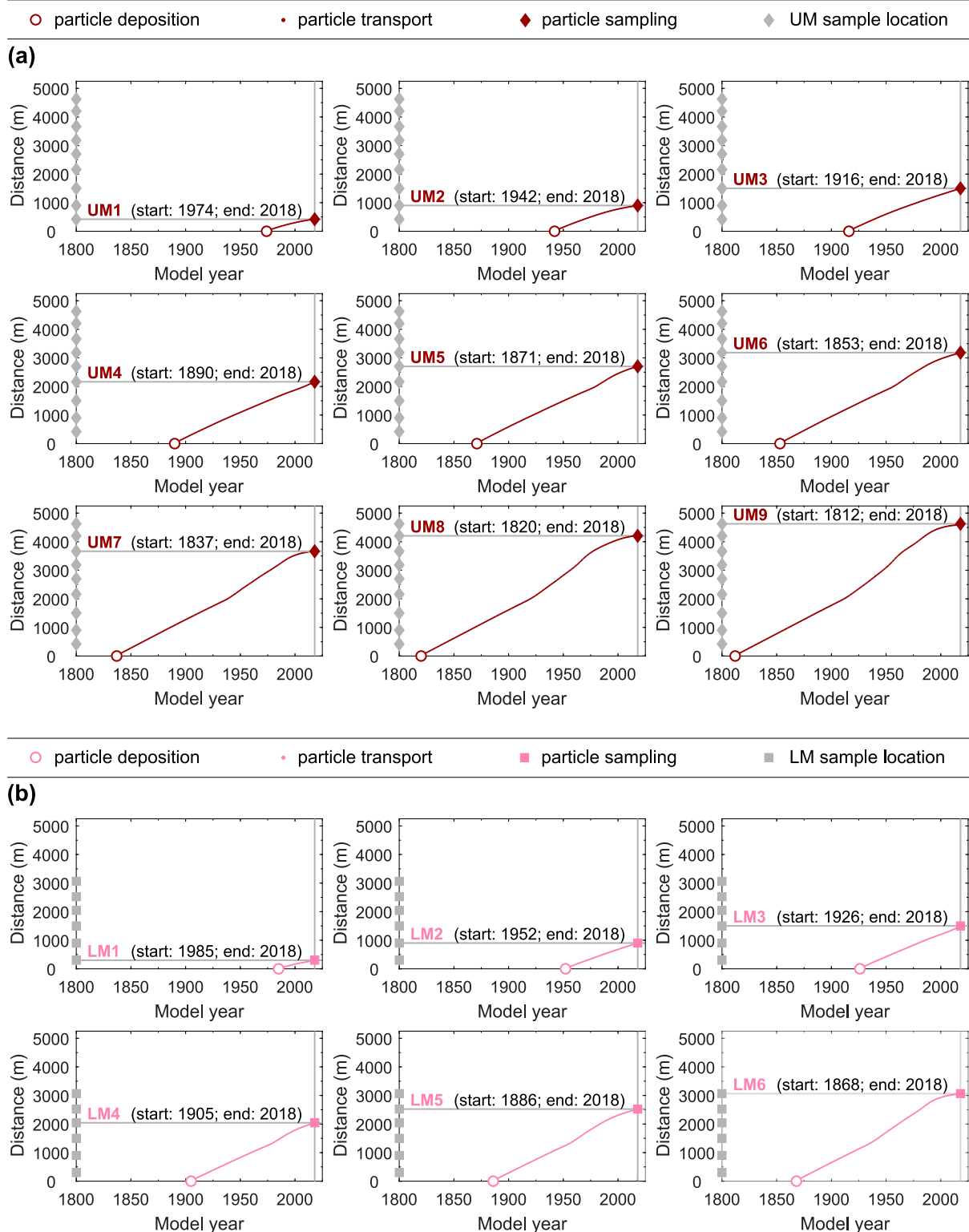


**Figure A6:** Downglacier debris particle distances between the headwalls and sample locations of Glacier d’Otemma in relation to the model year. **(a)** UM samples. **(b)** LM samples. Note that each graph stands for one individual sample and that for reference all UM/LM sample locations are indicated in grey on the y axis. For an individual sample, debris particle transport needs to start in the start year X to make the particle reach the location of this sample in the sampling/end year 2018. Particle transport distances through time are indicated in colour. Where the two grey lines intersect, a debris particle has reached the distance of the 2018 sample location. Years in brackets refer to start and end year of debris particle transport. UM/LM: upper/lower medial moraine

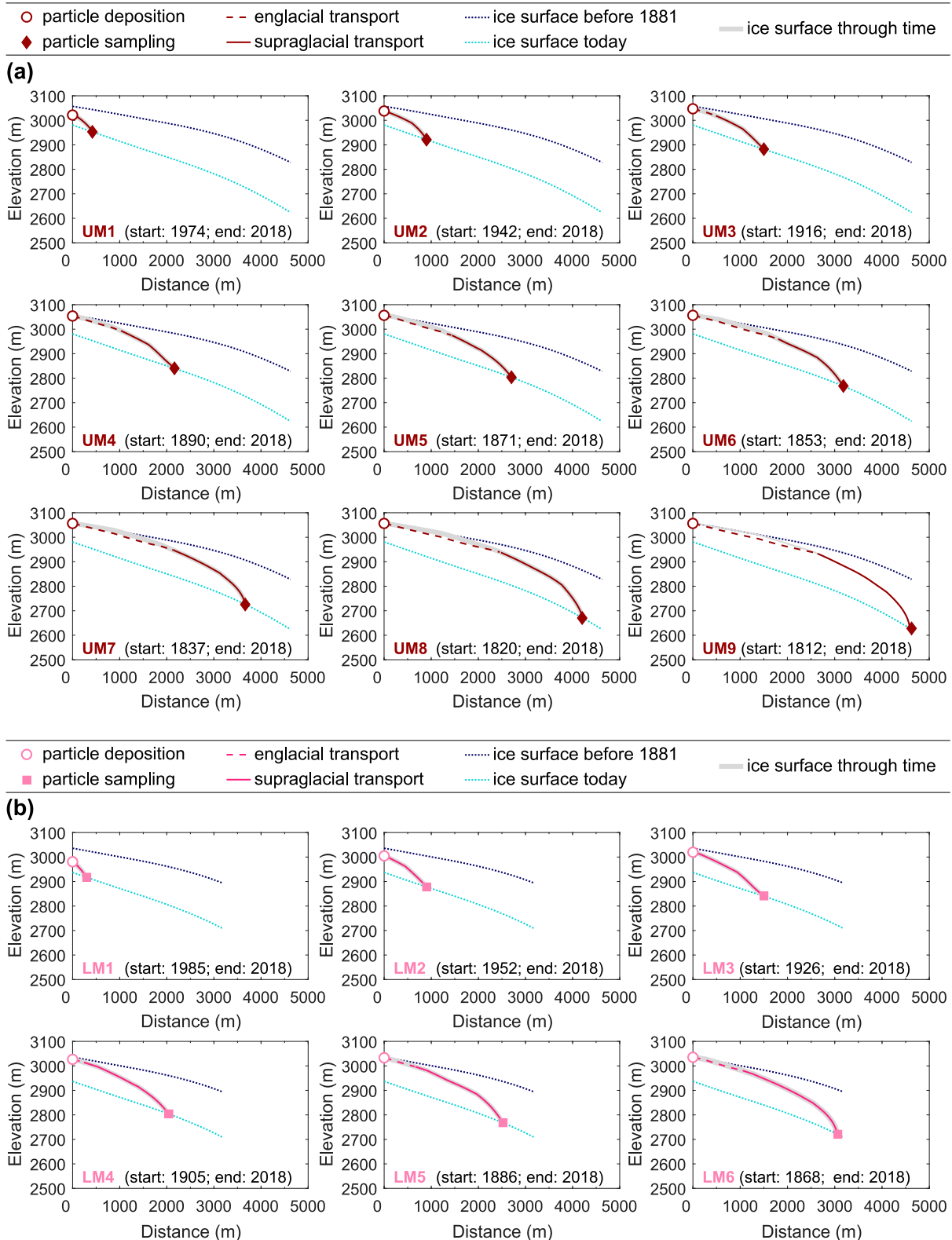


**Figure A7:** Debris particle trajectories tracing englacial/supraglacial transport from headwalls to sample locations through Glacier d'Otemma. **(a)** UM samples. **(b)** LM samples. Note that each graph stands for one individual sample. For an individual sample, debris particle transport starts at the ice surface elevation of the start year X. Note that the grey line traces the elevation of the lowering ice surface through time and hence displays the ice surface elevation at the specific year that the debris particle passed a certain distance. The recent and reconstructed ice surface elevation for years before 1881 are indicated for reference. Debris particle transport stops when a particle has reached the sample location at the ice surface elevation of the sampling/end year 2018. The red/pink coloured trajectories indicate whether particles were buried during transport. Dashed and solid trajectories run englacially and supraglacially, respectively. Trajectories represented by solid lines run exclusively supraglacially. Years in brackets refer to start and end year of debris particle transport. UM/LM: upper/lower medial moraine

## A2.4 Computation of transport $^{10}\text{Be}$ concentrations

To assess  $^{10}\text{Be}$  accumulation during glacial transport, we computed changes in  $^{10}\text{Be}$  production rates along the model path considering the downglacier distance  $x$  (m), the burial depth within the ice  $z_i$  (cm), and the transport time  $t$  (year). We estimated spallogenic  $^{10}\text{Be}$  surface production rates using the CRONUS online calculator version 2.3 functions (Balco *et al.*, 2008), the constant spallation scaling scheme ‘St’ (Lal, 1991; Stone, 2000) and a sea level high latitude (SLHL) spallation production rate of  $4.01 \pm 0.33$  atoms  $\text{g}^{-1} \text{yr}^{-1}$  (Borchers *et al.*, 2016). Temporal variations in production rates due to paleomagnetic intensity changes were neglected. Surface  $^{10}\text{Be}$  production rates were corrected for topographic shielding (Dunne *et al.*, 1999; Schwanghart & Scherler, 2014) and for an average debris cover of 5 cm thickness  $z_d$  and  $2.0 \text{ g cm}^{-3}$  density  $\rho_d$  (CRONUS online calculator version 2.3; Balco *et al.*, 2008). Additionally, we applied a correction for a mean annual snow cover  $z_s$  of 100 cm on the basis of recent snow cover data by nearby automatic snow stations at comparable altitude (Interkantonalessystem, IMIS; SLF, 2021). We assumed a mean snow density  $\rho_s$  of  $0.3 \text{ g cm}^{-3}$  based on empirical snow density estimates in the Swiss Alps (Jonas *et al.*, 2009). To account for shielding during englacial transport, we determined spallogenic production rates at a specific downglacier distance and burial depth  $P_{sp}(x, z)$  (atoms  $\text{g}^{-1} \text{yr}^{-1}$ ) based on the exponential decay of nuclide production with depth below the surface (Lal, 1991):

$$P_{sp}(x, z) = P_{sp}(x, 0) e^{-z \left(\frac{\rho}{\Lambda}\right)} \quad (\text{A2})$$

where  $P_{sp}(x, 0)$  is the surface production rate at a certain debris particle distance (atoms  $\text{g}^{-1} \text{yr}^{-1}$ ),  $\rho$  is the density of the medium water, snow, or debris ( $\text{g cm}^{-3}$ ), and  $\Lambda$  is the absorption mean free path ( $\text{g cm}^2$ ) (for parameter values used see **Table A1**). We further included  $^{10}\text{Be}$  production rates by muons at a certain distance and depth  $P_{mu}(x, z)$  (atoms  $\text{g}^{-1} \text{yr}^{-1}$ ), based on the Matlab function ‘‘P\_mu\_total.m’’ (CRONUS online calculator version 2.3; Balco *et al.*, 2008) and accounted for radioactive decay of  $^{10}\text{Be}$  produced during debris transport.

For every debris particle,  $[^{10}\text{Be}]_{\text{transport}}(x, z, t)$  is the  $^{10}\text{Be}$  concentration (atoms  $\text{g}^{-1}$ ) acquired during glacial transport as a function of  $x$ ,  $z$ , and  $t$  by year-to-year iteration of (Lal, 1991):

$$\begin{aligned} [^{10}\text{Be}]_{\text{transport}}(x, z, t) &= [^{10}\text{Be}]_{\text{transport}}(x, z, t-1) e^{-\lambda(t-(t-1))} \\ &+ \frac{P_{sp}(x, z)}{\lambda} (1 - e^{-\lambda(t-(t-1))}) + \frac{P_{mu}(x, z)}{\lambda} (1 - e^{-\lambda(t-(t-1))}) \end{aligned} \quad (\text{A3})$$

where  $[^{10}\text{Be}]_{\text{transport}}(x, z, t-1)$  is the initial transport  $^{10}\text{Be}$  concentration (atoms  $\text{g}^{-1}$ ), with which a particle arrives at a certain particle distance and depth, and  $\lambda$  is the decay constant ( $\text{yr}^{-1}$ ) (for parameter values used see **Table A1**). Finally, by subtracting the modelled  $[^{10}\text{Be}]_{\text{transport}}$  from the measured  $[^{10}\text{Be}]_{\text{measured}}$ , and by using the modelled sample ages to correct for radioactive decay, we obtained an estimate for  $[^{10}\text{Be}]_{\text{headwall}}$ .

**Figure A2e** indicates the  $^{10}\text{Be}$  production rate changes at the glacier surface along the medial moraines through time, corrected as stated above. Overall,  $^{10}\text{Be}$  production rates range between  $\sim 24$  and  $31$  atoms  $\text{g}^{-1} \text{yr}^{-1}$ . They decrease both with decreasing altitude along the model path and with ice surface lowering through time, by  $<6$  and  $<4$  atoms  $\text{g}^{-1} \text{yr}^{-1}$ , respectively.

## A2.5 Uncertainties

One of the more poorly constrained parts in our model with potentially high impact on our  $[^{10}\text{Be}]_{\text{transport}}$  estimates is slow supraglacial transport close to the source headwalls (see Section **A2.1**; **Figure A2c**). We are aware that defining past minimum velocities close to the headwalls (**Figure A2d**) without additional data from nearby involves uncertainties that are difficult to estimate.

Running our model with a slower past minimum velocity of  $15 \text{ m yr}^{-1}$  resulted in sample ages up to  $\sim 30$  years older.  $[^{10}\text{Be}]_{\text{transport}}$  varied up to  $\pm 400 \text{ atoms g}^{-1}$ . A faster past minimum velocity of  $25 \text{ m yr}^{-1}$  yielded sample ages up to  $\sim 20$  years younger and  $[^{10}\text{Be}]_{\text{transport}}$  varying up to  $\pm 300 \text{ atoms g}^{-1}$ . Eventually, for our derived  $\sim 200$ -year record of headwall erosion rates at Glacier d'Otemma (**Table 2.3**, **Figure 2.6**), this does not change our overall differentiation between samples being deposited rather during the Little Ice Age or during the following deglaciation. Also, changes in  $[^{10}\text{Be}]_{\text{transport}}$  in the order of few  $10^2 \text{ atoms g}^{-1}$ , due to proportional changes in englacial versus supraglacial transport, are small compared to the overall changes in  $[^{10}\text{Be}]_{\text{measured}}$  along the medial moraines, which are in the order of  $\sim 10^4 \text{ atoms g}^{-1}$  (**Figure 2.6a**). Still, these changes in  $[^{10}\text{Be}]_{\text{transport}}$  may affect especially samples younger than  $\sim 120$  years where  $[^{10}\text{Be}]_{\text{measured}}$  are comparatively low (**Table 2.2**) and where modelled transport occurs almost exclusively on the glacier surfaces (**Figure A7**), as it is the case for samples UM3/c and UM2/16. Samples older than  $\sim 120$  years were, according to our model, quickly buried within the ice and the slow transport close to the headwalls is negligible for their estimated  $[^{10}\text{Be}]_{\text{transport}}$ .

## Appendix B: supplement of Chapter 3

**Sections B1-B2 are published as supplement to Wetterauer & Scherler (2023a),  
available online at:**

<https://doi.org/10.5194/esurf-11-1013-2023-supplement>

**Sections B3-B4 are part of the accompanying data publication:**

Wetterauer, K. & Scherler, D. (2023b)  
Medial moraine cosmogenic  $^{10}\text{Be}$  data and glacier surface velocities from four Swiss valley  
glaciers around Pigne d'Arolla.

*GFZ Data Services.*

<https://doi.org/10.5880/GFZ.3.3.2023.002>

To avoid repetition, only the text sections and tables of the data publication are listed that  
contain additional information and data not presented in Chapter 3.

## B1 Uncertainty estimates on boulder velocities

We derived glacier surface velocities at Glacier du Brenay, Glacier de Cheilon, Glacier de Pièce, and Glacier de Tsijiore Nouve by manually tracing the displacement of medial moraine boulders across orthoimages between the years 1977 and 2020 (see Section 3.3.1.2). Uncertainties on these glacier surface velocities, respectively boulder velocities, mainly stem from three sources: (i) uncertainties in the positional accuracy for the orthoimages, (ii) uncertainties in the precision with which a boulder is identified and traced across successive orthoimages, and (iii) uncertainties in the length of the time period between two successive orthoimages. We discuss each of these points in the following paragraph.

(i) According to Swisstopo (2023), the positional accuracy for the orthoimages improves stepwise through time from  $\pm 1$  m (prior 1999) via  $\pm 0.5$  m (1998-2005) and  $\pm 0.25$  m (2005-2016) to  $\pm 0.1$  m (since 2017). (ii) The downglacier pathway and displacement of a medial moraine boulder is defined by tracing the boulder's centre as the reference point between the orthoimages. At all studied sites, the diameter of the tracked boulders typically varies between 2 and 4 m. We therefore approximate the relative uncertainty in identifying and tracing the boulder centre to no more than  $\pm 0.5$  m. (iii) The boulder velocity is given by the downglacier displacement divided by the time between two successive orthoimages. Unfortunately, exact acquisition dates for the orthoimages were unavailable, as the orthoimages are a mosaic of several individual black-and-white or colour aerial photographs from a particular year (Swisstopo, 2023). Therefore, we accounted for full years between the orthoimages. Nevertheless, the assumption that the orthoimages reflect a similar time during the summer season seems reasonable. At the studied sites, individual aerial photographs from the years 1977, 1983, 1988, 1995, 1999, and 2005 (available in the Swisstopo aerial imagery catalogue; Swisstopo, 2023) date to the beginning of September ( $\pm 1$  month) and have presumably been used for the orthoimage composition, resulting in temporal deviations of  $\pm 0.1$  years.

Since uncertainties due to the positional accuracy vary for individual boulder-tracking periods, we here provide as an example an average velocity uncertainty estimate for the four glaciers based on an early, a central, and a recent tracking period using Gaussian error propagation. For the early tracking period 1983-1988, the uncertainty for the average boulder displacement of  $\sim 100$  m over 5 years is less than approximately 3% (yielding an average velocity and uncertainty of  $20.0 \pm 0.5$  m yr<sup>-1</sup>). For the central tracking period 1999-2005, the uncertainty for the average boulder displacement of  $\sim 70$  m over 6 years is also less than approximately 3% (yielding an average velocity and uncertainty of  $11.7 \pm 0.3$  m yr<sup>-1</sup>). For the most recent tracking period 2017-2020, the uncertainty for the average boulder displacement of  $\sim 20$  m over 3 years approximates less than 5% (yielding an average velocity and uncertainty of  $6.7 \pm 0.3$  m yr<sup>-1</sup>). Overall, these uncertainties are small and have no significant effect on the modelled sample ages.

## B2 Figures B1-B6 and Table B1

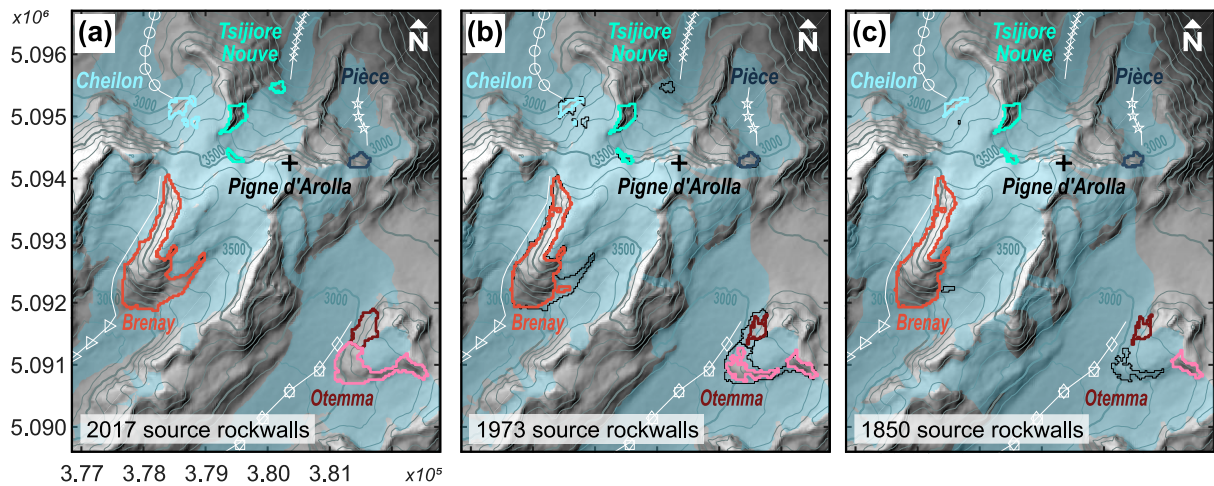


**Figure B1:** Hillshade images with elevation as greyscale (bright = high) outlining the studied ice-free source rockwalls around Pigne d'Arolla for the three time slices (a) 2017, (b) 1973, and (c) 1850. To visualize the temporal changes in ice cover across the debris source areas, source rockwall outlines of the year shown are coloured and underlain by the source rockwall outlines of the next younger time slice in black. 100 m contour lines are based on the recent DEM SRTM GL1 (NASA Shuttle Radar Topography Mission SRTM, 2013) and therefore on the glacier body itself only valid for the most recent time slice. For reference, the glacier extents (blue shade), medial moraine profiles (white lines), and 2019 sample locations (white symbols) of Glacier du Brenay, Glacier de Cheilon, Glacier d'Otemma, Glacier de Pièce, and Glacier de Tsijiore Nouve are indicated (glacier extents of 2016, 1973, and 1850 by Linsbauer *et al.*, 2021, Müller *et al.*, 1976, and Maisch *et al.*, 2000).

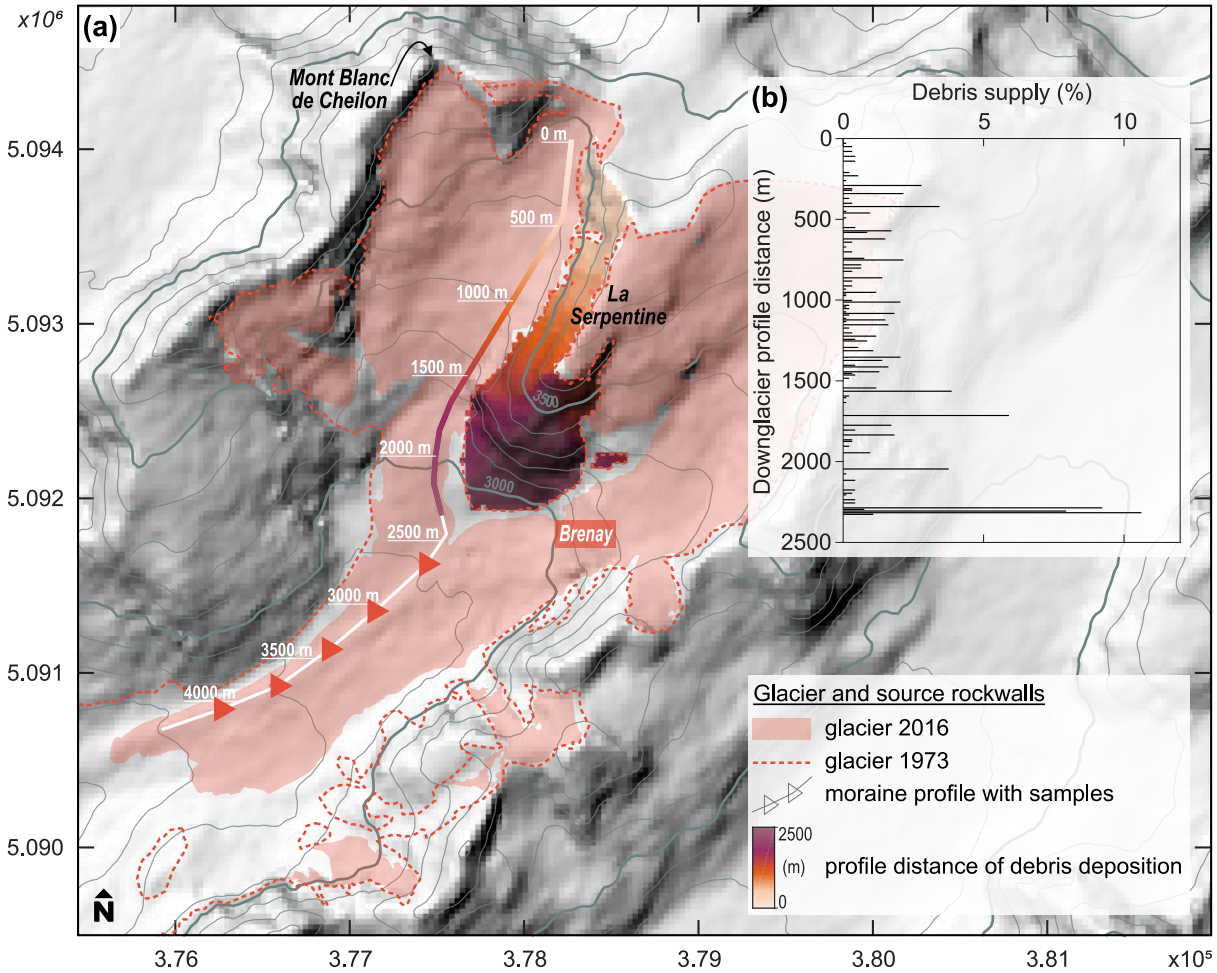


**Figure B2:** Weighted debris supply/deposition along the modelled medial moraine profile of Glacier du Brenay from ice-free source rockwalls of La Serpentine in 1973. **(a)** Hillshade image with elevation as greyscale (bright = high) showing that, due to the elongated nature of La Serpentine, debris deposition does not occur at a single confined location but along the first ~2.3 km of the modelled downglacier medial moraine profile. Therefore, at a sample location in 2019, trajectories of several debris particles will meet that were deposited at different profile distances and that experienced different transport times and exposures to cosmic radiation (see **Figure B3**). The colour gradient along the downglacier profile and across the source rockwall area indicates at which downglacier profile distance a rockwall/DEM pixel supplies a debris particle, according to the flow directions of the steepest descent. Hillshade and 100 m contour lines are based on the DEM SRTM GL1 (NASA Shuttle Radar Topography Mission SRTM, 2013). For reference, the 2016 and 1973 glacier extents, the medial moraine profile with downglacier distances, and the 2019 sample locations are indicated (glacier extents by Linsbauer *et al.*, 2021, and Müller *et al.*, 1976). **(b)** Inset aligning to the downglacier profile in **(a)** and showing the percentage debris particle supply along the first ~2.3 km profile distance, weighted by the overlying rockwall area. Assuming a constant erosion rate across La Serpentine, debris supply/deposition is relatively higher where more rockwall area towers above the ice, and thus those trajectories are more represented when estimating an average sample age based on all modelled trajectories.

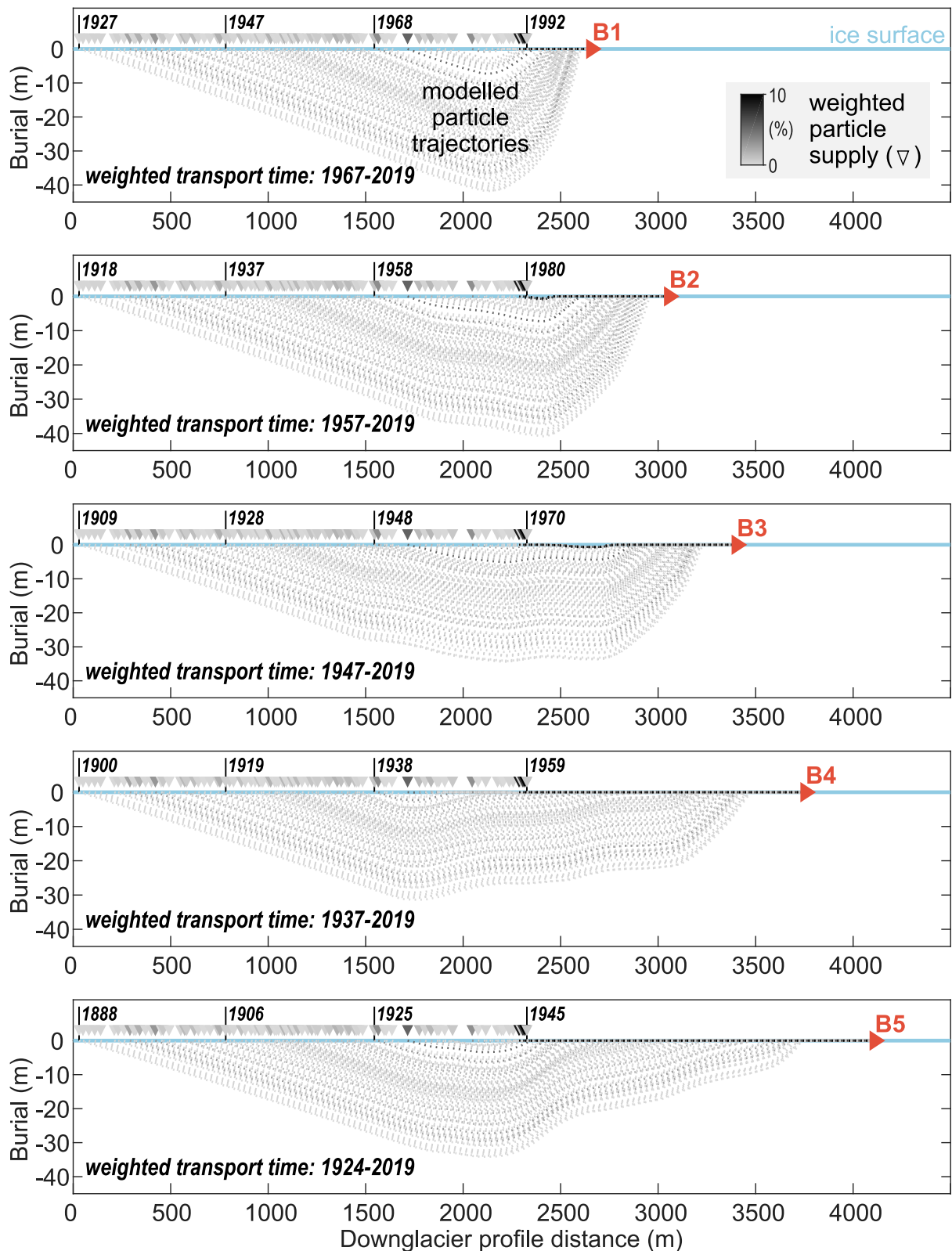


**Figure B3:** Modelled debris particle trajectories indicating the mode of downglacier particle transport from source rockwalls to sample locations B1-5 at Glacier du Brenay. Shown are all trajectories of particles deposited along the first ~2.3 km of the downglacier profile that arrive at the ice surface and downglacier distance of a sample's location in 2019. For reference, start years of four trajectories are given. The burial depth indicates whether a particle was transported within the ice (englacially; burial depth < 0 m) and shielded from cosmic radiation, or on the ice surface (supraglacially; burial depth = 0 m) and exposed to cosmic radiation. Graded colours indicate the percentage debris particle supply along the first ~2.3 km profile distance (see also **Figure B2b**) and the weight of its corresponding trajectory, used to estimate a weighted time of downglacier particle transport.

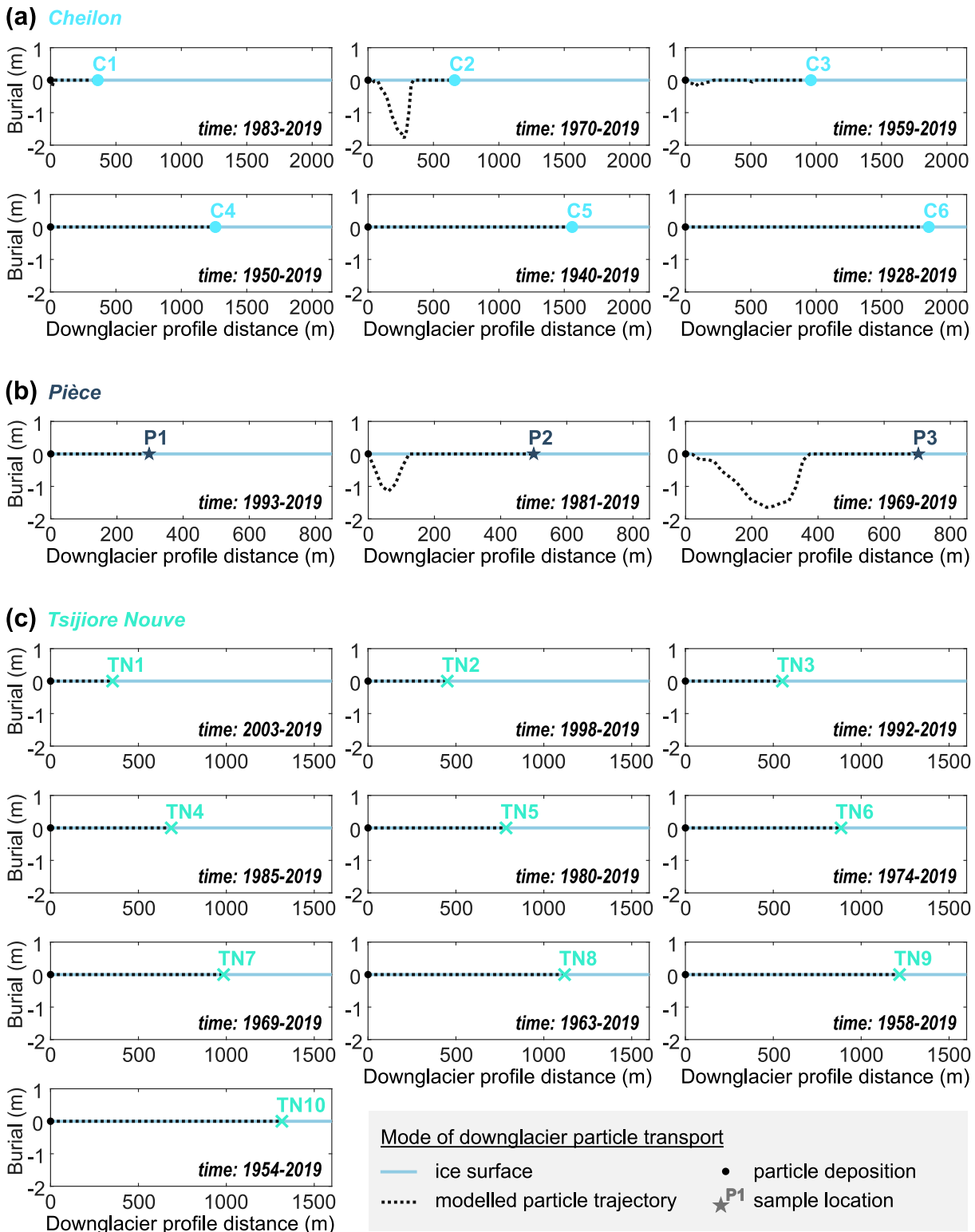


**Figure B4:** Modelled debris particle trajectories indicating the mode of downglacier particle transport from source rockwalls to sample locations at (a) Glacier de Cheilon, (b) Glacier de Pièce, and (c) Glacier de Tsijiore Nouvelle. Note that each graph stands for an individual sample. Shown is the burial depth of particles, which indicates whether a particle was transported within the ice (englacially; burial depth < 0 m) and shielded from cosmic radiation, or on the ice surface (supraglacially; burial depth = 0 m) and exposed to cosmic radiation. A particle's transport begins at the ice surface and profile head at the time as indicated and ends at the ice surface and downglacier distance of a sample's location in 2019.

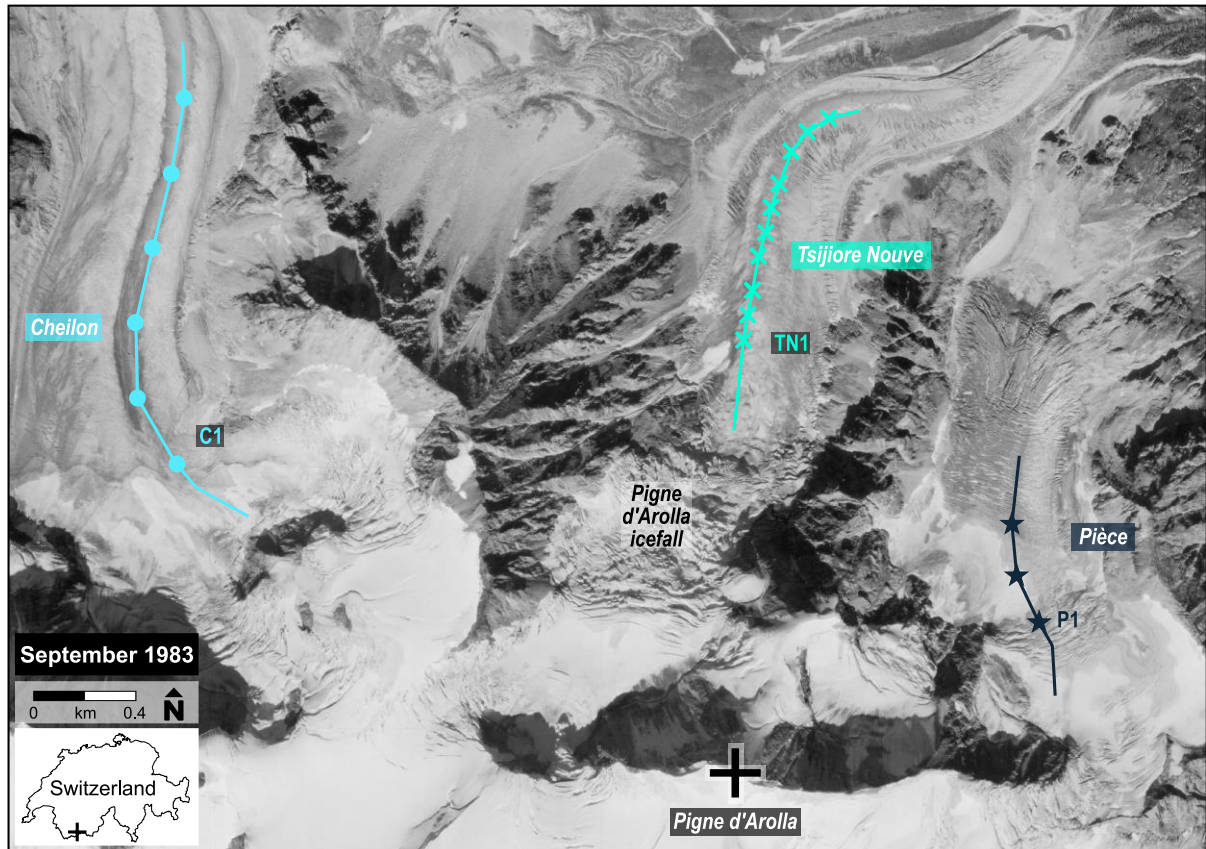


**Figure B5:** Orthoimage from 1983 indicating englacial debris transport close to the source rockwalls of Glacier de Cheilon and Glacier de Pièce as well as close to the base of the Pigne d'Arolla icefall at Glacier de Tsjiore Nouve. For reference, the respective medial moraine profiles and 2019 sample locations are indicated. The image excerpt is based on aerial images taken in September 1983 (orthoimage by Swisstopo, 2023).

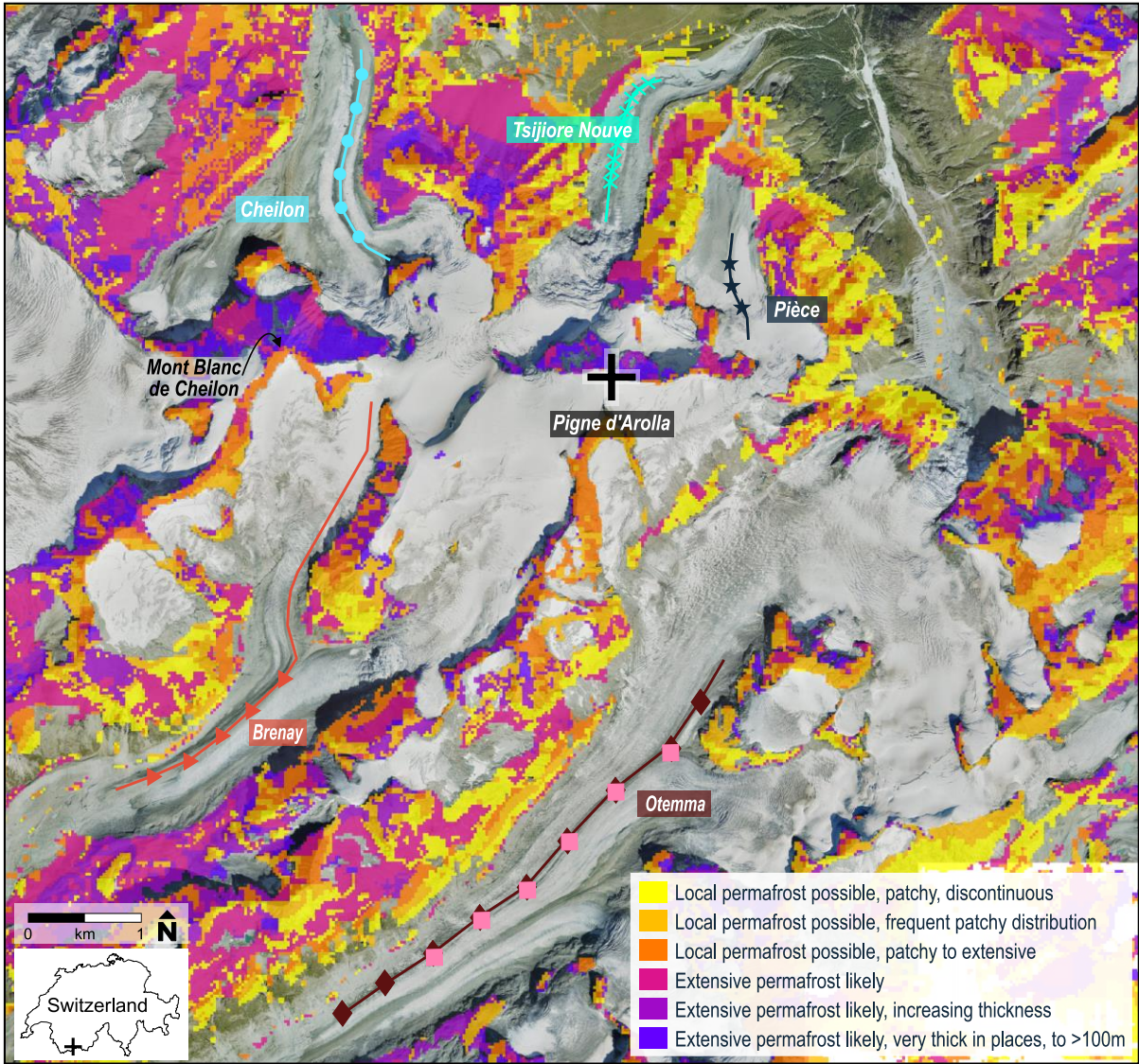


**Figure B6:** Permafrost distribution map showing the potential zone of modelled mountain permafrost across ice-free rockwalls and slopes in the area around Pigne d’Arolla. For reference, the respective medial moraine profiles and 2019 sample locations of Glacier du Brenay, Glacier de Cheilon, Glacier d’Otemma, Glacier de Pièce, and Glacier de Tsijiore Nouve are indicated. Note the extensive permafrost occurrence at the north faces of the east-west trending ridgeline between Pigne d’Arolla and Mont Blanc de Cheilon compared to the patchier permafrost occurrence to the south (potential permafrost distribution map by BAFU, 2005; orthoimage by Swisstopo, 2023).

**Table B1:** Comparison of model results for downglacier debris particle transport at Glacier du Brenay, Glacier de Cheilon, Glacier de Pièce, and Glacier de Tsijiore Nouve using different glacier surface velocity projections into the past for which we lack boulder tracking data. Listed are the sample ages, the additional  $^{10}\text{Be}$  accumulation ( $[^{10}\text{Be}]_{\text{transport}}$ ), and the transport-corrected apparent rockwall erosion rates based on (1) the velocity projections used in the study, as well as (2) half and (3) twice the velocity assumptions made. Note that the age estimates for the slower/faster glacier surface velocities largely differ by <5 years, except for few samples at Glacier de Cheilon where age differences with up to 14 years are still relatively small and do not affect our findings. The data were computed using the simple 1D particle trajectory model by Wetterauer *et al.* (2022b) and, except for the glacier surface velocities, settings/calculations were kept as described in the study.

Sample	Past velocity projections used			1/2× past velocity projections			2× past velocity projections		
	Age (yrs)	$[^{10}\text{Be}]_{\text{transport}}$ $\times 10^3$ (atoms $\text{g}^{-1}$ )	App. erosion rate (transport-corr.) (mm $\text{yr}^{-1}$ )	Age (yrs)	$[^{10}\text{Be}]_{\text{transport}}$ $\times 10^3$ (atoms $\text{g}^{-1}$ )	App. erosion rate (transport-corr.) (mm $\text{yr}^{-1}$ )	Age (yrs)	$[^{10}\text{Be}]_{\text{transport}}$ $\times 10^3$ (atoms $\text{g}^{-1}$ )	App. erosion rate (transport-corr.) (mm $\text{yr}^{-1}$ )
<i>Glacier du Brenay</i>									
B1	52	0.7	1.0	53	0.7	1.0	52	0.7	1.0
B2	63	0.9	0.7	63	0.8	0.7	62	0.9	0.7
B3	72	1.1	0.7	73	1.1	0.7	70	1.1	0.7
B4	83	1.5	0.8	84	1.5	0.8	80	1.6	0.8
B5	96	1.9	0.7	98	1.9	0.7	92	1.9	0.7
<i>Glacier de Cheilon</i>									
C1	36	1.0	5.1	36	1.0	5.1	36	1.0	5.1
C2	50	1.3	8.9	51	1.3	9.1	48	1.2	8.6
C3	61	1.7	4.5	65	1.8	4.7	55	1.6	4.4
C4	70	2.0	7.6	77	2.2	8.3	62	1.8	7.0
C5	80	2.3	36.7	90	2.5	87.5	70	2.0	23.2
C6	92	2.6	10.0	105	2.6	10.3	78	2.2	8.2
<i>Glacier de Pièce</i>									
P1	27	0.8	5.5	27	0.8	5.5	27	0.8	5.5
P2	39	1.0	5.9	39	1.0	5.9	39	1.0	5.9
P3	50	1.2	7.6	51	1.3	7.7	49	1.2	7.4
<i>Glacier de Tsijiore Nouve</i>									
TN1	16	0.4	10.6	16	0.4	10.6	16	0.4	10.6
TN2	21	0.5	12.7	21	0.5	12.7	21	0.5	12.7
TN3	27	0.6	18.7	27	0.6	18.7	27	0.6	18.7
TN4	34	0.8	15.6	34	0.8	15.6	34	0.8	15.6
TN5	40	0.9	21.3	40	0.9	21.3	40	0.9	21.3
TN6	45	1.0	7.4	45	1.0	7.4	45	1.0	7.4
TN7	50	1.1	15.1	50	1.1	15.1	50	1.1	15.1
TN8	56	1.3	9.3	56	1.3	9.3	56	1.3	9.3
TN9	61	1.4	34.5	61	1.4	34.5	60	1.4	33.2
TN10	65	1.5	18.9	66	1.5	19.3	65	1.4	18.7

### B3 Medial moraine sample data

Cosmogenic nuclide sample processing was carried out in the Helmholtz Laboratory for the Geochemistry of the Earth Surface (HELGES) at the GFZ German Research Centre for Geosciences in Potsdam, Germany, according to standard *in situ*-produced  $^{10}\text{Be}$  separation techniques (e.g., von Blanckenburg *et al.*, 2004). Debris samples were dried and sieved to a grain size fraction of 1-16 mm and then crushed down to the 0.125-1 mm fraction for further analysis. Quartz minerals were isolated and purified using physical (involving magnetic separator) and chemical (involving weak leaching procedures with hydrochloric acid, froth flotation, and repeatedly hydrofluoric acid and orthophosphoric acid leaches) separation techniques. *Meteoritic*  $^{10}\text{Be}$  was removed with an additional hydrofluoric acid leach. ~32-43 g of pure quartz were spiked with 0.2 g  $^9\text{Be}$  carrier (795 ppm) and decomposed in concentrated hydrofluoric acid. Cosmogenic  $^{10}\text{Be}$  was extracted using ion exchange chromatography, precipitated from the eluted solution, oxidized, and pressed into targets.

$^{10}\text{Be}/^9\text{Be}$  ratio measurements (**Table 3.1**) were carried out at the accelerator mass spectrometer (AMS) at the University of Cologne, Germany (Dewald *et al.*, 2013), normalized to the standards KN01-6-2 and KN01-5-3 with nominal  $^{10}\text{Be}/^9\text{Be}$  ratios of  $5.35 \times 10^{-13}$  and  $6.32 \times 10^{-12}$ , respectively.  $^{10}\text{Be}/^9\text{Be}$  ratios were converted into  $[\text{}^{10}\text{Be}]_{\text{measured}}$  and corrected for co-processed blanks with  $^{10}\text{Be}/^9\text{Be}$  ratios of  $1.19 \times 10^{-15}$  and  $1.56 \times 10^{-15}$ , according to the respective sample batches (**Table 3.1**).

### B4 Glacier surface velocities

Horizontal glacier surface velocities were reconstructed for years from 1977 to 2020 and along the sampled medial moraines at Glacier du Brenay (**Table B2**), Glacier de Cheilon (**Table B3**), Glacier de Pièce (**Table B4**), and Glacier de Tsijiore Nouve (**Table B5**). The datasets comprise ~40-year records, derived by manually tracing the displacement of medial moraine boulders between successive orthoimages for 10 tracking periods: 2017-2020, 2013-2017, 2010-2013, 2007-2010, 2005-2007, 1999-2005, 1995-1999, 1988-1995, 1983-1988, and 1977-1983.

Tables B2-B5 list all boulders that were tracked for each of the 10 boulder-tracking periods in downglacier order. To assign a boulder's path to a specific coordinate and to a single year, we provide for each tracked boulder the mean coordinate ( $X/Y$  in UTM) of its path projected onto the medial moraine profile as well as the derived glacier surface velocity ( $U$ ), and assign the data to the mean year of the respective tracking period.



No. of boulder	X	Y	U	X	Y	U	X	Y	U	X	Y	U	X	Y	U
	UTM	UTM	(m yr <sup>-1</sup> )	UTM	UTM	(m yr <sup>-1</sup> )	UTM	UTM	(m yr <sup>-1</sup> )	UTM	UTM	(m yr <sup>-1</sup> )	UTM	UTM	(m yr <sup>-1</sup> )
	Tracking period 2017-2020			Tracking period 2013-2017			Tracking period 2010-2013			Tracking period 2007-2010			Tracking period 2005-2007		
	mean: 2018_5			mean: 2015			mean: 2011_5			mean: 2008_5			mean: 2006		
89	376356	5090831	2.6												
90	376319	5090815	2.5												
91	376301	5090808	2.2												
92	376301	5090808	2.0												
93	376282	5090800	2.2												
94	376273	5090796	2.2												
95	376273	5090796	2.1												
96	376273	5090796	2.3												
97	376264	5090793	2.0												
98	376254	5090789	2.1												
99	376245	5090786	2.1												
100	376245	5090786	2.0												
101	376235	5090783	2.4												
102	376226	5090780	2.6												
103	376216	5090776	2.1												
104	376207	5090773	2.1												
105	376197	5090770	2.3												
106	376169	5090760	2.7												
107	376150	5090753	2.6												
108	376140	5090750	2.3												
109	376131	5090747	1.8												
No. of boulder	Tracking period 1999-2005			Tracking period 1995-1999			Tracking period 1988-1995			Tracking period 1983-1988			Tracking period 1977-1983		
	mean: 2002			mean: 1997			mean: 1991_5			mean: 1985_5			mean: 1980		
1	377501	5092301	32.4	376468	5090876	16.0	-	-	-	377307	5091503	29.4	377396	5091584	30.9
2	377554	5091800	7.0	376338	5090823	13.8				377270	5091469	29.6	377381	5091570	31.1
3	377554	5091800	6.3							377255	5091455	29.6	377233	5091435	34.8
4	377468	5091666	15.2							377028	5091258	31.2	377225	5091428	34.9
5	377457	5091649	13.7							376112	5090740	27.1	377173	5091381	35.3
6	377113	5091328	16.3							376008	5090704	26.2	377074	5091296	31.5
7	376951	5091193	17.2										376951	5091193	35.3
8	376936	5091180	17.1										376921	5091167	35.4
9	376882	5091135	17.5										376913	5091161	34.8
10	376768	5091053	17.4										376235	5090783	22.9
11	376711	5091012	18.0										376178	5090763	22.0
12	376662	5090977	17.1										376131	5090747	21.8
13	376662	5090977	17.1												
14	376551	5090911	16.1												
15	376468	5090876	15.8												
16	376338	5090823	12.1												
17	376282	5090800	9.9												
18	376226	5090780	8.3												
19	376178	5090763	8.4												

**Table B3:** 40-year record of glacier surface velocities at Glacier de Cheilon reconstructed from boulder tracking along its medial moraine profile. Note that the boulder order within each of the 10 datasets is independent from the other tracking periods, that data within the same row do not belong to the same boulder, and that the table is divided in an upper and lower part with five tracking periods each.

No. of boulder	X	Y	U	X	Y	U	X	Y	U	X	Y	U	X	Y	U
	UTM	UTM	(m yr <sup>-1</sup> )	UTM	UTM	(m yr <sup>-1</sup> )	UTM	UTM	(m yr <sup>-1</sup> )	UTM	UTM	(m yr <sup>-1</sup> )	UTM	UTM	(m yr <sup>-1</sup> )
	Tracking period 2017-2020			Tracking period 2013-2017			Tracking period 2010-2013			Tracking period 2007-2010			Tracking period 2005-2007		
	mean: 2018_5			mean: 2015			mean: 2011_5			mean: 2008_5			mean: 2006		
1	378442	5095308	2.9	378398	5095332	2.9	378371	5095347	4.2	378389	5095337	5.5	378398	5095332	8.2
2	378442	5095308	2.8	378389	5095337	3.4	378371	5095347	4.2	378389	5095337	5.5	378398	5095332	8.0
3	378415	5095322	4.7	378380	5095342	3.8	378371	5095347	5.9	378354	5095356	5.5	378371	5095347	8.4
4	378415	5095322	2.9	378362	5095352	3.9	378345	5095361	5.0	378354	5095356	6.5	378371	5095347	10.3
5	378415	5095322	4.3	378354	5095356	6.5	378336	5095366	5.9	378336	5095366	7.0	378354	5095356	8.3
6	378398	5095332	2.7	378354	5095356	4.5	378319	5095376	6.3	378336	5095366	6.5	378354	5095356	8.7
7	378389	5095337	3.0	378345	5095361	7.3	378319	5095376	5.9	378292	5095391	12.2	378319	5095376	14.3
8	378380	5095342	2.8	378336	5095366	5.0	378266	5095405	7.9	378292	5095391	8.6	378310	5095381	10.9
9	378371	5095347	3.5	378327	5095371	5.1	378239	5095435	8.8	378258	5095412	9.9	378275	5095400	11.7
10	378345	5095361	4.0	378319	5095376	5.9	378213	5095465	8.0	378226	5095450	8.7	378245	5095427	11.4
11	378345	5095361	6.2	378301	5095386	6.7	378165	5095530	8.1	378175	5095512	8.4	378110	5095626	9.5
12	378336	5095366	4.5	378258	5095412	8.2	378165	5095530	8.0	378175	5095512	8.4	378075	5095686	8.1
13	378336	5095366	4.5	378245	5095427	7.6	378165	5095530	8.0	378095	5095652	9.1	378029	5095855	9.3
14	378327	5095371	6.8	378239	5095435	8.6	378085	5095669	7.7	378065	5095704	7.1	378029	5095876	9.5
15	378327	5095371	4.7	378219	5095458	7.8	378054	5095721	6.5	378044	5095739	8.1	378029	5095896	10.4
16	378310	5095381	4.9	378193	5095488	7.8	378030	5095765	8.3	378029	5095855	8.3	378028	5095926	9.5
17	378301	5095386	5.8	378170	5095521	8.7	378029	5095876	8.1	378029	5095876	7.1	378028	5095946	9.0
18	378275	5095400	6.1	378150	5095556	9.3	378029	5095896	7.1	378029	5095896	7.8	378044	5096125	9.0
19	378275	5095400	6.6	378150	5095556	8.4	378029	5095916	7.0	378029	5095916	8.2	378046	5096135	9.9
20	378239	5095435	7.2	378110	5095626	6.9	378029	5095916	8.3	378028	5095926	7.9	378053	5096164	9.3
21	378232	5095442	7.6	378070	5095695	6.5	378028	5095946	8.1	378028	5095966	7.7	378056	5096174	9.5
22	378219	5095458	8.0	378065	5095704	8.5	378028	5095946	7.6	378028	5095976	6.9	378056	5096174	7.7
23	378200	5095481	7.7	378039	5095747	8.7	378028	5095986	8.2	378028	5095986	8.1	378103	5096359	2.5
24	378175	5095512	8.4	378034	5095756	7.7	378028	5095996	6.7	378028	5096006	8.1	378155	5096553	4.4
25	378155	5095547	5.8	378030	5095795	8.8	378028	5096006	7.6	378048	5096144	8.0			
26	378140	5095573	6.2	378029	5095906	8.4	378028	5096026	7.7	378051	5096154	7.7			
27	378135	5095582	5.1	378029	5095916	5.6	378028	5096026	7.8	378058	5096183	7.6			
28	378120	5095608	6.1	378028	5095946	7.2	378053	5096164	7.9	378061	5096193	7.8			
29	378100	5095643	4.7	378028	5095946	8.3	378056	5096174	8.1	378061	5096193	6.1			
30	378085	5095669	6.0	378028	5095976	8.6	378056	5096174	7.8	378073	5096242	7.9			
31	378060	5095713	5.2	378028	5095976	8.4	378066	5096213	6.7	378085	5096291	9.0			
32	378049	5095730	5.9	378028	5096006	7.9	378066	5096213	8.1	378085	5096291	8.8			
33	378030	5095765	5.8	378028	5096016	8.3	378078	5096261	8.1	378105	5096368	4.9			
34	378030	5095785	5.5	378028	5096026	8.3	378090	5096310	5.3	378111	5096388	7.2			
35	378029														



**Table B4:** 40-year record of glacier surface velocities at Glacier de Pièce reconstructed from boulder tracking along its medial moraine profile. Note that the boulder order within each of the 10 datasets is independent from the other tracking periods, that data within the same row do not belong to the same boulder, and that the table is divided in an upper and lower part with five tracking periods each.

No. of boulder	X Y U			X Y U			X Y U			X Y U			X Y U		
	UTM	UTM	(m yr <sup>-1</sup> )	UTM	UTM	(m yr <sup>-1</sup> )	UTM	UTM	(m yr <sup>-1</sup> )	UTM	UTM	(m yr <sup>-1</sup> )	UTM	UTM	(m yr <sup>-1</sup> )
	Tracking period 2017-2020			Tracking period 2013-2017			Tracking period 2010-2013			Tracking period 2007-2010			Tracking period 2005-2007		
	mean: 2018_5			mean: 2015			mean: 2011_5			mean: 2008_5			mean: 2006		
1	381604	5094541	5.5	381599	5094672	8.4	381600	5094642	8.2	381599	5094672	9.4	381598	5094682	12.3
2	381604	5094541	5.5	381593	5094732	8.8	381598	5094703	8.3	381599	5094672	9.0	381598	5094692	13.3
3	381601	5094622	7.0	381588	5094741	9.1	381598	5094703	7.7	381598	5094682	10.1	381598	5094692	12.8
4	381601	5094622	6.9	381564	5094785	9.4	381597	5094713	9.3	381528	5094857	9.4	381598	5094692	13.3
5	381600	5094652	7.0	381564	5094785	9.3	381583	5094750	9.4	381524	5094866	11.0	381598	5094703	12.7
6	381598	5094692	6.9	381559	5094794	9.4	381579	5094758	9.6	381519	5094876	11.0	381540	5094829	16.6
7	381598	5094703	7.4	381559	5094794	9.7	381579	5094758	9.8	381503	5094912	9.0	381536	5094839	15.6
8	381597	5094713	6.4	381511	5094894	6.3	381579	5094758	9.5	381499	5094922	8.0	381532	5094848	15.6
9	381597	5094723	6.5	381499	5094922	6.3	381519	5094876	6.5	381490	5094940	7.5	381499	5094922	10.8
10	381579	5094758	8.0	381499	5094922	6.7	381511	5094894	8.6	381490	5094940	9.1	381499	5094922	11.3
11	381574	5094767	7.6	381495	5094931	7.6	381507	5094903	7.7	381486	5094949	8.5	381499	5094922	12.3
12	381549	5094811	7.7	381486	5094949	5.9	381495	5094931	6.3	381486	5094949	8.6	381499	5094922	11.7
13	381549	5094811	7.9	381482	5094958	5.3	381490	5094940	6.0	381486	5094949	8.3	381499	5094922	11.9
14	381544	5094820	8.2	381470	5094986	5.4	381478	5094968	6.4	381478	5094968	6.8	381482	5094958	11.1
15	381544	5094820	7.5	381470	5094986	5.1	381478	5094968	5.4	381478	5094968	6.6	381478	5094968	11.2
16	381532	5094848	6.4	381470	5094986	5.7	381478	5094968	6.0	381474	5094977	5.5	381470	5094986	8.5
17	381511	5094894	5.5	381470	5094986	5.9	381478	5094968	6.3	381474	5094977	8.0	381470	5094986	9.4
18	381503	5094912	4.9	381466	5094995	5.0	381470	5094986	5.0	381470	5094986	8.0	381470	5094986	9.6
19	381490	5094940	5.3	381466	5094995	4.9	381470	5094986	4.6	381466	5094995	6.6	381462	5095025	8.4
20	381490	5094940	5.1	381463	5095005	4.6	381470	5094986	4.1	381463	5095005	6.0	381461	5095035	7.2
21	381486	5094949	5.2	381462	5095025	5.3	381463	5095086	6.1	381463	5095005	6.8	381460	5095045	8.4
22	381478	5094968	4.9	381462	5095025	5.5	381463	5095005	5.6	381463	5095005	7.3	381459	5095055	7.9
23	381474	5094977	4.2	381461	5095035	4.9	381463	5095005	5.2	381460	5095045	5.8	381459	5095065	9.3
24	381466	5094995	4.6	381461	5095035	5.3	381462	5095015	4.8	381459	5095055	5.3	381459	5095065	9.5
25	381466	5094995	5.0	381461	5095035	5.1	381462	5095015	5.0	381459	5095065	6.0	381455	5095106	10.4
26	381463	5095005	4.6	381460	5095045	5.4	381462	5095025	4.6	381458	5095075	6.0	381455	5095106	10.2
27	381463	5095005	5.1	381458	5095075	5.2	381462	5095025	5.4	381457	5095086	6.8	381452	5095146	8.0
28	381462	5095015	4.4	381456	5095096	4.9	381459	5095055	4.7	381457	5095086	7.0	381452	5095156	7.8
29	381462	5095015	3.9	381454	5095126	5.2	381457	5095086	4.7	381454	5095126	6.0	381452	5095156	8.0
30	381462	5095015	4.3	381454	5095126	4.2	381456	5095096	5.0	381454	5095126	6.1	381450	5095176	7.9
31	381461	5095035	4.7	381452	5095156	4.5	381455	5095106	5.0	381452	5095156	4.9	381449	5095186	7.9
32	381460	5095045	4.4	381452	5095156	4.5	381453	5095136	4.6	381451	5095166	5.7	381449	5095196	6.8
33	381459	5095055	4.6	381449	5095196	4.7	381452	5095146	4.4	381451	5095166	5.8	381448	5095206	7.9
34	381459	5095055	4.6	381448	5095206	4.5	381450	5095176	3.8	381449	5095186	5.6	381450	5095216	6.1
35	381459	5095065	4.5	381450	5095216	4.7	381450	5095176	4.5	381449	5095196	5.8	381451	5095226	6.7
36	381456	5095096	4.1	381450	5095216	4.0	381449	5095186	4.4	381449	5095196	5.0	381452	5095236	6.7
37	381455	5095106	4.5	381451	5095226	4.8	381449	5095196	4.5	381450	5095216	6.1	381452	5095236	7.5
38	381455	5095116	4.5	381451	5095226	3.2	381448	5095206	4.5	381450	5095216	3.8	381453	5095246	5.2
39	381452	5095146	4.0	381453	5095246	4.2	381448	5095206	3.6	381451	5095226	4.3	381455	5095256	9.5
40	381452	5095146	4.0	381455	5095256	4.3	381450	5095216	3.6	381451	5095226	5.6	381458	5095287	9.4
41	381451	5095166	3.8	381456	5095267	4.5	381451	5095226	4.0	381452	5095236	4.5	381460	5095297	9.1
42	381450	5095176	3.6	381456	5095267	5.0	381451	5095226	4.3	381453	5095246	4.7	381460	5095297	9.1
43	381450	5095176	4.0	381457	5095277	4.5	381451	5095226	3.8	381457	5095277	4.0	381460	5095297	8.2
44	381449	5095196	2.9	381458	5095287	4.6	381452	5095236	3.8	381457	5095277	6.0	381461	5095307	8.5
45	381449	5095196	3.5	381460	5095297	4.4	381453	5095246	4.5	381461	5095307	6.3	381463	5095327	7.2
46	381450	5095216	4.2	381460	5095297	4.8	381455	5095256	3.8	381462	5095317	6.1	381469	5095377	9.0
47	381450	5095216	4.1	381466	5095347	5.0	381455	5095256	4.1	381462	5095317	5.0	381469	5095377	7.8
48	381450	5095216	3.6	381466	5095347	5.2	381455	5095256	4.5	381462	5095317	6.4	381471	5095387	7.3
49	381451	5095226	4.2	381468	5095367	4.9	381458	5095287	3.7	381463	5095327	6.6	381472	5095397	8.2
50	381452	5095236	3.7	381468	5095367	4.1	381458	5095287	3.7	381463	5095327	5.9	381474	5095417	8.9
51	381452	5095236	3.7	381473	5095407	5.0	381460	5095297	4.8	381466	5095347	5.4			
52	381452	5095236	4.1	381473	5095407	4.3	381461	5095307	4.9	381469	5095377	6.0			
53	381453	5095246	3.2	381474	5095417	4.9	381463	5095327	4.9	381469	5095377	5.4			
54	381456	5095267	3.8				381463	5095327	4.8	381471	5095387	6.0			
55	381458	5095287	4.1				381463	5095327	5.3						
56	381460	5095297	4.7				381466	5095347	5.2						
57	381460	5095297	4.2				381467	5095357	4.0						
58	381460	5095297	4.6				381472	5095397	4.5						
59	381461	5095307	3.6				381472	5095397	4.3						
60	381462	5095317	3.7				381473	5095407	4.6						
61	381468	5095367	4.2												
62	381468	5095367	4.3												
63	381469	5095377	4.6												
64	381471	5095387	3.9												
65	381476	5095427	4.0												
66	381476	5095427	5.1												
67	381477	5095437	4.4												
No. of boulder	Tracking period 1999-2005			Tracking period 1995-1999			Tracking period 1988-1995			Tracking period 1983-1988			Tracking period 1977-1983		
	mean: 2002			mean: 1997			mean: 1991_5			mean: 1985_5			mean: 1980		
1	381503	5094912	13.6	381456	5095096	9.1	-	-	-	381457	5095277	18.8	-	-	-
2	381503	5094912	13.8	381455	5095116	8.6				381457	5095277	17.7			
3	381456	5095096	10.6	381454	5095126	8.2				381467	5095357	18.7			
4	381455	5095106	10.2	381453	5095136	8.7									
5	381451	5095166	9.3	381452	5095146	8.0									
6	381449	5095186	8.4	381452	5095156	8.0									
7	381448	5095206	8.2	381457	5095277	11.1									
8	381452	5095236	9.2	381461	5095307	10.2									
9	381468	5095367	10.9	381468	5095367	10.8									

**Table B5:** 40-year record of glacier surface velocities at Glacier de Tsijiore Nouve reconstructed from boulder tracking along its medial moraine profile. Note that the boulder order within each of the 10 datasets is independent from the other tracking periods, that data within the same row do not belong to the same boulder, and that the table is divided in an upper and lower part with five tracking periods each.

No. of boulder	X	Y	U	X	Y	U	X	Y	U	X	Y	U	X	Y	U
	UTM	UTM	(m yr <sup>-1</sup> )	UTM	UTM	(m yr <sup>-1</sup> )	UTM	UTM	(m yr <sup>-1</sup> )	UTM	UTM	(m yr <sup>-1</sup> )	UTM	UTM	(m yr <sup>-1</sup> )
	Tracking period 2017-2020			Tracking period 2013-2017			Tracking period 2010-2013			Tracking period 2007-2010			Tracking period 2005-2007		
	mean: 2018_5			mean: 2015			mean: 2011_5			mean: 2008_5			mean: 2006		
1	380377	5095656	23.7	380386	5095736	20.3	380408	5095916	17.3	380401	5095856	22.8	380394	5095796	27.8
2	380382	5095696	21.3	380386	5095736	19.2	380409	5095926	17.6	380402	5095866	23.2	380395	5095806	26.6
3	380383	5095706	20.2	380415	5095966	14.4	380415	5095966	11.4	380408	5095916	20.4	380401	5095856	24.5
4	380383	5095706	21.8	380417	5095976	18.2	380415	5095966	14.9	380408	5095916	21.2	380404	5095886	15.6
5	380384	5095716	19.7	380418	5095985	18.4	380417	5095976	16.0	380409	5095926	21.3	380410	5095936	17.3
6	380394	5095796	16.7	380420	5095995	11.0	380417	5095976	16.3	380409	5095926	13.1	380411	5095946	13.6
7	380396	5095816	13.9	380424	5096015	15.9	380442	5096104	9.8	380436	5096074	12.7	380411	5095946	22.9
8	380398	5095836	16.4	380427	5096035	18.0	380446	5096124	10.7	380438	5096084	12.5	380413	5095956	19.6
9	380399	5095846	13.7	380427	5096035	16.3	380454	5096163	6.0	380440	5096094	13.7	380415	5095966	19.2
10	380401	5095856	12.8	380431	5096055	14.7	380458	5096183	7.1	380440	5096094	13.7	380418	5095985	21.8
11	380407	5095906	11.1	380450	5096143	11.5	380458	5096183	10.1	380450	5096143	8.4	380420	5095995	19.1
12	380407	5095906	12.2	380454	5096163	11.7	380458	5096183	10.1	380454	5096163	8.2	380420	5095995	21.2
13	380411	5095946	13.6	380458	5096183	6.8	380467	5096233	9.0	380514	5096408	6.9	380427	5096035	20.1
14	380411	5095946	12.9	380462	5096203	7.6	380467	5096233	9.5	380523	5096447	7.7	380427	5096035	13.3
15	380413	5095956	13.2	380465	5096223	10.6	380467	5096233	9.1	380523	5096447	7.4	380431	5096055	14.8
16	380420	5095995	12.4	380465	5096223	10.3	380469	5096242	9.1	380523	5096447	8.5	380444	5096114	10.2
17	380420	5095995	12.1	380475	5096272	9.1	380469	5096242	9.5	380531	5096476	8.8	380444	5096114	12.5
18	380424	5096015	10.1	380475	5096272	9.9	380475	5096272	9.4	380553	5096532	6.8	380446	5096124	16.0
19	380424	5096015	12.9	380475	5096272	10.3	380531	5096476	7.6	380560	5096551	5.7	380448	5096134	10.5
20	380426	5096025	13.0	380475	5096272	10.7	380531	5096476	7.3	380571	5096579	7.8	380450	5096143	13.8
21	380426	5096025	12.1	380475	5096272	9.7	380531	5096476	8.2	380571	5096579	6.8	380450	5096143	13.8
22	380427	5096035	13.0	380484	5096301	9.3	380793	5096816	6.4	380574	5096589	7.4	380462	5096203	12.2
23	380429	5096045	13.1	380539	5096495	6.9	380803	5096819	6.6	380578	5096598	7.7	380463	5096213	13.1
24	380429	5096045	12.6	380542	5096504	7.1				380593	5096636	15.2	380477	5096282	12.9
25	380433	5096065	10.7	380542	5096504	7.4				380774	5096812	7.2	380496	5096339	11.4
26	380438	5096084	11.7	380624	5096698	5.9				380783	5096814	7.7	380502	5096359	11.0
27	380438	5096084	11.5	380624	5096698	5.7							380509	5096388	12.1
28	380440	5096094	10.3	380624	5096698	6.0							380514	5096408	8.7
29	380444	5096114	9.9	380624	5096698	7.6							380514	5096408	9.9
30	380450	5096143	10.1	380637	5096713	9.0							380516	5096417	11.2
31	380454	5096163	9.6	380813	5096821	4.4							380516	5096417	11.6
32	380456	5096173	8.1	380823	5096823	4.8							380525	5096457	11.0
33	380460	5096193	8.0										380542	5096504	9.0
34	380462	5096203	8.8										380542	5096504	11.4
35	380462	5096203	4.8										380556	5096542	12.1
36	380465	5096223	8.7										380564	5096561	10.4
37	380467	5096233	6.7										380571	5096579	6.9
38	380469	5096242	8.2										380582	5096608	7.2
39	380471	5096252	5.9										380585	5096617	6.1
40	380471	5096252	8.4										380589	5096626	8.0
41	380481	5096291	7.7										380631	5096705	6.8
42	380484	5096301	7.8										380746	5096800	5.8
43	380484	5096301	8.1										380755	5096805	6.1
44	380484	5096301	8.0										380764	5096809	7.0
45	380484	5096301	7.4										380774	5096812	11.7
46	380490	5096320	6.8										380774	5096812	6.5
47	380499	5096349	7.5												
48	380509	5096388	6.6												
49	380521	5096437	5.9												
50	380521	5096437	5.7												
51	380531	5096476	5.8												
52	380535	5096485	5.9												
53	380542	5096504	5.5												
54	380546	5096513	5.7												
55	380549	5096523	5.9												
56	380549	5096523	6.3												
57	380564	5096561	4.7												
58	380567	5096570	3.8												
59	380585	5096617	4.1												
60	380593	5096636	4.3												
61	380596	5096645	4.5												
62	380596	5096645	4.5												
63	380611	5096683	4.1												
64	380617	5096690	4.5												
65	380617	5096690	5.1												
66	380624	5096698	4.5												
67	380631	5096705	4.4												
68	380637	5096713	4.6												
69	380637	5096713	4.8												
70	380644	5096721	5.9												
71	380651	5096728	5.5												
72	380664	5096743	4.3												
73	380720	5096784	4.6												
74	380720	5096784	4.6												
75	380755	5096805	3.7												
76	380823	5096823	4.3												
77	380842	5096828	4.3												
78	380842	5096828	4.5												
79	380852	5096830	4.1												
	Tracking period 1999-2005			Tracking period 1995-1999			Tracking period 1988-1995			Tracking period 1983-1988			Tracking period 1977-1983		
	mean: 2002			mean: 1997			mean: 1991_5			mean: 1985_5			mean: 1980		
1	380431	5096055	18.3	380469	5096242	19.0	380469	5096242	16.3	380467	5096233	27.2	-	-	-
2	380436	5096074	18.7	380473	5096262	18.7	380499	5096349	13.0	380469	5096242	24.2	-	-	-
3	380477	5096282	16.2	380475	5096272	17.4	380502	5096359	16.9	380471	5096252	23.4	-	-	-
4	380481	5096291	15.8	380481	5096291	18.7	380505	5096368	16.6	380475	5096272	22.8	-	-	-
5	380509	5096388	12.2	380490	5096320	16.5	380509	5096388	16.6	-	-	-	-	-	-
6	380535	5096485	11.3	380493	5096330	15.7	380512	5096398	12.8	-	-	-	-	-	-

APPENDIX | **B**

No. of boulder	X	Y	U	X	Y	U	X	Y	U	X	Y	U	X	Y	U
	UTM	UTM	(m yr <sup>-1</sup> )	UTM	UTM	(m yr <sup>-1</sup> )	UTM	UTM	(m yr <sup>-1</sup> )	UTM	UTM	(m yr <sup>-1</sup> )	UTM	UTM	(m yr <sup>-1</sup> )
	Tracking period 1999-2005			Tracking period 1995-1999			Tracking period 1988-1995			Tracking period 1983-1988			Tracking period 1977-1983		
	mean: 2002			mean: 1997			mean: 1991_5			mean: 1985_5			mean: 1980		
7	380553	5096532	10.6	380496	5096339	15.5	380514	5096408	13.4						
8	380556	5096542	12.2	380516	5096417	15.3									
9	380571	5096579	11.7	380528	5096466	16.2									
10	380600	5096655	12.0	380531	5096476	15.7									
11	380657	5096736	12.5	380535	5096485	15.0									
12	380712	5096779	19.6	380549	5096523	15.3									
13				380567	5096570	14.5									
14				380582	5096608	14.8									
15				380585	5096617	17.6									
16				380611	5096683	14.7									
17				380651	5096728	15.4									
18				380670	5096751	15.9									
19				380677	5096758	16.2									
20				380783	5096814	13.3									

# Appendix C: sample IGSN

**Table C1:** List of medial moraine samples with their corresponding International Generic Sample Number IGSN.

Sample	Year of collection	IGSN	Sample	Year of collection	IGSN
<i>Glacier d'Otemma</i> (Wetterauer <i>et al.</i> , 2022a, 2022b)					
<i>/ upper medial moraine (UM)</i>			<i>/ lower medial moraine (LM)</i>		
UM1	2018	GFKW10007	LM1	2018	GFKW1000F
UM2	2018	GFKW1000G	LM2	2018	GFKW1000C
UM3	2018	GFKW10003	LM3	2018	GFKW10006
UM4	2018	GFKW10004	LM4	2018	GFKW1000E
UM5	2018	GFKW10000	LM5	2018	GFKW1000B
UM6	2018	GFKW10001	LM6	2018	GFKW10005
UM7	2018	GFKW10002			
UM8	2018	GFKW10009			
UM9	2018	GFKW1000A			
<i>Glacier du Brenay</i> (Wetterauer & Scherler, 2023a, 2023b)					
B1	2019	GFKW10019			
B2	2019	GFKW1001A			
B3	2019	GFKW1001B			
B4	2019	GFKW1001C			
B5	2019	GFKW1001D			
<i>Glacier de Cheilon</i> (Wetterauer & Scherler, 2023a, 2023b)					
C1	2019	GFKW1001H			
C2	2019	GFKW1001J			
C3	2019	GFKW1001K			
C4	2019	GFKW1001L			
C5	2019	GFKW1001M			
C6	2019	GFKW1001N			
<i>Glacier de Pièce</i> (Wetterauer & Scherler, 2023a, 2023b)					
P1	2019	GFKW1001E			
P2	2019	GFKW1001F			
P3	2019	GFKW1001G			
<i>Glacier de Tsjiore Nouvelle</i> (Wetterauer & Scherler, 2023a, 2023b)					
TN1	2019	GFKW1001P			
TN2	2019	GFKW1001Q			
TN3	2019	GFKW1001R			
TN4	2019	GFKW1001S			
TN5	2019	GFKW1001T			
TN6	2019	GFKW1001U			
TN7	2019	GFKW1001V			
TN8	2019	GFKW1001W			
TN9	2019	GFKW1001X			
TN10	2019	GFKW1001Y			
<i>Grosser Aletschgletscher</i> (Wetterauer & Scherler, in prep.)					
<i>/ Kranzberg medial moraine</i>			<i>/ Trugberg medial moraine</i>		
GA/K1	2019	GFKW1000L	GA/T1	2019	GFKW1000Z
GA/K2	2019	GFKW1000M	GA/T2	2019	GFKW10010
GA/K3	2019	GFKW1000N	GA/T3	2019	GFKW10011
GA/K4	2019	GFKW1000P	GA/T4	2019	GFKW10012
GA/K5	2019	GFKW1000Q	GA/T5	2019	GFKW10013
GA/K6	2019	GFKW1000R	GA/T6	2019	GFKW10014
GA/K7	2019	GFKW1000S	GA/T7	2019	GFKW10015
GA/K8	2019	GFKW1000T	GA/T8	2019	GFKW10016
GA/K9	2019	GFKW1000U	GA/T9	2019	GFKW10017
GA/K10	2019	GFKW1000V	GA/T10	2019	GFKW10018
GA/K11	2019	GFKW1000W	GA/T11	2019	GFKW1000K
GA/K12	2019	GFKW1000X	GA/T12	2019	GFKW1000J
GA/K13	2019	GFKW1000Y			



# Danksagung

At this point, I would like to thank everyone, who accompanied me in this work and during five great research years in Potsdam - whether in a professionally supporting, personally advising, or motivating manner.

First and foremost, I express my sincere gratitude to my supervisor Dirk Scherler. I am truly grateful for his scientific guidance, motivation, and constructive feedback during my PhD and my professional development. I am also very thankful for his care during years of pandemic home office with “MATLABing”, and his flexibility in terms of mobile working to balance my personal life with my work. Thank you, Dirk, for giving me the chance to be part of the COLD project and for believing in me and my work - I have gained many new skills during this time and would choose this very PhD project again anytime.

I am endless thankful and proud to have been part of the COLD project and team and grateful for the exceptional, enriching experiences and scientific insights that COLD and the ERC-grant (H2020-EU.1.1.; 759639) have enabled us to achieve. I very much appreciate the support from Leif Anderson during the first 1.5 years, whose fieldwork advices, numerous explanatory sketches, and introductory office-sessions on ice dynamics eased my entry into the world of glaciers and high-alpine landscapes. Special thank is owed to my PhD buddies Donovan Dennis and Deniz Gök for their company, four unforgettable and fascinating summers of fieldwork in the Alps, scientific and non-scientific discussions, and many hours of fun. Thank you, COLD'ers, for your strong backs, will, and energy to carry more than 400 kg of rocks with me downglacier and downvalley - the 5 COLD years were an incredible, adventurous and enriching experience for me that I would not want to miss.

I acknowledge that I had the opportunity to work and be trained in geochemistry laboratories of such high-quality standards. I am very grateful to Hella Wittmann, who took the time to teach me in the cosmogenic nuclide processing steps at the HELGES laboratory and helped me out with always practicable solutions when problems in the lab arose. Thank you, Hella, also for your very thoughtful and always prompt feedback on my studies. A big thank you also goes to my Hiwi Kristina Krüger, who assisted me in months of sample preparation. I thank Nadja Kuhl, René Kapannusch, Renee van Dongen, and Johannes Glodny who devoted time and energy to thoroughly train me in all the separation steps required for sample preparation. I thank Hartmut Liep, who always took care that I am still alive after long, dusty crushing sessions in the GFZ basement and to find the “healthiest” way for me to destroy my rocks. I thank Daniel Frick for his reliable help with sensitive measuring instruments and many administrative questions. After all, I am particularly thankful to Cathrin Schulz for accompanying me through all my sample batches in the “cosmo” lab, answering me with patience the same questions over and over again, and making my everyday “cosmo” life so much easier. Thank you - you all helped me to go confidently and safely through all (!) sample preparation steps, making long days of labwork successful and enjoyable.

Moreover, I thank Friedhelm von Blanckenburg and all the colleagues from the Earth Surface Geochemistry Section I crossed paths with for their support, input, and culturally enriching company. I am also very grateful for the administrative support by Conni Dettlaff, her always open ears, warm words, and cheerful manner. The group of Section 3.3 and its “Bier nach Vier”

made me always feel welcome inside and outside GFZ. Being a geomorphologist but located in geochemistry, I particularly thank the little reading group with Anne and Lizzie for our numerous meetings and encouraging discussions about geomorphological studies, science, and life that helped me to also maintain a broad view outside the “cosmo” world.

I would like to thank Emma, Helen, Richard, Sophia, Charlotte, Gunnar, Barbara, the AWI basketball crew, and many others for sharing not only science but also office, dinners, music, sports, many great activities, and lots of fun in Potsdam and Berlin. And, I thank Annö, Jil, and Seb for their friendship, their visits, and motivating calls despite the large distances.

I thank my boyfriend for his support, patience, and understanding as I pursue my goal.

Above all, I am deeply grateful to my parents and my brother. Knowing that you always stand behind me with your unconditional support, your advices, your encouragement, and your love drives my persistence and makes me find my way.